BOSTON UNIVERSITY

GRADUATE SCHOOL OF ARTS AND SCIENCES

Dissertation

HIGH ENERGY NEUTRINO ASTROPHYSICS WITH SUPER-KAMIOKANDE

by

SHANTANU DESAI

B.Tech., Indian Institute of Technology, 1995
M.A., Boston University, 1997

Submitted in partial fulfillment of the

requirements for the degree of

Doctor of Philosophy

2004

Approved by

First Reader

Lawrence R. Sulak, Ph.D.
Professor of Physics

Second Reader

Edward T. Kearns, Ph.D.
Associate Professor of Physics

Third Reader

Sheldon L. Glashow, Ph.D.
Professor of Physics

Acknowledgments

I would first like to thank my advisor Larry Sulak, who got me involved in the Super-K experiment and has given me exceptional advice, help and support throughout the course of my graduate career. I would also also like to thank Ed Kearns for his day to day guidance, advice, encouragement and making sure I never lose my focus. I am also grateful to Jim Stone for pushing me to finish my thesis on time. Much of the work in this thesis has been done in collaboration with Alec Habig, K. Nitta and C. Saji. I would like to thank each of them for patiently explaining many things over email when we were separated thousands of miles away. I am also grateful to other upmu members like Dave Casper, Todd Haines, T. Kajita, Danka Kielczewska, John Learned, A. Okada, Shige Matsuno, Kate Scholberg, Andy Stachyra, Bob Svoboda, M. Takita, and Jeff Wilkes for a lot of help, comments on my work and many stimulating discussions over email and in person. I am indebted to people outside the collaboration for answering all my questions and also offering very useful suggestions which have been incorporated, such as Joaquim Edsjo, Paolo Gondolo, Andrew Gould, Gerard Jungman, Marc Kamionkowski, Teresa Montaruli, Piero Ullio on Chapter[5]; Rob Duncan, Kevin Hurley, Jim Rhoads and Bing Zhang on Chapter[6], Tom Gaisser, Orlando Peres and Dave Seckel on Chapter[7].

I would also like to thank other members of my thesis committee like Ken Brecher, Shelly Glashow and Shyam Erramilli for challenging me with tough questions and offering very useful feedback on my work .

Being associated with the particle astrophysics group at Boston University has been an excellent learning experience. I am very much grateful to Alec Habig, Kate Scholberg and Chris Walter who trained me on Super-K software and analysis and always had an answer to all my questions. I always enjoyed the company of current and past members in our group such as Scott Clarke, Matt Earl, Serge Likhoded,

Mike Litos, Mark Messier, Chris Orth and Wei Wang.

While spending long months in Japan I enjoyed the company of other Super-K members such as Gene Guillian, Dawei Liu, Matthew Malek, Michael Smy, Dusan Turcan , and Mark Vagins.

Super-K benefits from the superb leadership of Y. Totsuka (prior to May 2002) and Y. Suzuki (post May 2002) as well as Hank Sobel and Jim Stone. I also admire their tenacity and resolve during the tough period we faced after the accident. I would also like to thank all the experts of the various detector subcomponents for their hard work and fixing problems in the middle of the night, to ensure Super-K has very good livetime.

I also like to thank other current and past Indian graduate students at Boston University for the wonderful time we had such as Arnab Majumdar, Janamjeya Chowdhury, Parantap Shukla, Prithwish Basu , and many more.

Before I joined the Super-K group I got a lot of help, advice, education and support from Chip Cohen, Mark Friedl, and Rai Weiss. Also I have learned a lot of astrophysics from the tough grilling questions asked by Ed Bertschinger, Paul Schechter, and Bruno Coppi to speakers in the MIT astrophysics colloquium series.

All my research and travel has been funded by U.S. Department of Energy.

HIGH ENERGY NEUTRINO ASTROPHYSICS WITH SUPER–KAMIOKANDE

(Order No.)

SHANTANU DESAI

Boston University Graduate School of Arts and Sciences, 2004

Major Professor: Lawrence R. Sulak, Professor of Physics

ABSTRACT

This dissertation presents various physics and astronomy results with upward going muons using the first five years of data from the Super–Kamiokande detector, which is a 50 kiloton water Cherenkov detector located in Japan. Upward muons produced by neutrinos interacting in the rock below the detector represent the highest energy neutrinos seen in Super–Kamiokande.

Using these events, I have searched for the signatures of annihilations of dark matter particles to high energy neutrinos in the center of Earth, Sun and the Galactic Center. Constraints on dark matter scattering cross-sections with nuclei using these results will be presented. Space-time coincidences from astrophysical transient sources such as gamma-ray bursts and soft gamma-ray repeaters are reported.

I have developed an algorithm to isolate a sample of events, called "showering upward going muons", which lose energy through radiative processes. We shall use this subset, whose parent neutrino energy is approximately 1 TeV, to do astrophysical searches in the high energy region, where the atmospheric neutrino background is reduced.

Contents

List of Tables

List of Figures

List of Abbreviations

ADC ..... Analog to Digital Converter

AGN ..... Active Galactic Nuclei

AMANDA ..... Antarctic Muon and Neutrino Detector Array

BATSE ..... Burst and Transient Source Experiment

CDM ..... Cold Dark Matter

CDMS ..... Cryogenic Dark Matter Search Experiment

CGRO ..... Compton Gamma-ray Observatory

DAMA ..... Dark Matter Search Experiment

DAQ ..... Data Acquisition

FRP ..... Fiber Reinforced Plastic

GNO ..... Gallium Neutrino Observatory

GPS ..... Global Positioning System

GRB ..... Gamma-ray Burst

GUT ..... Grand Unified Theories

HDM ..... Hot Dark Matter

HE ..... High Energy

HPW ..... Harvard Purdue Wisconsin

ID ..... Inner Detector

IMB ..... Irvine Michigan Brookhaven

IPN ..... Interplanetary Network

LE ..... Low Energy

LEP ..... Large Electron-Positron Storage Ring

MACRO ..... Monopole and Cosmic-ray Observatory

MINOS ..... Main Injector Neutrino Oscillation Search

MSSM ..... Minimal Supersymmetric Standard Model

OD ..... Outer Detector

PMT ..... Photomultiplier Tube

QTC ..... Charge to Time Converter

SAGE ..... Soviet American Gallium Experiment

SGR ..... Soft Gamma-ray Repeater

SLE ..... Super low energy

SNO ..... Sudbury Neutrino Observatory

SUSY ..... Supersymmetry

TDC ..... Time to Digital Converter

TQ ..... Time Charge

VME ..... Versa Module Europe

WIMP ..... Weakly Interacting Massive Particle

WMAP ..... Wilkinson Microwave Anisotropy Probe

Chapter 1

Introduction

This thesis deals with various physics and astronomy studies done using upward going muons with the Super–Kamiokande underground detector in Japan. We first start with a brief introduction and history of upward going muons and then review the importance of neutrino astronomy and neutrino physics. Finally we highlight how upward going muons can be used to study both these aspects.

1.1 Introduction to Upward Going Muons

Any particle physics experiment conducted on the ground is swamped by the overwhelming background of muons produced by cosmic ray interactions in the Earth's atmosphere. However this intensity decreases exponentially with increasing rock overburden as shown in Fig. 1.1. Rock overburden is usually indicated in units of density $\times$ column depth traversed in hg/cm^2 (where 1 hg = 0.1 kg) or in meters of water equivalent (mwe), where 1 mwe = 100 gm/cm^2. Besides the cosmic ray produced muons (which come from vertically above to near the horizon), a very small fraction of muons have been observed to travel upward into the detector. These muons cannot be from cosmic ray interactions since they would have to traverse more than

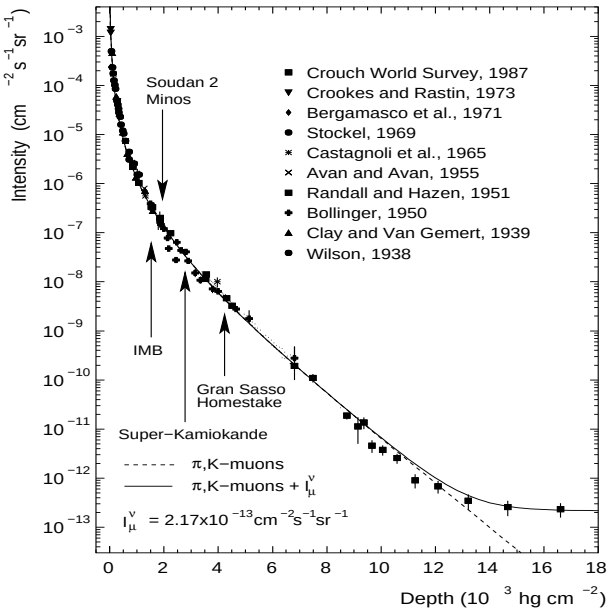

Figure 1.1: Measurements of cosmic ray muon flux as a function of depth in 1000 hg/cm^2 along with locations of various underground detectors [1].

6000 km through the rock. These muons which we shall refer to as "upward muons", are produced by charged-current interactions of muon neutrinos in the rock below the detector resulting in a muon which travels upward through the detector. The neutrinos are mainly produced from pion and kaon decays from cosmic ray interactions in the atmosphere on the opposite hemisphere of the Earth. This is illustrated in Fig. 1.2. Hence there are known as "atmospheric neutrinos". Within the flux of atmospheric neutrinos there could also be some neutrinos produced from extraterrestrial astrophysical sources. Such upward muons were first detected around 1965 in the Kolar mines in India [2] (located at a depth of 7500 mwe) and in the Witswatersands mine in South Africa [3] (located at a depth of 8800 mwe). Subsequently they have been measured by various underground detectors such as MACRO, Baksan, Nusex, HPW, Soudan, Frejus, SNO, IMB, MINOS, Kamiokande, Super-Kamiokande (this thesis) and also under-water/under-ice detectors such as AMANDA and Baikal. The

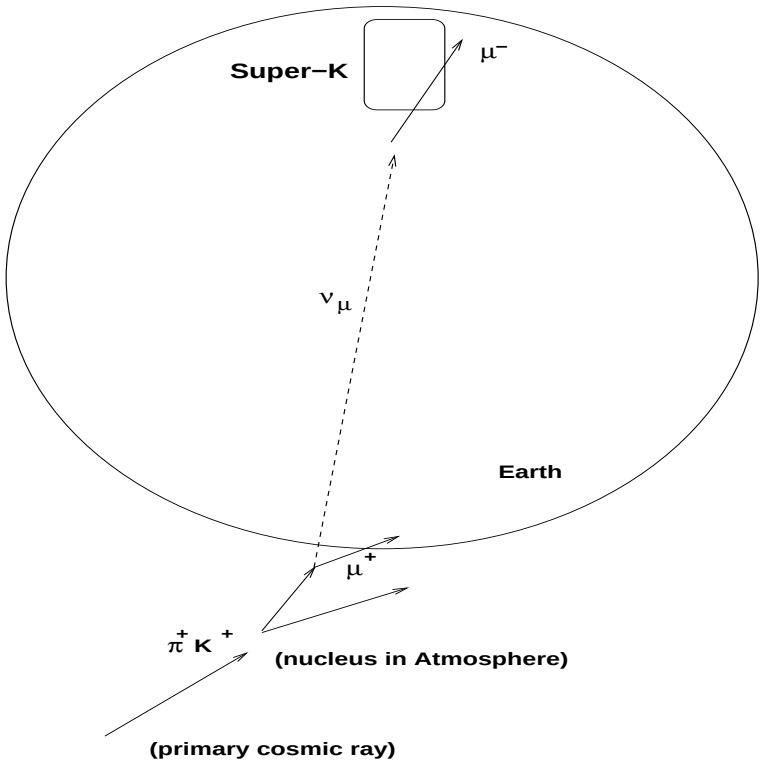

Figure 1.2: Schematic view of an upward going muon event.

measured flux of upward muons is about $10^{-13} cm^{-2} sec^{-1} sr^{-1}$ and is independent of depth. This is still several orders of magnitude smaller than the downward going muon flux (at Super-K depth, it is about 10^{-5} times smaller). The upward muons are mainly subdivided into two categories: upward thrugoing muons which punch through the detector and upward stopping muons, which decay inside the detector. Because of the 10^6 : 1 ratio of downward to upward muons in Super-K, we need very sophisticated muon reconstruction algorithms which can identify the direction of muons with very good angular resolution and efficiency to isolate the very small signal of upward muons, buried in the noise of a million or so downward muon events.

Besides upward muon events, the other category of atmospheric neutrino events seen in Super-K are called "contained events", in which neutrinos interact inside the

water of the detector to produce a lepton. These contained events are further subdivided into fully-contained events (in which the produced lepton stops inside the detector) and partially-contained events in which the lepton exits the detector. Of all these events the upward muons constitute the highest neutrino energy dataset. Since both the neutrino cross-section and the muon range increases with energy, the effective target volume for neutrino interactions via upward muons extends several kilometers into the rock as the neutrino energy increases. The neutrino energy spectrum of each of these category of events in Super-K is shown in Fig. 1.3

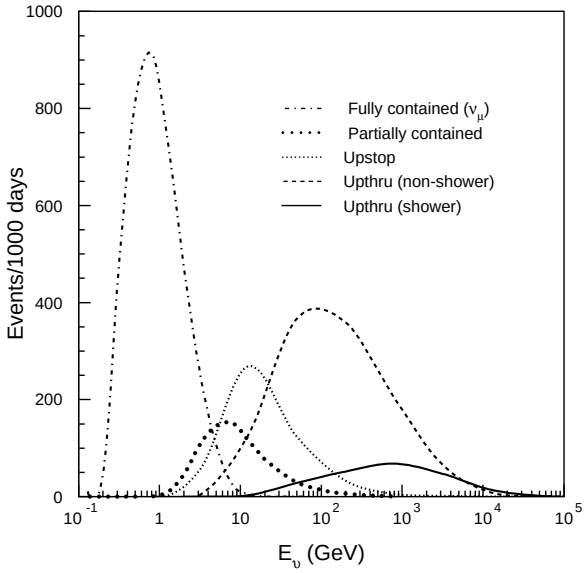

Figure 1.3: Neutrino energy spectrum of different datasets in Super-K.

1.2 Current Status of Neutrino Physics

Neutrino physics has undergone a revolution in the past 5 years. This started in 1998, when for the first time incontrovertible evidence was found for atmospheric neutrino oscillations in Super–Kamiokande [5, 6] indicating that neutrinos have non-zero mass.

Subsequently, further evidence for neutrino oscillations has mounted using different neutrino beams such as solar neutrinos [7, 8], reactor neutrinos [9] and accelerator produced neutrinos in a long baseline experiment [10]. A non-zero neutrino mass has far reaching consequences. It could provide clues to new physics beyond the Standard Model [11], baryogenesis [12] as well as for cosmology. In standard big bang model of cosmology, the number density of neutrinos per flavor is given by $n_\nu = \frac{3}{11} n_\gamma$ [13]. Using the observed value of $\Delta m^2 \simeq 10^{-3}$ eV^2 from atmospheric neutrino oscillations indicates that the density contribution of neutrinos is $\geq$ 0.1% [14], which is same that of the visible stars.

Since neutrino oscillations is an important component of this thesis, we outline the main physics of neutrino oscillations and indicate the evidence from Super-K (with contained events) which pinned the case for neutrino oscillations. More details of the phenomenology of neutrino oscillations and a complete derivation can be found in Ref.[15] and references therein.

If neutrinos have non-zero mass then the neutrino flavor eigenstates can be written as a superposition of its mass eigenstates. Assuming two neutrinos the oscillation probability is given by:

$$P(\nu_\mu \rightarrow \nu_\tau) = sin^2 2\theta sin^2 \left(\frac{1.27 \Delta m^2 (\mathrm{eV}^2) L(km)}{E(GeV)} \right), \tag{1.1}$$

where Δm^2 is the mass splitting between the two mass eigenstates ($\Delta m^2 = m_1^2 - m_2^2$), E is the neutrino energy, L is the distance traveled by the neutrino, and θ is an angle that characterizes mixing between the two states. The main evidence for atmospheric neutrino oscillations from ν_μ to ν_τ in Super–Kamiokande comes from the following pieces of evidences:

- Observation of the double ratio of ν_μ induced events to ν_e induced events in

data over Monte Carlo smaller than one. This is shown in Fig. 1.4 along with corresponding measurements from other experiments.

- Observation of up-down asymmetry in ν_μ-induced events as a function of zenith angle as shown in Fig. 1.5. Since neutrinos coming from below travel much larger path lengths than those coming from below they have a higher oscillation probability and thus there should be a deficit in the number of upward events as compared to expectation, and this is indeed observed.

- A deficit in the ratio of data to Monte Carlo for ν_μ induced events at large values of of L/E as shown shown in Fig. 1.6.

- The zenith angle distribution of upward thrugoing and stopping muons as well as the ratio of stopping to thrugoing muons is consistent with oscillations.

The best fit values for Δm^2 and $sin^2 2\theta$ are around 2×10^{-3} and 1.0 respectively. The exact allowed regions will be shown in Chapter 7. Besides this evidence for neutrino oscillations, another important development in neutrino physics has come from cosmology. In the last few years, the density fluctuation power spectrum has been measured with unprecedented accuracy over a wider variety of scales using CMB, galaxy redshift surveys, Lyman-α quasar absorption spectra etc. Since a small neutrino mass can erase small scale fluctuations, these measurements of power spectrum have enables us to obtain upper limits on neutrino mass. The current upper limits on neutrino mass obtained by combing data from WMAP and 2DF galaxy survey is: $\sum m_\nu < 0.7eV$ at 95% CL [17].

Inspite of this great progress there are still many unsolved problems in neutrino physics. We would like to know the absolute mass of all the 3 neutrino species, all the 3 neutrino mixing angles (which govern the oscillation probability of each neutrino

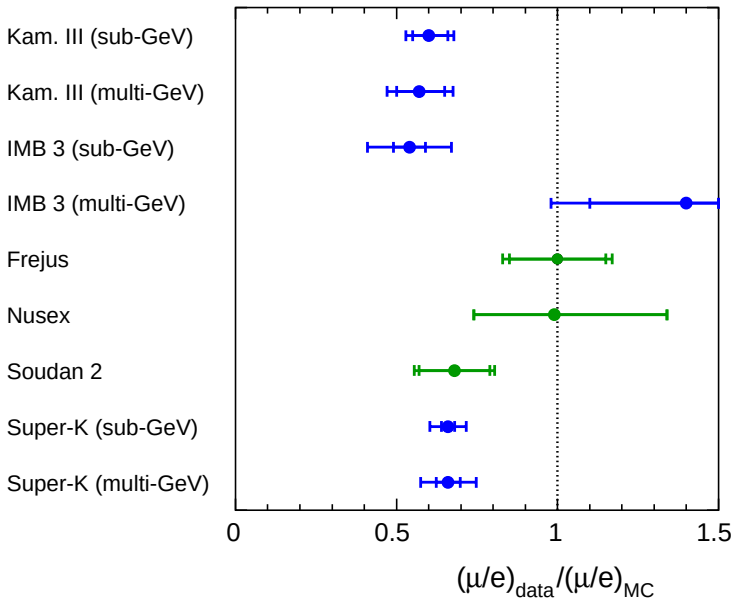

Figure 1.4: A Compendium of measurements of double ratio of ν_μ/ν_e for data over Monte Carlo. Figure from Ref. [16].

into the other two), neutrino chemical potential, neutrino magnetic moment. We would like to know of any CP violating effects, which would imply that the oscillation probability of neutrinos is different from anti-neutrinos.

1.3 Status of Neutrino Astronomy

Apart from cosmic rays, almost all our knowledge of the universe has come through electromagnetic astronomy spanning approximately 60 octaves in photon frequency from 10^4 cm radio waves to 10^{-14} cm. Though there has been no direct evidence for gravitational radiation, indirect evidence has been obtained with the high precision timing of PSR 1913+16 for more than two decades [18] as well as some other binary pulsars [19].

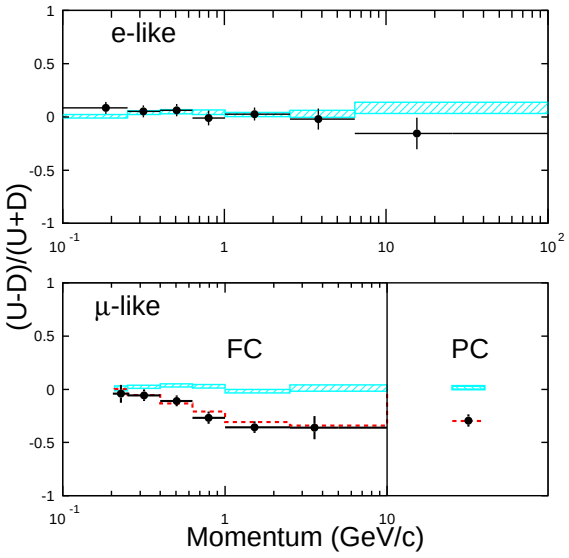

Figure 1.5: Up-down zenith angle asymmetry as a function of momentum for e-like as well as for μ-like events. The hatched lines show the expectations without oscillations. The dashed line shows the expectation for $\nu_\mu \rightarrow \nu_\tau$ assuming $\Delta m^2 = 0.0035$ eV^2, $sin^2 2\theta = 1.0$ [6].

Neutrino astronomy is still in a stage of infancy. To date, the only extraterrestrial neutrinos observed have been from the Sun and Supernova 1987A. Neutrinos resulting from nuclear fusion in the Sun have been observed with Homestake, Gallex/GNO, SAGE, Kamiokande, Super-Kamiokande and SNO experiments [20]. In the last 3 experiments, a direct correlation has been seen between the direction of the ν_e-induced events and the Sun as shown in Fig. 1.7. The observations of solar neutrinos demonstrated an important physics properties of neutrinos, viz. neutrino oscillations.

The first and only instance of extragalactic neutrinos being detected happened in 1987 when about 20 neutrinos were detected by the IMB [21] and Kamiokande collaboration [22] and about 5 tentative events by the BAKSAN Collaboration. The energies of these events as a function of time is shown in Fig. 1.9. The total energy released in neutrinos was estimated to be 6×10^{53} ergs [23]. These observations

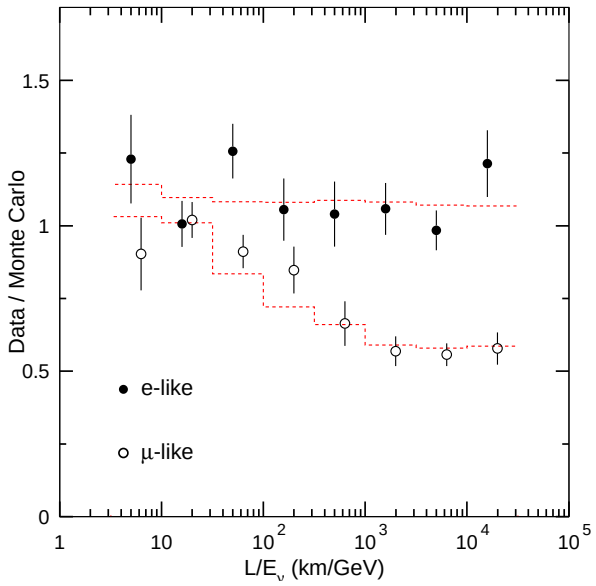

Figure 1.6: Ratio of data over Monte Carlo as a function of L/E_ν. The dashed line indicates the best fit assuming oscillations with the best fit values same as in Fig. 1.5 [6].

provided a wealth of information about stellar collapse, neutrino properties, as well as tests of special and general relativity [23]. Over the years more than hundreds of papers have appeared discussing these events in great details. A related source is diffuse relic neutrinos from all past supernovae in the 18-34 MeV region. These have not been observed. The current best limits are from Super-K [24] and this enables us to obtain strong constraints on star formation rate in galaxies [25].

Both the Sun and SN 1987A have been observed only at MeV energies. To date there has been no astrophysical observations at GeV energies. The main goal of high energy ($\sim$ GeV) neutrino astronomy is to peer into the interiors of astrophysical objects and to probe the high energy universe at very high redshifts. Unlike photons, high neutrinos rarely scatter and diffuse from their point of origin. Also the range of TeV γ rays is limited to about 10 Mpc [26], whereas high energy neutrinos

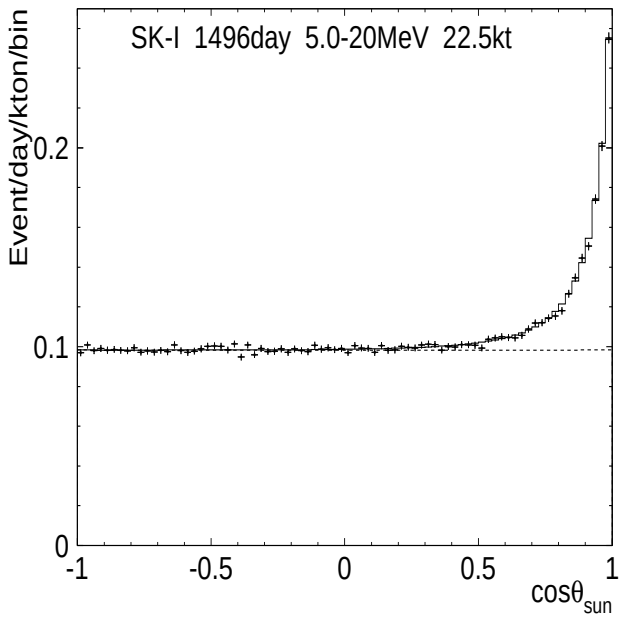

Figure 1.7: Solar neutrino peak as seen in Super-Kamiokande

can probe the very distant universe. A holy grail of ultra-high energy neutrino astronomy would be to detect the interactions from interactions of cosmic rays near the GZK cut-off with the 3°K Cosmic Microwave Background [27]. Other goals of neutrino astronomy are to search for neutrinos from cosmic acceleration processes like microquasars, supernova remnants, active galactic nuclei, gamma-ray bursts etc. Observations of these neutrinos could enable us to obtain insights on the physics of particle acceleration in these extreme astrophysical objects.

Another important source could be the annihilation of WIMPs. As discussed in Chap. 5, such an observation is important both from particle physics and cosmology. One of the main ingredients of the current standard hot big bang model [28] is that it contains about 27% cold dark matter. However the identity of the cold dark matter is still a mystery and WIMPs are one of the proposed candidates. Observations of neutrinos from WIMP annihilations could enable us to pin down some of the basic properties of WIMP dark matter such as its mass, couplings etc [29, 30] as well as

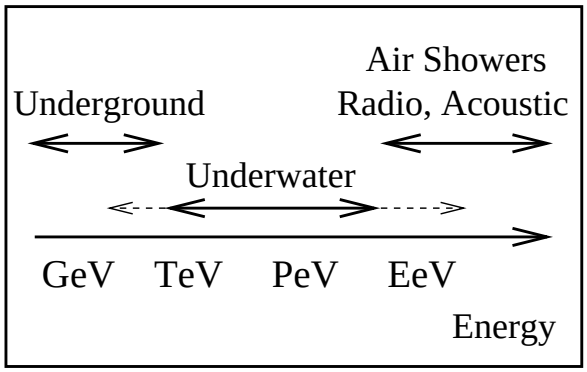

Figure 1.8: Neutrino energy range of various detection techniques. Figure from Ref. [26].

the WIMP relic density [31]. From the point of view of particle physics, observations of neutrinos from WIMP annihilations would point to evidence for supersymmetry and explain the origin of electroweak symmetry breaking.

Upward going muons in underground detectors are the ideal candidates to do studies of high energy neutrino astronomy in the energy region from GeV to TeV. TeV to PeV energies can be probed by current and future underwater km^2 detectors such as AMANDA, Antares, Baikal, Baksan, Icecube, Nestor. At energies above a PeV, acoustic and radio detection techniques need to be used. This is shown in Fig. 1.8.

At very low energies below KeV, there is a guaranteed source from the relic neutrino background left over from the Big Bang (whose existence was predicted even before the discovery of the neutrino [13]). However these are extremely hard to detect.

For these reasons it is important that the neutrino window to the universe be

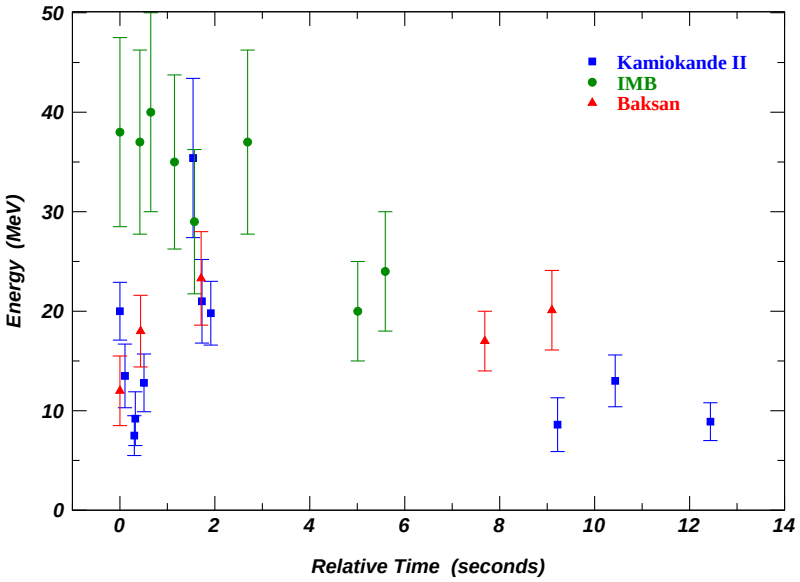

Figure 1.9: Electron/positron energies and relative times of the SN 1987A events recorded. Figure from Ref. [16].

exploited more. Also as the past history of astronomy has shown us that whenever a new window to the universe been opened it has thrown up surprises and revealed new sources which we never anticipated.

1.4 Importance of Upward Going Muons

Upward going muons can be used for studies of both neutrino oscillations as well as for neutrino astronomy above GeV energies. The main reason is that there is almost no background from other types of events resulting in a sample consisting of almost 100% pure muon neutrinos. Since their neutrinos travel through the earth, using matter effects upward thrugoing muons are used to distinguish between $\nu_\mu \rightarrow \nu_\tau$

from $\nu_\mu \rightarrow \nu_{sterile}$ oscillations [32]. Also because of their high energies they are correlated with the angles of their parent neutrinos. The mean angle between the reconstructed muon and parent neutrino is about 8.7° for upward stopping muons and 3.3° for upward thrugoing muons, assuming an atmospheric neutrino spectrum (which goes as $E^{-3.7}$). For astrophysical neutrinos where the spectrum can be harder, the relative angle is much smaller. This is in contrast to contained events, where the mean angle between the neutrino and lepton can be as large as 23° at p_l=1.2 GeV/c [6]. This strong correlation enables us to point the upward muons back to their sources with very good accuracy. From the point of view of neutrino physics, the upward muon sample provide an independent means of probing muon neutrino deficit as a function of both path-lengths (which ranges from 500 to 13000 km) as well as neutrino energy (which spans from 1 GeV to over 10 TeV). This would provide an independent confirmation of atmospheric neutrino oscillations. Assuming $\Delta m^2 \simeq 10^{-3}\text{eV}^2$ and $sin^2 2\theta \simeq 1.0$, a deficit of upward muons should mainly be seen at the nadir and not at the horizon. In addition there should be a greater deficit in upward stopping muons as compared to thrugoing muons. However there is still a 20% uncertainty in the absolute flux of upward muons and unlike contained events we cannot measure the flux of neutrino-induced muons above the horizon. Also from the point of view of astronomy the main irreducible background comes from atmospheric neutrinos which gets reduced in the energy range relevant to upward going muons. However, this can be turned around and upward going muons could be used to measure the high energy range of the atmospheric neutrino spectrum. This could be useful for next generation under-water neutrino telescopes designed solely for neutrino astrophysics. A global view of the atmospheric neutrino spectrum from about 15 MeV (below which it is swamped by the solar neutrino background) to about 100 TeV (where the flux of neutrinos from pions and kaons becomes equal to

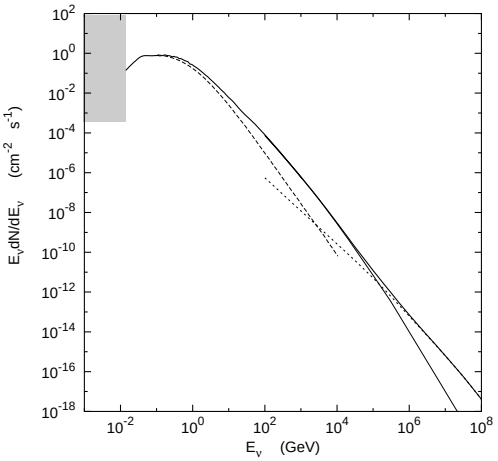

Figure 1.10: Global view of the atmospheric neutrino spectrum [4].

flux from charm production) [4] is shown in Fig. 1.10.

1.5 Outline of the Thesis

In Chapter 2, we describe the Super–Kamiokande detector which is used to record our dataset. Then in Chapter 3, we discuss the steps involved in the data reduction to extract the upward going muons and to calculate the livetime. In Chapter 4, we give a detailed summary of our observed dataset and describe the Monte Carlo used to simulate atmospheric upward going muon sample. We discuss what the upward stopping and thrugoing muon dataset tells us about neutrino oscillations. In Chapters 5 and 6 we discuss astrophysical searches such as WIMPs and other point sources. In Chapter 7 we bifurcate the upward thrugoing muon dataset into two categories : muons which undergo radiative energy losses called "showering upward muons" and those which don't. To the best of our knowledge, this has been done for

the first time in any neutrino/muon detector. Finally we repeat all the searches with the showering upward muon sample.

Chapter 2

The Super–Kamiokande Detector

2.1 Introduction

Super-Kamiokande stands for "Super" Kamioka Neutrino Detection Experiment. As the name indicates the Super–Kamiokande is a neutrino detector and is located in Kamioka, Japan. "Super" in Super–Kamiokande represents both its very large size (surface area of about 3900 m^2) as well as the vast energy range over which it can detect neutrinos spanning about 8 decades in energy range from a few MeV to over 1 TeV.

The Super–Kamiokande experiment has been used to study myriad physics and astronomy topics based on neutrinos such as solar neutrinos, neutrinos from both current and relic supernovae, atmospheric neutrinos, neutrinos from WIMP annihilation and high energy neutrinos resulting from variety of collapsed astrophysical objects. Super–Kamiokande has also been used to for nucleon stability studies like proton decay and neutron-antineutron oscillations. It can also detect cosmic ray muons and can be used to study cosmic ray related phenomenon. Super–Kamiokande also serves as the far detector for the K2K long-baseline neutrino oscillation experiment. This

thesis is based on high energy neutrinos seen in Super–Kamiokande. In this chapter we shall give a brief description of the various components of the detector. More details can be found in Ref. [33].

2.2 Location and History

The Super–Kamiokande detector is the world's largest underground water-Cherenkov detector. It contains 50000 tons of ultra-pure water and is located in Gifu Prefacture in Japan in a zinc mine under 1000 m of rock overburden.The cosmic ray muon rate in Super–Kamiokande is about 3 Hz. It uses photomultiplier tubes to detect the Cherenkov light. The geographic co-ordinates of Super–Kamiokande are $36°25'$ N Latitude and $137°18'$ E Longitude.

Super–Kamiokande started data-taking from April 1996 and continued uninterruptedly until July 2001 when it was shut-down for refurbishing the dead photomultiplier tubes. For rest of the thesis we shall refer to this phase as S-K-1. Near the end of this upgrade in November 2001 when the water level in the detector was about half-full there was a accident in which about 6800 photo-tubes got destroyed. Since then the detector has started re-taking data from about January 2003 with a different configuration. Throughout the operation of Super–Kamiokande the performance of the detector and various components, data-taking and environment has been monitored 24 hours a day by physicists in three 8 hour shifts per day.

2.3 Cherenkov Radiation

When a charged particle passes through a medium with a speed which is greater than the speed of light in the medium it creates an electromagnetic shock wave as

shown in Figure 2.1. This was first discovered in 1934 by P. Cherenkov and is called Cherenkov effect. The wavefront of the resulting radiation propagates at an angle given by $\theta = cos^{-1}\left(\frac{c}{nv}\right)$ where c is the speed of light in vacuum, v is the velocity of the particle and n is the refractive index of the medium. Super–Kamiokande uses the Cherenkov effect to detect particles and the Cherenkov photons are detected by photomultiplier tubes (PMTs) surrounding Super-K.

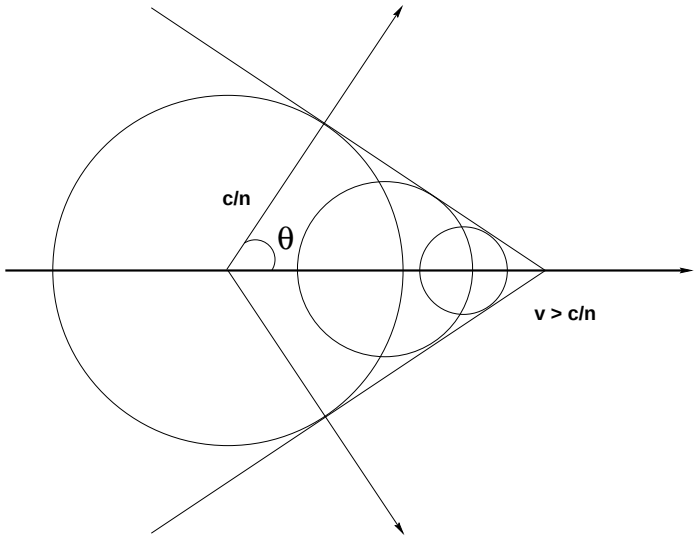

Figure 2.1: Illustration of Huygens' construction of the wavefront of Cherenkov radiation.

The number of Cherenkov photons emitted (N) per unit wavelength ($d\lambda$) and per unit length (dx) is given by [34] :

$$\frac{d^2N}{dxd\lambda} = \frac{2\pi\alpha}{\lambda^2}\left(1 - \frac{c^2}{v^2n^2(\lambda)}\right) \tag{2.1}$$

Here α is the fine-structure constant. For particles moving at the speed of light $\simeq$ 3400 photons/cm are emitted between 300-500 nm where the Super-K PMTs are most sensitive.

2.4 Detector Structure

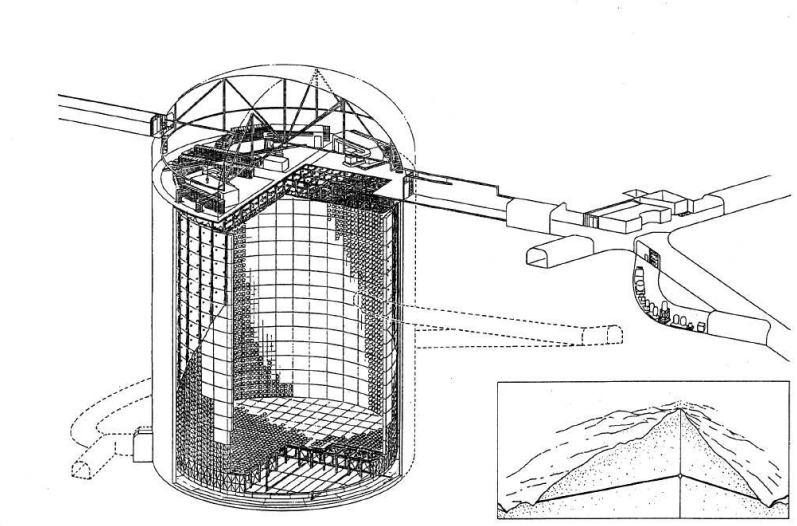

Figure 2.2: A rough schematic of Super–Kamiokande detector.

Super–Kamiokande consists of a cylindrical stainless steel tank, 39 m diameter and 42 m high. It is optically isolated into two regions : Inner Detector (ID) and Outer Detector (OD). ID consists of a concentric cylinder inside the tank with height of 36.2 m and diameter 33.8 m. The remaining region which is about 2.05 m thick along the detector walls and 2 m thick on the top and bottom constitutes the OD. The ID is surrounded by 11,146 20-inch PMT's facing inwards and the OD consists of 1885 outward facing 8 inch PMTs. A 55-cm dead region constitutes the support structure for both OD and ID pmts. The walls of the OD and both the top and bottom of the tank are covered with reflective Tyvek (manufactured by Dupont) to enhance the total light collected. The reflectivity of the Tyvek is about 90% at 400 nm falling to about 80% at about 340 nm.

To maximize water transparency and backgrounds due to natural radioactivity, the water in the detector is ultra-purified by a special multi-step purification scheme

which includes filtration, reverse osmosis and degasification. More details on the water purification scheme can be found in Ref. [33]. Also the inner surfaces of the tank contain about 26 Helmholtz coils which reduce the magnetic field at the site from 450 mG (which is problematic for the PMTs) to 50 mG.

2.5 Photomultiplier Tubes

Photomultipler tubes (PMTs) are the light sensitive elements of the Super–Kamiokande detector which detect the Cherenkov photons. They work on the basis of photo-electric effect.

2.5.1 ID PMT

The ID consists of 11146 50-cm PMT's (manufactured by Hamamatsu) with 40% photo-cathode coverage. A complete description of the 50-cm PMT can be found in [35]. A schematic view is shown in Figure 2.3 The photocathode is approximately hemi-spherical in shape and consist of a bialkali (Sb-K-Cs) photocathode with a peak quantum efficiency of about 20% at 360-400 nm. The average transit-time spread for 1 pe signal is 2.2 ns. The average dark noise rate at 0.25 pe level is about 3.5 Khz. They have a gain of 10^7 with voltages ranging from 1700 to 2700 V.

2.5.2 OD PMTs

The OD consists of 1885 20-cm PMTs. These PMTs were recycled from the IMB experiment after that experiment was terminated in 1991. To enhance the light collection efficiency of the OD, waveshifter plates are attached to each OD PMT [36]. The waveshifter plates are square acrylic panels of length 60cm and about 1.3 cm

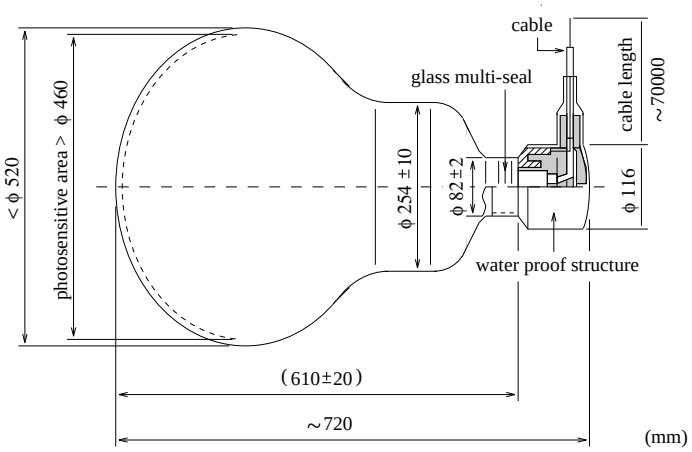

Figure 2.3: Schematic view of the 50-cm ID PMT.

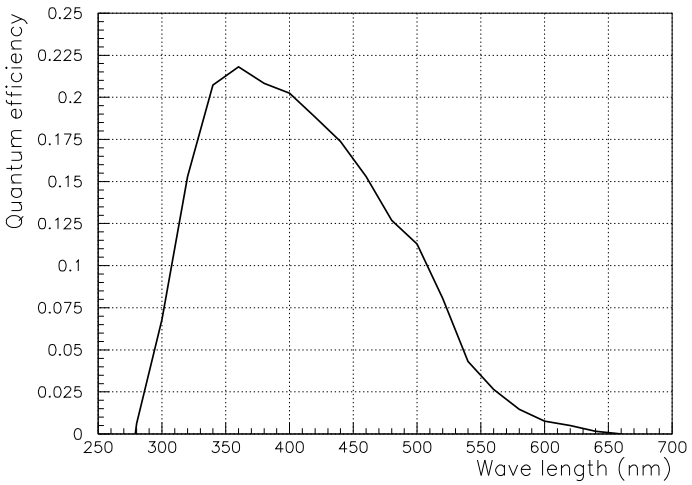

Figure 2.4: Photocathode quantum efficiency as a function of wavelength.

thick and are doped with 50 mg/l of bis-MSB. The PMT is mounted into a machined hole at the center of the plate. These plates absorb ultra-violet light and re-radiate in the blue-green where the PMT sensitivity peaks. The waveshifter plates increase the light collection efficiency of the OD by about 60%. The timing resolution of the OD pmts is 15 ns with the waveshifter plate and 13 ns without the waveshifter plate [36]. This is adequate for the OD since it is mainly used as a veto counter.

2.6 Data Acquisition System

The detector data acquisition system (DAQ) is responsible for recording and storing the size and time of electronic pulses from PMTs in a format suitable for Physics analysis. Brief descriptions of ID and OD DAQ is given in the next two sections. More details can be found in Ref. [33].

2.6.1 ID Electronics and DAQ

The signals from the ID PMTs are fed to 48 Tristan-KEK online crates. Each crate contains a Gong module which distributes the trigger information, a bus-interface Super-Controller Header and 20 Analog Timing Modules which work both as an ADC (Analog to digital converter) and a TDC (Time to digital converter). Each channel requires a threshold of 0.32 pe for a signal to be recorded. When a signal in a channel is recorded an -11mV, 200 ns wide pulse is generated. These pulses are added together with all other channels and if the sum exceeds a certain threshold, a global detector trigger is issued. This trigger then gets passed to a Super memory partner module for transfer to the online computers. These are then read by 8 Sun workstations through a bit 3 VME-sbus adapter card. This is then sent to a central online host computer where the data gets assembled into an event.

Each event in SK has 2 independent time stamps. The relative timing between two independent events is measured with a 48-bit counter driven by 50 MHz clock. This clock can be used to measure the time between two successive events to an accuracy of $\simeq 20$ ns. This clock is used for calculating the upward muon livetime as explained in Sect. 3.7. The absolute time of each event is also obtained from a GPS receiver with an accuracy of about 10 μ-sec. More details can be found in Ref [37].

2.7 OD Electronics and DAQ

The OD PMT signals are fed into the huts. A single coaxial cable feeds high voltage to the PMTs and registers its analog signals. High voltage is distributed by 4 Le Croy 1454 mainframes corresponding to each electronic hut. Each mainframe controls 48 channels of high voltage out of which 40 are actually used. Each high voltage channel is connected to a "paddle card" which fans out voltages to 12 PMTs. These paddle cards are used to distribute high voltage to 12 PMTs as well as to pick up the analog PMT signals through a high voltage capacitor and resistor network allowing a single cable to be used for both high voltage and signal.

The PMT signals from the paddle cards are fed to charge to time conversion modules (QTC's) which were designed and tested at Boston University during 1994-96. The QTC's measure charge and timing information from PMT pulses and convert it into a form so that it can be read by the TDC's. If the height of the PMT pulse exceeds $\simeq 0.25$ pe the QTC module generates a logic pulse. The start of the logic pulse indicates the hit time of each PMT signal and the width of the pulse is proportional to the total charge in the channel. They also generate a 25 mV and 200 ns wide pulse which is used for generating the OD trigger. Each QTC module calculates the "Hitsum" by adding these pulses. The Hitsums from each module are then sent to the central hut where they are summed to form the global Hitsum which is used to generate the OD trigger. More details of the QTC module and setup used to test the QTC's can be found in Ref. [38].

The output from the QTC pulse is digitized by LeCroy 1877 Fastbus Time-to-Digital Converter (TDC) which records the start and stop time of the ECL pulse. OD data gets recorded only if a global trigger is received from the central hut. OD hits get saved in a window which starts 10 μ sec before a global trigger and terminates 6

Trigger type	Threshold	No of hits	Energy	Trigger Rate
Super Low Energy	222 mV	20	3.5 MeV	550 Hz
Low Energy	320 mV	29	5 MeV	11 Hz
High Energy	340 mV	31	6 MeV	6 Hz
Outer Detector	N/A	19	N/A	3 Hz

Table 2.1: Summary of triggers used in Super–Kamiokande.

μ sec after it. The TDC data are sent via a Fastbus Smart Crate Controller module to a Sun workstation where it gets sent to an online host for addition to the event data. More details about the OD DAQ can be found in Ref. [39].

2.8 Triggers

During Super–Kamiokande data taking various triggers are used including special triggers for calibration data. This helps in designing cuts to filter out or select events depending on the physics analysis someone wants to do. A Hitsum signal of amplitude -11 mV and width 200 ns is generated when a ID PMT exceeds its threshold value. These Hitsum signals are then analog-summed per quadrant and then summed to generate the global Hitsum signal. This is then fed to many discriminators set at different thresholds to generate the SLE, LE and HE triggers. The OD trigger depends on the value the Hitsum signal generated by the QTC's. A summary of the various trigger types, thresholds and trigger rates used in Super–Kamiokande is shown in table 2.1. The trigger signals are fed to into the trigger module which generates a global trigger signal.

2.9 Radon Hut

Outside the mine entrance to the Super–Kamiokande detector there exists a prefabricated hut which contains the radon free air system and is called the radon hut. This is used to supply radon-free air in the air-space above the water tank. The radon free air is generated by drying the input air and passing it through charcoal filters. The carbon in the charcoal absorbs the radon gas thus preventing it from entering the detector. The air is then filtered and injected into the region above the water in the tank. The injected air concentration is about $10 mBq/m^3$. More details about the air purification system can be found in [33].

The radon hut also contains dual GPS antennae and receivers used for precise absolute time synchronization. The GPS receivers are linked to the data acquisition systems in the Super–Kamiokande detector via a 2 km long optical fiber cable. The GPS receivers are used to provide absolute timestamps for Super–Kamiokande data. The GPS receivers receive their data (with $\simeq$ 100 ns accuracy) from the GPS satellite network, provided by the US Naval Observatory.

2.10 Calibration

Understanding the behavior of various components of Super–Kamiokande is a very important step for any physics analysis done. First proper calibrations of the PMTs need to be done to convert the ADC and TDC counts recorded into PMT charge and timing information in pico-coulombs and nano-seconds respectively. The hit charge needs to be converted to an energy scale.

Also light scattering and absorption in the water used in the tank as well as its time variations is important in order to understand how many photons emitted from

Cherenkov radiation get absorbed/scattered before reaching the PMTs.

Here we shall briefly describe the calibrations used to understand and tune the PMT properties. We shall skip the details about energy calibration using LINAC and DT generator which is mainly important for low energy neutrino analysis. Details about energy calibration as well as charge and timing calibration can be found in Ref. [33].

2.10.1 Relative PMT Gain Calibration

At the beginning of the experiment, the high voltages of all PMTs were set so that all of them have equal gains.

Light which is generated by a Xe lamp gets passed through an ultraviolet filter which gets injected into a scintillator ball via an optical fibre. The scintillator is an acrylic ball doped with BBOT scintillator and MgO powder. BBOT absorbs ultraviolet light and re-emits it in the blue-green region with a peak at about 440 nm where the PMTs are most sensitive. The intensity of the light is monitored using a 2 photodiodes and a 2-inch PMT which is also used to trigger the detector.

The high voltage of each PMT is adjusted so that the "corrected charge" after accounting for PMT acceptance, light attenuation due to distance and finite water-transparency is the same for all PMTs. This measurement is done for various positions of the scintillator ball and high voltage settings. The long term stability of PMT gain was monitored using the same method and around September 1998 the standard deviation of the relative PMT gain increased to about 7.7 %. The spread in relative gains is corrected in the software.

2.10.2 Absolute PMT Gain Calibration

The absolute gain of each PMT at the single photo-electron level is measured using gamma rays from a Nickel-Californium source. This allows us to convert the PMT charge measured in pico-Coulombs (pC) to the number of photo-electrons (p.e.). The photons are generated by neutron capture on Ni with energy of about 9 MeV. Such low energy ensures that the number of photo-electrons detected by each PMT rarely exceeds 1. Therefore the response of each PMT to these events gives the single-photo-electron distribution. A sample distribution for one PMT is shown in Fig. 2.5. The thumb rule for conversion between PMT charge and p.e. is : 2.05pC $\equiv$ 1p.e.

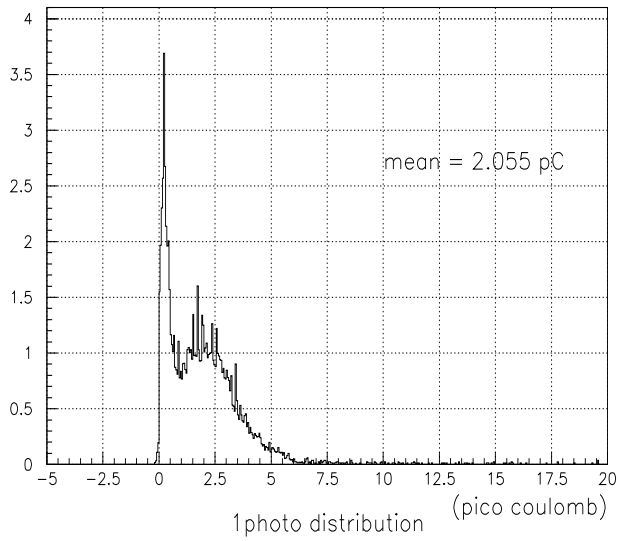

Figure 2.5: Sample single photoelectron distribution.

2.10.3 PMT Timing Calibration

The relative timing offset of each PMT must be measured very accurately for event reconstruction. This depends on signal cable length as well as the electronics response time.

A laser calibration system is used to measure these offsets. A pulsed nitrogen laser with $\simeq 3\ ns$ pulse width is attached via an optical fiber to a diffuse ball in the detector. The timing offsets are measured at various light levels to generate a "TQ" map which is a lookup table of the timing offset for each PMT tube as a function of the measured light. A typical TQ map is shown in Figure 2.6

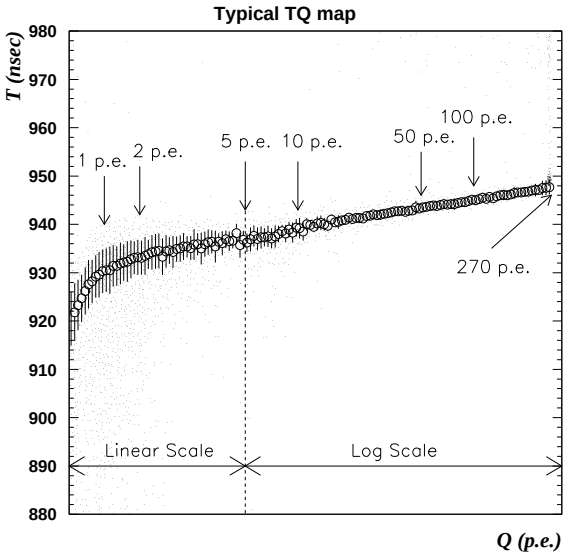

Figure 2.6: TQ map for a typical PMT.

2.11 Water Transparency

Photons generated by Cherenkov radiation in Super–Kamiokande get absorbed and scattered in the water resulting in an exponential attenuation of number of photons as a function of distance from they get emitted. This optical attenuation length in water is called water transparency and measures the combined effects of scattering and absorption. In Super–Kamiokande the water transparency as a function of wavelength (including the scattering and absorption parameters) is measured using a dye and nitrogen lasers. More details on this can be found in [33]. The comparison of

measurements of water attenuation length with these methods with the estimated attenuation length using Monte-Carlo simulations is shown in Fig 2.7. Here we shall focus on an indirect method using cosmic ray muons to measure the wavelength averaged attenuation length.

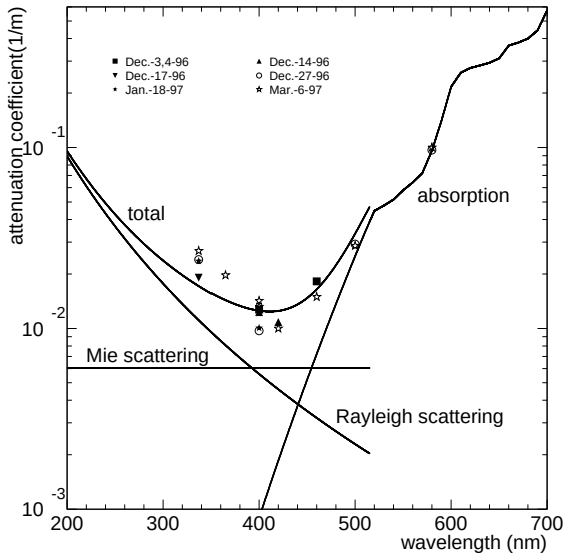

Figure 2.7: The attenuation coefficient $(1/L(\lambda))$ measured in Super–Kamiokande at various wavelengths along with the estimated length (solid line) obtained using Monte-Carlo simulations

The cosmic ray muon rate in Super–Kamiokande is about 3 Hz. Cosmic ray muons which lose energy via ionization deposit a constant number of Cherenkov photons per unit track length. The no of p.e's detected by a PMT can be expressed as

$$Q = \text{const}\frac{f(\theta)}{l}\exp\left(-\frac{l}{L}\right). \tag{2.2}$$

where Q, is expressed in terms of l, the flight distance for the Cherenkov photon from the muon track to the PMT, $f(\theta)$, the PMT acceptance as a function of the angle θ which is the angle between normal to the PMT and photon direction, L, the average water attenuation length which accounts for both scattering and absorption.

To find the value of L a fit is made to cosmic ray muons passing through the center of the detector with total pe's between 50000 and 125000 so as to avoid selecting any muons which undergo Bremsstrahlung. A plot of $Ql/f(\theta)$ as a function of path-length can be found in Figure 2.8. The slope of this curve gives the water transparency (which is estimated to be about 101 m) and the Y-intercept gives the PMT gain which is estimated to be about 405 pe [40].

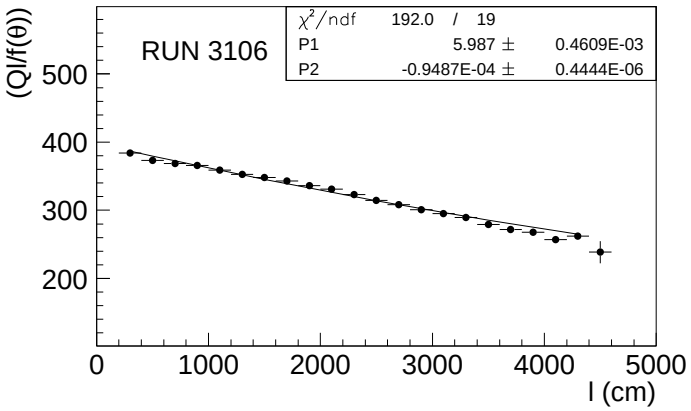

Figure 2.8: $\left(\frac{Ql}{f(\theta)}\right)$ versus l for cosmic ray muons in a single run of Super–Kamiokande data taking.

The time variation of the water transparency as a function of time from the beginning to the end of Super–Kamiokande-I can be found in figure 2.9

2.12 Super–Kamiokande Accident

As mentioned in the beginning of this chapter, Super–Kamiokande stopped regular data taking in July 2001 to refurbish about 200 dead PMTs in both ID and OD. To do this the water in the tank was slowly drained and both dead ID and OD PMTs starting from the top to the bottom were replaced using boats floating on the water. The replacement was finished in September 2001 and on 18th September 2001

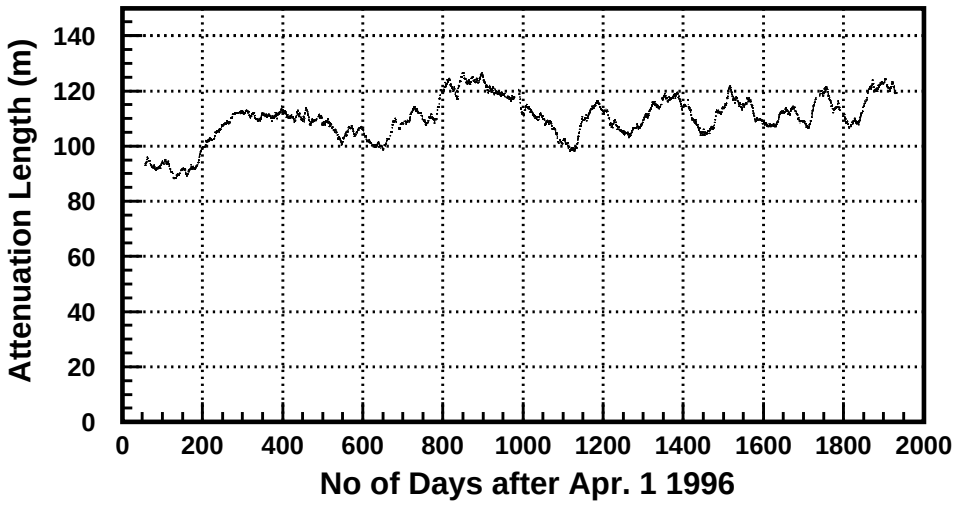

Figure 2.9: Water-Transparency as a function of time using cosmic ray muons during Super–Kamiokande-I.

water filling had restarted. On November 12th when the water level in the tank was about 32 m, a single PMT at the bottom of the tank imploded. The resulting chain reaction destroyed about 6779 ID PMTs (almost all of them were $\simeq$ 5 m below the water surface), 885 OD PMTs and about 700 wave-shifter plates. The sound caused by the implosions lasted about 5-10 seconds. During the accident the trigger rate increased to about 1 MHz from about 10 Hz and clogged the DAQ. The total energy released in the implosions has been estimated by G.W. Foster [41] to be roughly 170 MJ.

By looking at the event displays in the first 8 ms after the accident the probable PMT which imploded first was traced to one of 2 PMTs at the bottom : one was a PMT which was installed during the upgrade in summer 2001 and another one was an old PMT which was installed in 1996. A committee which was set up to investigate the cause of accident and to outline further preventive measures has narrowed the

cause of the accident to one of the two possibilities below depending on which was the first PMT which imploded.

- While replacing the tubes at the bottom of the detector Styrofoam pads were put on top of ID PMT's and people walked around these to replace the ID tubes at the bottom. This might have caused stress on the old PMT causing it to implode.

- In case the first imploded tube was a new one its base could have suffered a slight crack during transportation if it was not handled properly.

A corrective measure to prevent such implosions in the future was designed. All PMTs would be enclosed in a secondary shell comprised of a transparent acrylic hemisphere surrounding the photo-cathode and a fibre-glass shell with small holes surrounding the rest of the tube. Implosion tests have been done with this design and it has been demonstrated that if a PMT with such a coating implodes the shock wave gets contained within the protective shell thus preventing any chain reactions.

The Super-K experiment had to be restarted within a year to resume the K2K experiment and it was not possible to manufacture 6000 odd PMTs within such a short time span. Hence the experiment was restarted within a year of the accident by using the remaining ID tubes plus a few spares, enclosing them in the fibre glass + acrylic cases and redistributing these over the entire ID. A two-dimensional cross-section of FRP (where FRP stands for fibre reinforced plastic) + acrylic case is shown in Fig. 2.10.

Phase 2 of the experiment called Super–Kamiokande-II contains 5183 PMTs in the ID with about 20 % photo-cathode coverage. The number of PMTs in the OD is same as before. Super–Kamiokande has re-started data taking with this configuration from January 2003. Super–Kamiokande-II in this configuration is scheduled to take

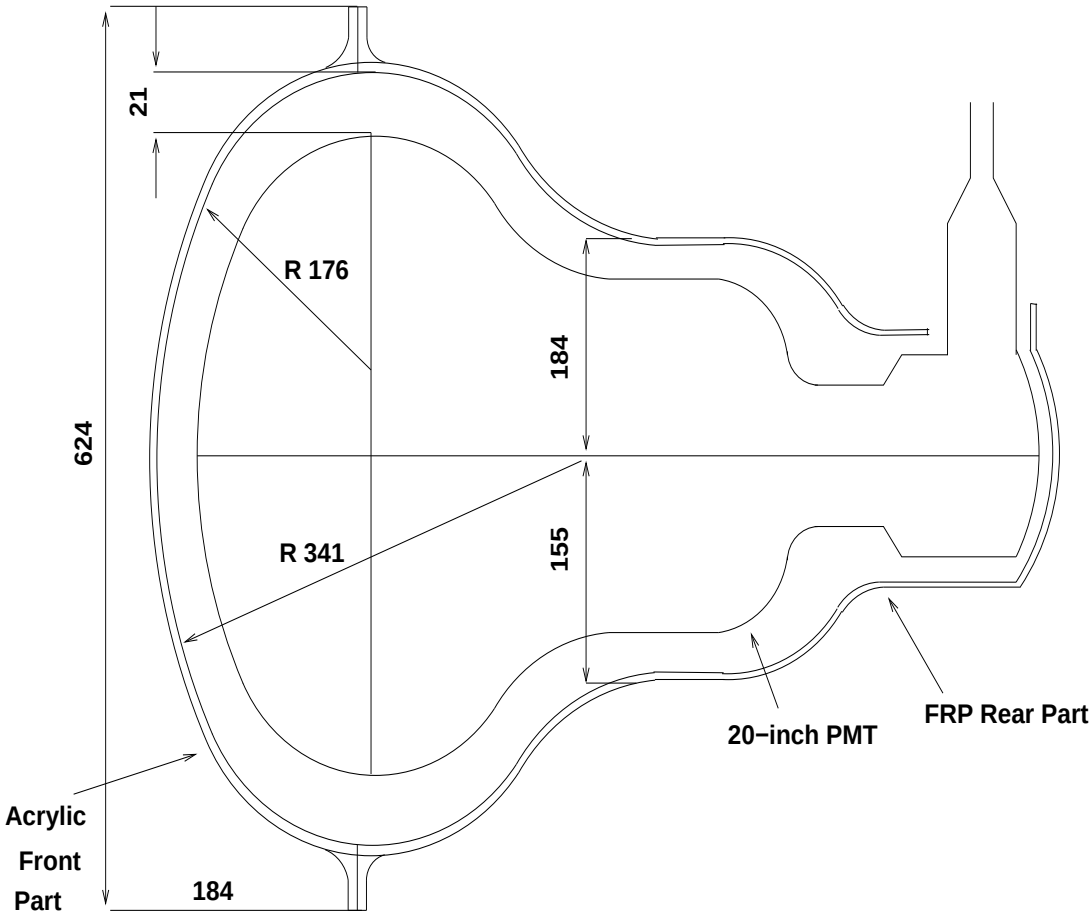

Figure 2.10: A two-dimensional view of the FRP+acrylic covering used on the PMTs in Super–Kamiokande-II. All indicated dimensions are in mm

data until the latter half of 2005. The full detector with ID PMT coverage same as in Super–Kamiokande-I is scheduled to be restored around 2005. More details on the accident can be found in Ref. [42].

Chapter 3

Upward Muon Data Reduction

3.1 Introduction

Super-Kamiokande started taking data on April 1 1996 and continued data taking uninterruptedly (except for calibration purposes) until July 19th 2001. The data set used in this thesis covers this entire period and is referred to as Super-Kamiokande-I or SK1 .

The data is subdivided into runs whose maximum time-span is 24 hours. The SK1 run numbers spanned from 1000 to 10444. Each run consisted of subruns which span 10 minutes or until the length of the subrun was 10 Mbytes. The total number of events in raw Super–Kamiokande data ranged from about 1.2×10^6 events per day (with total file size being 10 Gbytes) around the start of the experiment to about 1.4×10^8 events per day (with total file size being 0.15 Tbytes) at the end of SK1. This was because the Super-Low energy trigger (which controls the number of low energy events in the Super–Kamiokande dataset) was lowered several times since the start of the experiment [33]. Among these, there are about 2.5×10^5 events downward going muons (total size being 8 GB). From this data set, our final goal is to isolate

upward muons which are produced by neutrino interactions in the rock below the detector, and to classify these into two categories for physics analysis:

- **Upward stopping muons** : These are muons produced by neutrino interactions in the rock below the detector and the resultant muon stops inside the detector.

- **Upward thrugoing muons** : These are muons produced by neutrino interactions in the rock below the detector and the resultant muon exits the detector[1].

Super-K detects about 1.4 upward muons per day. A schematic view of an upward through-going and an upward-stopping muon is shown in Fig. 3.1.

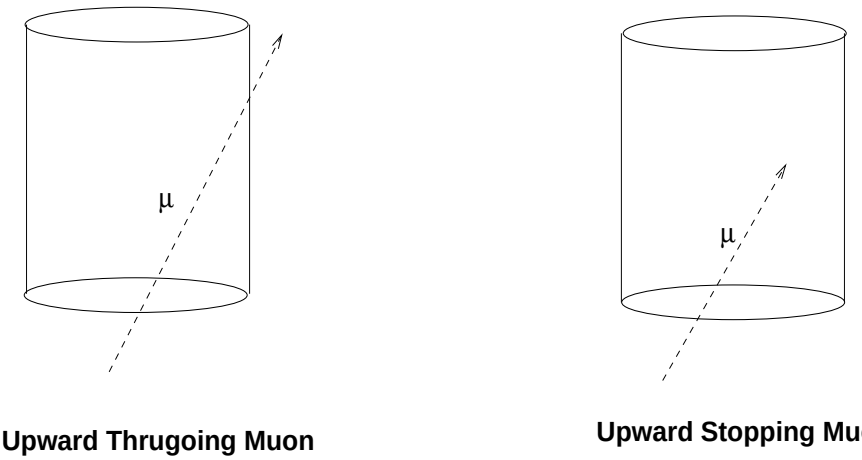

Figure 3.1: A schematic diagram showing the two different kinds of upward muons which need to be detected.

Besides isolating the upward going muons from the large background of cosmic ray muons the upward muon reduction needs to perform the following tasks:

1. To save all muons close to the horizon ($0 < cos\theta < 0.1$) in order to estimate the contamination of downward going muons in the upward going muon data set.

[1]Later in this thesis we shall split subdivide this dataset into showering and non-showering.

2. To save the decay electrons associated with upward and horizontal stopping muons.

3. To save the ultra-high energy events for further analysis.

3.2 General Considerations

Searching for a few signal events among a million events and rejecting the rest with very high efficiency imposes formidable data analysis challenges. To meet this challenge we use a total of 7 fitters, some of which are specialized to fit particular category of events but which have drawbacks for others. Each fitter has different processing speeds and accuracy. Each of these does one or both of the following tasks :

- Classify the topology of the muon event into thrugoing, stopping, multiple muons (in which more than one muon appears in each event), corner-clipper etc.

- Calculate the muon entry point in the tank as well as its direction.

  Some fitters are optimized to fit particular kinds of muons. Each event is passed from one fitter to another until it is either saved by a particular fitter or rejected at the end.

3.2.1 Basic Charge Cut

As explained in the next chapter we only use upward muons whose reconstructed path-length is greater than 7 meter for physics analysis. The basic charge cut we use to select muons is that total ID charge (Q) in the event satisfies: 8000 pe <= Q < 1750000 pe. On average as we can see from Fig 3.2, $Q(pe) \simeq 25 * L(cm)$ where

Q is the total charge deposited by the muon in ID and L is the total length of the muon. Thus a muon with path-length close to 7 meter will have on average 17500 photo-electrons. Thus a cut at 8000 photo-electrons is a safe cut as there is no danger of throwing out any event with muon path-length greater than 7 meter.

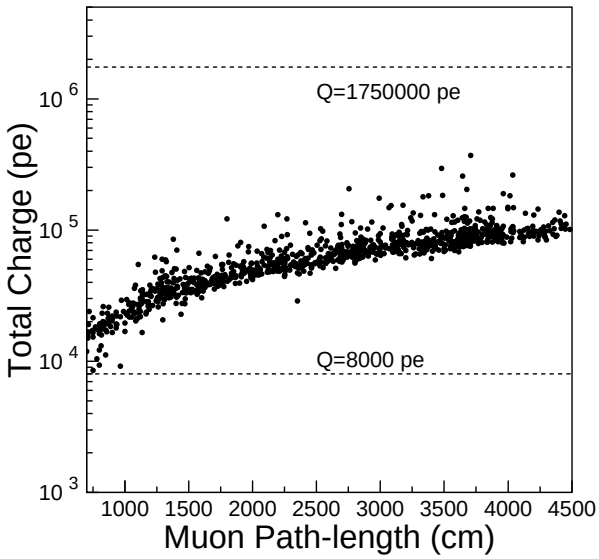

Figure 3.2: Total charge in photo-electrons as a function muon path-length for a sample of downward thrugoing and stopping muons with path-length > 7m.

Events with $Q < 8000$ pe are short-path length muons or contained events of lower energy. However we automatically save all events with $Q > 1750000$ pe for specialized astrophysical searches.

3.2.2 Fitters Used

We now list the fitters used in the reduction in the same order that an event has to pass through. All fitters are described in detail in Appendix 1.

1. `Stopmu1st` :

`Stopmu1st` is the first fitter used in the reduction chain. It only classifies topology of the muon event using only the Outer-Detector information (OD) and passes the event to the next fitter.

2. `Muboy`

   `Muboy` is the main fitter which gets rid of most of the background from cosmic ray muons. Moreover it is the only fitter which provides a fit as well as classification of muon topology.

3. `Stopmu2nd`

   `Stopmu2nd` is designed to efficiently fit stopping muons and is run on only those events which are classified as stoppers either by `Muboy` or `Stopmu1st`

4. `Thrumu1st`

   `Thrumu1st` is a fast muon fitter specialized for thrugoing muons and is more likely to result misfits.

5. `Fstmu`

   `Fstmu` is a fast muon fitter specialized for thrugoing muons.

6. `Thrumu2nd`

   `Thrumu2nd` is specialized to fit multiple muons and Bremsstrahlung muon events.

7. `NNfit`

   `NNfit` is a fitter which is specialized for fitting Bremsstrahlung muon events which have high charge.

3.3 Basic Decision Logic in Upmu Reduction

The aim of the reduction is to save all the upward and horizontal muon events and to reject downward muons and other junk events with maximum efficiency. The junk events include corner clippers, double/multiple downward muons, downward Bremsstrahlung events, partially or fully-contained events (which are neutrino interactions in the Super–Kamiokande fiducial volume), split events (in which one part of the detector is completely blank followed by another one in which the complementary part is blank) etc. To speed up the reduction procedure all events with only the Low-E and/or SLE trigger bit set were vetoed [2]. This reduces the number of events to be read by about 90%. As a general guideline the following rules are used for every fitter starting from `Muboy` in order to decide whether to save an event or whether to reject it or whether to pass it on to the next fitter.

- If an event is classified as thrugoing/stopping by either `Muboy` or `Stopmu1st` and is considered a good-fit with direction upward (where good-fit depends on the fitter goodness) it is saved and the reduction proceeds to the next event. The only exception is `Thrumu1st` where the event is passed on to the next fitter even if the fit is good and the event is classified as upward, since it is more likely to return mis-fits than others.

- For an event classified as stopping by either `Stopmu1st` or `Muboy` and which gets passed to `Stopmu2nd`, an event gets saved if `Stopmu1st` classifies it as horizontal/upward or if it gives a no-fit but if `Muboy` classifies it as horizontal.

- If an event is classified as downward with a good-fit by any fitter the event is rejected and the reduction proceeds to the next event.

[2] The only exception to this and the charge cut is for decay electron selection.

- If an event is classified thrugoing/stopping by either `Muboy` or `Stopmu1st` and its direction is horizontal and is considered a good fit, the event is "tagged" as horizontal and is passed on to the next fitter until it is classified as upward/downward by the next fitters. For a muon event classified as stopping the direction is considered horizontal if $0 < \cos\,\theta_z < 0.12$, where $cos\theta_z$ is the z-direction cosine and $\cos\,\theta_z = -1$ a vertical up-going muon. For all other muons the event is considered horizontal if $0 < \cos\theta_z < 0.1$.

- If an event cannot be classified either because of a goodness value which is below threshold or because the fitter cannot be run on the event, then it is passed on to the next fitter. If not a single fitter can fit it then the event is rejected; whereas if it is classified as horizontal by at least one fitter or upward by `Thrumu1st`1st then it gets saved.

- All fitters for which muon enters the top of the tank and for which $\sqrt{X_{ent}^2 + Y_{ent}^2} <$ 13.9 m (which is essentially more than 3 m from the edges of the inner detector) are classified downward.

The entire reduction scheme is summarized with the help of a flowchart in Figs. 3.9 and 3.10.

Also since we cannot afford to get rid of any upward muons as their rate is very small for many of the fitters looser cuts are used on the goodness, in case the event is classified as upward as opposed to if the event is classified as horizontal/downward . The number of horizontal muons lost because of this cut is estimated to be less than 3% . Also another aim is to get rid of downward going muons with high efficiency.

3.3.1 Cuts Used to Reject Junk Events

The following cuts are used to get rid of non-muon events and other background.

- **Pedestal cut**: All pedestal events are removed on basis of their pedestal flag. This cut takes place in `Stopmu1st`.

- **Corner clipper cut**: Since `Muboy` can recognize corner-clippers we utilize this information to get rid of corner clippers. An event is rejected as a corner clipper if either of the two conditions are satisfied:

  - `Muboy` classifies the event as corner-clipper and goodness value is > 0.35.
  - `Muboy` classifies the event as thrugoing or stopping and muon length is less than 4 meter and muboy *gof* is greater than 0.35 and direction is downward.

  The efficiency of the above corner clipper cut is $\sim 80\%$

- **Double Muon Cut**: If *both* `Muboy` and `Stopmu1st` classify an event as multiple muon then this event gets rejected. The efficiency of this cut in removing multiple muons is $\sim 60\%$.

All the goodness cuts used in the various fitters are summarized in Table 3.1. If the goodness values of any of the above fitters is above/below the threshold values in the above table, the event is classified as a no-fit and passed on to the next fitters.

In Table 3.2 we give some statistics of the total number of events spanning 5 years of Super-K data which the reduction had to process. Table 3.3 indicates number of events which get saved after every fitter.

Table 3.4 indicates the number of events which get rejected after every fitter.

3.3.2 Output of Reduction

As mentioned in the beginning of chapter the goal of upmu reduction was to save horizontal and upward muon events and to reject other kinds of events. The total number

Fitter	Event direction	Goodness Cut
Muboy	Downward	gof> 0.45
Muboy	Horizontal	gof> 0.45 & $f_{cone} > 0.8$
Muboy	Upward	$f_{cone} > 0.8$
Stopmu2nd	All	stopmu2ndgof > 0.75 & rcone< 0.7
Thrumu1st	Upward/Downward	muyn=1 & rcone< 0.7
Thrumu1st	Horizontal	muyn =1 & rcone < 0.25
Fstmu	All	goodness< 10
Thrumu2nd	Downward	rcone < 0.7 and tofsgm < 7 and rtofsgm< 0.4
Thrumu2nd	Upward	(rcone/0.3 + tofsgm/3.0)< 2.4 and rtofsgm< 0.4
Thrumu2nd	Horizontal	rcone< 0.3 and tofsgm< 3.0 and rtofsgm< 0.4
Nnfit	Horizontal	goodness> 5.0
Nnfit	Upward/Downward	goodness < 1.0

Table 3.1: Goodness Cuts used in various fitters.

Charge range (pe)	No of events saved	No of events rejected
8000 =< Q < 1750000	89911	288114671
Q >= 1750000	52188	0
Q < 8000	39725	N/A

Table 3.2: Summary of the total number of events in each charge range which which were saved and rejected.

Fitter After which Event gets saved	% of events saved	Reason
Muboy	9.0 %	Upward by Muboy
Stopmu2nd	20.8 %	Upward by Stopmu2nd
Stopmu2nd	29.4 %	Horizontal by Muboy & No fit/horizontal by Stopmu2nd
Fstmu	2.8 %	Upward by Fstmu
Thrumu2nd	2.9 %	Upward by Thrumu2nd
NNfit	6.9 %	Upward by Nnfit
NNfit	28.2%	Horizontal by at least 1 fitter & no fitter could classify it as upward

Table 3.3: Percentage of events which automatically get saved after each fitter and the reason.

Fitter	% of events rejected	Reason
Stopmu1st	3.4%	Pedestal or OD off.
Muboy	87.6%	Downward
Muboy	1.0%	Corner-Clipper
Muboy	4.9%	Double-Muon
Stopmu2nd	0.1%	Downward
Thrumu1st	0.9%	Downward
Fstmu	1.0%	Downward
Thrumu2nd	0.9%	Downward
NNfit	0.1%	Downward
NNfit	0.1%	No fit by all fitters

Table 3.4: Percentage of events rejected after each fitter in the reduction.

of events with total charge between 8000 and 1750000 pe after the output of reduction is about 50 per day. Among these, the number of upward muons and horizontal events is about 25, which means the purity of the upmu reduction is about 50%. About 40% of the remaining events are mainly downward Bremsstrahlung muons which get misfit by any of the 7 fitters as upward/horizontal and none of the other fitters could reject it with a good goodness. The remaining 10% of events are double muons or corner clippers (which could not be rejected), events with missing sections of detector, electron showers, partially and fully-contained events, etc.

The upward muon reduction process was done with the condor high throughput batch processing computing environment on different subruns in parallel processing mode. A total of 595796 subruns constituting the entire Super–Kamiokande-I dataset were processed and it took approximately 2 minutes to process one subrun.

3.3.3 Performance of Fitters in Selecting Upward Muons

We use a total of 6 fitters in deciding whether to save or reject the upward muons. There are a total of 36 (out of 3904 possible ways) different combinations of decisions

by various fitters because of which all the upward muons used for our analysis were saved. To uniquely identify the reason because of which an upward muon event was saved the decision of each fitter on an event was encoded in the variable $fitter\_history$ where $fitter\_history$ is defined in Eqn 3.1.

$$\begin{aligned} fitter\_history = 10^5 dec_{muboy} + 10^4 dec_{stopmu2nd} + 10^3 dec_{thrumu1st} \\ +10^2 dec_{fstmu} + 10 dec_{thrumu2nd} + dec_{nnfit} \end{aligned} \tag{3.1}$$

where the variable *dec* of all fitters (except `Muboy`) can take one of the following 4 values :

- 0 : Implies that the fitter gave no fit.
- 2 : Implies that the fitter classified the event as horizontal
- 3 : Implies that the fitter classified the event as upward.
- 9 : Implies that this fitter was not run on the event. This can happen if the event was already saved before that the fitter was run or if the event was not classified as stopping by `Muboy` or `Stopmu1st`, in which case it does not get passed to `Stopmu2nd`.

All events with 8000 $=< Q <$ 1750000 pe have to pass through `Muboy`. Hence dec_{muboy} can never be 9. If the muon path-length classified by `Muboy` is less than 3 m, but if the $gof < 0.35$ then the variable $dec_{muboy} = 6$. Otherwise if an event is classified as upward, horizontal or no-fit, the values of dec_{muboy} are same as the values of the *decision* variable of other fitters. The number of upward muons showing different values of $fitter\_history$ is shown in Table 3.5. As we can see about 93% of events have $fitter\_history = 39999$. These events automatically get saved after

`Muboy` without passing through any other fitter. All these have been classified by `Muboy` as thrugoing or stopping, upward and with goodness greater than threshold.

3.4 Precision Fitter and its Performance

The precise muon vertex and direction is determined using the precision fitter which is used for all the analysis done in this thesis. All events from the output of upmu reduction get passed to precision fitter. The precision fitter is made up of 3 fitters called Upmu-fit, OD-fit, and TDC fit. It has been mainly developed by K. Nitta. This is computationally more intensive as compared to the fitters used in the normal reduction since this fitter is intended to obtain precise fit directions and entry points, whereas all the fitters in the reduction were also designed to reject the large background from junk and downward muon events.

3.4.1 Upmu Fit

Upmufit has been adapted from the M-S fitter [46] used in the contained event analysis and been modified for upward muon analysis.

The basic idea in the fitter is that for each PMT the expected amount of Cherenkov light is calculated and compared to the observed values. The expected number of p.e's due to Cherenkov light is given by :

$$N_i^{exp} = \left[\alpha_\mu \frac{1}{l_i(\sin\theta_i + l_i\frac{d\theta}{dx})}\sin^2\theta_i + N_i^\delta(\theta_i)\right]\exp\left(-\frac{l_i}{L_{atten}}\right)f(\Theta) + S_i, \qquad (3.2)$$

where α_μ is a normalization factor, θ_i is the incident angle normal to the $i_{\rm th}$ PMT, N_i^δ is the number of p.e. expected from δ-ray production, L_{atten} is the Water attenuation length, and $f(\Theta)$ is the effective photosensitive area of a PMT as a function of Θ.

fitter_history	No of upward muons with this value
399999	2201
93399	24
93039	15
239999	15
293399	13
393399	12
90399	11
90039	10
90003	9
39999	8
229999	7
3399	4
292239	3
393039	2
390399	2
399	2
239	1
290039	1
290200	1
290399	1
292023	1
292399	1
293223	1
293239	1
29999	1
3003	1
3039	1
33	1
390003	1
393239	1
639999	1
690039	1
90002	1
90030	1
90033	1
90339	1

Table 3.5: Frequency of occurrence of various values of $fitter\_history$ variable for all the upward muon events in Super–Kamiokande-1, where $fitter\_history$ is defined in Eqn 3.1.

The factor $1/l_i(\sin\theta_i + l_i\frac{d\theta}{dx})$ reflects the change in the Cherenkov angle due to the energy loss of the muon. The total likelihood is then calculated for all PMTs within a cone less than 1.5 times the Cherenkov Angle :

$$\mathcal{L} = \prod_{\theta_i < 1.5\theta_c} P(N_i^{exp}, N_i^{obs}) \tag{3.3}$$

The function $P(N_i^{exp}, N_i^{obs})$ is the probability distribution of observing N_i^{obs} photo-electrons given N_i^{exp} photo-electrons and is approximated by a Gaussian distribution when $N_i^{exp} > 20$ whereas when $N_i^{exp} < 20$ the probability is computed based on a single p.e. distribution table. The fitter then calculates a χ^2 given by

$$\chi^2 = \frac{-2log\mathcal{L}}{R_{cone}} \tag{3.4}$$

Here $\mathcal{L}$ is described in Eqn 3.3 and R_{cone} is the same function as used in Eqn A.8.

The fitter then undergoes many iterations to maximize the χ^2 given by Eqn 3.4 to find the vertex and entry point.

3.4.2 OD Fit

Upmu-fit is very sensitive to the edge of the Cherenkov ring. For muon events which undergo Bremsstrahlung the edge of the Cherenkov ring is quite fuzzy. For these events the fit vertex and direction is obtained using an OD clustering algorithm called OD fit as well as using TDC fit described in Sect 3.4.3 . In OD fit the muon entry and exit point is chosen using only the OD with a clustering algorithm. OD fit makes clusters around a PMT if it has at least 8 nearest neighbors hit between 800 ns and 1300 ns. The cluster with the earliest average time of all PMTs in it is chosen as the entry point and the cluster which has the maximum number of PMTs

is chosen as the exit point.

3.4.3 TDC Fit

TDC fit is discussed in detail in Chapter[5] of Ref [46] and like Upmufit, it has been adapted from contained event analysis.

We give a very brief synopsis. TDC fit is based on three steps: Point fit, Ring Edge Fit and fine vertex tuning. In "Point fit" a rough vertex and track is found so that the timing residuals of all PMTs are approximately equal.

The next step consists of "Cherenkov ring edge" search in which the direction is varied so that the effective charge given in Eqn 3.5 is maximized.

$$Q = \frac{\int_0^{\theta_{edge}} CH(\theta)d(\theta)}{sin\theta_{edge}} \left(\frac{dCH(\theta)}{d\theta}\right)^2 exp\left(-\frac{(\theta_{edge}-\theta_c)^2}{2\sigma_\theta^2}\right) \tag{3.5}$$

where θ_c is the Cherenkov opening angle, $CH(\theta)$ is the angle between the track direction and the photon travel direction. The track direction and θ_{edge} are varied so that Q is maximized. In the "fine vertex tuning stage" the vertex and direction are further refined after taking into account effects of scattered light and maximizing a goodness function which depends on the timing residuals. The last two fits are iterated until the distance between the vertex in two consecutive iterations is less than 50 cm.

For each event a vertex and track direction is found using all the 3 fits. The angular direction between each of the 3 fits is compared and the final fit is used from one of these fitters using criterion described in Appendix B of Ref [47].

3.4.4 Performance of Precision Fitter

The accuracy of the muon fit direction by the precision fitter was tested by applying the precision fitter to an equivalent 40 year atmospheric neutrino Monte Carlo and comparing the precision fit directions and the true Monte Carlo directions. These plots for thrugoing muons and stopping muons are shown in Figs 3.3. The angular resolution for upward thrugoing muons is about 1.05° and for stopping muons is about 1.5°

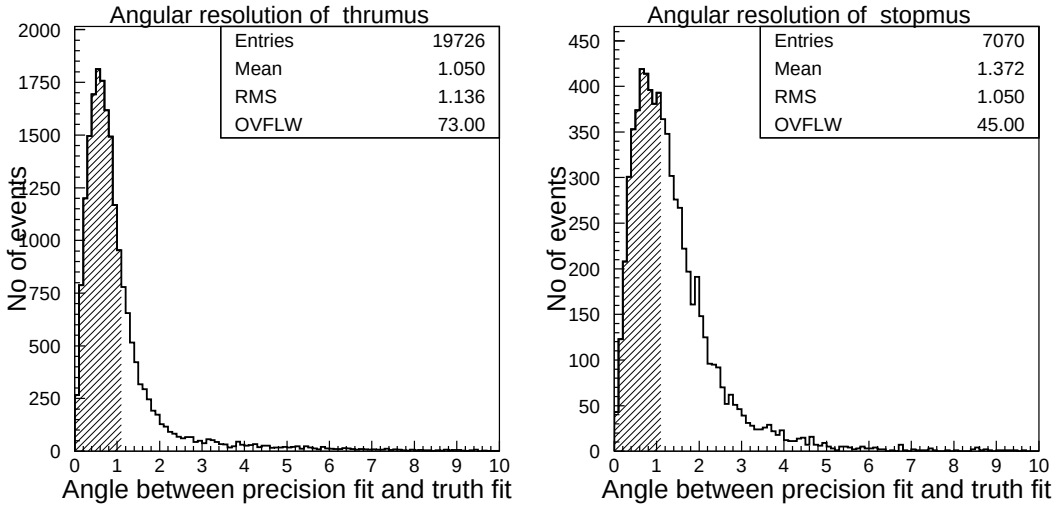

Figure 3.3: Angular direction between the precision fit and true fit directions for upward thrugoing muons (left panel) and upward stopping muons (right panel) as measured with a 40 year Monte Carlo sample. The shaded histogram represents 68 % of the total area and corresponds to $\simeq 1.05°$ and $\simeq 1.5°$ for thrugoing and stopping muons respectively.

3.5 Final Event Selection and Classification

3.5.1 Expert Scanning

Once precise entry points and directions have been found for every saved event from the reduction, for all events a final selection has to be done to select the upward going muons and to classify them into thrugoing and stopping. All events with precision fit z-direction cosine > 0 (i.e. if the event was classified as upward by the precision fitter) are selected. The total number of such events is 4266. Each of these events is then scanned independently by K. Nitta and myself to throw out potential non-upward muon events. These are mainly downward muons misfit by the precision fitter as upward by more than 5 degrees, electron showers or other junk events. Each candidate upward muon is visually checked for consistency between OD and ID timing and whether the direction is upward.

This subset is then classified into upward thrugoing and upward stopping and any contained events are then thrown out using criteria described in the next section.

3.5.2 Stop/Thru separation

To make a final classification of the category of the muon the following quantities are calculated.

- N_{entod} = Number of OD hits within 800 ns and 1300 ns and 8 m of projected entry point in OD
- N_{exitod} = Number of OD hits within 800 ns and 1300 ns and within 8 m of projected exit point in OD

A muon is considered stopping if it satisfies all the conditions below:

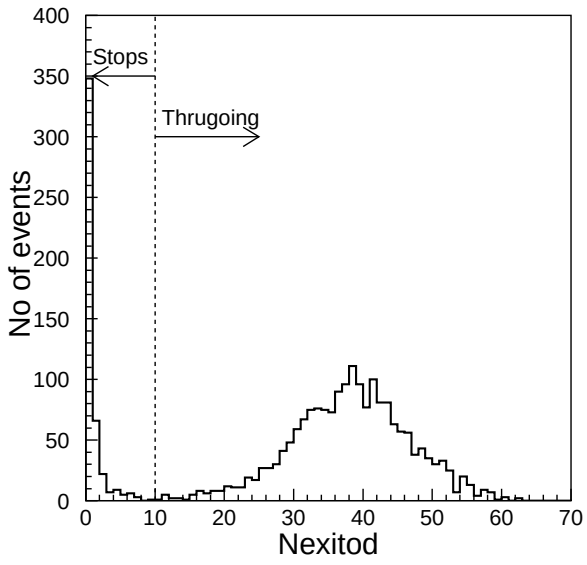

Figure 3.4: N_{exitod} distribution for upward thrugoing muons and upward stopping muons. The threshold value for N_{exitod} to separate thrugoing from stopping muons is 10.

1. $N_{exitod} < 10$

2. $N_{entod} >= 10$

A muon is considered thrugoing if it satisfies all the conditions below :

1. $N_{exitod} >= 10$

2. $N_{entod} >= 10$

The distributions of N_{exitod} and N_{entod} for upward thrugoing and stopping muons is shown in Figs 3.4, 3.5 respectively.

3.5.3 Length Determination

For a thrugoing muon the length is given by the distance from the entry point to the exit point in the ID. Any muon which cannot be classified as thrugoing or stopping

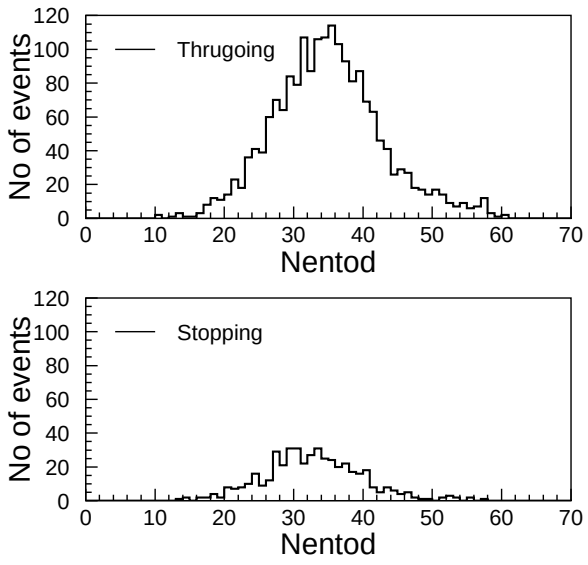

Figure 3.5: N_{entod} distribution for upward thrugoing muons (top panel) and upward stopping muons (bottom panel).

is probably a partially-contained event and is discarded. For a stopping muon the location of the stopping point is determined from the muon momentum at the ID entrance, from which one can get the muon range using lookup tables in [45]. The muon momentum is obtained using the entry point and direction by counting the effective number of number of pe (after correcting for water attenuation and PMT acceptance) inside a cone with 70° opening angle within a time window between -50 and 250 ns of the time peak. The conversion from momentum to corrected photo-electrons is obtained using conversion tables obtained from Monte Carlo and more details on this can be found in Ref. [6].

3.6 Other Aspects of Reduction

3.6.1 Decay Electron Selection

In addition to saving upward and horizontal muon events the reduction also saves the electrons produced by the decay of an upward or horizontal stopping muon. These events are used to estimate the ratio of ν_μ to $\bar{\nu}_\mu$ as discussed in Ref. [130].

Since these events are of much lower energy than muon events, the main charge and trigger cuts used in the reduction are bypassed. The following steps are used in selecting a decay electron:

- All events selected as horizontal or upward stopping muon are tagged with a special flag.
- For each event the reduction checks if this flag is on. If so it saves all events (irrespective of the total number of photo-electrons or the event trigger) within 30000 ns of the parent stopping muon.

3.6.2 Livetime Calculation

A precise value of livetime is necessary in order to calculate the flux of upward muons for physics analysis as well as for calculating the exposure to any source for astronomy analysis. During the entire Super-K data-taking the detector operated with about 90% duty cycle. The rest of the time, the detector was turned off for routine maintenance or calibration or in case of some minor malfunction which hindered data taking. The upward muon livetime is defined as the total time when both the ID and OD were taking normal data and could have detected upward muons.

In Super–Kamiokande, livetime is calculated for every subrun on an event by event basis. To calculate the livetime for each subrun it calculates the total data

taking time and subtracts various sources of dead time to get the total livetime per subrun. The total livetime is obtained by adding the livetime of all subruns used in the analysis. The total data-taking time per subrun is given by Eqn 3.6.

$$T_{data} = \sum_{i=1}^{N-1} [T_{i+1} - T_i] \tag{3.6}$$

where T_i is the time of each event obtained using the 48 bit clock and the sum extends over all events except those which have only a low-E or SLE trigger bit set.

The various sources of deadtime are indicated below:

- **ID dead time (T_{iddead})**: If any of ID work stations is off or if the time interval between two successive events is greater than 5 seconds, then the time interval between this event and the previous event is counted as dead time due to ID being off (T_{iddead}).

- **Calibration Dead Time (T_{cal})** : In each run there are occasional pedestal events which are special purpose calibration events. For these events, a pedestal flag gets set in the event status flag corresponding to each event in Super–Kamiokande. For these events the time interval between this event and the previous event is counted as dead time due to pedestal events. In addition there are other auto-calibration events (from Xe and laser calibration) in a given run which need to be counted as dead time. These events are initiated by a special CLK trigger followed by calibration events, after-trigger events and after-pulse events. These auto-calibration events end in between two events. Any time interval that falls within 30 μ-sec following the CLK trigger is counted as auto-calibration dead-time. The total dead time due to pedestal and auto-calibration dead time is counted calibration dead time (T_{cali}).

- **OD dead time (T_{oddead})** : If the OD is off then the time interval between this event and the previous event is counted as dead time due to OD being off (T_{oddead}).

- **No OD data ($T_{nooddata}$)** : If the number of OD hits is 0 inspite of the OD being on and this dead time cannot be attributed towards BIP dead time (described in next bulletin), then the time interval between this event and the previous event is counted as dead time due to no OD data even though it is on ($T_{nooddata}$).

- **BIP Dead time (T_{bip})** : BIP stands for *Busy In Progress*. When TDC's receive a trigger they go dead for a few microseconds, while they save hit information to a buffer area in their memory. During this time interval TDC's cannot record any more hits. This dead time is called BIP dead time and starts in the time interval between two events and ends in the time interval between two other events. BIP dead time begins 6 μ-sec after the current event. The BIP end time is given by the difference between the time at the end of the BIP signal and the time of the split trigger signal of the TDC. The BIP dead time is given by difference between BIP start and end times.

The total upmu livetime is defined in Equation 3.7

$$T_{livetime} = T_{data} - \sum_{i=1}^{N-1} [T_{iddead} + T_{cal} + T_{oddead} + T_{nooddata} + T_{bip}] \qquad (3.7)$$

The terms on the right indicate various sources of dead time when normal data taking was not possible for reasons explained in outlined in above section.

Note that if an "alive" event (for which both ID and OD are taking data) is followed by a "dead" event then the time interval between these events is counted towards dead time and is subtracted from total data-taking time. Else if a "dead"

event is followed by an "alive" event, the time interval between these events is considered to be active for upward muons and this time interval is NOT counted to the dead time. This timing diagram is illustrated in Fig. 3.6

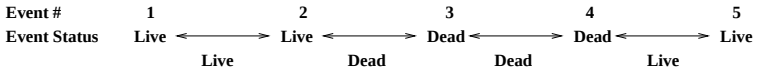

Figure 3.6: A livetime timing diagram which illustrates when an interval of time between two events is considered dead and when it is considered alive for detection of upward muons.

3.6.3 Ultra-High Energy Events

In the entire Super–Kamiokande-I data-set there are 52188 events which deposit more than 1750000 photo-electrons. Most of these events saturate the entire ID and none of the regular muon fitters would work on such events. Most of these events are either electronic noise or downward Bremsstrahlung muon events. However such events could also result from ultra-high energy neutrinos from astrophysical sources (such as AGNs). These events were first analyzed with a specialized fitter which uses only OD information by F Fowler (a high school honors student) during Summer 2001. This algorithm was then further refined by K. McConnell and results based on this can be found in Ref. [48].

3.7 Intermediate Stage Reduction

For all regular muon events with $8000 =< Q < 1750000$ photo-electrons, looser cuts than in the final stage of the upmu reduction get applied to events after the `Stopmu1st` and `Muboy` stage and these events are stored in a separate file. In this stage of reduction only those events for which `Muboy` classified an event as downward

Reduction stage	No of muon events
Raw data	288204582
Intermediate Reduction	2732726
Final Stage Reduction	89911
Precision Fitter	4266
Eye Scan	2447
Stop/thru Separation	1892 (upthrus) 467 (upstops)

Table 3.6: Number of muon events with $1750000 > Q >= 8000$ *pe* present at every step of the process involved in selecting upward muons from the raw data

and with good fit (muboy gof > 0.35) are rejected. An event here is considered downward if:

- For an event classified as stopping by either `Stopmu1st` or `Muboy`, $cos\theta_z > 0.2$
- For all other events $\cos\theta_z > 0.1$

All other events get saved after this intermediate step. Thus there are no corner clipper, double muon or the cut on events entering the top of the tank as applied in the main reduction. The total number of events saved after this intermediate step is 2732726 which is about 30 times more than the number of normal charge muon events in the final stage reduction.

This finishes all steps and processes involved in the reduction. The entire process along with number of events in every step is summarized in Fig. 3.11. Also the a summary of the total number of muon events in the entire Super–Kamiokande dataset is summarized in Table 3.6.

The upward going muon data set obtained during the entire Super–Kamiokande-1 running period is described in the next chapter. An event display of a thrugoing muon along with the fitter direction is shown in Fig. 3.7, whereas the event display for an upward stopping muon is shown in Fig 3.8

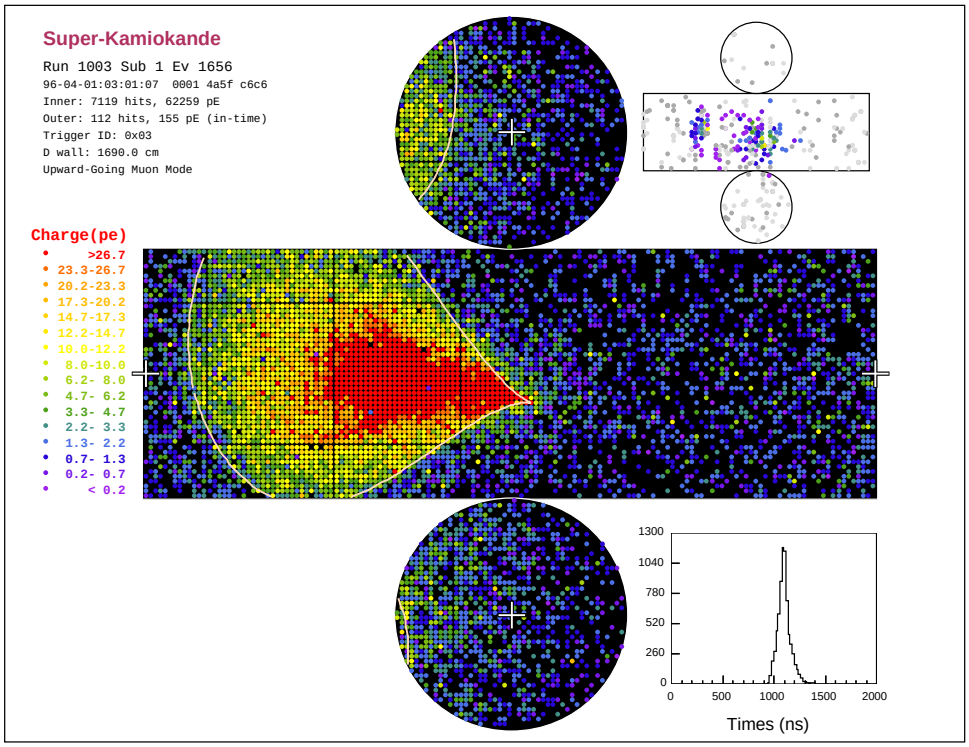

Figure 3.7: Event Display of an upward thrugoing muon in Super–Kamiokande in charge mode. The main large rectangle in the display and the two circles above and below it represent the projected 2-D view of the ID and the dots indicate the charge of an ID PMT from the muon. The solid line shows the fitted Cherenkov cone. The smaller replica of this in the upper right-hand corner shows the same for OD.

3.8 Estimation of Background from Cosmic Ray Muons

For upward thrugoing and stopping muons there is a contamination from downward going cosmic ray muons in the zenith angle bin closest to the horizon. This is caused by finite angular resolution of the fitter as well as multiple coulomb scattering in the rock. To estimate the background we need the distribution of cosmic ray muons

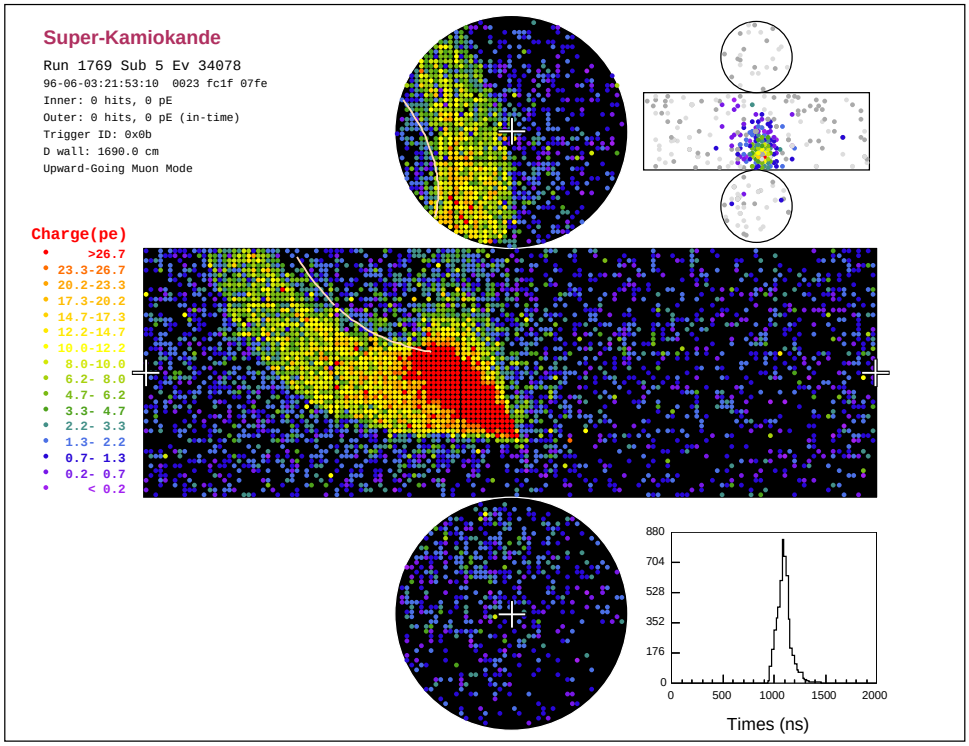

Figure 3.8: Event Display of an upward stopping muon in Super–Kamiokande in charge mode. The various parts in the event display are same as in Fig 3.7.

above the horizon in the near-horizontal region. The results will be discussed in the next chapter. Here we shall explain the strategy used to select horizontal muons.

Since the estimated rate of cosmic ray muons near the horizon is large, a subset of events from Super–Kamiokande-1 data corresponding to $\simeq$ 641.4 days were chosen for background estimation to reduce the scanning load. The total number in each zenith angle bin was then scaled by livetime.

The events saved after the intermediate stage analysis (Sect. 3.7) from run numbers 2000 to 8899 (while skipping run nos 2100-2199, 2300-2399 and so on) were chosen. The total livetime of this dataset is 641.4 days. The events were then separated into stopping and thrugoing muons using the algorithm specified in Sect. 3.5.2. All thrugoing muons with $0 < cos(\theta) < 0.08$ and stopping muons $0 < cos(\theta) < 0.1$

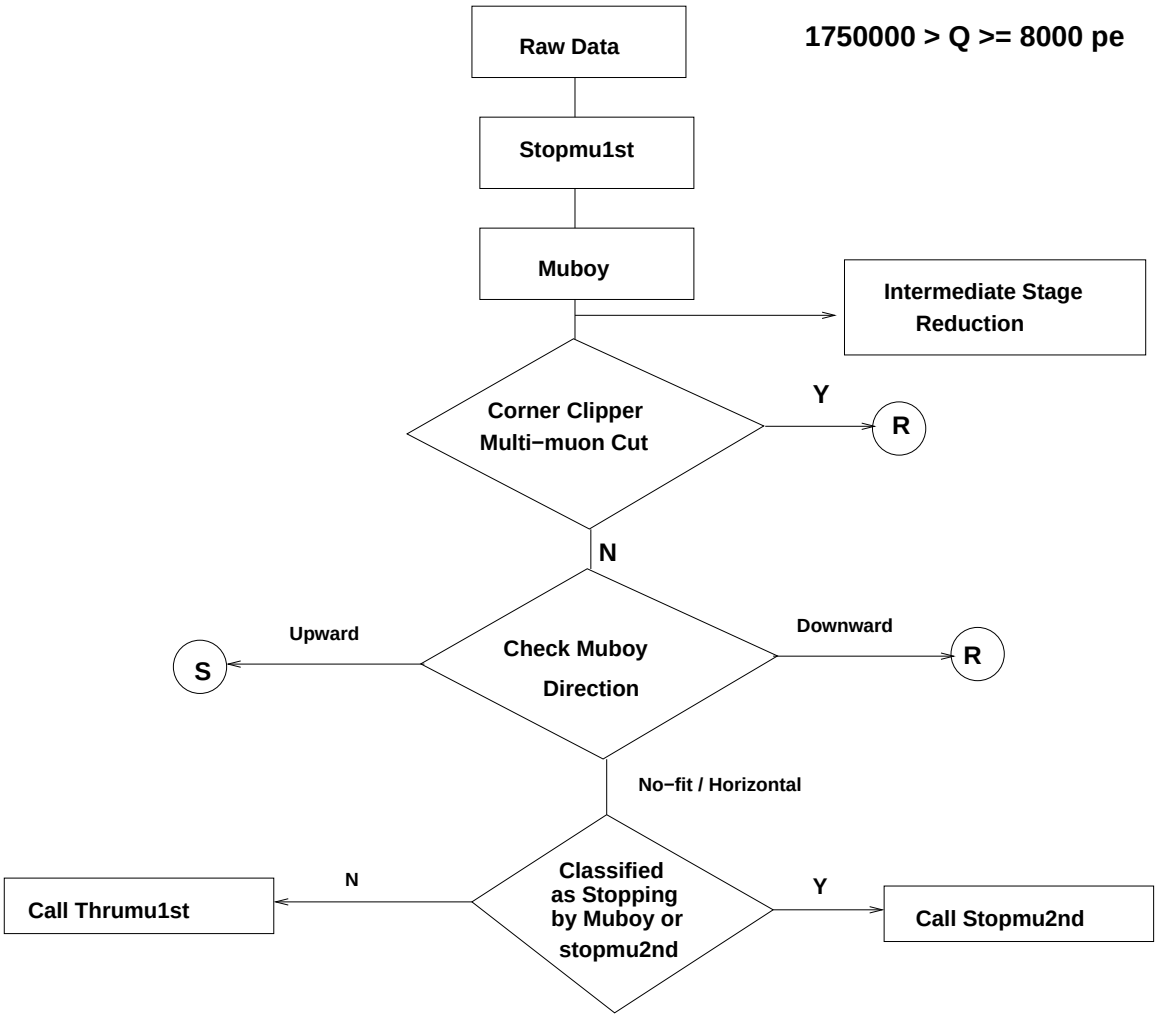

Figure 3.9: Flowchart used for the first part of upmu reduction (starting from the raw Data to `Muboy`) for an event with 8000 =< Q < 1750000 pe.

were selected. For stopping muons the multiple coulomb scattering is more than thrugoing muons since these are of a lower energy. Hence a larger zenith angle band was chosen for cosmic ray stopping muons. Both thrugoing and stopping downward going muons are required to have path length greater than 7m. These events were then expert scanned once to filter out any bad misfits using the same criterion, which was using in expert scanning the upward muon events. The number of horizontal thrugoing and stopping muons after each stage is shown in Table 3.7. The zenith

	Thrugoing	**Stopping Muons**
Path Length Cut	$> 7meter$	$> 7meter$
Zenith angle cut	$0.08 > cos(\theta) > 0$	$0.1 > cos(\theta) > 0$
No of events after Intermediate Stage Reduction	2712	1143
No of events after expert scanning	2564	1110

Table 3.7: Number of thrugoing and stopping cosmic ray muons near the horizon in about 641 days of Super–Kamiokande data. All events in the last row are used for estimation of contamination from down going muons in the upward muon sample.

and azimuthal distribution of these horizontal muons and calculation of estimated background will be explained in the next chapter.

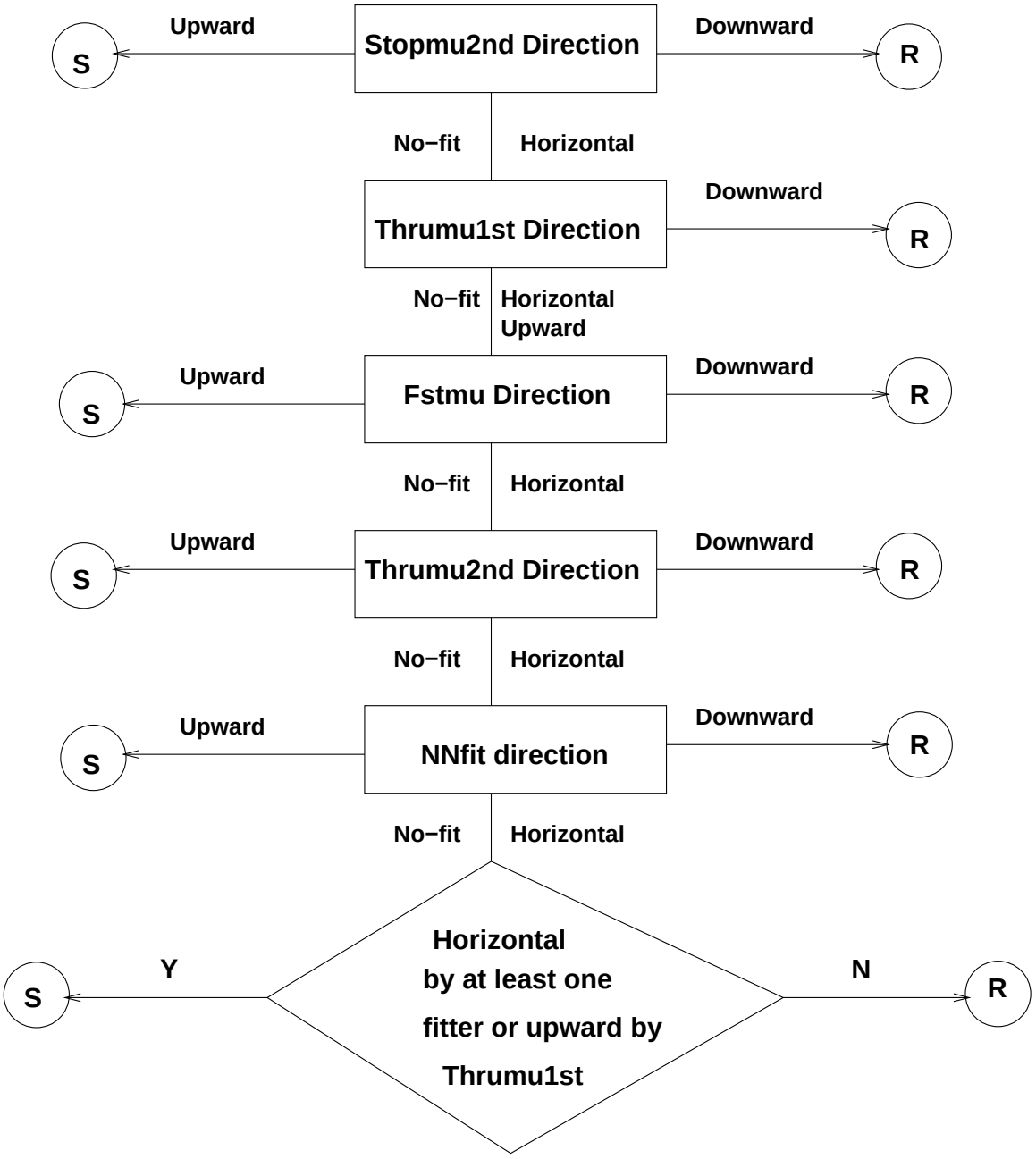

Figure 3.10: Flowchart used in the second stage of upmu reduction (starting from `Stopmu2nd` to the end) for an event with 8000 =< Q < 1750000 pe indicating the decision logic used to save or reject the event after every fitter.

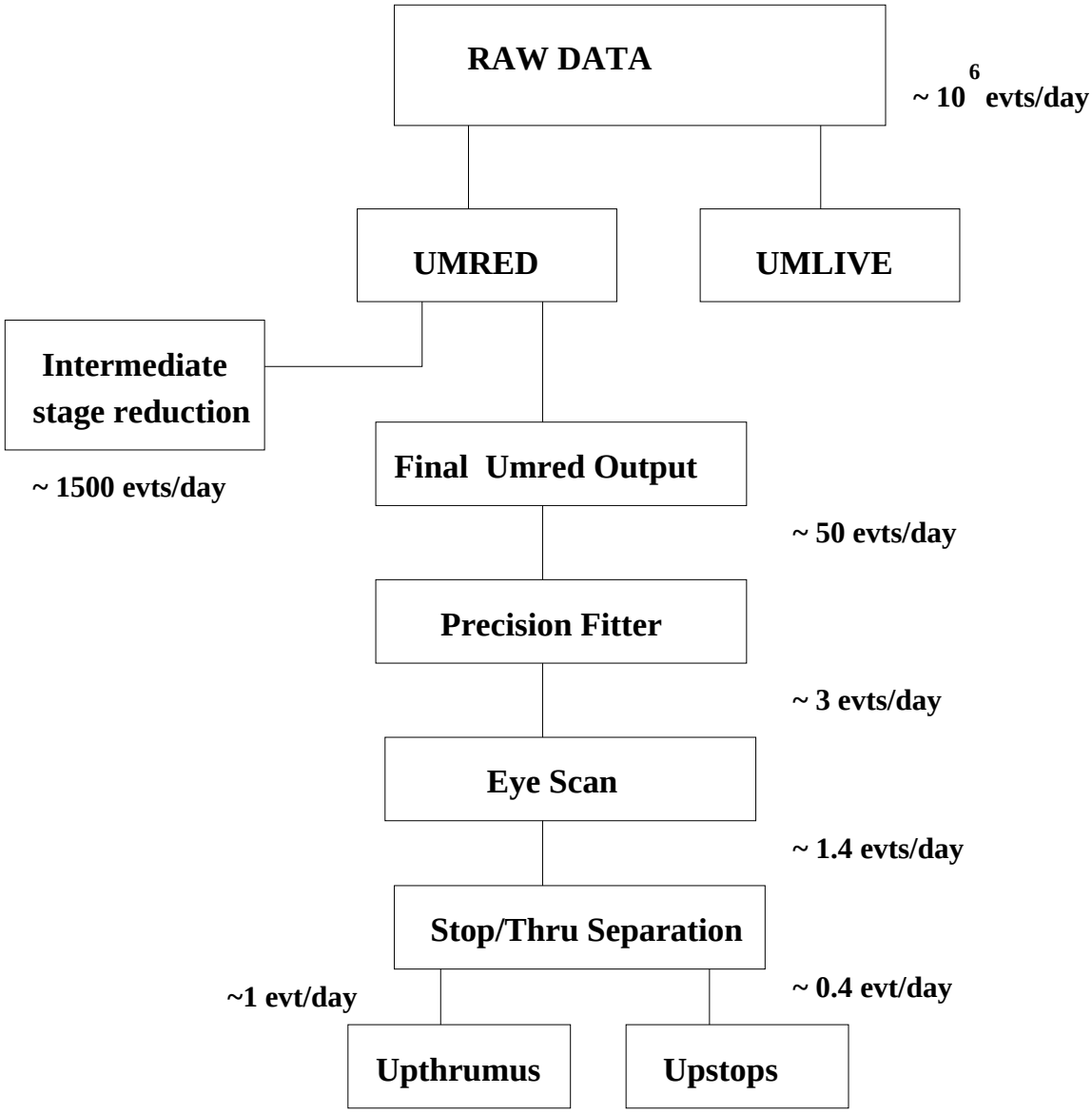

Figure 3.11: Summary of all steps involved starting from selecting the raw data to the final upward going muon selection and event classification along with approximate number of muon events per day present at every step in the process

Chapter 4

Upward Muon Sample and Expected Flux

The analysis done in this thesis uses 1679.6 live-days of Super-Kamiokande from April 1st 1996 to July 19th 2001. A full detector simulation of atmospheric neutrinos producing upward going muons corresponding to 40 live years has been processed through the same reduction and reconstruction scheme as described in the previous chapter. In this chapter we shall describe the details of the upward going muon data set and explain how atmospheric ν's which gives rise to upward going muons have been simulated. We will then discuss what kind of physics we have learned from a comparison of the observed and expected data.

4.1 Path-length Cut

In our background of neutrino produced upward through-going and stopping muons there could be a potential background from upward going pions produced in inelastic interactions of downward cosmic ray muons in the rock surrounding the detector ($\mu + N \rightarrow \mu + \pi^{\pm} + X$). To reduce the background from such cosmic ray photo-

produced pions we need to impose a path-length cut so that with increasing target in water, the background from these events becomes negligible. The absolute rate as well as the rate of events for different values of range in the detector have been measured by the MACRO collaboration [43]. As pointed out in the previous chapter, we use a 7 m cut, in which the pathlength for thrugoing muons is estimated from geometry and for stopping muons, is estimated from the reconstructed momentum. This 7 m cut corresponding to a range of 700 gm/cm^2 in water. We estimate the background in our dataset using a simple extrapolation from the MACRO measurements. The MACRO measurement of number of upward pion events at different values of detector depth is shown in Fig. 4.1. We have fit these measurements by a simple exponential as shown in Fig. 4.1

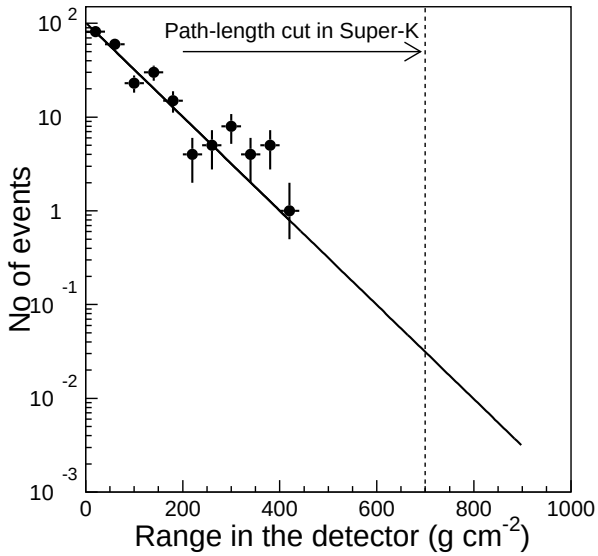

Figure 4.1: The dots represent the distribution of effective depth of 243 cosmic-ray induced upward pions corresponding to about 1.5 years of livetime measured by the MACRO collaboration [43]. The line shows an exponential fit to the measurements given by $exp(4.6271 - 0.011561 * x)$ where x is the amount of grammage measured in gcm^{-2}.

The total number of up-going pions in MACRO with range $> 200\ gm\ cm^{-2}$ which get identified as upward through-going muon $\simeq 2.1/yr$ The corresponding number for the entire Super–Kamiokande-1 dataset corresponding to 1680 days live time can be estimated in Eqn 4.1.

$$N_{pionbkgd} \simeq \left(\frac{N_{R>700gcm^{-2}}}{R>200gcm^{-2}}\right)_{\text{MACRO}} \text{S-K livetime (yrs)} \frac{\text{S-K } \mu\uparrow \text{flux}}{\text{MACRO } \mu\uparrow \text{flux}}. \quad (4.1)$$

Note that Eqn. 4.1 assumes that the detector acceptance and efficiency in MACRO is same as in Super-K and this is not strictly true. In Eqn. 4.1, $N_{R>700gcm^{-2}}$ is obtained by integrating the exponential fit shown in Fig. 4.1 from 700 gcm^{-2} to 4500 gcm^{-2} (which approximately corresponds to the longest muon path-length in Super-K). This gives the total number of photo-produced upward pions in Super–Kamiokande which appear in the upward through-going muon sample $\simeq 0.18$, corresponding to about 0.01% contamination. The total number of up-going pions in MACRO with range $> 200gcm^{-2}$ which get identified as an upward-stopping muon $\simeq 8.8/yr$. Using Eqn. 4.1, the total number of photo-produced upward pions in Super–Kamiokande which can fake as upward stopping muons (for path-length $\geq 7m$) $\simeq 1.4$ corresponding to about 0.3% contamination. Thus the 7 meter path-length cut ensures that the total contamination of photo-produced upward pions at the location of Super–Kamiokande is less than about 1%. Given the 7 m path-length cut, the threshold muon energy (assuming that energy loss is through ionization) is 1.6 GeV following the tables in Ref. [45].

4.2 Data Distributions

Super–Kamiokande has detected 1892 upward thrugoing and 467 stopping muons. The zenith angle distribution of the above upward thrugoing and stopping muons as a function of zenith angle is shown in Figs. 4.2. However near the horizon, there is a background from downward going cosmic ray muons which get identified as upward muons due to multiple coulomb scattering and finite angular resolution. This needs to be subtracted. We now discuss how this is estimated and subtracted.

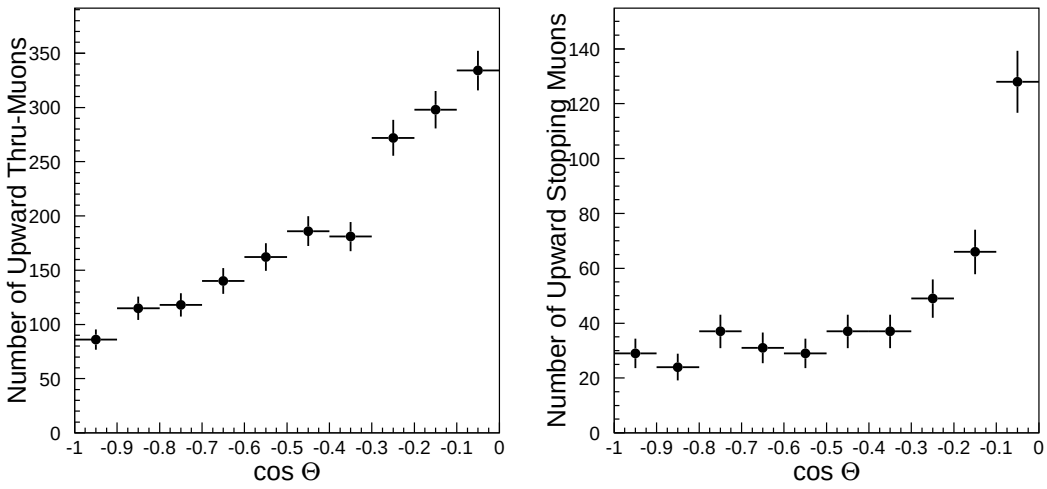

Figure 4.2: Zenith angle distribution of all events identified as upward thrugoing muons (left) and upward stopping muons (right) in Super–Kamiokande.

4.2.1 Cosmic Ray Muon Contamination

The cosmic ray through-going and stopping muons which penetrate the Ikenoyama mountain (under which Super-K is located) and enter the detector could be mis-identified as upward muons. The cosmic ray contamination in various directions depends on the amount of overburden through which the muon travels. To determine this background, we selected a sample of 641.44 days worth of downward thrugoing

muons as described in Sec. 3.8. The zenith and azimuthal distribution of these thrugoing and stopping near-horizontal muons (along with that of upward muons in the same run range) is shown in Fig. 4.3. Most of the clusters come from the thin rock part of the mountain where the overburden is shallow.

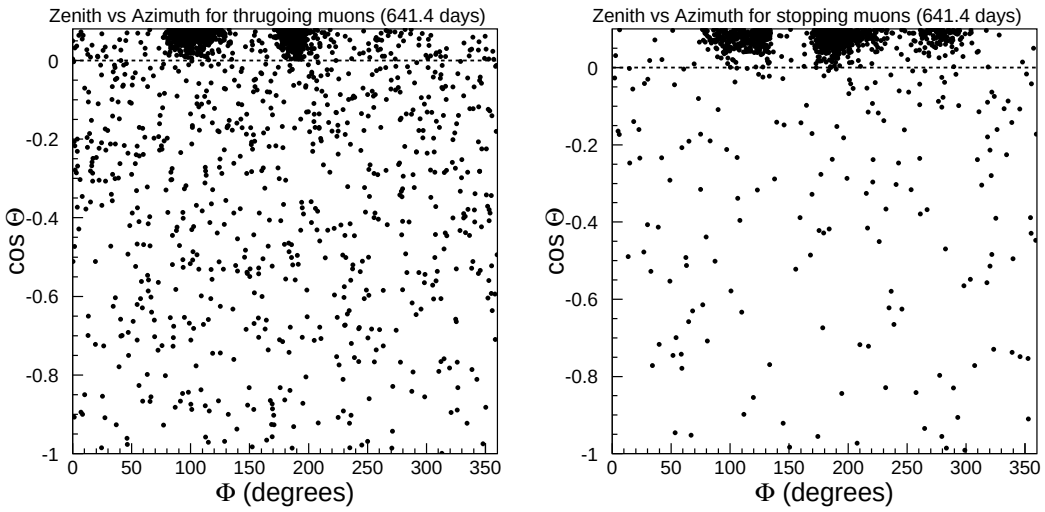

Figure 4.3: Zenith and azimuthal distribution of horizontal and upward thrugoing muons (left), and horizontal and upward stopping muons (right) corresponding to about 641.4 days in Super–Kamiokande. The dense blobs around $\phi = 100°$ and $\phi = 200°$ correspond to thin parts of the mountain.

To determine the thin rock region of the mountain through which a lot of cosmic rays penetrate, we plotted the azimuth distribution of all thrugoing and stopping muons as shown in Fig. 4.4 and Fig. 4.5 respectively. For thrugoing muons the thin-rock corresponds to $60° < \Phi < 240°$ and for stopping muons the thin rock corresponds to $60° < \Phi < 310°$. Since the energy of stopping muons is smaller than thrugoing muons, they multiple-scatter more than thrugoing muons.

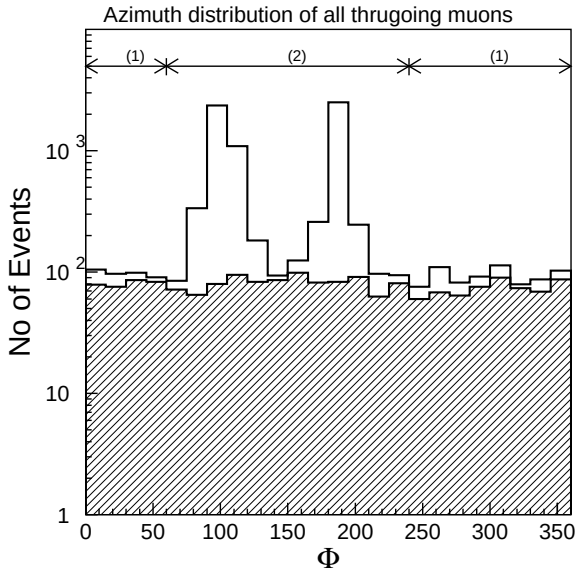

Figure 4.4: The azimuthal distribution of all thrugoing muons in Super–Kamiokande with $-1.0 < cos(\theta) < 0.08$ The region labeled (2) which corresponds to $60° < \Phi < 240°$ represents the thin rock region of the mountain, whereas the region labeled (1) represents the thick rock region of the mountain. The shaded histogram represents the azimuth distribution of all upward through-going muons.

4.2.2 Estimation of Background Contamination

To estimate the background from downward stopping muons penetrating the thin region of mountain, we removed all downward muon events which enter the top of the tank. Since an upward going muon can never satisfy this condition, there can be no contamination from muons which enter the top of the detector. For thrugoing muons we made an additional cut on muons which exit the bottom of the detector. The near horizontal distribution for thrugoing muons and stopping muons is shown in Fig 4.6 and Fig 4.7 respectively. The shape of thrugoing and stopping muon distribution in the thin rock region was fitted to the function

$$f[cos(\theta)] = p1 + e^{[p2+p3cos(\theta)]}. \tag{4.2}$$

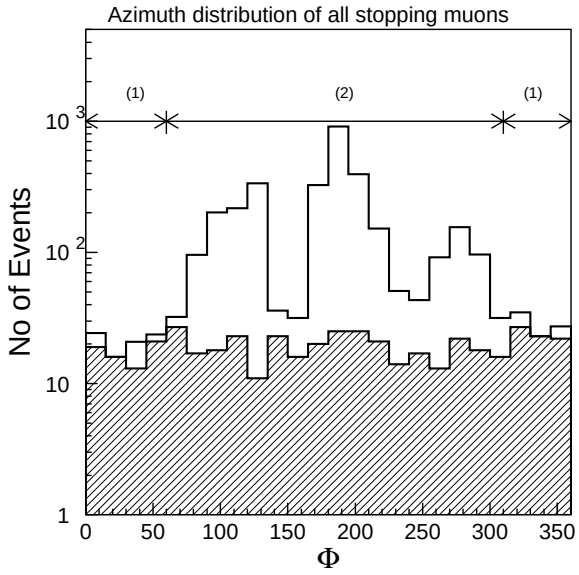

Figure 4.5: The azimuthal distribution of all stopping muons in Super–Kamiokande with $-1.0 < cos(\theta) < 0.08$ The region labeled (2) which corresponds to $60^\circ < \Phi < 310^\circ$ represents the thin rock region of the mountain, whereas the region labeled (1) represents the thick rock region of the mountain. The shaded histogram represents the azimuth distribution of all upward stopping muons.

The background from downward going muons in upward going muon distribution upto zenith angle bin ($\cos\theta_x$) is given by $N_{bkgd} = \int_{cos\theta_x}^{0} e^{[p2+p3cos(\theta)]} d(cos\theta)$. The best fit values for $p1$, $p2$ and $p3$ for stopping and thrugoing muons are shown in Figs. 4.6 and 4.7 respectively. The total number of contamination from cosmic ray muons in upward stopping muon sample is estimated to be 41.0 ± 9.6 for $-0.1 < cos(\theta) < 0$ and 0.42 ± 0.2 for $-0.2 < cos(\theta) < -0.1$. For upward thrugoing muons the corresponding number is estimated to be 13.0 ± 6.6 and all this lie in the $-0.1 < cos(\theta) < 0$ bin.

The observed upward going muon data after background subtraction is shown in Fig. 4.8.

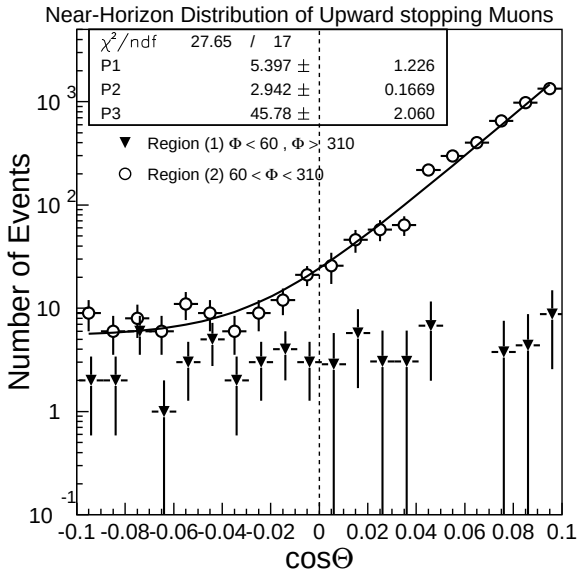

Figure 4.6: Near-horizontal distribution of stopping muons for $-0.1 < cos(\theta) < 0.08$ in the thin rock and thick rock region after a cut on events which enter the top. The line represents a best-fit (using Eqn 4.2) to this distribution.

4.3 Observed Flux

The upward going muon flux $[\Phi(\theta)]$ in each zenith angle bin θ is given by :

$$\Phi(\theta) = \frac{N(\theta)}{2\pi\epsilon(\theta)A(\theta)T}, \tag{4.3}$$

where T is the Super–Kamiokande livetime for upward going muons (1679.59 days), $A(\theta)$ is the detector effective area for upward muons with path-length greater than 7 m, and $\epsilon(\theta)$ is the efficiency for detecting upward muons. We now now discuss how $\epsilon(\theta)$ and $A(\theta)$ are calculated.

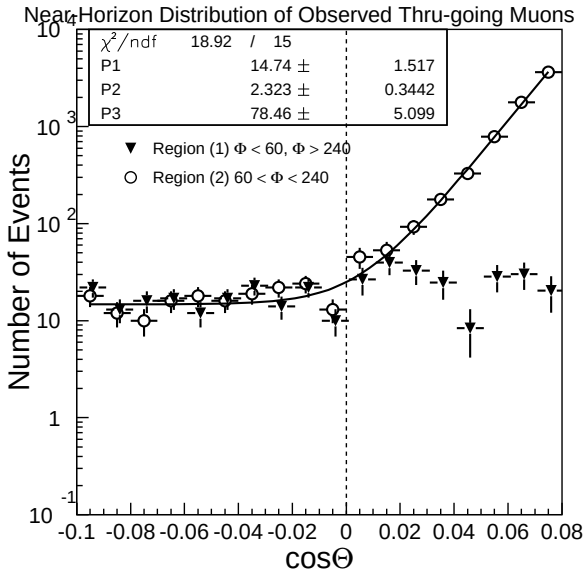

Figure 4.7: Near-horizontal distribution of thrugoing muons for $-0.1 < cos(\theta) < 0.08$ in the thin rock and thick rock region after a cut on events which enetr the top or exit the bottom. The line represents a best-fit (using Eqn 4.2) to this distribution.

4.3.1 Effective Area

To calculate the observed flux of upward muons we need to calculate the area perpendicular to the direction of incidence for all tracks with track-length inside Super–Kamiokande ID greater than 7 m at different zenith angles. The details of the calculation are outlined in Ref. [130, 47]. The effective area for an upward muon with path-length $\geq 7m$ is shown in Fig. 4.9.

4.3.2 Detection Efficiency

We estimated the detection efficiency using the 40-year atmospheric neutrino Monte Carlo (which is described in Sect. 4.4). Now for each Monte Carlo event we know the truth variables such as the true muon direction, true muon length, true neutrino interaction point, etc. To estimate the detection efficiency (for upward-thrugoing

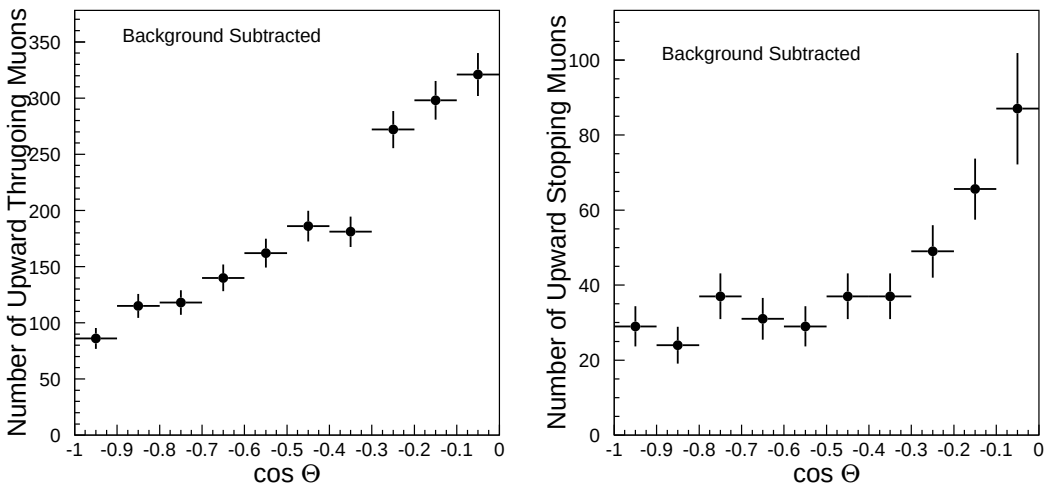

Figure 4.8: Zenith angle distribution of all upward thrugoing muons (left) and upward stopping muons (right) after background subtraction from cosmic ray muons. The error in the last bin includes systematic error from background subtraction.

and stopping muons,) we divided the total number of reconstructed upward muons by the number of Monte Carlo events which satisfy the following conditions :

- Truth direction of muon is upward.
- Muon truth path-length is greater than 7 m.
- Truth neutrino interaction point is in the OD or rock.
- Truth classification of the muon is thrugoing/stopping.

The detection efficiency as a function of reconstructed cosine of zenith angle for upward thrugoing and stopping muons is shown in Fig 4.10. For some of the bins the efficiency is greater than 1 because there are some events which don't satisfy the above conditions, but which creep in the reconstructed sample. The fraction of events which are not "true " upward muons but which appear in the reconstructed Monte Carlo sample is 3.5% for thrugoing muons and 6.3% for stopping muons.

The total upward thrugoing and stopping muon flux is shown in Fig. 4.11

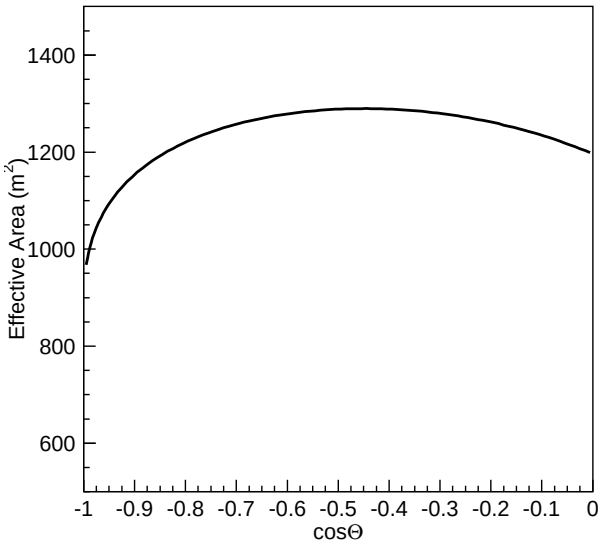

Figure 4.9: Effective area in Super–Kamiokande for a muon which travels at least 7 meters in the ID as a function of zenith angle.

4.3.3 Systematic Errors

The systematic errors which affect upward thrugoing and stopping muon flux mainly can be divided into following categories:

- **Livetime Error**

  The livetime calculation is explained in Sect. 3.7. The condition under which the time-interval between two events is considered dead or alive is shown in Fig. 3.6. To calculate the livetime systematic error, we then swap the definition of dead and alive time-interval from Fig. 3.6 and recalculate the livetime. In other words if a dead event is followed by an alive event, this time-interval is counted towards dead-time and vice-versa. The total livetime obtained with this method is 1656.9 days. The livetime systematic error is then the difference between these estimates and is equal to 1.35%.

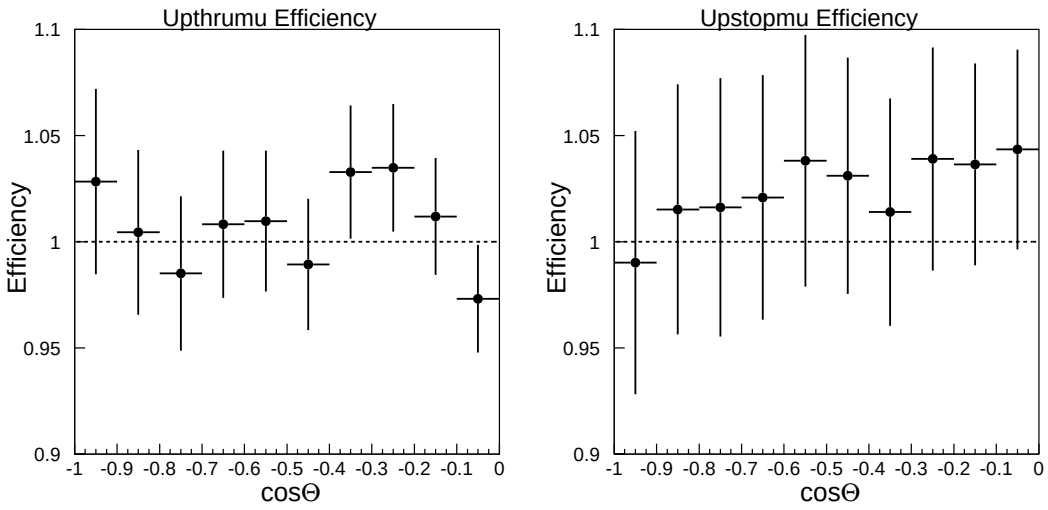

Figure 4.10: Efficiency for reconstructing upward-thru going (left panel) and upward stopping muons (right panel) as a function of reconstructed cosine of zenith angle.

- **Track-Length and Effective Area Error**

  We estimated the path-length resolution by comparing the fitted track-length vs the Monte Carlo truth path-length. This is shown in Fig. 4.12. The track-length resolution for thrugoing muons is 45 cm and for stopping muon is about 60 cm. When the track-length threshold for changed by ± 45 cm for thrugoing and ± 60 cm for stopping muons, the flux of upward thrugoing and stopping muons changed by $\pm 0.9\%$ and $\pm 5.7\%$ respectively. The uncertainty because of effective area is about 0.3% which comes from the geometric uncertainty of the detector.

- **Stopping/Thrugoing mis-identification**

  Using the Monte Carlo we find that the contamination from upward stopping muons in the thrugoing muon sample is about 0.1%, whereas the contamination from upward thrugoing muons in the upward stopping muon sample is about 2.87%. The amount of contamination from electron showers is estimated

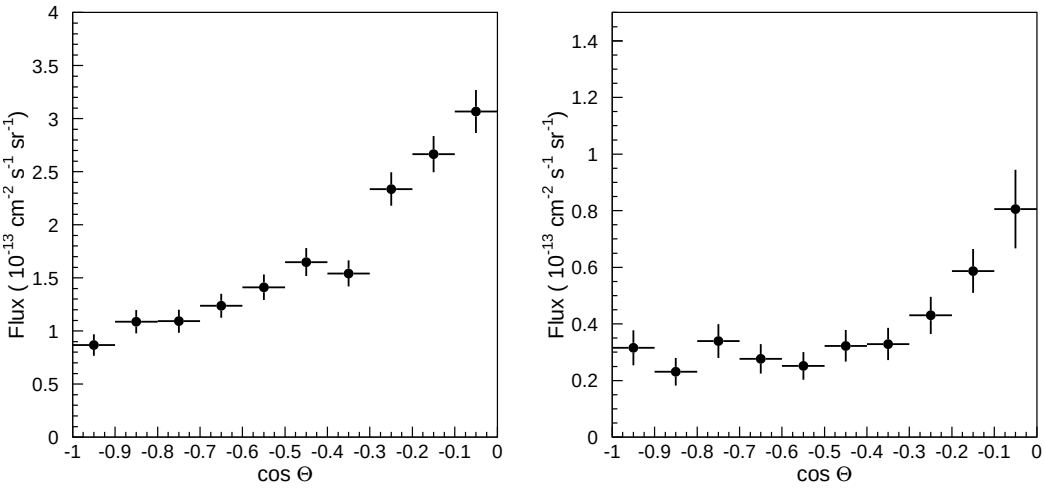

Figure 4.11: The observed flux of upward thrugoing muons (left panel) and stopping muons (right panel).

Error Source	Thrugoing Muons	Stopping Muons
Livetime	1.35%	1.35%
Effective Area	0.3%	0.3%
7 m cut	0.9%	5.7%
Mis-identification	0.1%	2.87%
Total Error	±1.65%	±6.5%

Table 4.1: Summary of observed systematic errors for upward thrugoing and stopping muons.

to be $\simeq 0.1\%$ and $\simeq 0.5\%$ in the upward thrugoing and stopping muon sample respectively, and hence can be neglected.

A summary of the dominant systematic errors for thrugoing and stopping muons is shown in Table 4.1.

4.3.4 Total Observed Flux

In 1679.6 days the total observed flux of upward thrugoing and stopping muons, and their ratio can be written as :

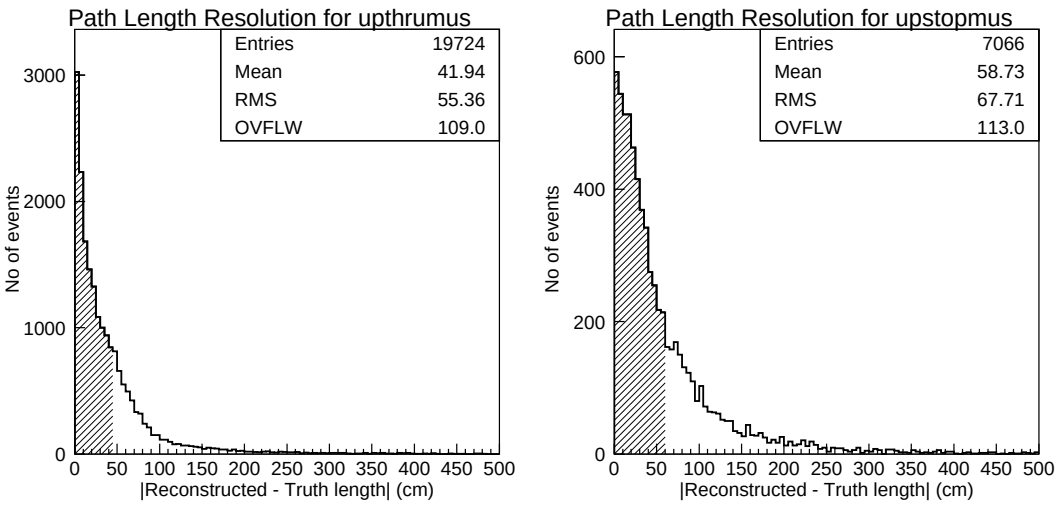

Figure 4.12: Path-length resolution for upward thrugoing muons (left panel) and stopping muons (right panel). The shaded region contains 68 % of the total area and is equal to 45 cm for thrugoing muons and 60 cm for stopping muons.

$$\Phi_{thru} = 1.71 \pm 0.04(stat.) \pm 0.03(syst.) \times 10^{-13}(cm^{-2}s^{-1}sr^{-1})$$

$$\Phi_{stop} = 0.39 \pm 0.02(stat.) \pm 0.03(syst.) \times 10^{-13}(cm^{-2}s^{-1}sr^{-1})$$

$$\Phi_{thru+stop} = 2.1 \pm 0.05(stat.) \pm 0.04(syst.) \times 10^{-13}(cm^{-2}s^{-1}sr^{-1})$$

$$\frac{\Phi_{stop}}{\Phi_{thru}} = 0.228 \pm 0.014(stat.) \pm 0.018(syst.)$$

4.3.5 Neutrino-induced Muons Above Horizon

As we can see from Fig. 4.4 and 4.5, the distribution in the thick region is flat and these predominantly come from neutrinos. One can estimate the flux of these neutrino-induced muons and the zenith angle distribution of upward muons can be extrapolated to above the horizon. However because it is hard to estimate the background from cosmic ray muons in this region, we considered a narrower ϕ region than what was used in Sect. 4.2.1. To do this we scaled the number of muons in the region $60 < \Phi < 310°$ by the effective area which is decreased from that in Fig. 4.3.1 by about a factor of 3.7. The resulting flux of neutrino induced thrugoing muons

above the horizon is estimated to $(4.0 \pm 1.07(stat) \pm 0.07) \times 10^{-13}(cm^{-2}s^{-1}sr^{-1})$ in the $0 < cos(\theta) < 0.08$ zenith angle bin. The flux of neutrino induced stopping muons above the horizon is estimated to $(0.9 \pm 0.47(stat) \pm 0.07) \times 10^{-13}(cm^{-2}s^{-1}sr^{-1})$ in the $0 < cos(\theta) < 0.1$ zenith angle bin. The zenith angle distribution of all neutrino-induced thrugoing and stopping muons (including these events above the horizon) is shown in Fig. 4.13. However due to the large error bars and additional uncertainty from cosmic ray background in this region, the neutrino-induced flux above the horizon is not used for any physics or astronomy analysis in this thesis.

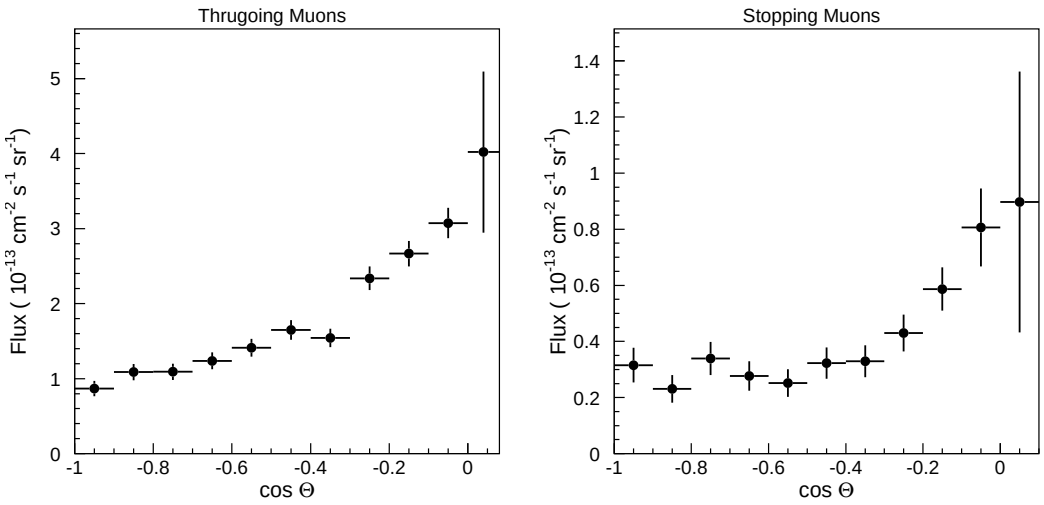

Figure 4.13: Flux of all neutrino-induced thrugoing muons (left panel) and stopping muons (right panel) in Super–Kamiokande.

4.4 Expected flux and Monte Carlo Simulation

The observed upward going muons come from atmospheric neutrinos. The atmospheric neutrinos are produced from pion and kaon decay which in turn are the spallation products of cosmic ray interactions with the atmosphere. The energy spectrum of cosmic rays is given by : $\frac{dN}{dE} \propto E^{-2.7}$. The neutrinos then travel through the

earth and undergo a charged current interaction with the rock below the detector to produce a muon : $[\nu_\mu(\bar{\nu_\mu}) + N \rightarrow \mu^-(\mu^+) + X]$, where N is the nucleus with which the neutrino interacts, X is the resulting hadron. The expected flux of upward muons can be calculated either analytically or through Monte Carlo simulation. The upward going muon flux can be written as [130] :

$$\frac{d\Phi_\mu}{d\Omega} = \int_{E_{th}}^{\infty} P(E_\nu, E_{th}) \frac{d^2\Phi_\nu(E_\nu, cos(\theta))}{dE_\nu d\Omega} dE_\nu, \tag{4.4}$$

where $P(E_\nu, E_{th})$ is the probability that a neutrino E_ν makes a muon with energy greater than E_{th} and is given by :

$$\frac{d\Phi}{d\Omega} = \int_0^1 \left[\int_0^1 \frac{d^2\sigma}{dxdy} dx \right] dE_\nu \tag{4.5}$$

Thus given the atmospheric neutrino flux, neutrino cross-section and muon range, one can integrate the above function to calculate the upward muon flux analytically. However most results in this dissertation are based upon a Monte Carlo simulation. The Monte Carlo has been generated with the Nuance neutrino generation package [49]. We first describes some Physics input aspects which are needed for both analytic flux calculation or to do Monte Carlo calculation.

4.4.1 Atmospheric Neutrino Flux

The atmospheric neutrino flux has been calculated by several groups [50],[51],[52]. Details of atmospheric neutrino flux calculations and uncertainties have been reviewed in Ref. [53]. The Monte Carlo code uses the neutrino fluxes calculated by the Bartol group [51] which have provided flux tables upto 100 TeV. The comparison of atmospheric ν_μ as calculated by different groups is shown in Fig. 4.14. The relative

importance of pions and kaons which give rise to atmospheric neutrinos is shown in Fig. 4.15 [4]. The ratio of horizontal to vertical flux is shown in Fig. 4.16 [4].

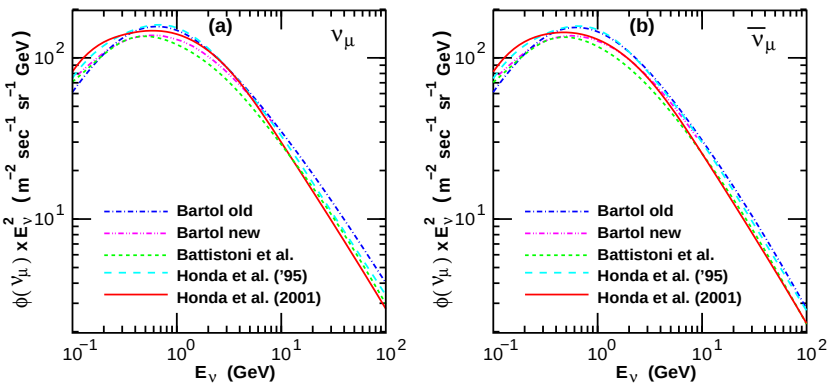

Figure 4.14: Comparison of angle-averaged atmospheric-neutrino flux at Kamioka by different groups. Figure obtained from Ref. [53].

4.4.2 Neutrino-Nucleon Cross-section

The neutrino charged-current cross-section is given by sum of contribution from deep-inelastic scattering, quasi-elastic scattering and single-pion production. The deep-inelastic cross-section depends on the model adopted for the Parton distribution function (which is basically the wave function of quarks inside the nucleus). In this thesis we shall use the GRV-94 PDF [54].

4.4.3 Muon Propagation

Muon propagation in the rock is simulated using a library of routines provided by Lipari and Stanev [55]. The mean muon energy loss in rock due to ionization and radiative processes is shown in Fig. 4.17. The muon range in rock is shown in

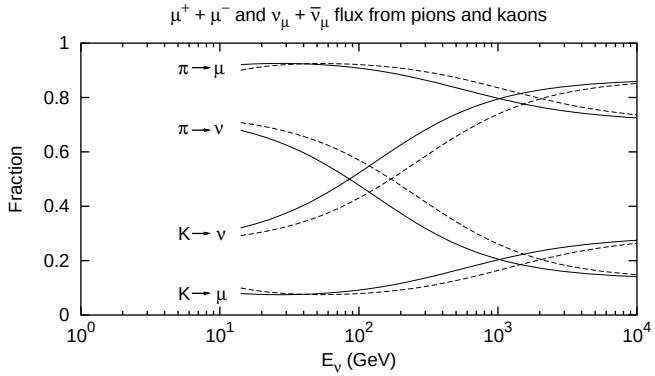

Figure 4.15: Fraction of ν_μ from pions and kaons as a function of neutrino energy. Solid line represents flux at vertical and dashed line represents flux at 60°. Figure obtained from Ref. [4].

Fig. 4.18. However there are fluctuations in radiative energy losses which dominate at higher energies. Correspondingly the range distribution for a given muon energy becomes wider as the energy increases. The composition of rock is assumed to be "standard rock " for which $\rho = 2.65 g/cc$, $Z = 11$ and A=22 [129].

4.5 Event Generation

Monte Carlo muon events are generated with appropriate energy and zenith angle from the atmospheric neutrino energy spectrum. The effective volume for event generation is given by $V_{eff}(E_0, \Omega_f, E_{min}) = A(\Omega_f) R_{eff}(E_0, E_{min})$ where E_0 is the initial muon energy, $R_{eff}(E_0, E_{min})$ is the effective muon range, and $A(\Omega_f)$ is the projected area of the detector in the direction of Ω_f. Then only those events are accepted for which $V_{eff}(E_0, \Omega_f, E_{min}) > V(E_\nu) \times rn$, where rn is a random number

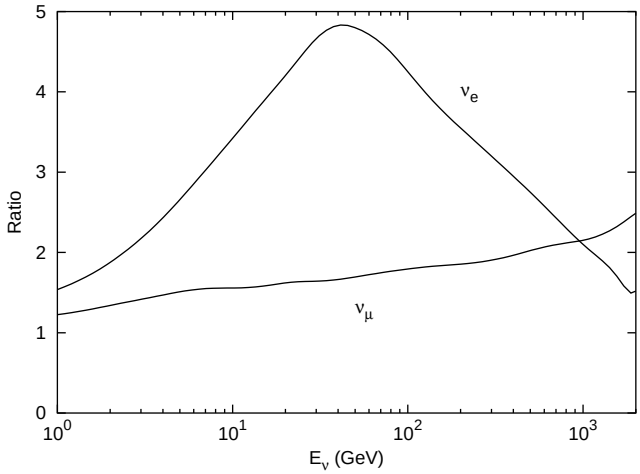

Figure 4.16: Ratio of horizontal ($0 < |cos\theta| < 0.375$) to vertical flux ($0.675 < |cos\theta| < 1$) of atmospheric neutrinos as a function of energy. Figure obtained from Ref. [4].

between 0 and 1. To obtain the initial muon energy the cumulative probability distribution as a function of effective depth (X_{eff}) is defined as:

$$P(X_\mu) = \frac{\int_0^{X_\mu} dX' p_{surv}(E_0, E_{min}, X')}{R_{eff}(E_0, E_{min})}, \tag{4.6}$$

where R_{eff} is the effective range for a muon of a given energy and is given by :

$$R_{eff} = \frac{\int_0^\infty p_{surv}(E_0, E_{min}, X')}{\rho}, \tag{4.7}$$

$p_{surv}(E_0, E_{min}, X')$ is the muon survival probability which is defined in Ref. [55]. Once $P(X_\mu)$ is assigned a random value between 0 and 1, one obtains the value of the muon effective range. Once the muons are generated at the detector they are passed through the GEANT based detector simulation.

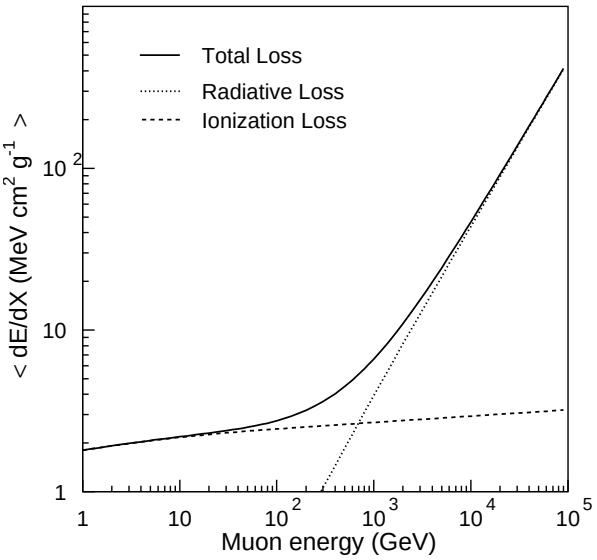

Figure 4.17: $\left\langle \frac{dE}{dX} \right\rangle$ for muon in rock [129] including contributions from ionization and radiative processes.

4.6 Monte Carlo Sample

In all a 40-year equivalent of atmospheric neutrino sample was generated All the generated events were than passed through the same reduction, reconstruction and stop/thru classification procedure as described in the previous chapter. However, unlike the upward going muon data this sample was not expert-scanned. The summary of number of events is shown in Table 4.2. In all we obtained 19760 upward thrugoing and 7121 upward stopping muons in this sample. Of all the reconstructed upward thrugoing muons, 1.2% of them result from neutrino interactions in the OD. For upward stopping muons, about 4.8% result from neutrino interactions in the OD. The flux of this 40-year sample along with a comparison with analytic flux is shown in Fig. 4.19. The energy spectrum of the parent neutrinos of the upward thrugoing and stopping muons is shown in Fig. 4.20. As we can see the mean energy of the parent neutrinos of upward thrugoing muons is $\simeq 100\ GeV$ and for stopping muons

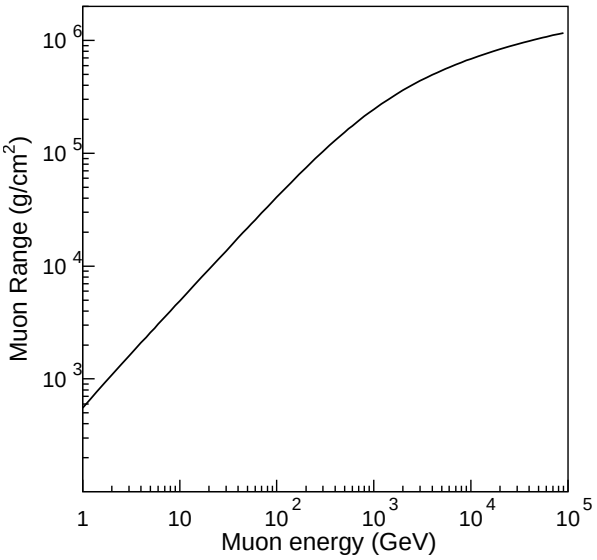

Figure 4.18: Muon range in "standard rock" as a function of energy [129].

Reduction Stage	No of events	Charge Range	Muon Type
Raw Events	128802	N/A	N/A
Pre-Reduction	77412	$Q >= 8000pe$	N/A
Post-Reduction	42450	$1750000 > Q >= 8000pe$	N/A
Post-Reduction	5	$Q > 1750000$	N/A
Post-Reconstruction	19760	$1750000 > Q >= 8000pe$	Thrumus
Post-Reconstruction	7121	$1750000 > Q >= 8000pe$	Stopmus

Table 4.2: Number of generated Monte Carlo events in a 40-yr equivalent atmospheric neutrino sample.

is $\simeq 10\ GeV$. The muon energy spectrum is shown in Fig. 4.21. The mean initial muon energy of the the thrugoing and stopping muon sample is 20 GeV and 4 GeV respectively.

4.6.1 Uncertainties in Expected Flux

The main uncertainty in the absolute flux comes from uncertainty in the primary cosmic ray flux. The uncertainty in the primary flux is estimated to be $\pm 20\%$ [51]. The

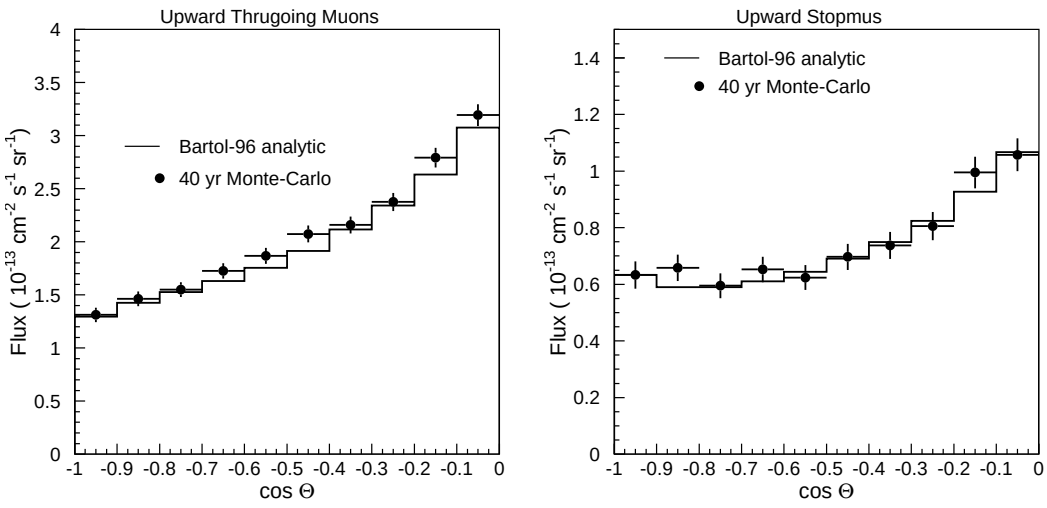

Figure 4.19: Comparison of absolute upward muon flux as calculation with 40 year Monte Carlo with analytic calculation for thrugoing muon (left panel) and stopping muons (right panel).

systematic uncertainty because of model-dependence is estimated by comparing the difference between the Honda and Bartol flux in each bin. This is shown in Ref. [47]. This uncertainty from model-dependence of neutrino flux is about ±10%. The uncertainty in the ratio of upward thrugoing to stopping muon flux comes from uncertainty in the primary cosmic ray spectral index which is estimated to be ± 5% [56]. To estimate how this uncertainty would affect the ratio of upward stopping to thrugoing muon flux, we weighted the number of upward events in each energy bin by $(E/50GeV)^{\pm 0.05}$ (instead of 1) and recounted the total number of events. When this is done the ratio changes to +11.6% and -10.7%.

4.7 Comparison of Data and Expected Flux

It has been shown that the shape of the observed zenith angle distribution of upward thrugoing and stopping muons, and the ratio of upward stopping to thrugoing muons

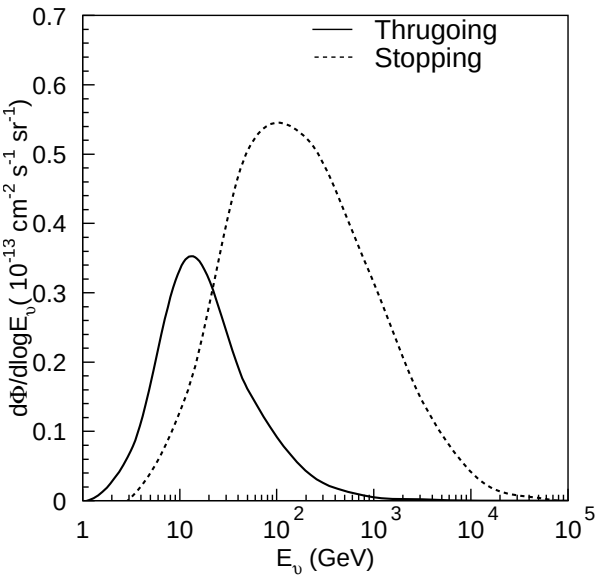

Figure 4.20: Energy spectrum of parent neutrinos making upward thrugoing and stopping muons as measured with the 40-year Monte Carlo.

is inconsistent with the expected atmospheric neutrino flux obtained using analytic calculation [57, 58]. The best fit to the observed distribution is obtained after adding contributions from $\nu_\mu \rightarrow \nu_\tau$ oscillations. Here we shall address the same questions using the Monte Carlo.

4.7.1 Thrugoing Muons

To do this analysis with thrugoing muons we defined a χ^2 given by:

$$\chi^2 = \sum_{i=1}^{10} \left[\frac{\left(\frac{d\phi^{data}}{d\Omega}\right)_i - (1+\alpha)(1+2\epsilon(cos\theta_i + 0.5)) \left(\frac{d\phi^{MC}}{d\Omega}\right)_i (sin^2 2\theta, \Delta m^2)}{\sqrt{(\sigma^i_{stat})^2 + (\sigma^i_{syst})^2}} \right] + \left(\frac{\alpha}{\sigma_\alpha}\right)^2 + \left(\frac{\epsilon}{\sigma_\epsilon}\right)^2 \tag{4.8}$$

where $\left(\frac{d\phi}{d\Omega}\right)_i$ is the observed flux in bin i, $\left(\frac{d\phi^{MC}}{d\Omega}\right)_i (sin^2 2\theta, \Delta m^2)$ is the oscillated Monte Carlo flux in bin i as a function of mixing parameters $sin^2 2\theta$ and Δm^2, σ^i_{stat} is the statistical error in the observed flux, and σ^i_{syst} is the bin-by-bin uncorrelated

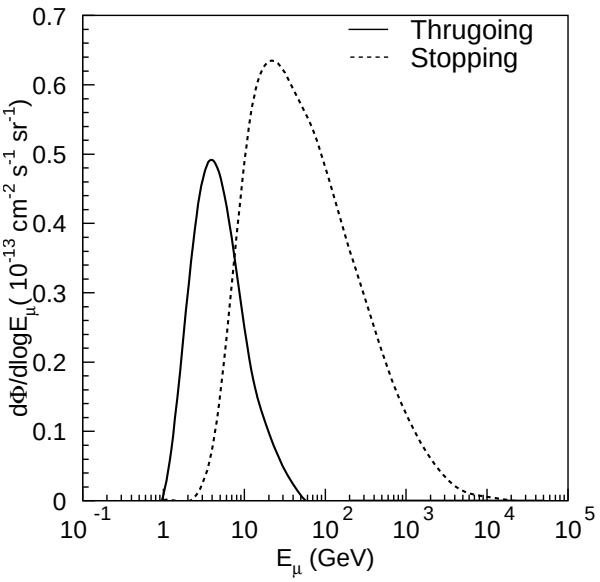

Figure 4.21: Energy spectrum of upward-thrugoing and stopping muons as measured with the 40-year Monte Carlo.

systematic error which comes from model dependence and has been estimated in [47], $\sigma_\alpha = 0.224$ is the error in the absolute normalization, and $\sigma_\epsilon = 0.03$ in the uncertainty in the kaon to pion ratio which affects the horizontal to vertical ratio. The denominator in Eqn. 4.8 indicates the statistical and systematic error in the observed data and Monte Carlo. The best fit value of χ^2 in Eqn. 4.8 in the physical region (for which $sin^2 2\theta <= 1$) occurs at $\chi^2 = 6.49$ corresponding to 8 d.o.f when $sin^2 2\theta = 1.00$, $\Delta m^2 = 0.00329$ eV^2, $\alpha = -0.022$ and $\epsilon = 0.06$. The best fit in the unphysical region occurs at $\chi^2 = 6.45$, when $sin^2 2\theta = 1.054, \Delta m^2 = 0.00329$ eV^2, $\alpha = -0.022$ and $\epsilon = -0.01$. For null oscillation case, $\chi^2 = 23.1$ for 10 dof, when $\alpha = -0.193$ and $\epsilon = 0.06$. We then obtained allowed regions in $(\Delta m^2, sin^2 2\theta)$ parameter space at 68%, 90 % and 99% CL. These were obtained by finding locus of points for which $\Delta\chi^2$= 2.28, 4.606, and 9.212 respectively, where $\Delta\chi^2 = \chi^2 - \chi^2_{min}$. The allowed regions for neutrino oscillation parameters using upward thrugoing muons along with

the zenith angle distribution at the best fit is shown in Fig. 4.22.

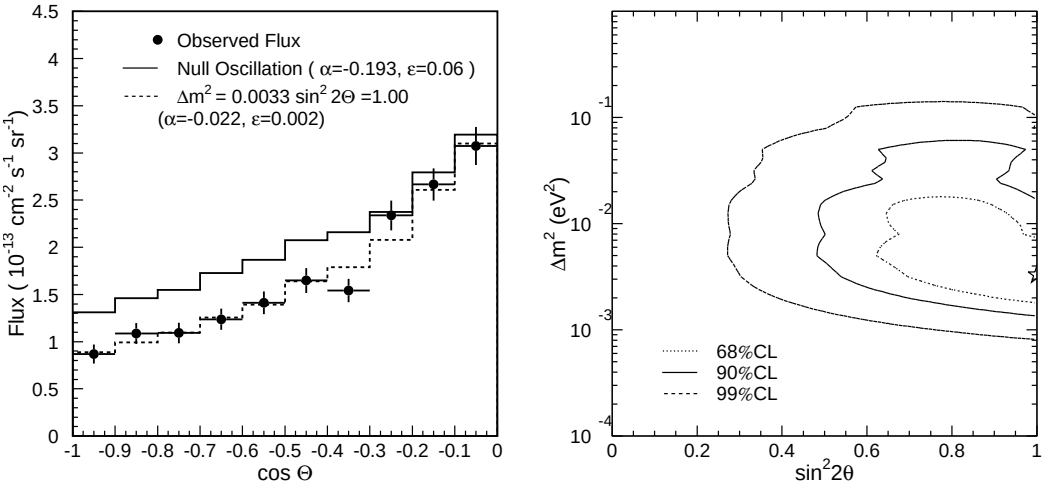

Figure 4.22: Oscillation results using upward-thrugoing muons.

4.7.2 Stopping Muons

To do the oscillation analysis with upward stopping muons, we used the same definition of χ^2 as in Eqn. 4.8. The best value for χ^2 in the physical region is obtained when $\chi^2 = 5.613$ corresponding to 8 d.o.f when $sin^2 2\theta = 1.00$ and $\Delta m^2 = 0.003845$ eV^2, $\alpha = -0.063$ and $\epsilon = 0.009$. The best fit in the unphysical region occurs when $sin^2 2\theta = 1.087, \Delta m^2 = 0.00395$ eV^2, $\alpha = 0.016$ and $\epsilon = 0.007$ and corresponds to $\chi^2 = 5.36$. For null oscillation case, $\chi^2 = 17.46$ for 10 dof when $\alpha = -0.511$ and $\epsilon = 0.018$. The allowed regions for neutrino oscillation using only upward stopping muons along with the zenith angle distribution at the best fit is shown in Fig. 4.23.

4.7.3 Thrugoing/Stopping Ratio

A more useful quantity than the absolute flux for probing neutrino oscillations is the stopping/thrugoing flux ratio, since this cancels much of the large ($\simeq$ 20%)

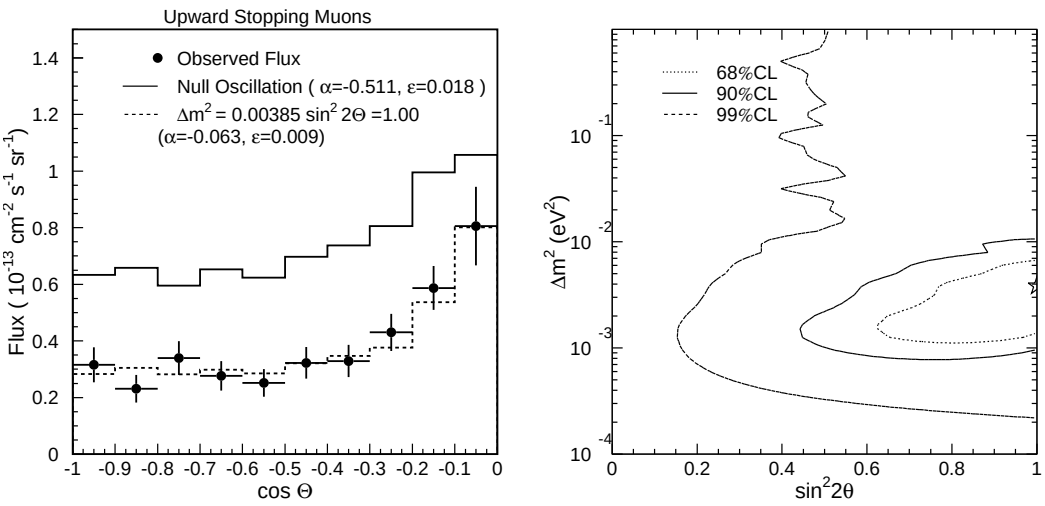

Figure 4.23: Oscillation results using upward stopping muons.

uncertainty in the normalization of the absolute flux and the neutrino cross-sections. The definition of χ^2 for the ratio is given by :

$$\chi^2_{ratio} = \sum_{i=1}^{10} \left[\frac{R^i_{obs} - (1+\beta)R^i_{theo}}{\sqrt{(\sigma^i_{R,stat})^2 + (\sigma^i_{R,syst})^2}} \right]^2 + \left[\frac{\beta}{\sigma_\beta} \right]^2 \tag{4.9}$$

The best fit value of χ^2 in Eqn 4.9 is obtained at $\chi^2 = 5.978$ when $sin^2 2\theta = 0.995, \Delta m^2 = 0.002529$ eV^2, and $\beta = -0.339$. For null oscillation case, $\chi^2 = 13.7$ for 10 dof when $\beta = -0.089$.

4.8 Conclusion

The overall shape of zenith angle distribution of thrugoing and stopping muon is consistent with oscillation from $\nu_\mu \rightarrow \nu_\tau$. Also the allowed regions are in agreement with those found by Super–Kamiokande contained events (which are of a lower energy than upward muons and hence more sensitive to oscillations). Finally in Chapter [7], we shall split the upward thrugoing muon sample into two categories and will do a

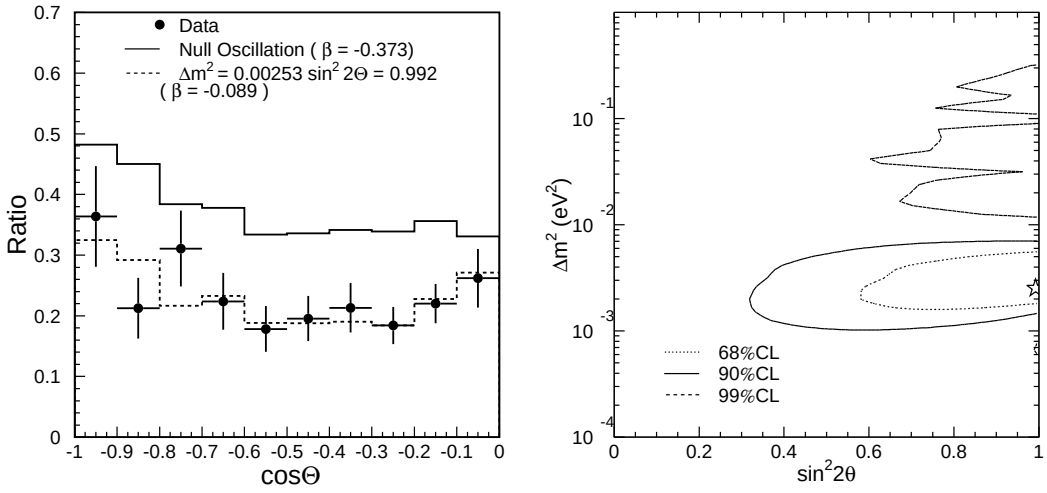

Figure 4.24: Oscillation results using the ratio of flux of upward stopping muons to thrugoing muons.

combined oscillation analysis with all 3 data samples.

Chapter 5

Indirect Searches for WIMPs

5.1 Introduction

The "dark matter" problem is one of the most important unsolved problems in physics and the answer could lie in particle physics beyond the Standard Model.

By dark matter, we mean any form of matter or energy density which does not emit or absorb electromagnetic radiation and manifests itself only through gravity. Astronomical observations on a variety of scales indicates that most of the mass/energy density of the universe is dominated by dark matter which cannot be ordinary baryons. In Sect. 5.2 we give a brief overview of evidence for dark matter in our galaxy (as this is important for experimental dark matter searches). Then we shall outline why within the framework of Standard Cosmology about 30% of this dark matter contains "cold dark matter" and how Supersymmetry (which is one of the proposed extensions to the Standard Model of particle physics) could provide a cold dark matter candidate. We then outline the two main avenues of their detection through direct and indirect searches with neutrinos. We then review the constraints on cold dark matter from Super–Kamiokande.

5.2 Evidence for Dark Matter in our Galaxy

The most incontrovertible evidence for dark matter at galactic scales comes from observations of flat rotation curves of spiral galaxies up to very large distances. From the amount of gas and stars one would have expected the rotation curves to fall off with distance. This is illustrated in Fig. 5.1. The same feature is true for many spiral galaxies.

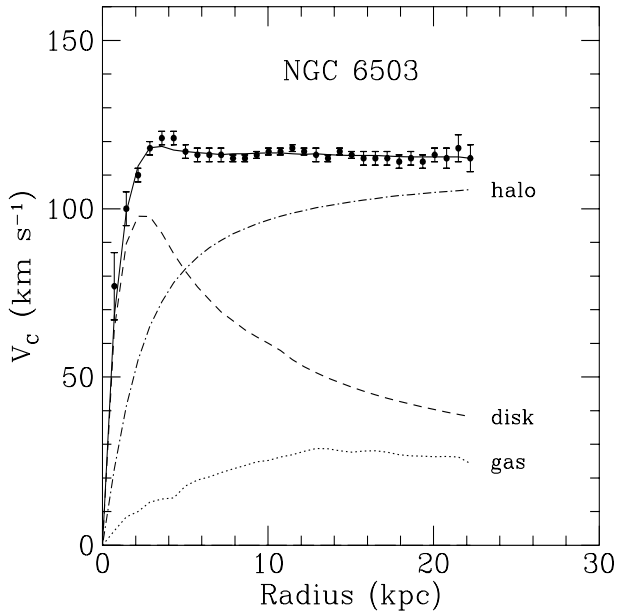

Figure 5.1: Typical rotation curve of a spiral galaxy (NGC6503). The dashed and dotted curves indicate the estimated contribution to the rotation curve from the gas and disk respectively. Figure is from Ref. [59].

Unfortunately because of our location *in* the galaxy, the rotation curve of the Milky Way cannot be measured with the same precision as that of others especially beyond about 20 kpc. However the qualitative features are same as that of other spiral galaxies. The circular speed rises from 0 and asymptotes to roughly 220 km s^{-1} near the Sun and remains flat up to $\simeq$ 25 kpc. The luminous disk of our Galaxy extends roughly up to 10 kpc from the Galactic Center. From Kepler's laws the

rotation speed should fall off as $v \propto r^{-1/2}$ at radii larger than the extent of the visible disk. By studying the proper motions of satellite galaxies of the Milky Way Sakamoto et. al. [60] have derived the total mass of the Milky Way galaxy to be $2.5^{+0.5}_{-1.0} \times 10^{12} M_{\odot}$ which means the total mass to light ratio in our galaxy is about 100 times the solar value. The dark matter in our galaxy is embedded in a spherical halo and the most favored model for the dark matter density distribution is given by the Navarro-Frank-White profile [61]. The local dark matter density is approximately $0.3 Gev/cm^3$. The velocity distribution of the dark matter particles is inferred to be isotropic with a Maxwell-Boltzmann distribution with mean velocity of 0 and r.m.s velocity of about 220 km/s. However there are factors of two uncertainties in the dark matter density and rms velocity. Very little is known about the bulk rotation speed of the dark matter halo and the simplest assumption is that this is 0.

5.3 Dark Matter Classification

Dark matter is broadly divided into two categories: baryonic and non-baryonic dark matter. Baryonic dark matter includes anything which in its most elementary form constitutes baryons and possibilities include Jupiters, brown dwarfs, collapsed stellar objects, stellar mass black holes etc. All these objects are dubbed Massive Astrophysical Compact Halo Objects (MACHOs). Various micro-lensing searches which have looked for such MACHOs in our galaxy have failed to find any. The MACHO project have excluded at 95% c.l. objects in the mass range of 0.3–30.0 $M_{\odot}$ from contributing more than $4 \times 10^{11} M_{\odot}$ to the Galactic halo [62]. Also the amplitude of fluctuations in the CMB anisotropy power spectrum would be much larger than observed if most of the universe was made of baryonic dark matter. Also the total amount of baryons from observed deuterium abundance and the theory of Big Bang

Nucleosynthesis [63] and from observations of power spectrum (summarized in Section 5.4) indicate that the inferred density of baryons in the universe is only about 4%.

5.3.1 Non-Baryonic Dark Matter

Non-Baryonic dark matter is broadly classified into two categories : "Hot" and "Cold" dark matter. If dark matter particles are moving at relativistic speeds when the cosmic horizon encompassed about $10^{12} M_{\odot}$, they are called hot dark matter. Cold dark matter refers to particles moving at non-relativistic velocities. Structure formation in the universe proceeds completely differently depending on whether hot or cold dark matter is the dominant dark matter component. The main example of hot dark matter is a light neutrino. The main argument against hot dark matter comes from structure formation. The scale of galaxy clustering in hot dark matter dominated models is much larger than observed [64]. In hot dark matter dominated models structure formation proceeds in a top-down scenario where the first objects to form first are superclusters of mass about 10^{16} times that of the Sun which then fragment to form smaller structures [65]. This is not observed, as galaxies are found to be much older than superclusters. Other problems with hot dark matter models are discussed in Ref. [65]. Also, given the limits on neutrino mass the maximum allowed phase-space density of neutrinos from Pauli's exclusion principle is less than the density of dark matter in dwarf galaxies [66]. Thus, hot dark matter is ruled out as the major component of dark matter. As we show in the next section the current best fit concordance models indicate that about 27 % of the universe is made up of non-baryonic cold dark matter.

5.4 Global Cosmological Parameters

Standard Cosmology is based on the assumptions that today's universe evolved from a Hot Big Bang, the large scale structure of the universe is determined by gravitational interactions, and the universe is homogeneous and isotropic at very large scales [67]. The geometry of the universe is determined by Einstein's equations and dynamics of the universe is determined by the amount of mass-energy content of the universe.

Standard Cosmology assumes that there were small deviations from homogeneity (produced by quantum fluctuations from inflation or some similar mechanism) and cosmic structures were formed by gravitational agglomeration of these perturbations. These density fluctuations can be probed using observations of cosmic-microwave background anisotropies, gravitational lensing, clustering of galaxies and galaxy clusters and gas clouds which absorb quasar light (called Lyman- α forest) over wide range of scales and redshifts. These density perturbations are characterized by a power spectrum P(k,z) which is the variance of the fluctuations as a a function of wavenumber k and red-shift z.

The measurement of power spectrum using the latest CMB data from WMAP along with the 2df galaxy catalog and Lyman α indicates that we live in a flat universe in which about 27 % of the universe is made of matter, out of which only about 4% is made of Baryons and the rest is made of mark matter which moves at non-relativistic velocities when galaxies are form, called cold dark matter [17]. Remaining 73% is made up of "dark energy" with negative pressure and which causes the universe to accelerate. The remarkable agreement of this concordance model with the high precision angular power spectrum measured using the WMAP experiment is shown in Fig 5.2

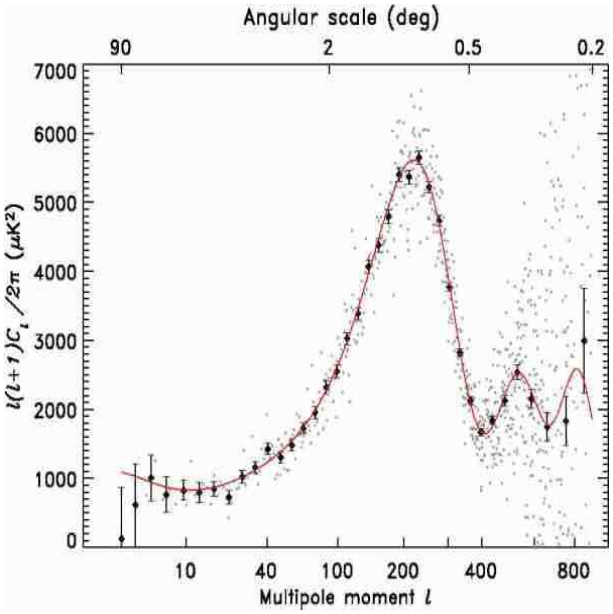

Figure 5.2: This figure compares the best fit power law ΛCDM model to the WMAP temperature angular power spectrum. The gray dots are the unbinned data. Figure is obtained from Ref [17].

5.5 Cold Dark Matter

The main particle-physics motivated cold dark matter candidate is a Weakly-Interacting Massive Particle (WIMP). These are proposed to be neutral stable particles with masses of around 100 GeV and are predicted to have electro-weak scale cross-sections with matter [70]. It is a remarkable coincidence that such relic particles have just the relevant relic abundance and decoupling temperatures for it to be a cold dark matter candidate. We give a brief overview of the physics of decoupling of a thermal relic in an expanding universe, which is adapted from Ref. [81].

Consider a stable relic massive particle of mass M_χ which is in thermal equilibrium in the early universe. Its equilibrium number density distribution is governed by Fermi-Dirac or Bose-Einstein distribution depending on whether it is a fermion or a boson. This equilibrium is maintained by this particle annihilating into lighter

particles and vice-versa. This process continues at high temperatures where $T > m_\chi$ since at these temperatures $n_\chi \propto T^3$ where n_χ is the number density of these relic particles, since the annihilation rate $\Gamma_A = < \sigma_a v > n_\chi$ is proportional to the number density of relic particles. As the universe cools, $n_\chi \propto e^{-m/T} T^{3/2}$. After a certain point the expansion rate falls below the Hubble rate ($\simeq 70$ km/s/Mpc) . At this point the relic particle ceases to annihilate, its co-moving equilibrium abundance freezes and it drops out of thermal equilibrium. When this calculation is done for a relic particle with weak-scale interactions, the particle drops out of thermal equilibrium at non-relativistic velocities and its relic abundance is just about the same as that of cold dark matter, which means that if such a particle exists it is the cold dark matter. The evolution of number density is shown in Fig 5.3 where we have plotted the co-moving number density as a function of $\frac{m_\chi}{T}$.

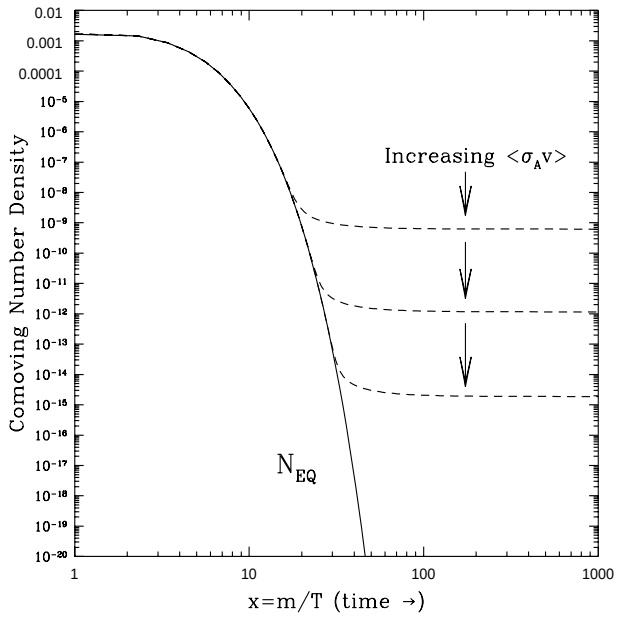

Figure 5.3: Co-moving number density of a relic thermal particle in the Early universe. Figure from Ref. [67].

We give an order of magnitude estimate (from Ref. [71]) of how this comes about.

More rigorous calculations obtained by numerically solving the Boltzmann equation can be found in Ref [68]. The equilibrium relic abundance is given approximately by

$$\Omega_\chi h^2 \approx \left(\frac{3 \times 10^{-27} cm^3 sec^{-1}}{< \sigma_A v >} \right), \tag{5.1}$$

where h is the Hubble constant scaled by 100 km/s/Mpc. Thus the relic abundance mainly depends on the annihilation cross-section. For a thermal relic with weak-scale cross-section $\sigma_{weak} \simeq \frac{\alpha^2}{M^2_{weak}}$. Assuming M_{weak} =$\mathcal{O}$(100 GeV), σ_{weak} is roughly $10^{-9} GeV^{-2}$. Thus, for a relic particle with electroweak scale cross-sections, Eqn 5.1 implies that this particle would have relic abundance $\simeq \mathcal{O}(0.1)$ which is what is needed for the particle to have the same relic abundance as that of dark matter. Thus, neutral stable particles with masses and interactions characteristic of electro-weak scale would have relic abundance of order unity and would decouple at non-relativistic velocities, thus satisfying all characteristics of a cold dark matter candidate. For this reason WIMPs are one of the most favored cold dark matter candidates. Also WIMP masses of $\mathcal{O}$(GeV) are also important from the point of view of particle physics for completely different reasons as discussed in Sect. 5.6. The first (and the simplest) WIMPs to be considered were massive Dirac and Majorana neutrinos with masses in the range of a few GeV to to about 100 GeV (in order to have appreciable relic abundance) and with Standard Model couplings [70].

The only free parameter for such a neutrino is its mass since its coupling is fixed by gauge interactions. If the WIMP is a Dirac neutrino it will have coherent vector interactions leading to detectable event rates in a direct detection experiment. However null results from double-beta decay experiments [72] in the late 80's as well as measurements of Z-width by LEP ruled out Dirac neutrinos from a few GeV to TeV as the primary component of the dark matter halo [73]. If the WIMP was a Majorana

neutrino it would interact only via axial-vector interaction. Such neutrinos would accumulate in the Sun and would decay to light energetic neutrinos which could be detected by neutrino detectors. Null results from the Kamiokande experiment ruled out such Majorana neutrinos with masses less than a few hundred GeV thus ruling out such neutrinos as the major dark matter component [74] The current most well motivated WIMP candidate is the lightest supersymmetric particle (LSP) and the existence of LSP has a strong particle physics motivation. which we describe in the next section. However there are many other particle physics motivated cold dark matter candidates. (See Ref. [81] for a review of other possibilities.)

5.6 Supersymmetry and WIMPs

It is beyond the scope of this thesis to go into details of supersymmetry. We will only give a brief overview of motivations for supersymmetry (SUSY) and indicate how SUSY provides a cold dark matter candidate. More details on supersymmetry can be found in Ref [75].

One of the main defects of the Standard Model of particle physics [76] is the gauge hierarchy problem, which is that the electro-weak scale($\simeq$ 100 GeV) is so much less than the Planck scale($\simeq 10^{19}$GeV). Because of this, quantum corrections to the electroweak scale, given by Eqn 5.2 are quadratically divergent.

$$\delta m_W^2 \sim \mathcal{O}(\frac{\alpha}{\pi})\Lambda^2, \tag{5.2}$$

where Λ is a cut-off which represents the maximum cut-off at which the Standard Model is valid.

Low energy supersymmetry is one solution to this problem. In this model, for

every Standard Model fermion there exists a corresponding partner boson (called superpartner) and vice-versa. Because of this, quadratic corrections almost cancel and Eqn 5.2 becomes:

$$\delta m_W^2 \sim \mathcal{O}(\frac{\alpha}{\pi})|m_B^2 - m_F^2|, \tag{5.3}$$

which $\sim m_W^2$ if $|m_B^2 - m_F^2| \sim 1\ TeV^2$. Therefore if low energy SUSY is correct, one expects superpartners to appear at around the TeV scale [77].

Also low energy SUSY offers unification of coupling constants at around 10^{16} GeV as seen in Figure 5.4 [78].

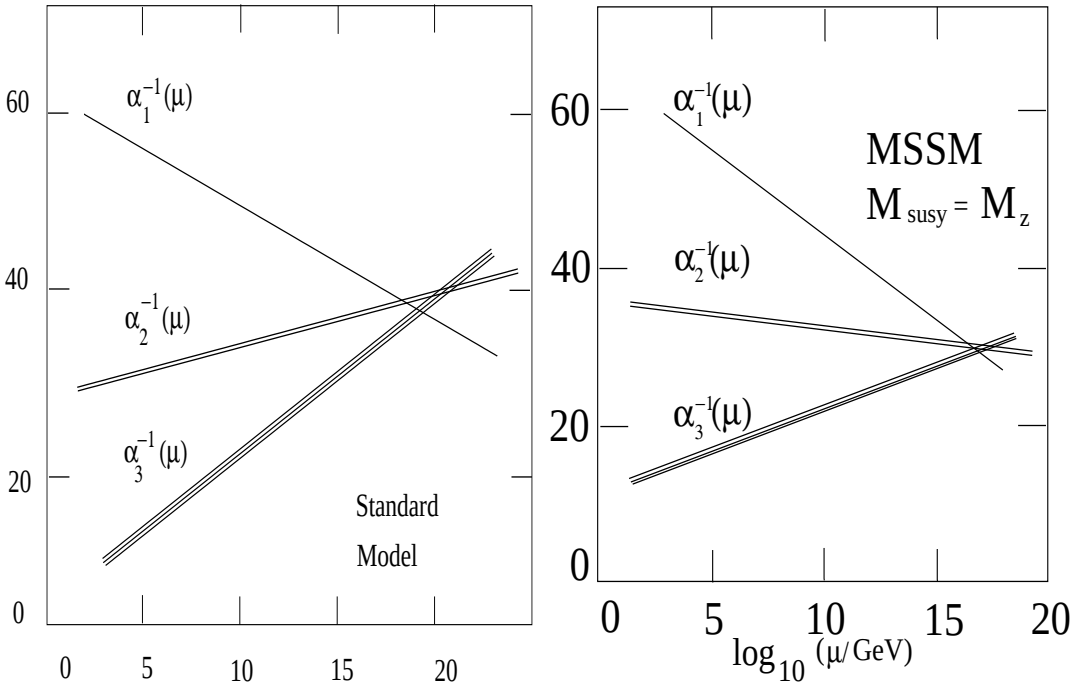

Figure 5.4: Running of coupling constants $\alpha_1, \alpha_2, \alpha_3$ based on renormalization group. The plot on the left is for the Standard Model SU(5) GUT. The plot on the right is for MSSM SU(5) GUT. Bands indicate the post-LEP experimental uncertainties. Figure from Ref. [78].

SUSY contains a multiplicatively conserved quantum number called R-parity (which serves to prevent rapid proton-decay) which takes the value +1 for all Standard Model particles and -1 for their superpartners. Because of R-parity conser-

vation, all superpartners will annihilate/produce in pairs. Therefore, the lightest supersymmetric particle (LSP) will be stable since it can no longer decay into lighter particles. Moreover since the mass scale of SUSY must be of order the electroweak scale in order to cure the hierarchy problem, the LSP will only have electroweak scale interactions with ordinary matter. Thus the LSP satisfies all criteria for it to be a cold dark matter candidate [79, 80].

5.6.1 Minimal Super-symmetric Standard Model

There are various low energy SUSY models and the model dependence arises from the source of SUSY breaking. We give a brief synopsis of the simplest SUSY model called Minimal supersymmetric extension of the Standard Model (MSSM) and we follow the notation in Ref. [81, 82]. More details on MSSM can be found in Ref. [83].

MSSM contains the same particles as the Standard Model, plus their superpartners and two Higgs doublets (as opposed to one in the Standard Model) since two Higgs doublets are needed to give mass to up and down squarks. Also there are two squarks for each quark. Thus there are a total of 6 up squarks and 6 down squarks. The superpartners of the W and charged Higgs bosons, the charged higgsino and gaugino carry the same $SU(3) \times U(1)$ quantum numbers and therefore will mix after electro-weak symmetry breaking. The two resulting mass eigenstates are called charginos ($\chi^{\pm}$). The same thing happens for the superpartners of the photon, Z boson, and the two neutral Higgs Bosons. These fields create 4 mass eigenstates called neutralinos. As explained in section 5.6.2 the lightest neutralino is most likely to be the LSP. The entire MSSM particle content is shown in Table 5.1.

MSSM contains about 63 free parameters. First there are the 3 gaugino masses, M_1, M_2 and M_3 the Higgsino mass parameter μ (which describes the bilinear cou-

plings between the Higgs fields), $tan\beta$ which is the ratio of the Higgs VEV, mass of the pseudo-scalar Higgs Boson M_A The remaining parameters are 3 3×3 symmetric squark mass-squared matrices ($M^2_{\tilde{u}}, M^2_{\tilde{d}}$ and $M^2_{\tilde{Q}}$), 2 slepton mass-squared parameter matrices ($M^2_{\tilde{e}}, M^2_{\tilde{l}}$) and 3 3×3 soft-supersymmetry breaking matrices (A_u, A_d and A_e). To reduce the free parameters, a number of simplifying assumptions are made [95].

The gaugino mass parameters are related using GUT relations as described in Eqn 5.4.

$$M_1 = \frac{5}{3} tan^2\theta_W M_2; M_2 = \frac{\alpha}{sin^2\theta_W \alpha_s} M_3 \tag{5.4}$$

Also the ansatz made for the soft-supersymmetry breaking terms mass matrices. is :

$$\begin{aligned} A_u &= diag(0, 0, A_t) \\ A_d &= diag(0, 0, A_b) \\ A_e &= 0 \end{aligned} \tag{5.5}$$

Also all sfermion mass parameters are assumed to be equal with:
$M_{\tilde{u}} = M_{\tilde{Q}} = M_{\tilde{u}} = M_{\tilde{E}} = M_{\tilde{L}} = M_o$ This reduces the number of free parameters to 6 which are :

- M_2 Gaugino mass parameter
- M_A Mass of the pseudo-scale Higgs boson
- μ Higgsino mass term
- $tan\beta$ Ratio of Higgs vacuum expectation value
- A_t Soft SUSY breaking parameter
- M_o Sfermion mass parameter

Normal Particles		SUSY partners	
Symbol	**Name**	**Symbol**	**Name**
u, c, t	up-quarks	$\tilde{q}_u^1..\tilde{q}_u^6$	up squarks
d, s, b	down-quarks	$\tilde{q}_d^1..\tilde{q}_d^6$	down squarks
e, μ, τ	leptons	$\tilde{l}^1..\tilde{l}^6$	sleptons
μ_e, μ_ν, μ_τ	neutrinos	$\tilde{\nu}_1..\tilde{\nu}_3$	sneutrino
$W^\pm$	W boson		
$H^\pm$	charged Higgs boson	$\chi_\pm^1, \chi_\pm^2$	charginos
B	B-field	Bino	
W^3	W^3-field	Wino	
h,H,A	Higgs Bosons	$\tilde{H}_1, \tilde{H}_2$	higgsino

Table 5.1: Spectrum of particles and fields in the MSSM

5.6.2 The Neutralino

In the MSSM, as shown in Table 5.1, the superpartners of the photon, Z^0 and the neutral Higgs Bosons mix after electroweak symmetry breaking and the 4 resulting mass eigenstates are called the neutralinos.

$$\tilde{\chi} \;=\; a_1\tilde{\gamma} + a_2\tilde{\mathrm{Z}} + a_3\tilde{H}_1 + a_4\tilde{H}_2 \tag{5.6}$$

where $\tilde{\gamma}$ and $\tilde{\mathrm{Z}}$ are the supersymmetric partners of the photon and the Z boson; $\tilde{H}_1$ and $\tilde{H}_2$ are Higgsino states. The phenomenology of the Neutralino is described by the gaugino fraction $f_g = |a_1|^2 + |a_2|^2$. The parameters $a_1..a_4$ and the mass of the neutralinos (M_χ) is given by the eigenvalues and eigenvectors of the following matrix:

$$M_\chi = \begin{bmatrix} M_1 & 0 & -M_z cos\beta sin\theta_W & M_z sin\beta sin\theta_W \\ 0 & M_2 & M_z cos\beta cos\theta_W & -M_z sin\beta cos\theta_W \\ -M_z cos\beta sin\theta_W & -M_z cos\beta cos\theta_W & 0 & -\mu \\ M_z sin\beta sin\theta_W & -M_z sin\beta cos\theta_W & -\mu & 0 \end{bmatrix} \tag{5.7}$$

Contours of M_χ for various values of μ and $tan\beta$ are shown in Fig 5.5.

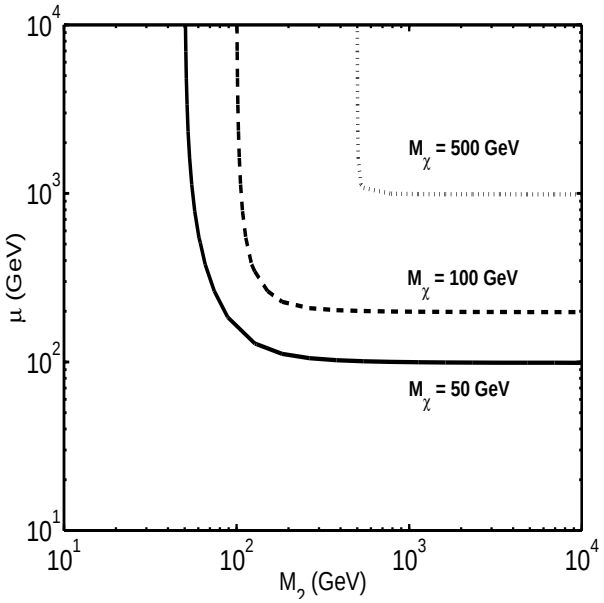

Figure 5.5: Contours of lightest neutralino mass M_χ for various values of M_2 and μ. The value of $tan\beta$ is assumed to be 10.

In most SUSY models the lightest of these neutralinos (χ) is the LSP and hence the cold dark matter candidate [80]. The main reason is that the only other possibility is the sneutrino which is ruled out from direct detection experiments [84] since the sneutrino-nucleus cross-section is about four times the Dirac neutrino-nucleon cross-section. Also the data from LEP implies that sneutrino is heavier than 44.6 GeV at 95 % c.l [85]. However within MSSM, if sneutrino is to be LSP its mass has to be less than 44.3 GeV [85]. Thus within MSSM, sneutrino cannot be the LSP. The limits on the neutralino mass depend on the model assumed for SUSY breaking as well from limits on searches for sparticles at LEP e^+e^- and Tevatron hadron colliders. A model independent lower limit for neutralino mass without any assumption on SUSY breaking mechanism and taking into account accelerator based searches is inferred to be about 18 GeV. [86]. The upper limit on neutralino mass is assumed

to be 10 TeV [87]. During rest of the chapter we shall use WIMP and neutralino interchangeably, since though neutralino is the most favored WIMP candidate our results would be valid for any other WIMP candidate with the same phenomenology.

5.7 Overview of WIMP Searches

The smoking gun for the evidence for cold dark matter particle would be obtained if one obtains an unambiguous signature of WIMPs which can enable us to measure its properties. There are two kinds of non-accelerator based searches for WIMPs. The first kind is referred to as direct detection searches in which one looks for a WIMP elastically scattering off a nucleus in a low background laboratory based detector. The other category is indirect searches for WIMPs where one looks for byproducts of WIMP-pair annihilation into neutrinos, photons, antiprotons or positrons. In this chapter we shall mainly describe the phenomenology of indirect searches for WIMPs through neutrinos which is mainly adapted from Ref [81] and present results from Super–Kamiokande. We summarize the results from direct detection searches and then compare the results from Super–Kamiokande with these.

5.8 WIMP-Nucleon Cross-section

The WIMP-nucleon cross-section mainly depends upon WIMP-quark coupling, the wave function of quarks inside the nucleon and the distribution of nucleons inside the nucleus. From the given annihilation cross-section the WIMP-nucleon cross-section can be estimated by crossing symmetry to be $\simeq 10^{-36} cm^2$ [81]. WIMPs undergo two kinds of interactions with quarks [88] : scalar (or spin-independent) interactions in which the WIMP couples to the mass of the nucleon and axial vector (or spin-

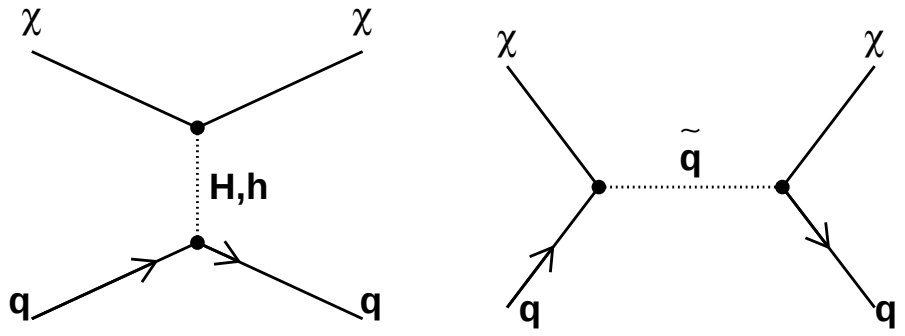

Figure 5.6: Feynman diagrams which contribute to neutralino-quark scalar interactions. Figure from Ref. [81].

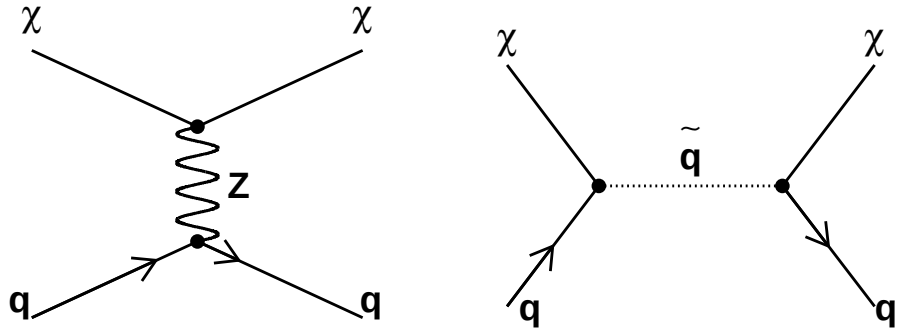

Figure 5.7: Feynman diagrams which contribute to neutralino-quark spin-dependent interactions. Figure from Ref [81].

dependent) interactions in which WIMP couples to the spin of the nucleon. Using relativistic field theory notation (see Ref [81]) the WIMP-quark scalar interaction can be written as $\bar{\psi}\psi$, whereas the WIMP-quark axial vector interaction can be written as $\bar{\psi}\gamma^{\mu}\gamma^{5}\psi$. All other interactions for a non-relativistic Majorana fermion turn out to be 0. The axial-vector interaction takes place through exchange of Z-boson and s-quarks, whereas the scalar interaction takes place through squark or Higgs boson exchange. The Feynman diagrams for axial vector and scalar interactions are shown in Figs. 5.6 and 5.7 respectively.

The total WIMP-nucleon spin-interaction at zero-momentum transfer (σ_{spin0})

can be written as [81] :

$$\sigma_{spin0} = \frac{8}{\pi} G_F^2 m_r^2 \Lambda^2 J(J+1) \tag{5.8}$$

where m_r is the reduced mass of the WIMP nucleon system, J is the total angular momentum of the system, Λ encodes the physics of both wimp-quark couplings (which is obtained from the MSSM Lagrangian) as well as the average value of the spin of the proton and neutron (which depends on nuclear wave function and other nuclear physics details).

The total WIMP-nucleon scalar-interaction at zero-momentum transfer ($\sigma_{scalar0}$) is given by [81]:

$$\sigma_{scalar0} = \frac{4 m_\chi^2 m_N^4}{\pi (m_\chi + m_N)^2} | < L_{sc} > |^2, \tag{5.9}$$

where m_N is the nuclear mass, and $< L_{sc} >$ is the nucleon matrix element of the effective Lagrangian for the scalar neutralino-nucleus interaction and is independent of nuclear mass. The total scalar or spin cross-section for a given momentum transfer is obtained by:

$$\sigma = \int_0^{4 m_r^2 v^2} \frac{\sigma_o}{4 m_r^2 v^2} F\left(|\vec{q}|\right)^2, \tag{5.10}$$

where v is the WIMP speed relative to the target and $F(|\vec{q}|)$ the Nucleus form factor as a function of momentum transfer $\vec{q}$ and σ_o is obtained using Eqn 5.9 or 5.8. Though relative values for the scalar and axial vector cross-section between a given WIMP and nucleus is very model-dependent, as a general rule of thumb scalar interaction is dominant for any nucleus with $A > 20$ [81].

In this chapter we shall skip the details involved in calculating the WIMP -nucleon cross-section from the SUSY Lagrangian as this is incredibly complicated, model-dependent and beyond the scope of this thesis. However if the WIMP-nucleon spin-dependent or scalar cross-section is known, rest of the physics calculations needed

for indirect searches through neutrinos or direct detection searches can be done in more or less model-independent fashion.

5.9 Neutrinos from WIMP Annihilation

As WIMPs orbit the galaxy pass through Earth and Sun there is a finite probability of elastically scattering with the elements in the core because of the large target mass of the Earth and the Sun. If after doing so, the WIMP recoil with a velocity less than the escape velocity it becomes gravitationally bound to the object. It eventually settles to the core of the Sun or the Earth after going some additional scatters. The time needed for a WIMP to settle to the core of an astronomical object after it undergoes its first scatter is approximately given by $\frac{P}{n\sigma R}$ [89] where P is the period of a particle orbiting the Sun/Earth; R is its radius ; n is the mean number density of nuclei with which the WIMP interacts.

Once many WIMPs have accumulated they will start self-annihilating into Standard Model fermion-fermion or boson-boson pairs. The decays of these annihilation products produce energetic muon neutrinos which can be detected in Super-K and other neutrino detectors. The energy spectrum of these neutrinos is different from atmospheric neutrinos and they mainly point back to the source because of their high energy. Thus observation of high energy neutrinos coming from Sun and Earth could provide an unambiguous signature for WIMP dark matter. The physics of WIMP annihilation near the Galactic Center is different and is discussed in Sect 5.13. The calculation of upward muon fluxes from WIMP annihilation is quite complicated. The physics inputs involved in this calculation are capture rates in the Earth and the Sun, branching ratios for WIMPs to different annihilation channels, fragmentation and interaction of annihilation products in the Earth and Sun, production of

high energy neutrinos from decay of annihilation products and production of upward going muons from the high energy neutrinos in the rock below the detector. We shall discuss calculation of capture rates in the Earth and Sun in Sect. 5.10. The calculation of WIMP branching ratios to different annihilation channels manly depends on the SUSY model assumed and we shall skip its details except while doing a model-independent comparison to direct detection rates. Production of high energy neutrinos from WIMP annihilation products is discussed in Sec. 5.12

5.10 WIMP Capture

In this section we shall give an overview of the main physics involved in accretion of WIMPs onto both Earth and the Sun and then compare and contrast the salient features for both the Earth and the Sun.

The time evolution of WIMPs in a given astronomical object is given by :

$$\frac{dN}{dT} = C - C_A N^2 \tag{5.11}$$

where C is the capture rate of WIMPs onto Earth. The quantity C_A is a term which depends on WIMP annihilation cross-section and effective volumes available for WIMP capture in Sun and Earth and is described in Ref [81]. Solving Eqn 5.11 one gets for the annihilation rate:

$$\Gamma_A = \frac{C}{2} tanh^2(t/\tau) \tag{5.12}$$

As we can see from Eqn 5.12, if $t/\tau >> 1$ which occurs when capture and annihilation come in equilibrium then $\Gamma_A = \frac{C}{2}$. In this case the annihilation rate is solely determined by the capture rate. For the Sun, the ratio of equilibrium time scale to

its age is given by :

$$\frac{t_\odot}{\tau_\odot} = 330 \left(\frac{C_\odot}{sec^{-1}}\right)^{1/2} \left(\frac{<\sigma_a v>}{cm^3 sec^{-1}}\right)^{1/2} \left(\frac{m_\chi}{10GeV}\right)^{3/4} \tag{5.13}$$

and

$$\frac{t_\oplus}{\tau_\oplus} = 1.9 \times 10^4 \left(\frac{C_\oplus}{sec^{-1}}\right)^{1/2} \left(\frac{<\sigma_a v>}{cm^3 sec^{-1}}\right)^{1/2} \left(\frac{m_\chi}{10GeV}\right)^{3/4} \tag{5.14}$$

where $C_\odot$ and $C_\oplus$ are the capture rates in the Sun and the Earth respectively.

The ratio of equilibrium time-scales to the age for both the Sun and the Earth is shown in Fig. 5.8 and 5.9 respectively.

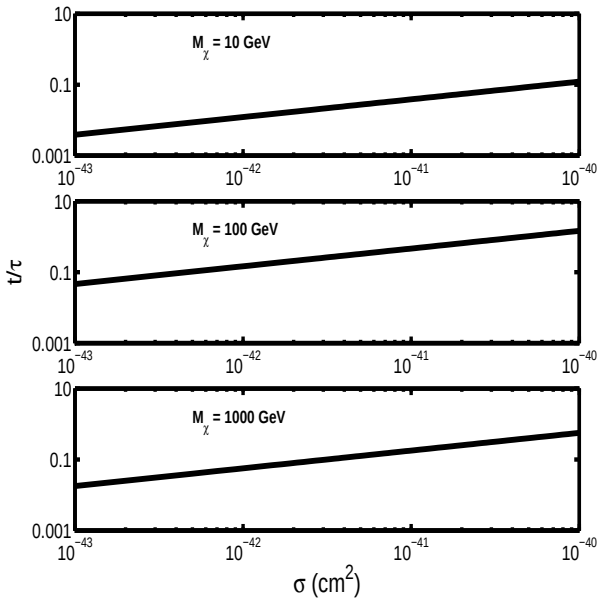

Figure 5.8: The ratio of time scale for WIMP annihilation to be in equilibrium with capture to the age of the Earth as a function of WIMP-proton scalar cross-section for a WIMP with mass 10 GeV (top panel), 100 GeV (middle panel), 1000 GeV (bottom panel). Age of the Earth is assumed to be 4.5 Gyr; $\rho_\chi = 0.3$ GeV/cc ; $v_{rot} = 220$ km/sec and $<\sigma_A v> = 3 \times 10^{-27} cm^3 sec^{-1}$.

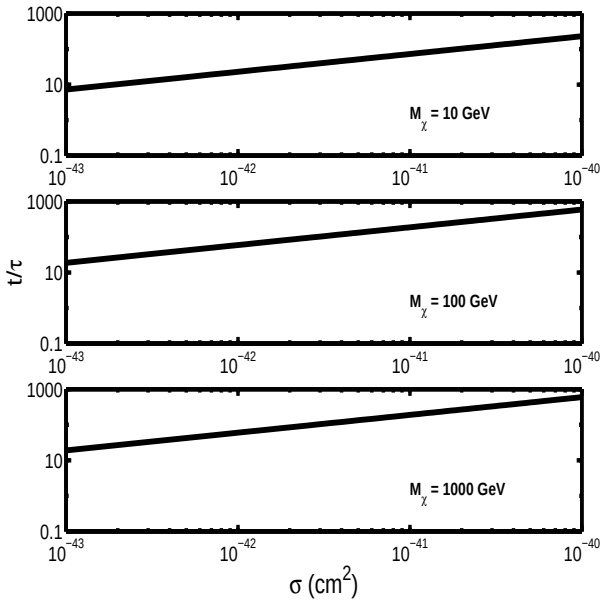

Figure 5.9: The ratio of time scale for WIMP annihilation to be in equilibrium with capture to the age of the Sun as a function of WIMP-proton scalar cross-section for a WIMP with mass 10 GeV (top panel), 100 GeV (middle panel), 1000 GeV (bottom panel). Age of the Sun is assumed to be 4.5 Gyr. all other WIMP parameters are same as in Fig 5.8.

5.11 WIMP Capture rates in the Sun and Earth

The most important factor which determines WIMP-induced upward muon flux is the rate of capture of WIMPs onto the Sun and the Earth. WIMP capture rates for the both Sun and the Earth have been evaluated in great detail by A. Gould and complete expressions can be found in Refs. [90, 91]. These expressions are quite complicated. In this chapter we shall us Kamionkowski's approximations to Gould's complete results for the WIMP capture rate[92].

We shall outline the main physics issues involved in calculating the capture rates and will compare and contrast the main features for Sun and the Earth. A WIMP gets captured if its recoil velocity after elastically scattering off the elements in Sun or the Earth's core is less than the corresponding escape velocity. The probability

of WIMP losing its energy in an elastic scattering event gets maximized when the WIMP mass matches the nuclear mass from which it scatters. Gould [90] has shown that this occurs in Earth for WIMPs in the mass range of 10-75 GeV because the Earth contains significant abundance of O (A = 16), Si (A = 28), Mg (A = 24), and Fe (A = 56). Thus the WIMP capture rates around these mass values gets enhanced. For all other masses, the WIMP capture rate by Earth is quite small since the escape velocity of the Earth (11 km/s) is about 20 times smaller than the WIMP rms velocity and only WIMPs in the low velocity tail get captured for masses outside the Gould resonance region. For Sun, the Gould resonance is not important since Sun's escape velocity(about 612 km/s) is much larger than the WIMP rms velocity.

If a WIMP scatters via scalar interactions at high momentum transfer there will be a form-factor suppression when the momentum transfer is large compared to the inverse of the nuclear radius, since the WIMP does not see the entire nucleus. The form factor suppression is given by :

$$F(Q) = exp\left(\frac{-Q}{2Q_0}\right) \tag{5.15}$$

where Q = energy loss of the WIMP and $Q_0 = 1.5/(2M_N R_0^2)$. Form-factor suppression is important in the Sun where the WIMP undergoes a much harder scatter when it is captured in the Sun. Because of this in the Sun, scattering off elements in the mass range 12-32 is moderately suppressed while scattering off iron is suppressed by several orders of magnitude. Hence in the Sun for a WIMP with scalar interactions capture is dominated by scattering off oxygen.

Form factor suppression is negligible in the Earth for WIMPs with mass $\geq$ 80 GeV and for lighter WIMPs the maximum loss from factor factor suppression is about 28 %. WIMP capture rate in the Earth for a WIMP with scalar interactions

is given by :

$$C_{\oplus} = 2.4 \times 10^{28} sec^{-1} (\rho_{\chi}/0.3GeV) f_{\oplus}(m_{\chi}) \left(\frac{|<L_{sc}>|}{GeV^{-3}} \right)^2 \tag{5.16}$$

The WIMP capture rate in the Sun for a WIMP with scalar interactions is given by :

$$C_{\odot} = 2.4 \times 10^{37} sec^{-1} (\rho_{\chi}/0.3GeV) f_{\odot}(m_{\chi}) \left(\frac{|<L_{sc}>|}{GeV^{-3}} \right)^2 \tag{5.17}$$

The functions $f(m_{\chi})$ for the Earth and Sun in Eqn 5.16 and Eqn 5.17 indicate the mass-dependence of capture rates due to resonance effects, form factor suppression, etc. and is given is Eqn. 9.28 in Ref. [81].

The WIMP capture rates in both the Earth and the Sun for a WIMP with WIMP-nucleon scalar cross-section of $10^{-41} cm^2$ as a function of mass is shown in Figs 5.10 and 5.11 respectively. One can clearly see the importance of resonance effects for Earth from Fig. 5.10.

For a WIMP with axial-vector coupling, capture occurs only in the Sun and not in the Earth. This is because 75% of the solar mass is made of hydrogen [81]. For the Earth the mass fraction of nuclei with odd mass number is only about 1% [93] and hence WIMPs with only axial vector interactions do not get captured in the Earth.

The capture Rate in the Sun for a WIMP with axial vector interactions is given by Eqn 5.18 [81] and is plotted in Fig. 5.12.

$$C_{ax}^{\odot} = (1.3 \times 10^{25} sec^{-1}) \frac{(\rho_{\chi}/0.3GeV)(\sigma_{spin0}/10^{-40} cm^2) S(m_{\chi}/m_H)}{M_{\chi}(GeV)(v/270km/sec)} \tag{5.18}$$

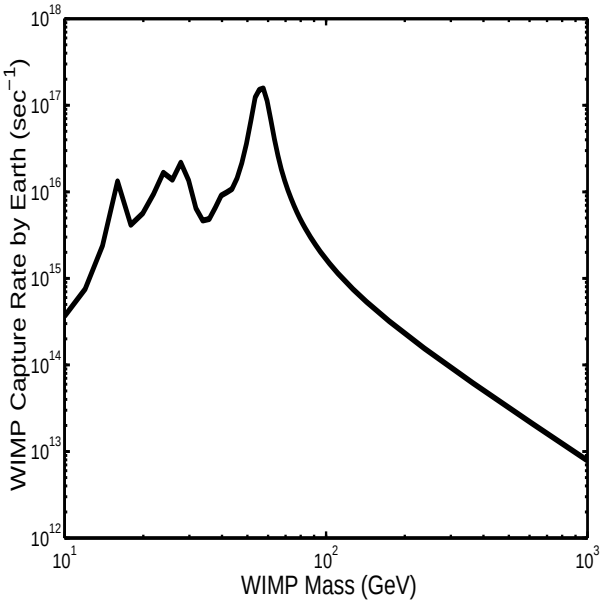

Figure 5.10: WIMP capture rates in the Earth as a function of mass for WIMP-nucleon scalar cross-section of $10^{-41}cm^2$. The peaks occur at 16 GeV, 24 GeV, 28 GeV and 56 GeV which correspond to resonance effects with oxygen, magnesium, silicon and iron respectively.

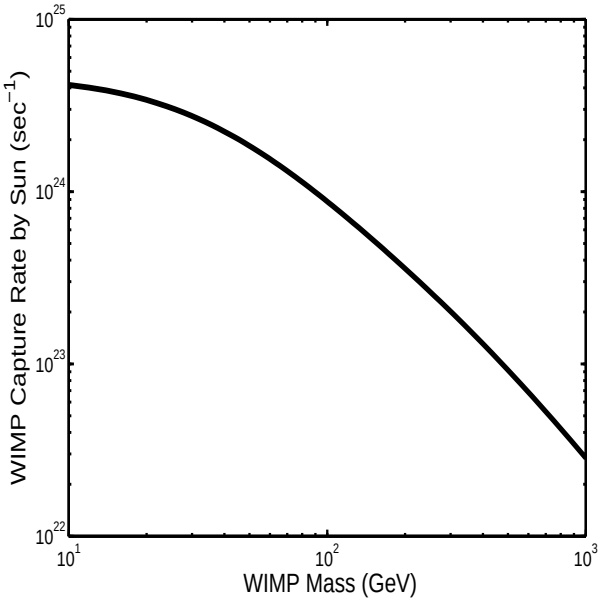

Figure 5.11: WIMP capture rates in the Sun as a function of mass for WIMP-nucleon scalar cross-section of $10^{-41}cm^2$.

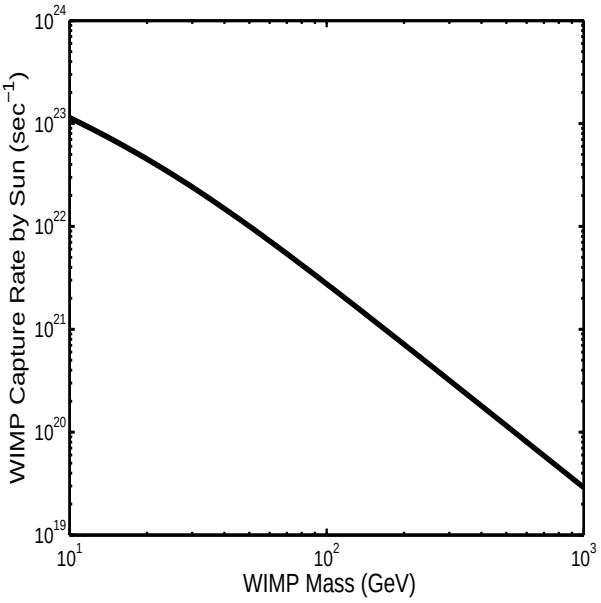

Figure 5.12: WIMP capture rates in the Sun as a function of mass for WIMP-proton axial-vector cross-section of $10^{-41} cm^2$.

5.12 WIMP Annihilation Rates

Since the neutralino is a Majorana particle and its mass is in the GeV range and above, it does not decay directly to neutrinos [79]. Energetic neutrinos are produced by decays of WIMP annihilation products such as τ leptons, b, c and t quarks and gauge and Higgs bosons. The differential neutrino energy spectrum from different WIMP annihilation channels have been calculated by a variety of groups either using analytic calculation [94] or with Monte Carlo simulations [95, 96, 97, 98, 99]. In this chapter we shall follow the analytical treatment in Ref [94]. Other groups have done detailed Monte Carlo simulations [95, 96] to calculate neutrino energy spectrum from WIMP annihilation.

The differential energy flux of neutrinos from WIMP annihilation is given by

Eqn 5.19:

$$\left(\frac{d\phi}{dE}\right) = \Gamma_a \sum_F B_f \left(\frac{dN}{dE}\right), \tag{5.19}$$

where Γ_a is the WIMP annihilation rate and R is the distance from the detector to the source. The sum in Eqn 5.19 is over all WIMP annihilation channels F and B_f is the WIMP branching ratio to that annihilation channel.

The flux of upward muons resulting from WIMP annihilation is given by :

$$\Gamma_{\mu\uparrow} = d\tanh^2(t/\tau)\rho_\chi f(m_\chi)\xi(m_\chi)(m_\chi/GeV)^2 \left(\frac{< L_{sc} >}{GeV^{-3}}\right)^2, \tag{5.20}$$

where $d_\odot = 2.9 \times 10^8 m^{-2} yr^{-1}$, and $d_\oplus = 1.5 \times 10^8 m^{-2} yr^{-1}$, $f(m_\chi)$ is a function which describes the neutralino-mass dependence of the capture rates in the Sun and the Earth respectively The function $\xi(m_\chi)$ which contains information about the neutrino spectrum and the production rate of upward muons and is given by :

$$\xi(m_\chi) = \sum_F [3.47 < Nz^2 >_{F,\nu} (m_\chi) + 2.08 < Nz^2 >_{F,\overline{\nu}} (m_\chi)], \tag{5.21}$$

where the sum is over all annihilation channels F available to any specific neutralino candidate, and B_F is the branching ratio for annihilation into F. $< Nz^2 >$ is the scaled second moment of the neutrino energy spectrum from final state F for a given neutralino mass and is given by:

$$< Nz^2 >_{f,i} (E) = \frac{1}{E^2} \int \left(\frac{dN}{dE}\right)_{f,i} (E_\nu, E_{in}) E_\nu^2 d\nu \tag{5.22}$$

The neutrino energy spectrum from WIMP annihilation depends on WIMP mass as well as the neutrino energy. The neutrino energy spectrum also depends on hadronization of annihilation products and for the case of the Sun, neutrino absorption and stopping and stopping of heavy hadrons (containing b and c quarks).

For the case of the Earth the neutrino energy spectrum is same for neutrinos and anti-neutrinos. Tha main neutrino annihilation channels come from decay of W and Z bosons, top quark, b and c-quark and τ leptons. Analytical expressions for the neutrino energy spectrum as well as the second moment of the neutrino energy spectrum are given in Ref. [94]. Also other groups have treated neutrino generation and propagation through the Earth and Sun (by accounting for the effects below) with Monte Carlo simulations [100].

The neutrino energy spectrum obtained by them from Monte Carlo simulations for a variety of annihilation channels can be found in Ref. [100]

- Neutrino Absorption and Stopping

  In the case of Earth effective thickness is too small for neutrino energy loss or absorption to be of importance and hence can be neglected. However energetic neutrinos injected in the core of the Sun lose energy through neutral-current interactions and get absorbed via charged current interactions. The final energy of a neutrino with energy E_i at the core is given by [98] :

$$E_f = \frac{E}{1 + E\tau_i} \tag{5.23}$$

  where $\tau_\nu \simeq 10^{-3} GeV^{-1}$ and $\tau_{\bar{\nu}} \simeq 4 \times 10^{-3} GeV^{-1}$. The probability of the neutrino escaping the Sun is given by:

$$P = \left(\frac{1}{1 + E\tau_i}\right)^{\alpha_i} \tag{5.24}$$

  where $\alpha_\nu = 5.1$ and $\alpha_{\bar{\nu}} = 9.0$. The probability for a neutrino of energy E to escape the Sun is given in Fig. 5.13.

  Hence given the neutrino energy distribution in the Earth, the neutrino energy

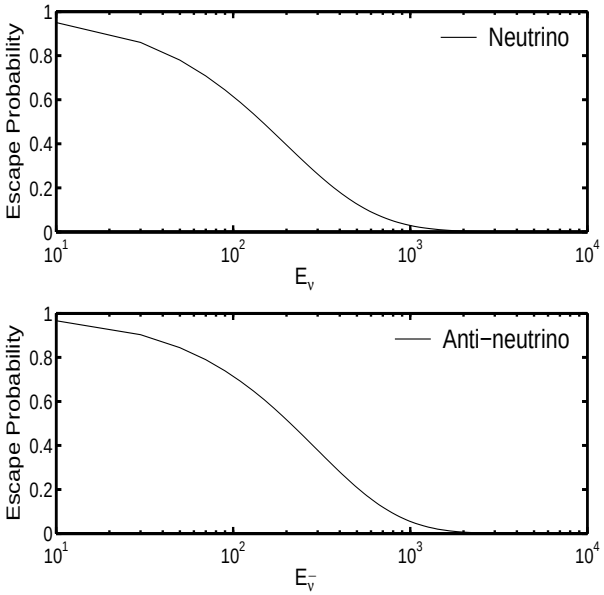

Figure 5.13: Probability of a neutrino with energy E_ν to escape from the Sun (top panel). Same plot is shown in bottom panel for anti-neutrino.

distribution in the Sun is given by:

$$\left(\frac{dN}{dE}\right)_i^{\odot}(E_d, E_\nu) = (1 - E_\nu)^{\alpha_i - 2}\left(\frac{dN}{dE}\right)^{\oplus}(E_d, E_m) \tag{5.25}$$

where $E_m = \frac{E_\nu}{1-E_\nu}$

- Hadronization

  A b or c quark injected into the center of the Earth will lose energy through hadronization. The energy at which hadron decays in the Earth is related to the injection energy by : $E_d = z_f E_i$, where $z_f = 0.58$ for c-quarks and 0.73 for b quarks.

- Stopping of heavy hadrons

  In the Sun the hadrons produced by b and c quarks interact with the solar

medium and get slowed down. If the initial energy of the hadron is E_0 then it will decay and the distribution of decay energies is given by:

$$\left(\frac{1}{N}\frac{dN}{dE_d}\right)^{hadron}(E_0, E_d) = \frac{E_c}{E_d^2} exp\left[E_c\left(\frac{1}{E_0} - \frac{1}{E_d}\right)\right] \tag{5.26}$$

where $E_c = 250$ GeV for c quarks and 470 GeV for b-quarks.

5.13 WIMP Annihilation in the Galactic Center

Recently, Gondolo and Silk [101] have shown that for certain class of dark matter density profiles there could be a large flux of muon neutrinos from WIMP annihilation in the Galactic Center. The center of the galaxy contains a black hole with mass given by $M_{bh} = (2.6 \pm 0.2) \times 10^6 M_\odot$ [102]. The basic idea is that WIMPs near the Galactic Center get accreted by the central black hole into a dense spike where $\rho \simeq r^{-\gamma_{sp}}$. The slope of the spike depends on the dark matter density profile. For dark profiles with a finite core such as the isothermal core [103], $\gamma_{sp} \simeq 3/2$, whereas for dark matter density profiles with an inner cusp, slope of the spike can be much steeper. This is shown in Fig. 5.14. Since the dark matter annihilation rate is proportional to square of the density one can get huge enhancement of signals from dark matter annihilations near the Galactic Center. Assuming $\gamma_{sp} = 1.5$ the expected flux muon neutrinos is shown in Fig. 5.15. More details of the physics of WIMP annihilation near the Galactic Center is explained in Ref. [101].

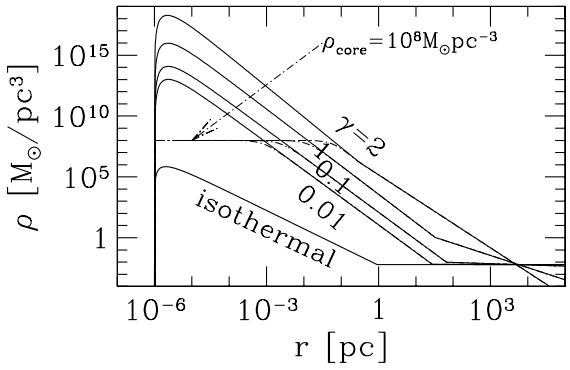

Figure 5.14: Examples of different possible spike density profiles. Figure taken from Ref. [101]

5.14 WIMP Angular Distribution

Once WIMPs are captured in the Sun and the Earth they settle to the core with an isothermal distribution equal to the core temperature of the Sun or the Earth [90]. While the Sun is effectively a point sources of energetic neutrinos resulting from WIMP annihilations, the Earth is not for WIMPs with mass less than 50 GeV. For the Earth the angular size of the annihilation region has been estimated by [97, 90] to be:

$$G(\theta) \simeq 4 m_\chi \alpha e^{-2 m_\chi \alpha \sin^2 \theta}, \tag{5.27}$$

where θ is the nadir angle; α is a parameter depending on the central temperature, the central density and radius of the Earth. Note that for WIMP masses above 50 GeV Earth is also a point source for WIMP annihilations. In addition muons scatter from the incoming direction of their parent neutrino due to multiple coulomb

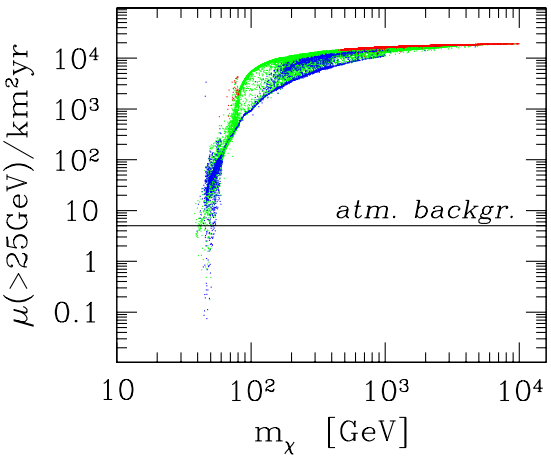

Figure 5.15: Maximum flux of neutrino induced muons from WIMP annihilations in the Galactic Center. Figure taken from Ref. [101].

scattering and charged current interactions in the rock below the detector. We used the Monte Carlo simulations done in Ref. [104] to calculate the angular windows for Sun and Earth which contain 90% of the signal for various neutralino masses taking into account the spread because of neutrino physics as well as the finite angular size of the WIMP annihilation region for the Earth. For the neutrino energy spectrum the simulations assumed that 80% of the annihilation products are from $b\bar{b}$, 10% from $c\bar{c}$ and 10% from $\tau^+\tau^-$. However the neutrino-muon scattering angle is mainly dependent on the neutralino mass and does not change much with different branching ratios [105]. These cones for both the Sun and Earth are shown in Fig. 5.16. In the Galactic Center, since the angular size of the spike where annihilations occur is very small, the Galactic Center can be considered a point source for WIMP annihilation [101]. Like the Sun angular deviation mainly arises from neutrino physics effects like charge-current interaction and multiple-Coulomb scattering.

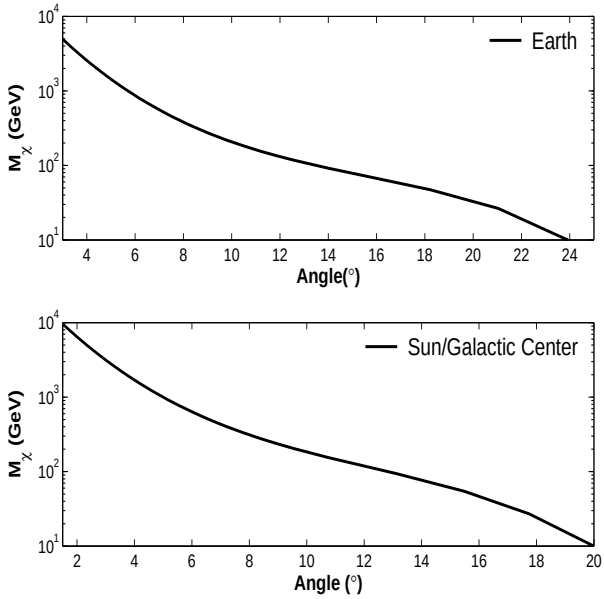

Figure 5.16: Cones which contain 90% of flux from WIMP annihilations in the Earth, Sun and Galactic Center for various WIMP masses.

5.15 Super–Kamiokande WIMP searches

5.15.1 Zenith angle Comparison

To do WIMP searches we use only upward-thrugoing muons, since they statistically come from a higher neutrino energy sample and given the lower limit on WIMP mass most of the signal is expected to be seen in upward muons.

To do this search, we look for a statistically significant excess in cones from 5° to 30° in order to optimize signal to background ratios for various WIMP masses. These cone sizes considered are conservative since with the current LEP lower limits, most of the signal should be seen within about 20° as we can see from Fig. 5.16. As explained in Chap.[4] the upward thru-going muon data is consistent with oscillations, to evaluate the background for WIMP searches we use the 40 year atmospheric neutrino Monte Carlo after taking into account oscillations. The zenith angle distribution for

the data and background and also their comparison in cones with half-angles ranging from 5 to 30° is shown in Fig. 5.17. The oscillated Monte Carlo was normalized to the total observed upward thru-muons. As we can see that there is no statistically significant excess in any of these cones. To evaluate the background for WIMP

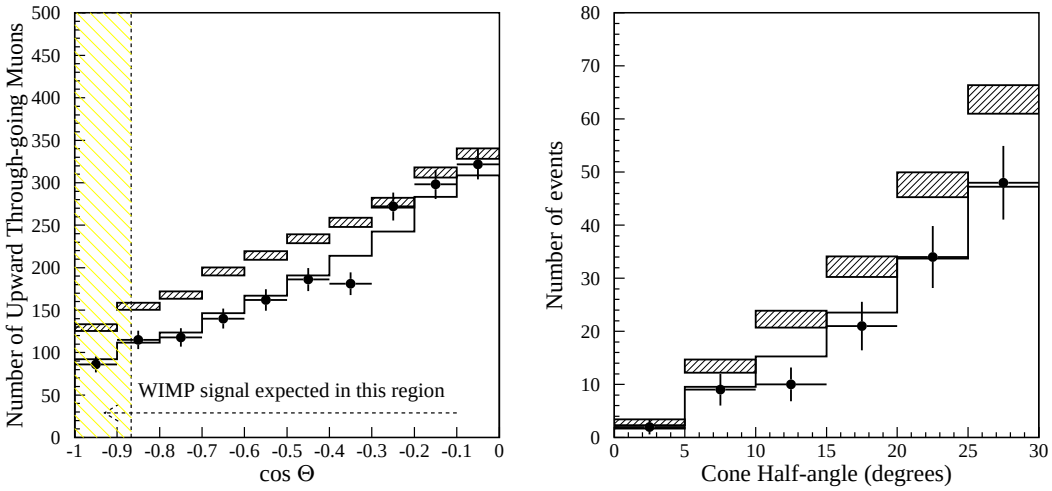

Figure 5.17: The left panel shows zenith angle distribution of data and background with respect to Earth. The right panel indicates the same in cones with half-angles from 5° to 30°.

searches from the Sun and the Galactic Center, each Monte Carlo event needs to be assigned a "fake" time in order to obtain the position of the celestial source during the Monte Carlo event. Each Monte Carlo event was assigned a time based on the arrival time of upward thrugoing muons. This enables us to map the livetime distribution of the observed data correctly. The zenith angle distribution for upward thrugoing muons with respect to the Sun, along with the expected background using the Monte Carlo (with and without oscillation) is shown in Fig. 5.18. For the Sun, there is an additional background of high energy neutrinos resulting from cosmic ray interactions in the Sun, but this is about 3 orders of magnitude less than the observed atmospheric ν flux and hence can be neglected [106]. The distribution in cones with

half-angles ranging from 5° to 30° is also shown in the same figure. The corresponding plots for the Galactic Center are shown in Fig. 5.19. As we can see there is no statistically significant excess of upward muons coming from the center of the Sun and Galactic Center. Hence we do not see any evidence for WIMP annihilations from the center of Earth, Sun or Galactic Center. Also other upward muon detectors like IMB, Kamiokande, MACRO, BAKSAN, AMANDA etc have also done WIMP searches and they do not see any signatures of WIMP annihilation The WIMP flux limits for the Earth and the Sun by IMB, Kamiokande, MACRO, and Baksan are in Refs. [108, 104, 43, 107] respectively, and the WIMP flux limits for the Galactic Center by the above detectors are in Refs. [112, 110, 109, 111] respectively.

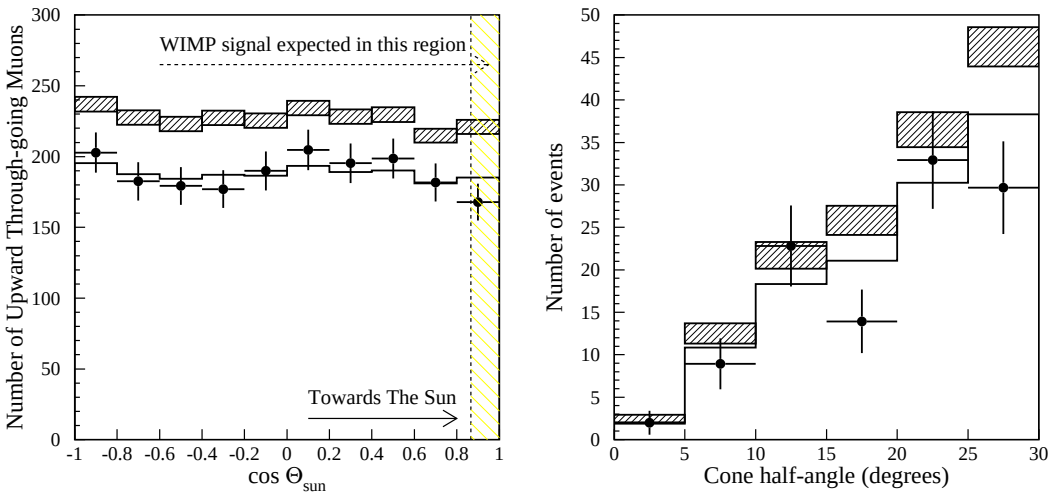

Figure 5.18: The left panel shows the zenith angle distribution of data and background with respect to the Sun. The right panel indicates the same in cones with half-angles from 5° to 30°. All labels are same as in Fig. 5.17.

5.15.2 Super–Kamiokande Flux Limits

We evaluate the flux limits in different cone sizes from the Earth, Sun and Galactic Center and we compare our limits with those from other detectors. The flux limits

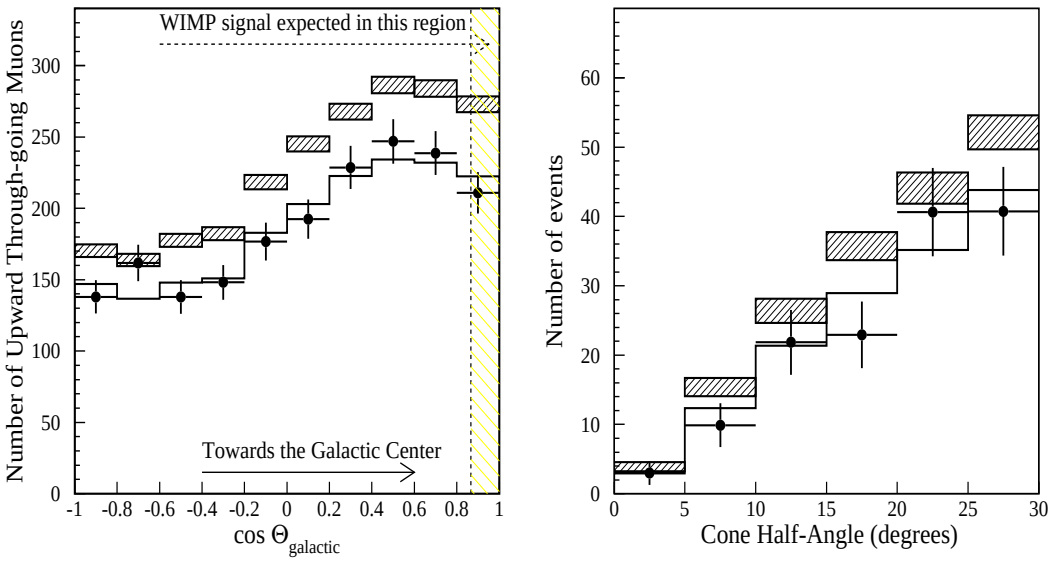

Figure 5.19: The left panel shows the zenith angle distribution of data and background with respect to the Galactic Center. The right panel indicates the same in cones with half-angles from 5° to 30°. All labels are same as in Fig. 5.17.

for the case of Earth, Sun, and Galactic Center in different cone sizes is shown in Fig. 5.20, 5.21 and 5.22.

We now convert these flux limits evaluated in different cone sizes to flux limits as a function of WIMP mass. To do these for each mass we find the corresponding cone which contains 90 % of the flux from Fig. 5.16 and then find the flux limit in the corresponding cone and correct for its collection efficiency. The resulting flux limits for the Earth, Sun, and Galactic Center as a function of WIMP mass are shown in Fig. 5.23, 5.24, 5.25 respectively along with corresponding limits from other detectors. These limits have been plotted up to 18 GeV.

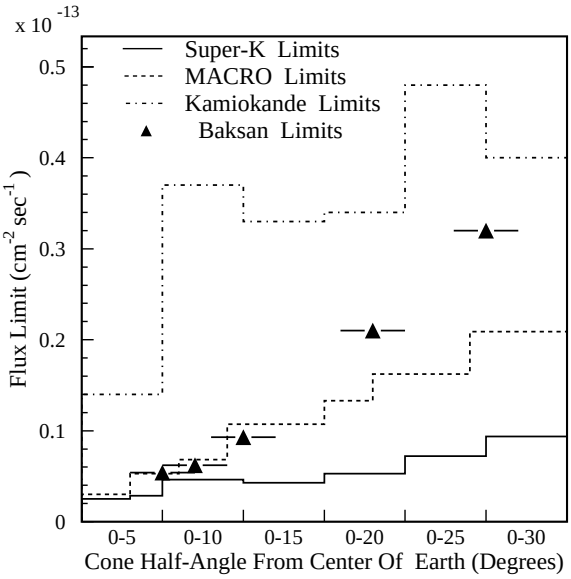

Figure 5.20: Comparison of Super-K 90 % c.l. excess neutrino-induced upward muon flux limits from the Earth in different cone half-angles with those from other experiments.

5.16 Comparison with Expected Flux

Since MSSM contains many free parameters which are poorly constrained it is difficult to rule out individual parameters which govern the MSSM Lagrangian. Nevertheless as an exercise we have used `Neutdriver` code written by G. Jungman [81] to generate many MSSM models by varying its input parameters and calculating the expected flux from WIMP annihilation in the Earth and the Sun and compare it with Super-K limits. Also given the parameters of MSSM, one can calculate various quantities for which there are experimental constraints from accelerator-based searches for SUSY from LEP and the Tevatron. We generated a total of 24000 MSSM models by varying M_2 between 100 and 10000 GeV, μ between -200 GeV and 200 GeV, $\tan(\beta)$ between 40 and 100, M_A between 200 and 500 GeV, M_0^2 between 1.0×10^6 and $8.0 \times 10^8 GeV^2$. (All symbols and other assumptions used are explained in Sect. 5.6.1.) We then reject

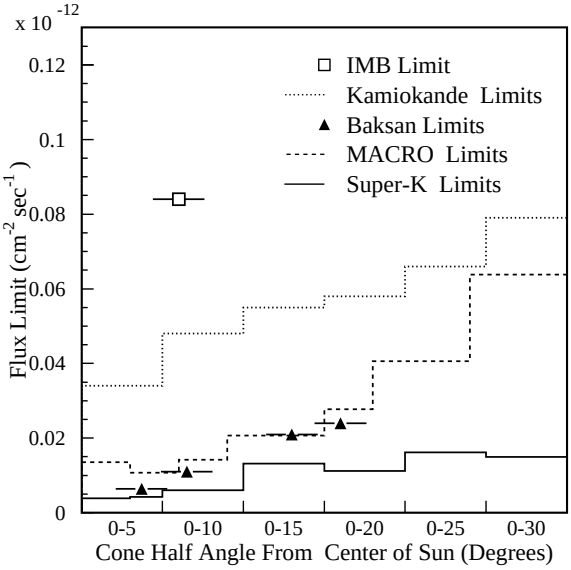

Figure 5.21: Comparison of Super-K 90 % c.l. excess neutrino-induced upward muon flux limits from the Sun in different cone half-angles with those from other experiments.

models for which vacuum state breaks charge/color symmetry. Then only models which satisfied the following conditions were accepted:

- 18 GeV $< m_\chi <$ 300 TeV
- $\Omega h^2 \leq 1.0$
- $1.0 \times 10^{-4} < Br(b \rightarrow s + \gamma) < 5.0 \times 10^{-4}$
- Mass of Lightest Higgs $>$ 82 GeV
- $m_{\chi^\pm} >$ 103.5 GeV
- $m_\chi < m_{\chi^\pm}$
- $Br(Z \rightarrow \chi + \chi) < 2.0 \times 10^{-3}$
- Squark mass $>$ 176 GeV

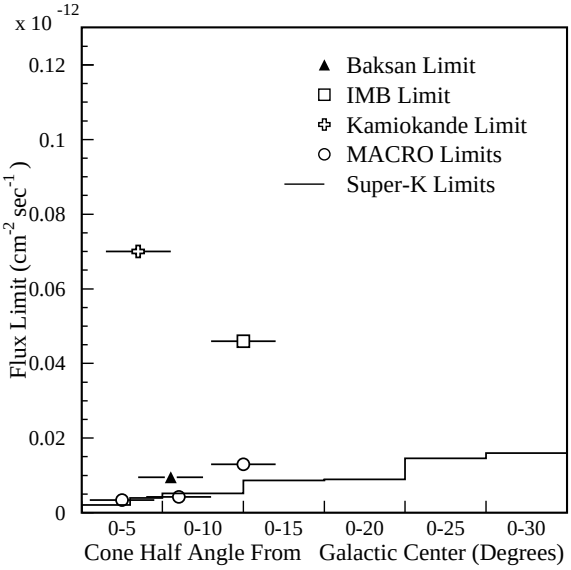

Figure 5.22: Comparison of Super-K 90 % c.l. excess neutrino-induced upward muon flux limits from the Galactic Center in different cone half-angles with those from other experiments.

18609 models survive the above cuts. The expected upward muon flux from WIMP annihilation from Earth and Sun using `Neutdriver` along with 90% c.l. flux limits from Earth and Sun is shown in Fig. 5.26. Note that this sampling of points we have chosen is just one possibility. A more detailed analysis of different ways of sampling of points in MSSM parameter space has been considered in detail by P. Gondolo and collaborators, and this is beyond the scope of the thesis.

5.17 Limits on Annihilation Rates

Given the WIMP flux limits as a function of mass, one can obtain limits on WIMP annihilation rates for different annihilation channels. We have used the online program available [96, 114] which has been calculated using DARKSUSY to obtain limits on annihilation rates. The WIMP annihilation rates from gauge boson annihilation

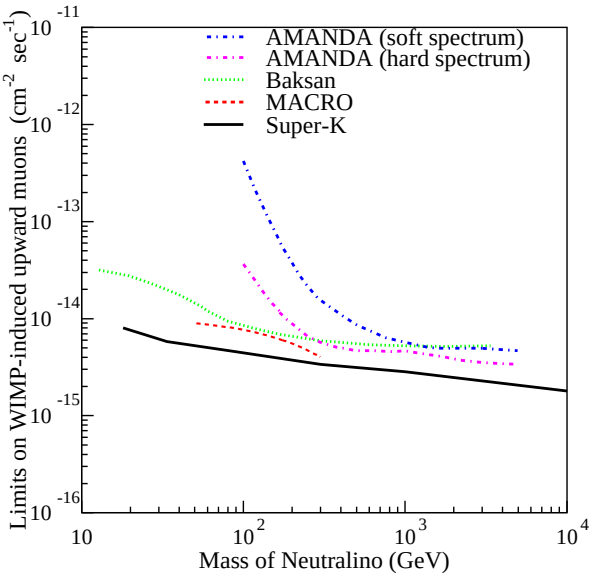

Figure 5.23: Super-K 90 % c.l. WIMP-induced upward muon flux limits from the Earth for different WIMP masses along with corresponding limits from other detectors.

and b-quark and c-quark annihilation for the Earth and Sun are shown in Fig. 5.27 and Fig. 5.28 respectively. The annihilation rates from $\tau^+\tau^-$ and $t\bar{t}$ annihilation take on intermediate values. Since the annihilation rates in the galactic center are model-dependent and depend mainly on the spike density profile these have not been evaluated.

5.18 Comparison with Direct Detection Searches

WIMPs from the galactic halo could be directly detected by measuring and distinguishing from background the nuclear recoil produced by elastic scattering off target nuclei in low background detectors. The main targets used are Ge, NaI, Xe, CaF_2 etc. An overview of all direct detection experiments currently planned or in operation along with the targets used and the exposures achieved so far can be found in

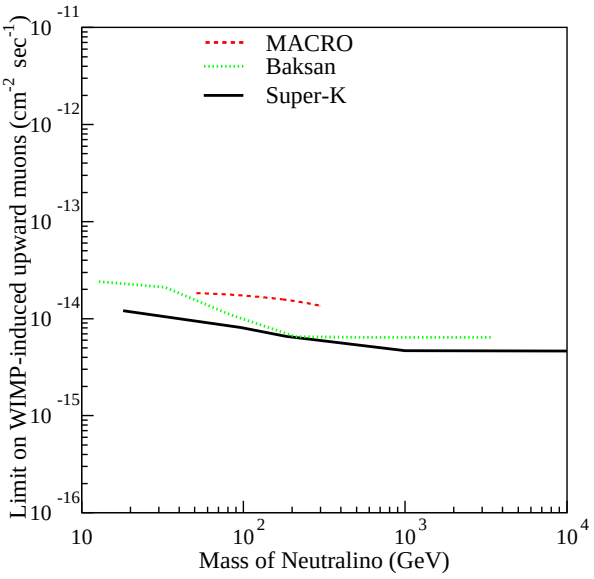

Figure 5.24: Super-K 90 % c.l. WIMP-induced upward muon flux limits from the Sun for different WIMP masses along with corresponding limits from other detectors.

Ref. [115]. The event rates are given by $R \approx \frac{n\sigma v}{m_N}$, where n is the WIMP number density, σ is the elastic scattering cross-section, m_N is the target mass, v is the average speed of the WIMP relative to the target mass. The event rates range from $R \simeq 1-10$ counts/kg/day and the energy deposited is of the $\mathcal{O}$ (KeV). The sensitivity of each experiment depends on the energy threshold, target mass and the level of background. To get more accurate expressions for the event rate one needs to take into account the WIMP velocity distribution, the form-factor suppression and energy threshold. Once this is done the event rate can be written as [81]:

$$R = \frac{\sigma_o \rho}{\sqrt{\pi} m_\chi m_N} \frac{v_0^2}{v_e b} \chi(A_-, A_+) \left[e^{-E_T/E_0} - (1+b)^{0.5} exp\left(-\frac{b}{1+b} \frac{v_e^2}{v_0^2} \right) \right], \qquad (5.28)$$

where $\chi(x_1, x_2) = \frac{\sqrt{\pi}}{2}[erf(x_2 - x_1)]$, and $A_\pm = A_T \pm v_e/v_0$, and $A_T^2 = \frac{m_n E_T}{2m_r^2 v_0^2}$. The main smoking gun for a WIMP comes from the time dependence in the above equation

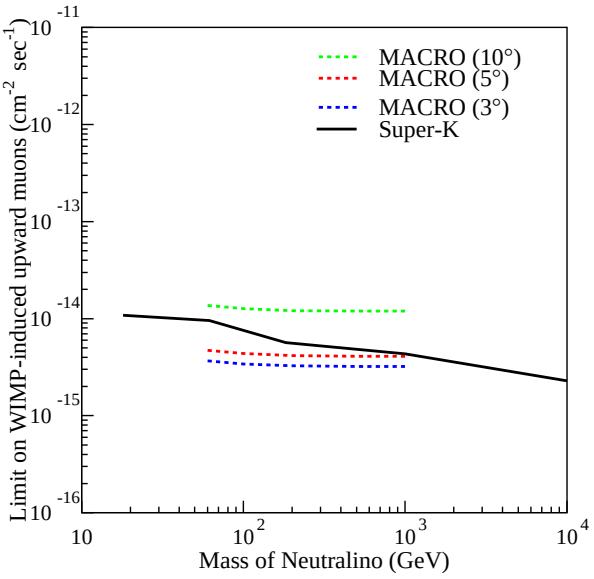

Figure 5.25: Super-K 90 % c.l. WIMP-induced upward muon flux limits from the Galactic Center for different WIMP masses along with corresponding limits from other detectors.

due to the periodic motion of Earth and Sun through the galactic halo. Since the WIMPs have a Maxwellian velocity distribution, their mean speed is taken to be 0. The Sun moves with respect to the Galaxy at a speed of about 220 km/sec. The ecliptic is inclined at about 62° relative to the galactic plane.

The Earth's revolution speed around the Sun is about 30 km/sec and in the summer this adds to the Sun's speed with a peak speed occurring at about June 2nd. In the winter, the net speed with respect to the Sun is subtracted. Thus the signal of a WIMP would be an annual modulation of event rate with peak in June and minimum in December. This is shown in Fig. 5.29.

DAMA is the only experiment which has announced evidence for WIMP detection. In 1998 they first announced evidence for annual modulation based on 12.5 kg yr exposure. They confirmed it in 2000 with total exposure of 105 kg yr [118] and in 2002 [119] with an exposure of 295 kg yr. with about 4 σ c.l. They claim

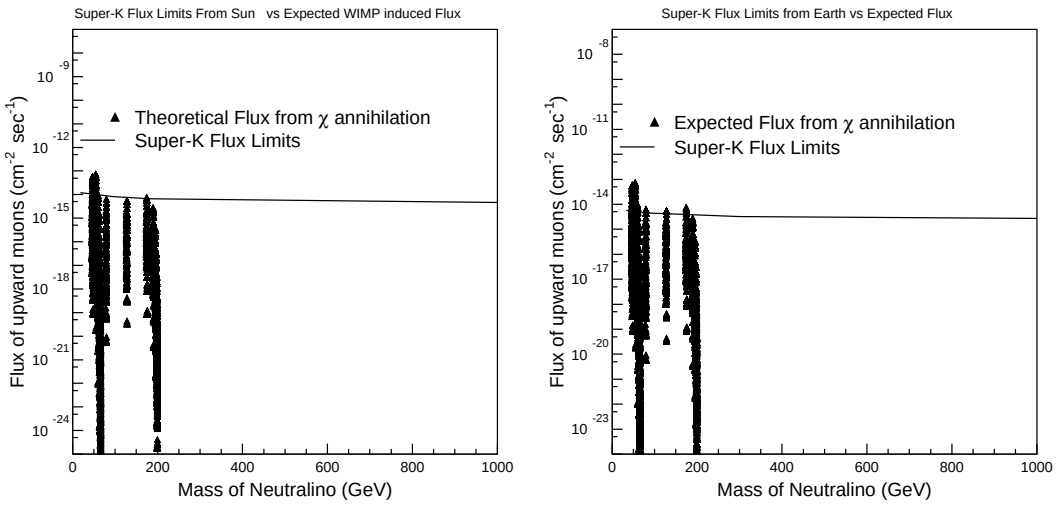

Figure 5.26: Expected upward muon flux from χ annihilations evaluated using `Neutdriver` [81] along with Super-K limits for the case of Earth (left panel) and Sun (right panel).

their event rate is consistent with the following signatures for a WIMP signal: The annual modulation shows the expected 7% amplitude variation, the correct phase and period. The hits occur only in the low energy bins. The DAMA best fit point is at $M_w = 52$ GeV and $\sigma = 7.2 \pm 10^{-6}$ pb. However there are several problems with this claim. A detailed critique can be found in Ref. [117]. The DAMA annual modulation signal in the (2-6) keV energy bin is shown in Fig. 5.30.

Moreover no other direct dark matter detection experiment has seen any evidence for a WIMP signal and all other experiments have obtained 90 % upper limits on WIMP-nucleon cross-section as a function of WIMP mass which have ruled out either most o all of DAMA allowed region. In 2000 CDMS [120] excluded a large portion of the DAMA allowed region with a total exposure of 12 kg day at more than 99 % c.l. Subsequently the CDMS group has obtained stricter limits [121, 122] The Edelweiss experiment [123] using total exposure of 12kg day excludes the whole of DAMA region at more than 99 % c.l. Also the ZEPLIN collaboration which uses

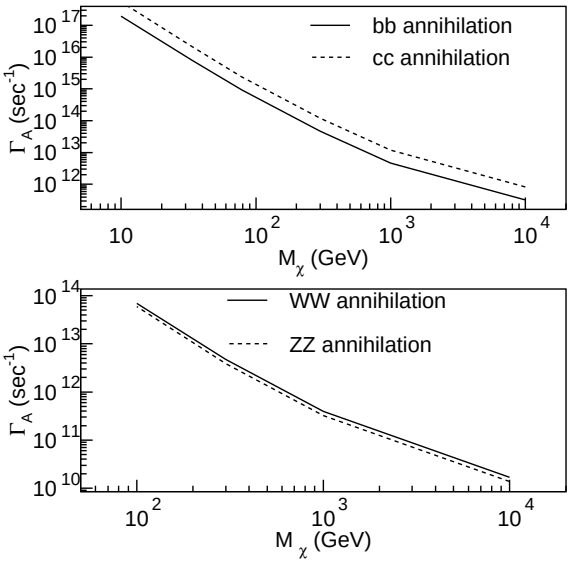

Figure 5.27: Super-K 90 % c.l. upper limit on WIMP annihilation rate in the Earth for different annihilation channels.

liquid Xe as target and total exposure of 90 kg-day also ruled out most of DAMA region. The DAMA allowed region along with 90 % c.l. upper limits from other direct detection experiments can be found in Fig. 5.31.

5.19 Model-Independent Comparison of Direct and Indirect Searches

Given the large number of free parameters it is impossible to do a comparison between direct and indirect searches. However if the WIMP mass and cross-section is known, then one can make a one-to-one correspondence between direct detection rates and indirect detection rates from WIMP annihilations in Earth and the Sun by making realistic assumptions about the model-dependent uncertainties which cannot be accounted for since both rates depend on WIMP nucleon cross-section. Here

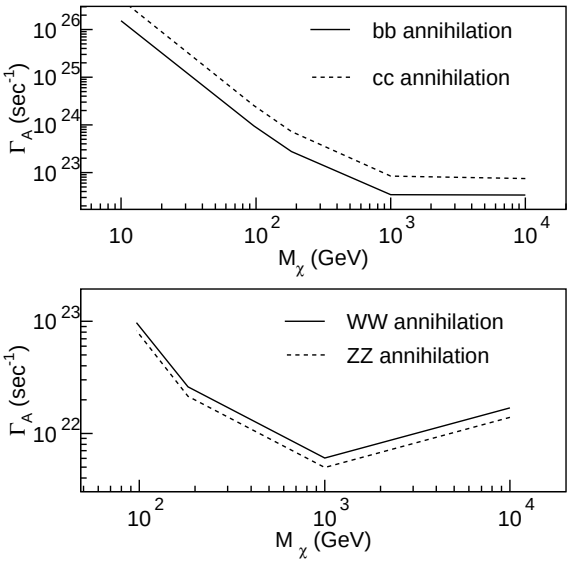

Figure 5.28: Super-K 90 % c.l. upper limit on WIMP annihilation rate in the Sun for different annihilation channels.

we outline the pioneering approach of Kamionkowski and collaborators in making a model-independent comparison of the sensitivities of Direct detection experiments and upward muon detectors. More details are explained in Ref. [81, 125]. Thus once such a comparison is made, one can obtain limits on WIMP-nucleon cross-section as a function of mass from the Super-K limits which can then be compared with the results of direct detection experiments.

The direct detection rate for scalar and spin-dependent interactions is given in Eqn. 5.28 and indirect detection rate in Eqn 5.20. The first model-dependent quantity which arises in calculating the flux of upward muons from WIMP annihilations but not in the direct detection rate is the quantity $\xi(m_\chi)$ given in Eqn 5.21. In general this will depend on details of the SUSY model. However the neutralino predominantly will decay into the boson or lepton state whose mass is closest to that of the neutralino. Hence for a given neutralino mass, the function $\xi(m_\chi)$ can have an upper and lower

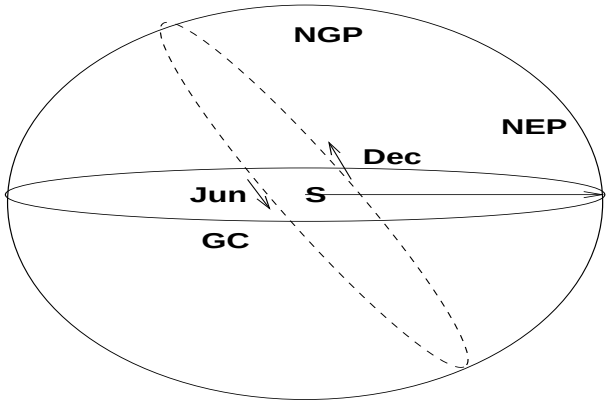

Figure 5.29: Annual modulation because of motion of Sun through galactic halo and Earth's evolution around the Sun. In June sum of Earth and Sun's velocity reaches a maximum of 248 km/sec, whereas in December the sum of Earth and Sun's velocity reaches a minimum of 219 km/sec. Figure obtained from Ref. [116].

bound. The key assumption made in Ref. [125] is that if neutralino is heavier than top quark then its maximum (minimum) value will come from annihilation to top-quarks (W and Z bosons). If the neutralino is lighter than W-boson mass then its maximum (minimum) value will come from annihilation to tau-leptons (b quarks). This is shown in Fig. 5.32. The solid (dashed) curves represent the bounds for Earth and Sun between which $\xi(m_\chi)$ is constrained.

The second quantity which arises in the indirect detection rate but not in the direct detection rate is the equilibriation-time-scale $tanh^2(t/\tau)$ given by Eqn 5.13,5.14. This depends upon $< \sigma_a v >$ as well as the WIMP-nucleon coupling. To account for this effect, $< \sigma_a v >$ is assumed to be $10^{-26} cm^3 sec^{-1}$. With this $\Omega h^2 \approx 0.25$ which is the current abundance of cold dark matter. Then only those models which give neutrino fluxes in the range $10^{-4} < \Gamma_{\mu\uparrow} < 10^{-2} m^{-2} yr^{-1}$ are considered. With these

assumptions and using Eqn 5.20, one can constrain $< L_{sc} >$. Thus the extremum ratio of rates in a WIMP elastic scattering experiment (from Ge in this case) to the flux of upward muons can be calculated for a WIMP with both scalar interactions. This has been done by Kamionkowski *et. al.* and is shown in Fig. 5.33. These can then be scaled for any other target mass since scalar cross-section is proportional to the total nucleon number. For a WIMP with axial vector interactions, the com-

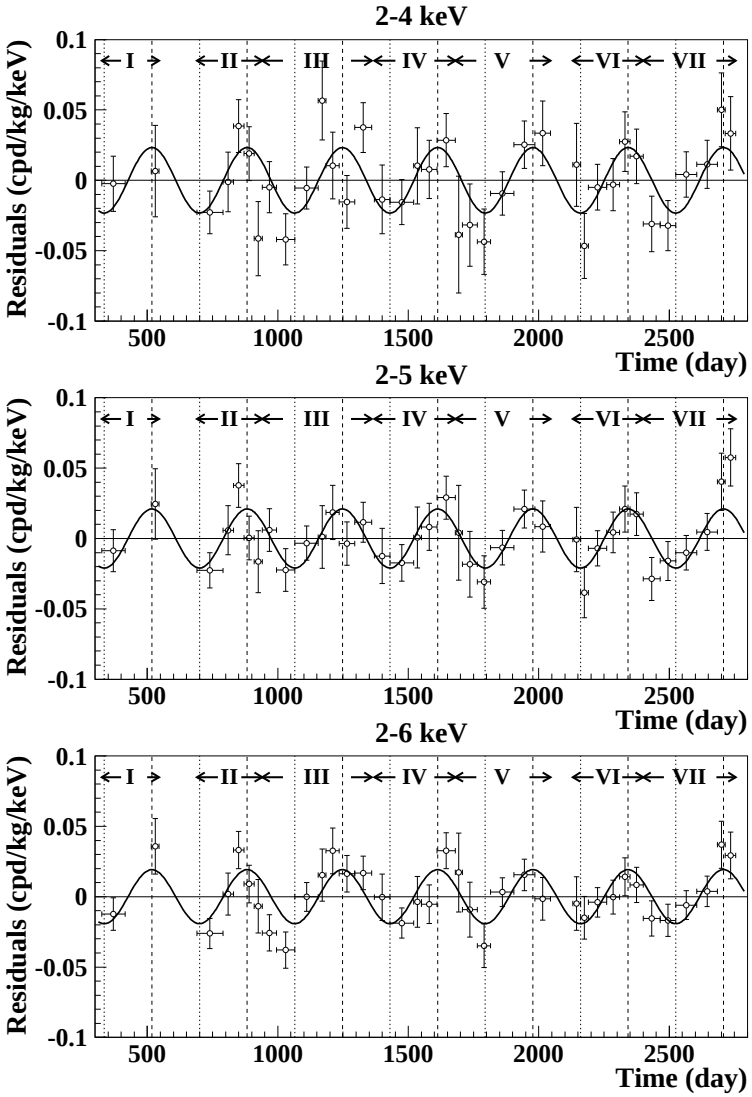

Figure 5.30: Annual modulation of the residual single-hit event rate in the DAMA experiment as a function of time. The total exposure used is 107731 kg day.

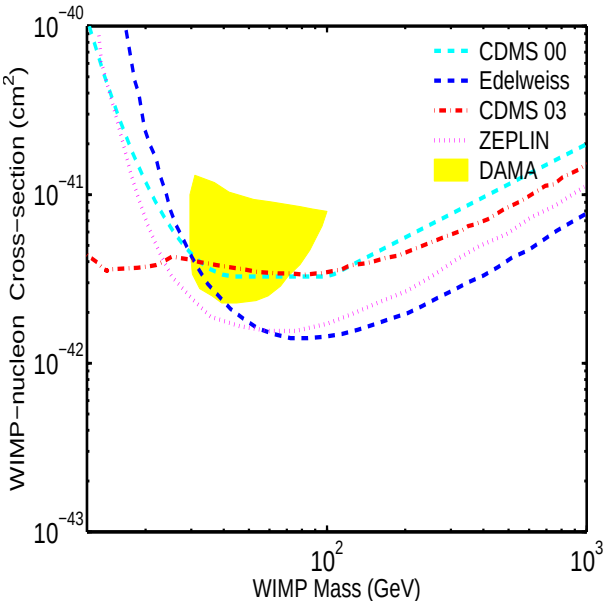

Figure 5.31: The DAMA 3σ allowed region together with 90 % c.l. limits from other direct detection experiments.

parison is straightforward since these can be captured only by the Sun. Also for a WIMP with axial vector interactions $tanh(t/\tau) \approx 1$. Therefore, using the values of $\xi(m_\chi)$ for the Sun one can evaluate the maximum and minimum ratio of direct detection rate for scattering off Hydrogen to the flux of upward muons from WIMP annihilations in the Sun for an axial vector WIMP. This is shown in the lower two curves in Fig. 5.33. Note that these results cannot be scaled to other target nuclei since the WIMP spin coupling to neutrons need not be same as that to protons. This is discussed in further detail in Ref. [125].

These extremum values are independent of the underlying SUSY model. The true ratios will lie in between these curves and they depend upon the values chosen for the free parameters in SUSY/SUGRA model. To get a rough idea of the sensitivities one finds that the event rate in a 1 kg of Germanium detector is equivalent to the event rate in $10^4 - 10^6\ m^2$ of upward muon detector for a WIMP with scalar couplings and

the event rate in a 50-gm hydrogen detector is roughly same as that in a $10-500m^2$ muon detector

For a WIMP with scalar coupling, Fig 5.33 includes the sum of fluxes from WIMP annihilation in the Earth and Sun. Hence we first obtained a combined flux limit from the Earth and Sun. This was done by adding the observed and expected flux in each cone corresponding to a given mass for the Sun and Earth after scaling by the different exposures and then obtaining a combined 90 % c.l. limit. This is shown in Fig. 5.34.

Since we want to obtain conservative 90 % c.l. upper limits we chose the top-most curve to make a correspondence between direct and indirect detection rates. The reason being, this is the maximum inferred ratio of direct to indirect detection

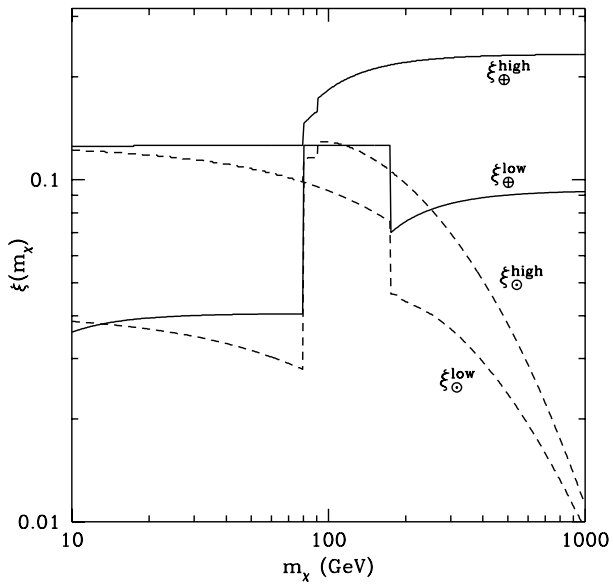

Figure 5.32: Upper and lower limits for $\xi(m_\chi)$ in both Earth and Sun. Figure from Ref. [81].

rates. Hence for a given direct detection rate, using the top most curve in Fig 5.33 one can get a minimum value of upward muon flux from WIMP annihilation. Thus if for a given value of WIMP mass and cross-section this inferred upward muon flux is greater than Super-K limits than this value is ruled out at 90 % c.l. Generalising this, in order to obtain 90 % c.l. upper limit on WIMP-nucleon cross-section we solved Eqn 5.29 to get σ for a given value of WIMP mass.

$$\text{Max Ratio (M)} = \frac{\text{Direct Detection Rate (M, } \sigma \text{)}}{\text{Super-K limit (M)}} \tag{5.29}$$

Thus using the top-most dashed curve in Fig. 5.33 (for scalar WIMPs), the combined Super-K limits from Earth and Sun shown in Fig. 5.34 in the denominator of Eqn 5.29, and using Eqn 5.28, one can solve for σ for a given WIMP mass. This enales us to get 90 % c.l. upper limit on WIMP-nucleon cross-section. This is shown in Fig. 5.35 along with CDMS, Edelwiess upper limits and DAMA best fit region.

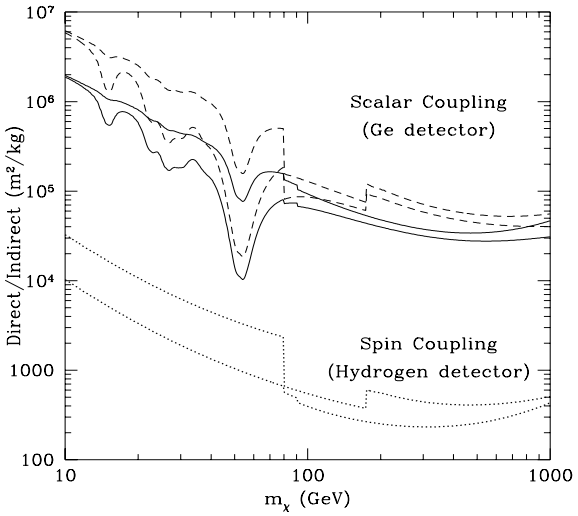

Figure 5.33: Maximum and minimum ratio of direct vs indirect detection rates for scalar and spin-coupled WIMPs. Figure from Ref. [81].

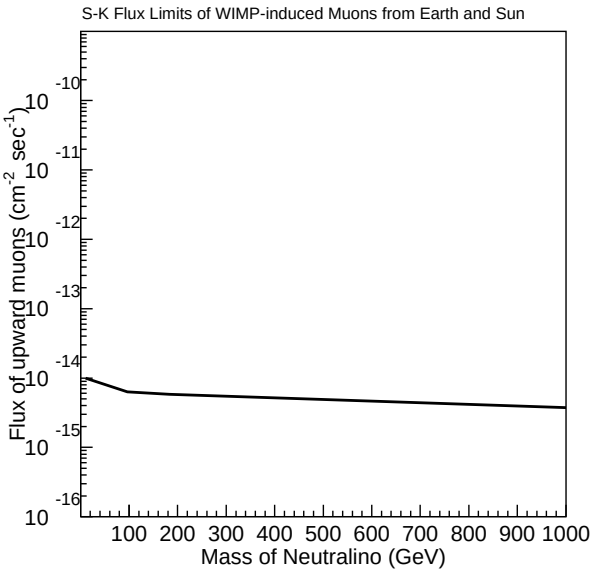

Figure 5.34: Combined Flux limits from the Earth and Sun as a function of neutralino mass.

Thus we see that we do rule out a signification portion of the WIMP parameter space favored by the DAMA experiment.

We then carry out the same exercise for axial vector WIMPs. Now in Eqn. 5.29, we use the Super-K limits from the Sun (shown in Fig 5.24) in the denominator and we use the maximum expected ratio for a spin-coupled WIMP (which is the upper dotted curve in Fig. 5.33). The Super-K limits on WIMP-proton cross-section are shown in Figure 5.36 along with limits from other direct experiments like UK Dark Matter collaboration [126] and Elegant-V [127]. As we can see from this figure the Super-K limits on WIMP-proton cross-section are about 100 times more sensitive than those from other direct detection experiments.

Also a limit on WIMP-proton spin-dependent cross-section using Super-K limits from the Sun (with first 1073.6 days) has been by calculated by Ullio *et. al.* [128], where they showed that the annual modulation seen in DAMA cannot be because

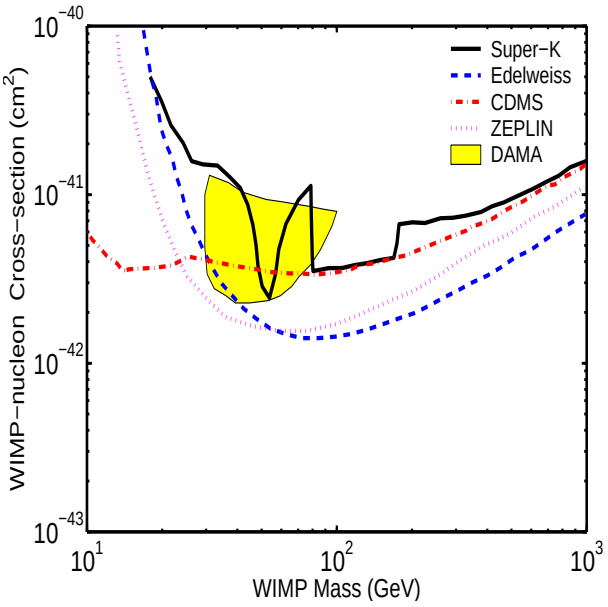

Figure 5.35: Super-K 90 % c.l. exclusion region (solid line) for a WIMP-nucelon scalar cross-section along with corresponding results from other direct detection experiments.

of a WIMP with axial vector coupling to a proton since this is ruled out by null searches for WIMP-induced annihilations in the Sun from Super-K. This is shown in Fig. 5.37.

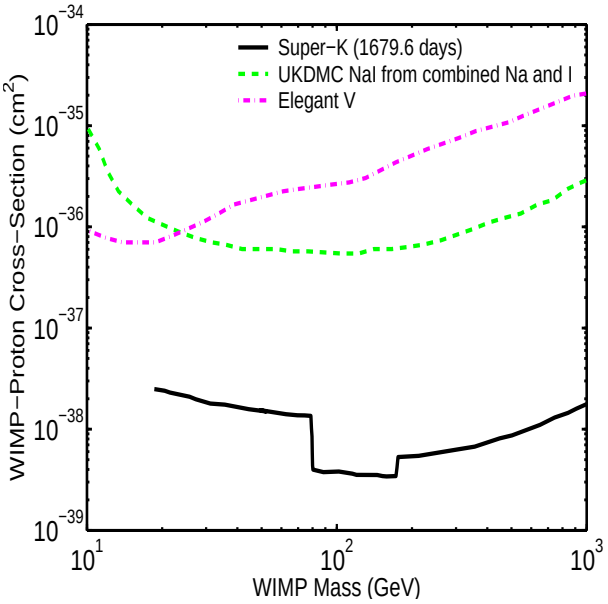

Figure 5.36: Super-K 90 % c.l. exclusion region for WIMP-proton axial vector cross-section along with corresponding 90 % c.l. exclusion limits from other detectors.

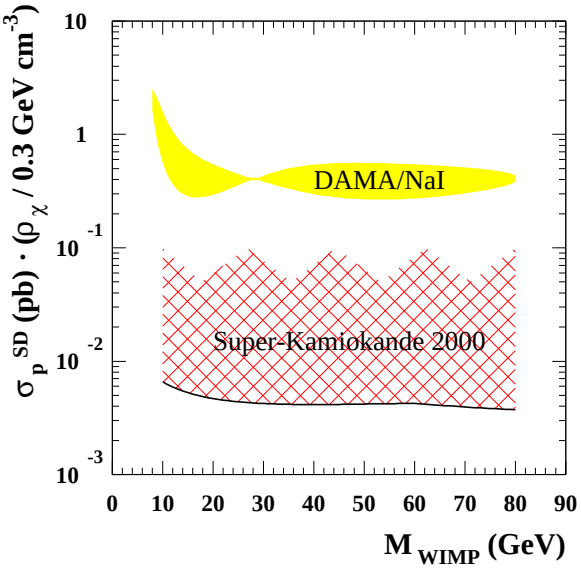

Figure 5.37: Estimates of Super-K limits on WIMP-proton searches made by Ullio *et. al.* along with the DAMA allowed region using their annual modulation is caused by a WIMP with spin-coupling to protons. Figure from [128].

Chapter 6

Other Astrophysical Searches

6.1 Introduction to GRBs

Gamma-Ray-Bursts (GRBs) are short and intense bursts of $\simeq$ 100 KeV to 1 MeV photons which were first discovered in the 60's by the Vela satellites. The time profile of a typical GRB is shown in Fig. 6.1. Their durations range from about 30 ms to over 1000 s. They are the most luminous sources in the universe with total power emitted is $\simeq 10^{51} - 10^{54}$ erg/s . They show a non-thermal spectra with the number of photons per unit energy interval $N(\epsilon) \simeq \epsilon^{-\alpha}$ where $\alpha \simeq 1$ at low energies and and changes to $\alpha \simeq 2 - 3$ for $\epsilon_\gamma \leq 0.1 - 1$ MeV [132]. The power law dependence varies upto GeV energies and one GRB has been tentatively detected at TeV energies [131]. They are mainly produced at cosmological distances and red-shifts exceeding 4 have been measured. For many GRB's, afterglows extending upto radio waves have been detected after the initial burst, which can last upto several days. More details on GRBs can be found in Ref. [133].

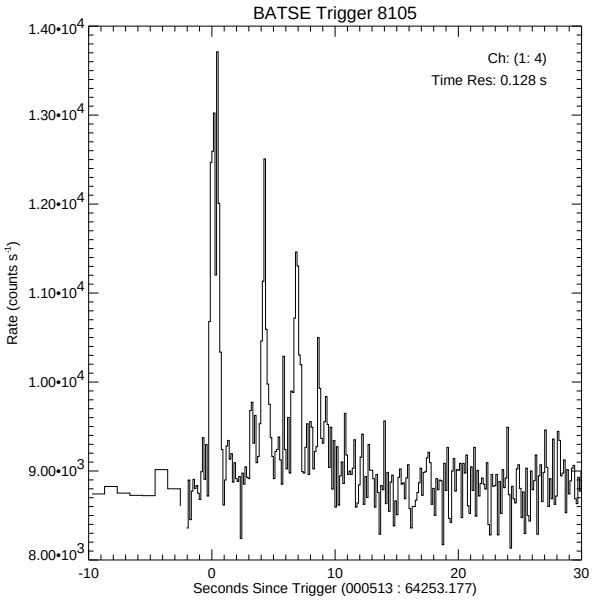

Figure 6.1: Time profile of a typical GRB. Light curve obtained from Ref. [135]. Note that there is tremendous diversity in their time structures and the range of their durations 30ms to over 1000s.

6.1.1 BATSE GRB data

BATSE (which stands for Burst and Transient Satellite Experiment) detector was launched abroad the Compton Gamma Ray Observatory (CGRO) in 1991. BATSE operated for about 9 years until CGRO was removed from orbit by NASA on June 2000. During its operation, BATSE recorded 2704 GRBs at the rate of about 1 /day . The angular distribution of BATSE GRB's were isotropic across the entire sky which ruled out a galactic origin for the GRBs [134].

BATSE consisted of 8 $50.8cm \times 1.27cm$ thick NaI scintillator, sensitive to γ rays from 25 to 2000 keV. Bursts were determined by simultaneous statistically significant increases, above preset thresholds, in the count rates of two or more detectors in a specified energy range. More details of the BATSE detector can be found in Ref. [137]. The position of the burst (including the size of error box), the trigger time,

and the spectrum for every burst is publicly available on the world-wide web [136]. BATSE dataset consisted of 1218 GRBs after Super–Kamiokande started operation. For our analysis we also considered the non-triggered supplement to the BATSE catalog. These are bursts which did not activate the real-time burst detection algorithm onboard the space-craft. These were detected by searching the BATSE archival data with lower detection thresholds and different background averaging schemes than the ones used onboard the satellite. This catalog is available in Ref. [138]. A total of 236 GRBs have been detected in this catalog after Super–Kamiokande commenced data taking. We also consider 3 bursts detected by HETE (which is the followup satellite to BATSE) during Super–Kamiokande-1 data taking.

6.1.2 Possible neutrino emission mechanisms from GRBs

The current most favored models for the GRB prompt emission and afterglow are : Cannonball Model [139], Electromagnetic Model [140] and the Fireball Model [141]. In the Cannonball Model, GRBs are produced by baryonic cannonballs, emitted subsequently in a core-collapse Supernova and the prompt GRB emission is caused by the inverse Compton scattering of light in the near SN environment by the electrons in the cannonball's' plasma. In the "Electromagnetic " model a relativistic rotating stellar-mass progenitor loses its rotational spin energy in an electromagnetically dominated outflow, which powers the emission of GRBs. In the "Fireball" model, the kinetic energy from the bulk expansion of a relativistic wind of baryons, leptons and photons with Lorentz factors > 1000 gets dissipated into radiation after interaction with interstellar medium. However given the vast diversity of the different GRB observables, other emission mechanisms cannot be completely ruled out. Neutrino production could arise from p-γ interactions, p-n collisions, p-p collisions,

shock accelerated protons in jets, etc. The energies of these neutrinos range from several GeV to about 10^{19} ev though the spectrum is model-dependent. A review of different possible neutrino emission mechanisms in GRBs can be found in Ref. [142].

6.2 Space-Time coincidences between GRBs and upmus

The essential idea in looking for GRB-induced upward going muons is that a neutrino coming from a GRB and producing an upward muon will be energetic enough and its direction will be strongly correlated with direction of the parent GRB. The mean angle between neutrino direction and reconstructed upward muon for a $1/E^2$ spectrum is 1.57°. In most neutrino emission mechanisms the neutrino is emitted instantly. However if GRBs are produced by a supernova like mechanism then the time delay could be upto a day. We essentially do 2 kinds of space-time searches.

- We first looked for space-time coincidences in a very tight space time window of $\Delta\theta = 5^\circ$ and $\Delta t = \pm 1000s$. We find one such GRB within this time window as shown in Fig. 6.2. This GRB is GRB 991004D from the BATSE catalog. The total photon flux from this burst is $5.9 \pm 0.3 cm^{-2}s^{-1}$. To evaluate the accidental expected background in this window due to chance, we used the 40-year atmospheric neutrino Monte Carlo after adding oscillations. The total background in a window of $\Delta t = \pm 1000s$ and $\Delta\theta = 5^\circ$ is 6.42×10^{-4}. However when we taken into account the no of bursts analyzed we find that the probability of the background fluctuating to the observed event is 0.94. Hence the probability is consistent with expectation from background.

- This search was done in a slightly larger space-time window. We looked in a

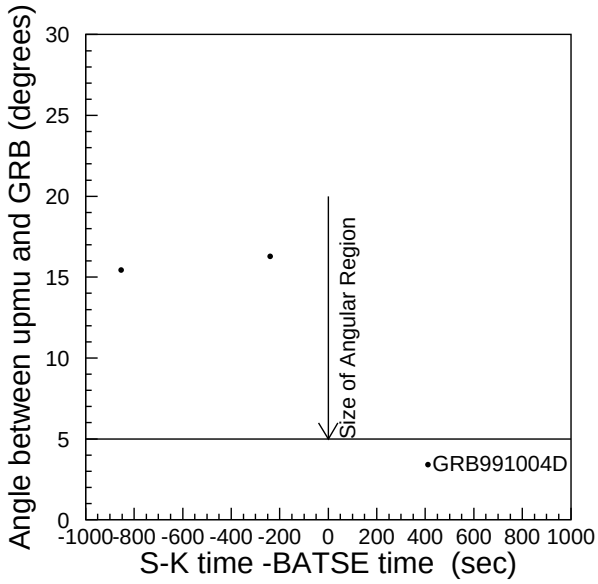

Figure 6.2: Space-Time coincidences between Super-K upward muons and GRBs in a time=window of $\Delta t = \pm 1000s$. Within this time window we looked for angular coincidences in a 5° window.

± 1 day window for clusters of upward muons correlated in direction within 15° of the GRB and within ± 1000 s of each other. The coincidences within a ± 1 day window can be found in Fig. 6.3. No such coincidences were found. The closest match we found was for GRB 970628C where we found 2 upward muons one of which was about 3.4 hours before the burst and within 6.5° and another upward muon about 2 hours after the burst and within 8°.

6.2.1 Fluence limits from GRBs

To calculate the total fluence limit per GRB we first need to calculate the limit on number of upward muon events per burst. To do this we calculated the total cumulative background expected from all GRBs in a space time window of 5° and ± 1000 s which is equal to 0.075. Given this background and one observed signal

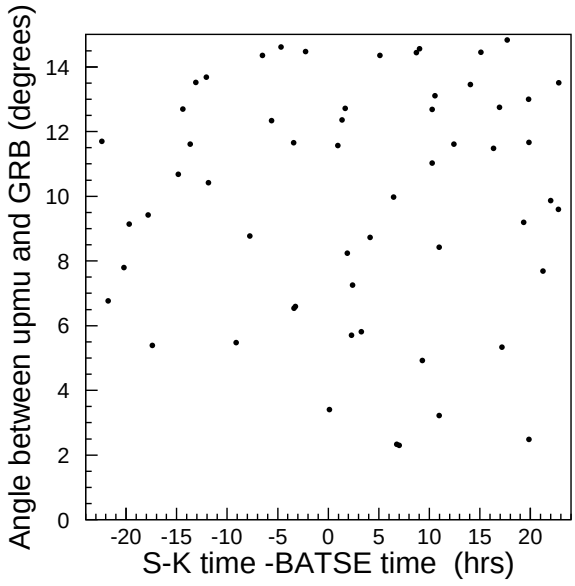

Figure 6.3: Space-Time coincidences between Super-K upward muons and GRBs in a $\pm$ 1 day time-window

event, the 90 % c.l. upper limit on number of GRB produced upward muons per burst (N_{90}) is equal to 2.6×10^{-3}. The average effective area for all bursts within $\pm 1000\ s$ is $630.5 m^2$. To calculate the neutrino fluence we assume a delta-function spectrum which means the fluence limit is a Green's function. This can be convolved with a particular spectrum to get the integrated fluence limit. More details can be found in Ref. [143]. The Green's function fluence limit is given by Eqn 6.1.

$$\Phi_{\mathrm{upmu}}(E) = \frac{N_{90}}{AN_a \int \left[\int_{E_{th}}^{E_\nu} \frac{d\sigma(E_\nu)}{dE_\mu} r(E_\mu) dE_\mu\right] \delta(E - E_\nu) dE_\nu}\ , \tag{6.1}$$

where A is the average Super-K effective area for each GRB within $\pm 1000s$, $r(E_\mu)$ is the effective range of the muon (including the rock), and N_a is Avogadro's number. Because of the delta function, the denominator becomes the probability for a neutrino to make a muon. This has been compiled in Ref. [109] for different neutrino energies.

The 90% c.l. neutrino fluence limits for neutrino and anti-neutrino induced muons from GRBs is shown in Fig. 6.4.

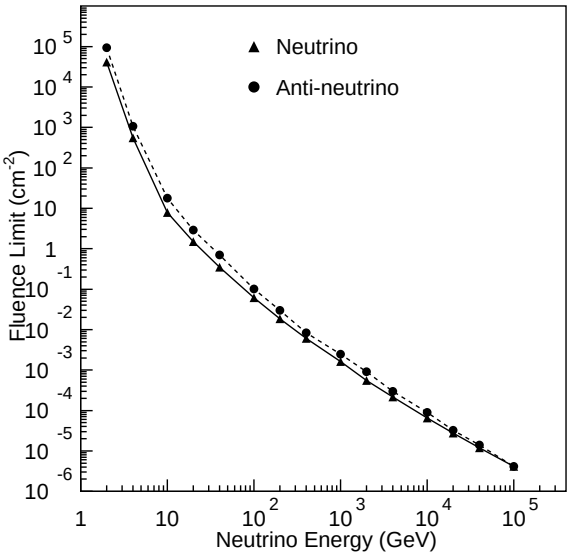

Figure 6.4: The fluence "Green function" limits (for a delta spectrum) for GRB induced upward muons as a function of Neutrino Energy.

6.3 Introduction to SGRs

Soft Gamma Repeaters (SGRs) emit bursts lasting from (0.1 to 500 sec) similar to GRBs. Their spectrum is slightly softer ($\leq 100keV$). On rare occasions SGRs have also emitted giant flares with hard spectra upto MeV. A typical SGR burst is shown in Fig. 6.5. The total energy emitted in X-rays is 10^{44} ergs. The total photon fluence received at earth varies from $10^{-9}erg/cm^2$ to almost $10^{-3}erg/cm^2$. The number of bursts as a function of energy is given by $\frac{dN}{dE} \approx E^{-1.7}$. However unlike GRBs (which are one-shot events), SGRs have been known to flare more than once separated by years or decades. Unlike GRBs which are mainly located at cosmological distances

SGRs are all located near the galactic plane. They also emit persistent pulsed X-ray emission with a regular period. See Ref. [144] for more details about SGRs. SGRs are phenomenologically similar to Anomalous X-Ray Pulsars (AXPs) which are X-Ray emitting pulsars which emit X-ray pulsations between 6-12 s and luminosities in the range $10^{33} - 10^{35}$ erg/sec. In all there are about 5 known SGRs and 7 AXPs. The current most plausible model for SGRs/AXPs which explains all their diverse properties, is they they are neutron stars with $B > 10^{14}G$ are collectively dubbed "magnetars" [146]. However other models (for example "strange quark stars") have also been proposed to explain these objects [147]. It has been argued [148] that for certain rapidly rotating magnetars in which the spin and magnetic moment are aligned in opposite directions, the acceleration potential is large enough to accelerate the protons above photo-meson threshold for neutrino production. According to their model, 4 SGRs/AXPs satisfy such a criterion. However the predicted fluxes are $\simeq 0.1 km^{-2} yr^{-1}$, which is too small to be detected in Super-K. However since lot of issues about the nature of SGRs/AXPs have to be settled, we would like to do space-time correlations to look for any high energy neutrinos coming during a SGR flare just like that for GRBs.

6.3.1 Space-Time Coincidences between neutrinos and SGRs

To do space-time correlations between SGRs and upward muons we have used IPN data which was kindly provided by Kevin Hurley. During Super-K-I operation only 4 SGRs have emitted bursts. These are SGR 1806-20 which emitted 33 bursts, SGR 1900+14 which emitted 67 bursts, SGR 1627-41 which emitted 51 bursts and SGR 1801-23 which emitted 2 bursts . We look for coincidences within a window of $\Delta t = \pm 1$ day and $\Delta\theta = 5^{\circ}$. Given this time window of ± 1 day, the total number of

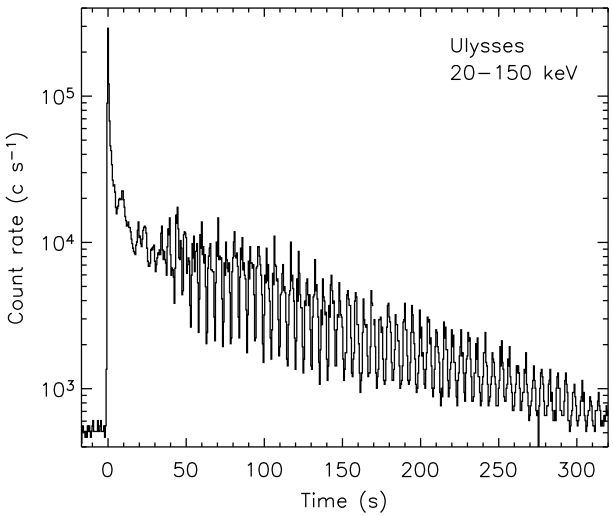

Figure 6.5: Flare observed from SGR 1900+14. Plot obtained from Ref. [144] which was made from data courtesy Kevin Hurley.

bursts from SGRs occurring in separate time bins is 74. The space-time coincidences between SGRs and upward muons is shown in shown in Fig. 6.6.

We find 0 such coincidences from SGR 1806-20, SGR 1627-41 and SGR 1801-23 and SGR 1627-41. We find one upward muon within 2° of SGR 1900+14 and within 1 day of 4 bursts starting from 26th May 1998 21:30:29 UT and ending at 27th May 1998 04:22:01 UT, the closest time interval between the burst and upward muon being 2 hours. This upward muon is a thrugoing muon with $cos(\theta) = -0.106$ and $\phi = 115.2°$. Thus this is close to the thin rock part of the mountain. The bursts from SGR 1900+14 as a function of time is shown in Fig. 6.7. The zenith angle distribution of SGR 1900+14 with respect to Super–Kamiokande between 26th and 27th May 1998 is shown in Fig. 6.8.

To calculate the expected background we followed the same procedure as in

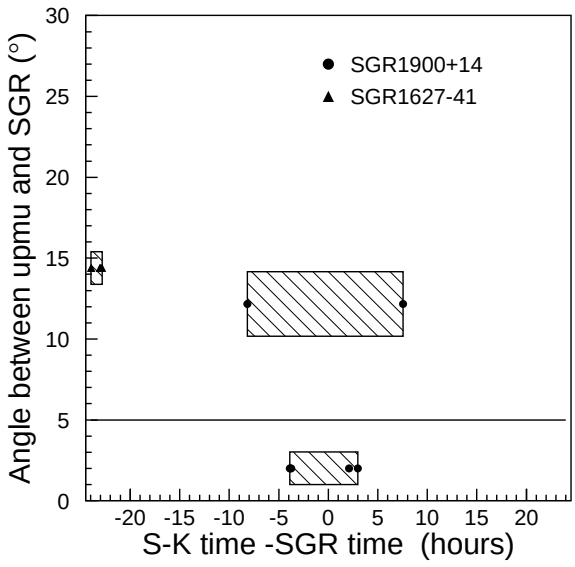

Figure 6.6: Space-Time Coincidences between SGRs and Super-K upward muons in a $\Delta t = \pm 1$ day window. The hatched box indicates the total time interval in which more than 1 SGR bursts are in coincidence with 1 upward muon.

Ref. 6.2 using the 40-year Monte Carlo. The amount of background in a $\Delta t = \pm$ 1 day window using this method is 0.013. Thus given the fact that we have looked at 74 different SGR bursts, the total background becomes 0.96, which means it is consistent with background and not statistically significant enough. Another way to estimate the background is by counting the number of events observed within 5° of SGR 1900+14 during the off-time, i.e. when this SGR was not emitting any bursts, and then scaling it by the ratio of on-source to off-source livetime. We find one event within $3.8 \pm 1.0°$ of this SGR which occurred on 5 Feb 1998 on 03:43:10 UT. As far as we know this SGR did not emit any bursts during this time. The estimated background with this method is about 0.02. Thus using both methods,we find that this event is consistent with background. We also find another upward occurring within 12.2° and within 24 hours of 2 bursts occurring on 27th June 2001

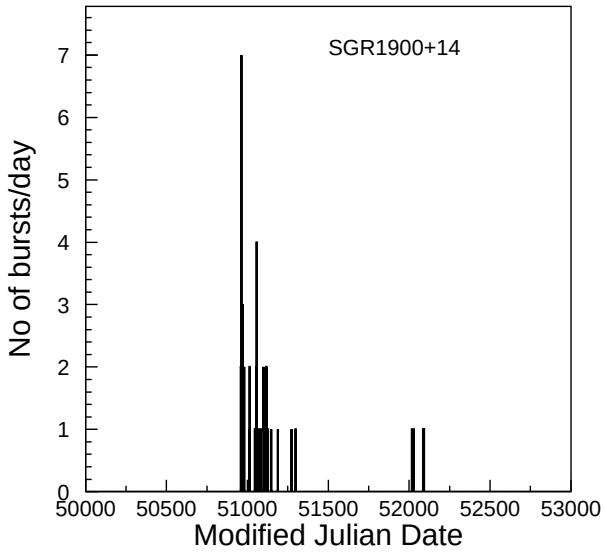

Figure 6.7: No of bursts from SGR 1900+14 per day during Super-K-1 operation. Plot done using IPN data courtesy Kevin Hurley.

at 23:24:18 UT and 28th June 2001 at 15:06:36 UT, but this is outside our search window. Thus we conclude that no upward muons are coming from any of SGR bursts during Super–Kamiokande-1 data taking.

6.4 Diffuse Flux Searches from Galactic Plane

Cosmic rays propagating through the interstellar medium could give rise to neutrinos due to hadronic interactions. The mean density between stars is about 1 particle/cm^3 and $< B > \approx 3 - 5\mu G$. Because of the low density of the interstellar medium,the interaction length is longer than the decay length and the mesons will decay before interacting. The resulting dynamics of neutrino production is similar to the production of atmospheric neutrinos and several calculations have been done. The spectrum of muon neutrinos from cosmic rays hitting the interstellar medium from one of the

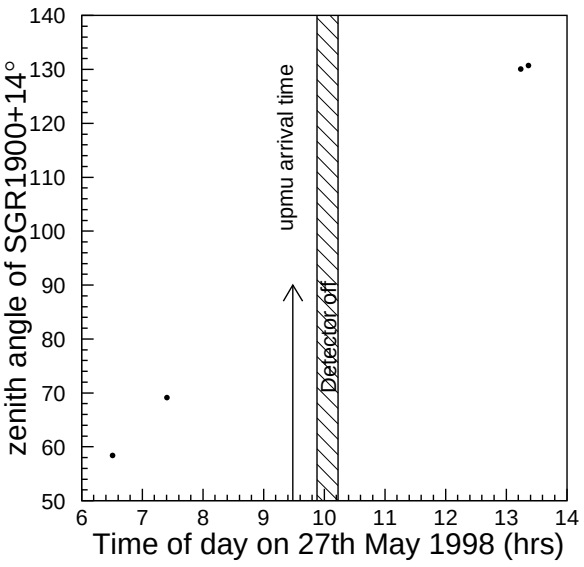

Figure 6.8: Zenith angle distribution of SGR 1900+14 with respect to Super–Kamiokande during its bursts between 26th May and 27th May 1998. The shaded region indicates Super–Kamiokande off-time and arrow indicates the arrival time of upward muon

calculations [149] is shown in Fig. 6.9.

The density of hydrogen in our galaxy scales with height as $\rho \propto exp^{-h/h_0}$ with $h_0 = 0.26\ kpc$. We are located at about 8.5 kpc from the Galactic Center. Thus, most of the signal would come from the galactic plane. To do this search we mainly look for an excess within $\pm 10°$ around the galactic plane (which is at galactic latitude (b) of 0°). We did this search with both upward through-going and stopping muons. The distribution of upward thru-going and upward stopping muons as a function of galactic latitude is shown in Fig. 6.10. To compare against the null hypothesis, we plotted the same distribution for the upward muon 40 yr Monte Carlo after adding oscillations with $\Delta m^2 = 2 \times 10^{-3}$ and $sin^2(2\theta) = 1$. As we can see there is no statistically significant excess within $\pm 10°$ of $b = 0$. We conclude that at 90 % c.l. less than 21 upward-thru muons and 10 upward stopping muons come from cosmic

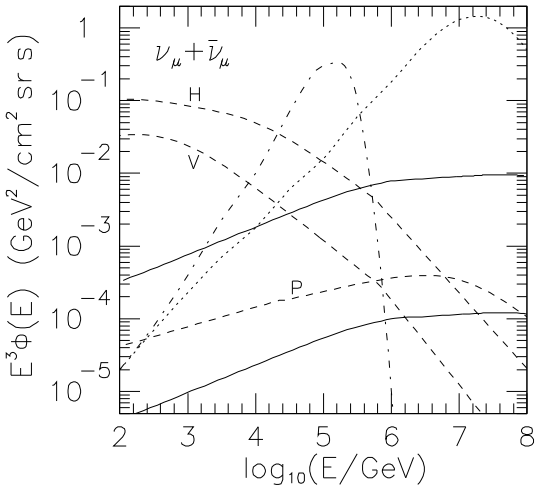

Figure 6.9: Fluxes of muon neutrinos from cosmic ray interactions with the interstellar medium toward the galactic center (upper solid curve) along with the flux from atmospheric neutrinos in the horizontal and vertical direction (dashed), diffuse flux from AGN (dotted). Figure from Ref. [149].

rays hitting the interstellar medium as opposed to Earth's atmosphere.

6.5 Searches from Other Point Sources

The equatorial coordinates of all upward going muons seen by Super-K is shown in Fig. 6.11.

Due to the large background of cosmic ray muons we can only detect a point source of neutrinos when the source is below the horizon. Given the latitude of Super–Kamiokande, we can only detect a source whose declination is less than 64°. Point source searches with Super–Kamiokande upward going muons using cluster based searches as well as using boot-strap technique have been done [150]. No evidence for astrophysical neutrinos was found. Here we do a point source search from selected

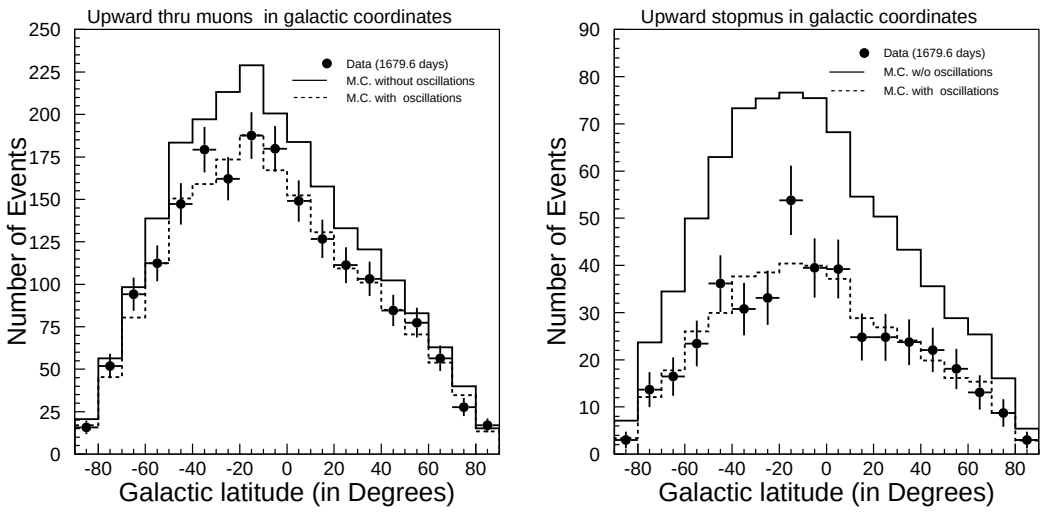

Figure 6.10: Galactic latitude distribution of upward thrumuons (left panel) and upward stopping muons (right panel).

astrophysical sources using only the upward through going muon sample since their mean neutrino energy is much larger. Here we present limits from select point sources from the sample chosen in Ref. [109]. These are mainly X-ray binary systems, active galactic nuclei or supernova remnants. In these systems cosmic rays are accelerated and interact with matter. Such sources could provide a beam-dump for production of neutrinos. (See Ref. [151] for a detailed review of neutrino astronomy and potential sources.) We count the number of observed upward muons within 5° of the source. To estimate the background due to atmospheric neutrinos, we followed the same procedure as in Sect. 6.4. The number of events and the observed background is shown in Table 6.1. As we can see there is no statistically significant excess. We calculate the 90 % c.l. muon flux limits which are summarized in Table 6.1.

So we see no evidence for point sources . The one fluctuation we see is from Cygnus X-1 with 8 events and background of 2.5 with chance fluctuation of 0.0031. However considering that we have looked at 42 sources the probability of such an excess is 13%.

Source	RA (°)	Dec (°)	No of events	Bbgd	90%$c.l.\mu$ flux limits ($10^{-15}cm^{-2}s^{-1}$)
SMC X-1 [1]	19.3	-73.4	7	7.1	3.13
LMC X-2 [1]	80.1	-72.0	8	8.1	3.30
SN 1987A [2]	83.9	-69.3	8	7.4	3.51
LMC X-2 [1]	83.2	-66.4	8	7.4	3.52
GX301.2 [1]	186.7	-62.8	10	7.2	4.7
Cen X-5 [1]	177.0	-62.2	6	5.8	3.10
GX 304-1 [1]	195.3	-61.6	8	6.0	4.06
Cen X-3 [1]	170.3	-60.5	2	6.2	1.65
Cir X-1 [1]	230.2	-57.2	12	7.1	5.37
2U 1637-53 [1]	250.2	-53.7	10	7.0	4.30
4U 1608-522 [1]	243.2	-52.4	9	6.2	4.46
GX 339.4 [1]	255.7	-48.8	4	5.4	2.48
Vela [3]	128.8	-45.2	6	3.7	4.39
GX 346-7 [1]	264.7	-44.4	5	6.8	2.89
AR X-1 0 [1]	256.6	-43.0	7	5.1	4.62
SN 1006 [2]	225.7	-41.9	3	4.2	3.06
Vela X-1 [1]	135.5	-40.6	9	3.9	8.25
2U 1700-37 [4]	226.0	-37.8	1	4.7	2.2
SGR X-4 [1]	275.9	-30.4	8	4.9	6.4
L10 [5]	269.4	-30.1	5	3.9	4.30
GX 1+4 [1]	263.0	-24.7	2	3.4	3.19
SN 1604 [2]	262.7	-21.4	1	3.7	2.64
GX 9.9 [1]	262.9	-17.0	2	4.1	3.21
Sco X-1 [1]	245.0	-15.6	2	3.3	3.40
Aqr X-1 [6]	310.0	-0.9	4	3.9	5.25
4U 336+01 [1]	54.2	0.6	5	4.6	5.91
Aql X-1 [1]	287.8	0.6	2	2.8	3.15
2U 1907+02 [7]	286.8	2.3	2	2.5	3.24
Ser X-1 [1]	280.0	5.0	4	3.7	4.62
SS433 [4]	287.9	5.0	5	2.5	6.5
2U 0613+09 [1]	93.4	9.1	3	4.0	4.67
Geminga [3]	98.4	17.8	5	3.2	8.00
Crab [3]	83.6	22.0	2	3.6	4.52
2U 035+30 [1]	58.8	31.0	3	3.3	5.30
Cyg X-1 [1]	299.5	35.2	8	2.5	15.66
Her X-1 [1]	254.4	35.3	3	3.4	7.07
Mrk 421 [8]	166.11	38.2	1	3.0	4.18
Cyg X-2 [1]	326.2	38.3	5	3.3	9.42
Mrk 501 [8]	253.5	39.8	4	3.4	9.75
Cyg X-3 [9]	308.1	40.9	4	2.2	9.56
Per X-1 [10]	49.6	41.5	1	3.5	4.66

Table 6.1: Summary of point source searches using upward thrugoing muons in Super-K.

[1] X-Ray Binary [2] SN Remnant [3] Pulsar [4] Emission Line Star
[5] Dark Nebula [6] Cataclysmic binary [7] Symbiotic Star
[8] Blazar [9] Wolf-Rayet Star [10] Cluster

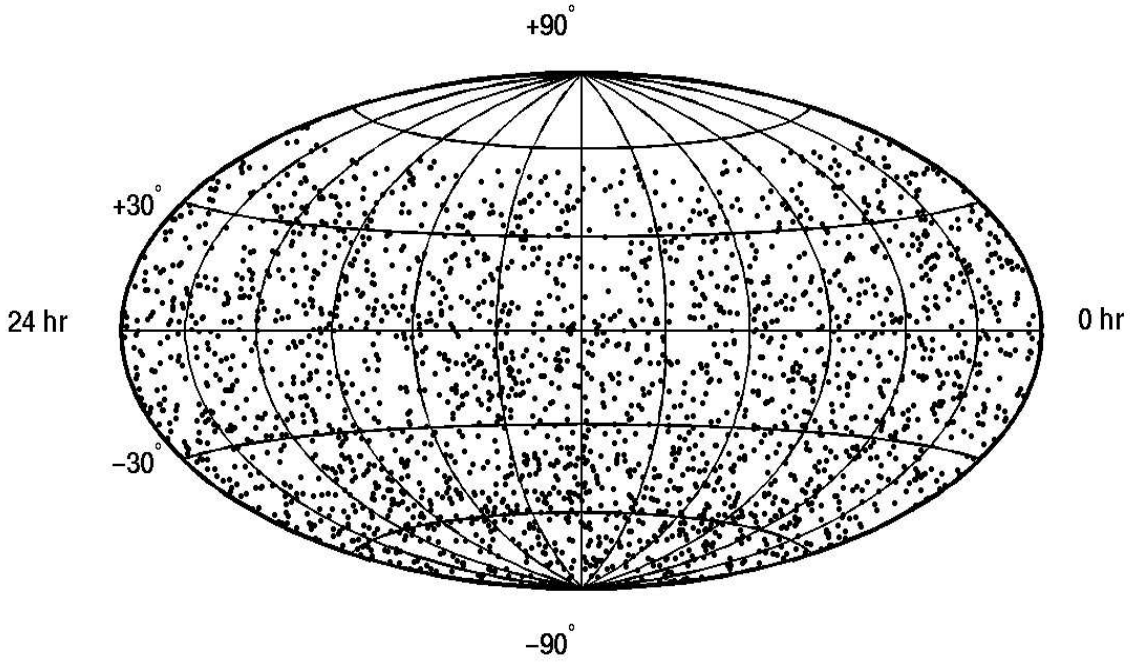

Figure 6.11: Equatorial coordinates of all upward muons in Super–Kamiokande. right ascension is in hours and declination is in degrees.

Chapter 7

Showering Upward-Muons

7.1 Introduction

As we saw in Chapters 3 and 4, upward going muons have been divided into two categories: upward thrugoing muons and upward stopping muons. The mean parent neutrino energy of these events is ~ 100 GeV and ~ 10 GeV as shown in Figure 4.20. In this chapter, we show how we can further split the thrugoing muon dataset into two categories: showering and non-showering muons. The physics basis on which this is done is explained in the next section.

7.2 Muon Energy loss

Muon energy loss as function of energy is given by: [152].

$$\left\langle -\frac{dE}{dX} \right\rangle = \alpha + \beta E \tag{7.1}$$

where $\alpha \simeq 2.4 MeV/(gcm^{-2})$ and $\beta \simeq 3 \times 10^{-6}/(gcm^{-2})$. At low energies the energy loss of muons is dominated by ionization of the medium through which the muon

passes and this is nearly constant ($\simeq$2.2 MeV/cm in water). However at high energies losses through muon pair production, Bremsstrahlung, and photonuclear interactions dominate. The muon energy loss in copper measured over 9 orders of magnitude is shown in Fig. 7.1. The corresponding plot for muon energy loss in water is shown in Fig. 7.2. The critical energy in water where Bremsstrahlung and ionization energy losses are equal is $\sim$ 1 TeV [129]. The mean muon energy of upward thrugoing muons is peaked at $\sim$ 20 GeV, but with a tail extending upto higher energies. One would expect that a small number of events from this sample contain upward muons which undergo radiative energy losses. Such muons are called "showering muons" This sample of showering muons would represent the highest energy neutrinos seen in Super-Kamiokande. Our aim is to isolate this sample for physics and astronomy studies. All thrugoing muons which lose energy only through ionization will be classified as non-showering muons.

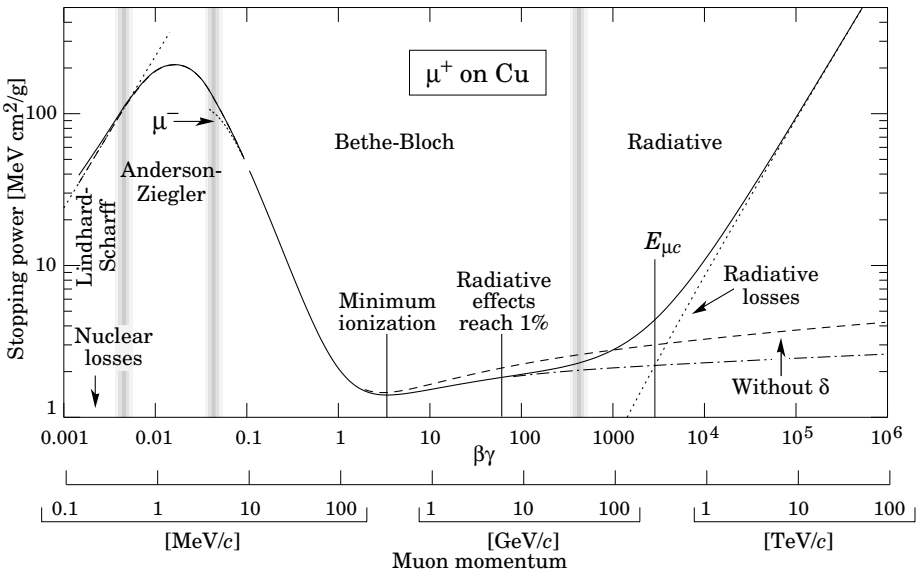

Figure 7.1: Muon energy loss as a function of energy

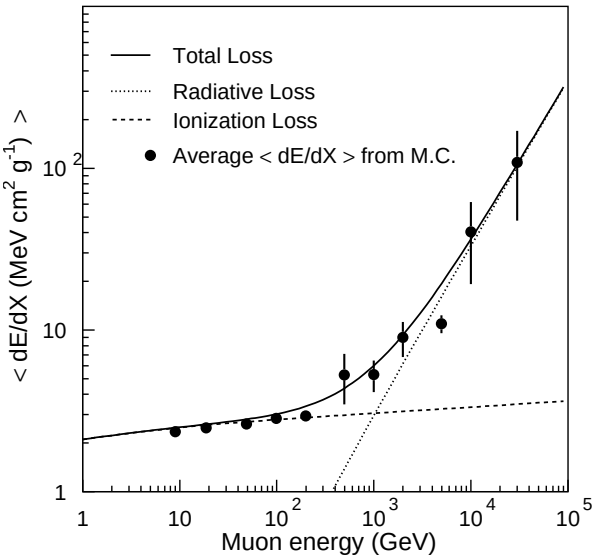

Figure 7.2: Muon energy loss in water as a function of energy including contributions from ionization and radiative processes [129]. The dots indicate $\langle dE/dX \rangle$ obtained by simulating about 100 muon events at each muon energy.

Before we formulated our algorithm, we simulated about 100 Monte Carlo muon events (whose directions and entry points were drawn from the downward muon data sample) at 10 GeV, 20 GeV, 50 GeV, 100 GeV, 200 GeV, 500 GeV, 1000 GeV, 2000 GeV, 5000 GeV, 10000 GeV, and 30000 GeV. This enables us to get a fair sample of showering as well as regular muons to test our algorithm as well as to understand the expected fraction of showering and non-showering events at various energies. To formulate a criterion to test the performance of our algorithm we classified an event as showering if $\frac{\Delta E}{\Delta X} > 2.85 MeV/cm$ where $\frac{\Delta E}{\Delta X}$ is the difference in the muon energy at entrance and exit points divided by the muon length in the ID. The threshold $\frac{\Delta E}{\Delta X}$ at which showering occurs was chosen to be 2.85 MeV/cm since by eye-scanning muon events around this energy, it was found that the onset of Bremsstrahlung begins at this energy. Also at 10 GeV, 2 events with $\frac{\Delta E}{\Delta X} > 2.85 MeV/cm$ are observed. Thus

the aim of our showering algorithm would be to select events with $\frac{\Delta E}{\Delta X} > 2.85 MeV/cm$ to reject events with $\frac{\Delta E}{\Delta X} < 2.85 MeV/cm$ with maximum efficiency.

The $\langle dE/dX \rangle$ of all Monte Carlo events at each muon energy along with the expected value is shown in Fig. 7.2. The agreement is quite good indicating that the GEANT detector simulation does model the muon energy loss in water reasonably well. However the distribution is sensitive to tails at very high energies and often many events need to be simulated to get the high energy tails. The $\frac{\Delta E}{\Delta X}$ for the Monte Carlo events is shown in Figure 7.31

7.3 Basic Outline of the Algorithm

Muon energy loss/unit length due to ionization is approximately constant as a function of muon energy and also constant number of photons are emitted per unit track length. However for a muon which undergoes radiative energy losses, the photons initiate an electomagnetic shower which in turn emit Cherenkov radiation, thus increasing the total Cherenkov light in the detector. Thus if one can calibrate the total "luminosity" emitted by a normal ionizing muon in Super-K (given the muon track), then any muon which emits excess luminosity over this amount will be identified as a Bremsstrahlung muon. Given this, our basic goal is to obtain the average charge in small track intervals (50 cm) along the muon track and construct an equivalent dL/dX histogram, where dL/dX is the amount of light deposited by the muon/track-length. Before that we need to apply a number of corrections to the raw charge which are described in the next section.

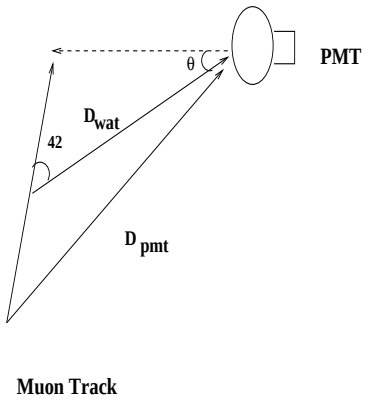

D_{wat} = Distance Travelled by light from photon emission point to PMT

D_{pmt} = Distance from muon entry point to PMT.

θ = Angle between normal to PMT and photon travel direction

Figure 7.3: Geometry of Cherenkov emission

7.3.1 Charge Correction

Although constant number of Cherenkov photons are emitted /track-length, the amount of charge received by each PMT is not uniform. There are 3 important sources of light attenuation which need to be corrected for.

1. A through-going muon provides a line source of light and hence the intensity varies as $\frac{1}{r}$ from the source of light production.

2. The likelihood of a photon hitting a PMT depends on the angle at which the photon is incident to the PMT and depends on the incident cross-sectional area. In addition at very oblique angles of incidences, corrections have to be done for shadowing effects by neighboring tubes. This acceptance and shadowing correction as a function of the angle between the photon and normal to PMT which is obtained from the calibration group is shown in Figure 7.4

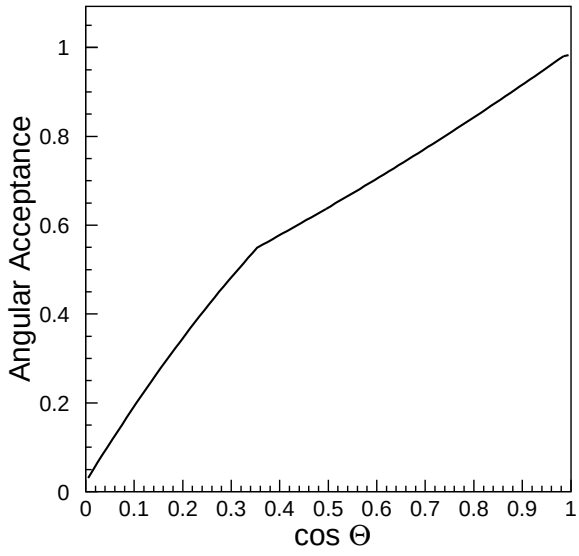

Figure 7.4: Angular acceptance and shadowing as a function of cos(θ) where θ is shown in figure 7.3

3. As photons propagate through the water they can get absorbed and scattered (because of Rayleigh and Mie scattering). The intensity of light because of finite water-transparency decreases exponentially with light-travel distance. This can be seen in figure 7.5 which shows the total charge detected by PMTs after correcting for $\frac{1}{r}$ attenuation and for PMT acceptance. To correct for this water transparency we multiply the raw charge by $e^{d_{water}/L_{wt}}$; where L_{wt} is the effective attenuation length averaged over the Cherenkov spectrum and is obtained for each run by fits to downward going muons as explained in Sect. 2.11.

Thus for each charge detected by the PMT we calculate a corrected charge q_{corr} given by

$$q_{corr} = K \frac{Q d_{water} exp\left(\frac{d_{water}}{L_{wt}}\right)}{F(\theta)} \tag{7.2}$$

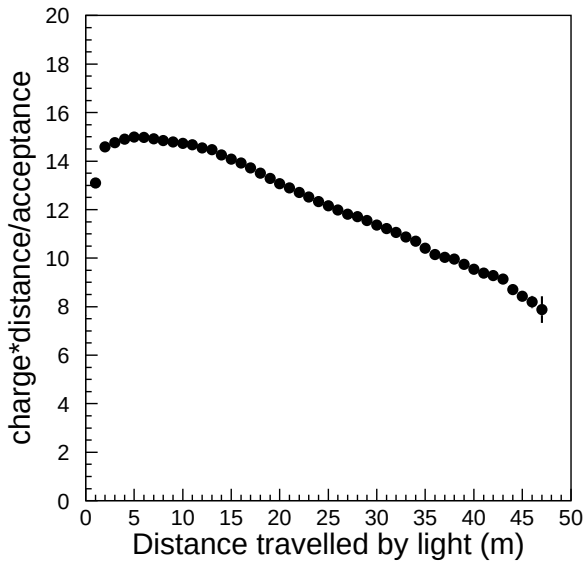

Figure 7.5: The exponential attenuation of charge after correcting for distance and PMT acceptance as a function of photon travel distance.

where Q is the raw charge detected by each PMT; d_{water} is shown in figure 7.3 and F(θ) is the PMT angular acceptance and shadowing as shown in Figure 7.4; $K = \frac{1}{2500}$ is an arbitrary normalization constant.

7.3.2 Cuts on PMTs Used

Because of PMT saturation, non-uniformity of the light source, bad fits to muon track and other reasons, the corrections to the raw PMT charge given in equation 7.2 can give rise to misleading and sometimes abnormally large values for certain PMTs. For this reason corrections are applied to the raw charge of only those PMTs which satisfy the following conditions:

- 400 cm $< d_{water} <$ 4000 cm
- $cos(\theta) > 0.2$.

- The projected point along the muon track has to be at greater than 2 m from the wall.

7.3.3 Additional Systematic Effect

Once above corrections and cuts are applied we obtain the average corrected charge along each 50 cm of the track (Q^i_{corr}) and its statistical error, σ_{q_i} :

$$Q^i_{corr} = \frac{\sum q_{corr}}{N_{pmt}}, \tag{7.3}$$

where q_{corr} is the correction applied to each PMT in the Cherenkov cone according to Eqn 7.2, and the sum is taken over all such PMTs (N_{pmt}) which fall within the given 50 cm bin and which pass the cuts in 7.3.2. We also need to calibrate the average charge ($< Q_{corr} >$) over the muon track-length of an ionizing thrugoing muon where:

$$< Q_{corr} >= \frac{\sum_{i=3}^{N-2} \left(Q^i_{corr} / \sigma^2_{Q^i_{corr}} \right)}{\sum_{i=3}^{N-2} 1/\sigma^2_{Q^i_{corr}}}, \tag{7.4}$$

where Q^i_{corr} is defined in Eqn. 7.3. Thus with these corrections and cuts, one would expect that $< Q_{corr} >$ will be constant for an ionizing muon. However this is not observed. Inspite of these corrections, the $< Q_{corr} >$ increases with muon path-length. To see this effect more prominently, we calculated the average corrected charge averaged over different values of distance traveled by light in water d_{water} for various Monte Carlo muon events which have $\frac{\Delta E}{\Delta X} < 2.85 MeV/cm$. This is shown in Figure 7.6. Thus one can see that the average corrected charge at same values of light travel distance is not constant and is correlated with total muon track-length. Higher the track-length, greater the charge and vice-versa.

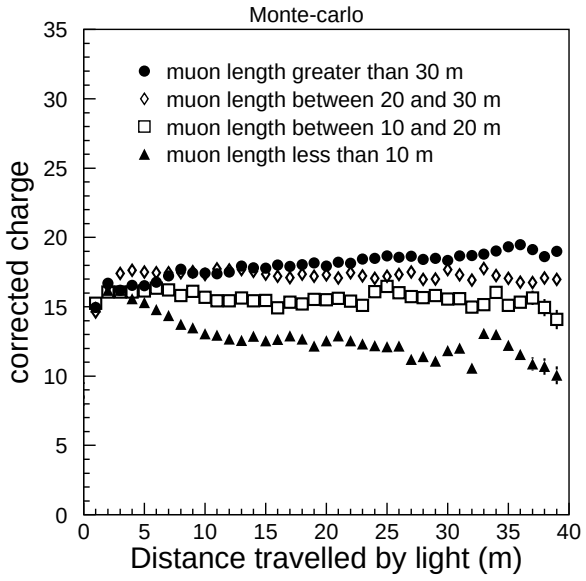

Figure 7.6: The average corrected charge using equation 7.2 as a function of photon travel distance for muons of various path-lengths. As we can see the average corrected charge increases with muon path-length.

One hypothesis to account for this is that, since the muon path-length increases, additional light from outside the Cherenkov cone gets scattered into the cone. To test this hypothesis, we regenerated Monte Carlo muon events at various path-lengths so that any photon which otherwise would have got scattered gets absorbed and redid the plot. Thus we effectively turned off light scattering. This plot is shown in Figure 7.7 where we see that the mean corrected charge is approximately constant and is independent of muon path-length.

To account for this effect in the Monte Carlo and data events, we calculated the mean corrected charge after applying the corrections in equation 7.2 and cutting out any PMTs which do not satisfy conditions for various muon path-lengths as outlined in section 7.3.2 and fitted a second-order polynomial described in Eqn 7.5. The variation of mean corrected charge as a function of muon path-length is shown in

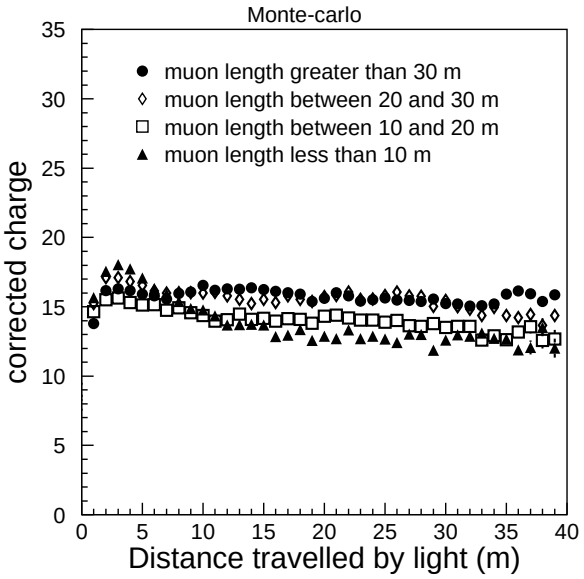

Figure 7.7: Same plot as in 7.6, except that for the Monte Carlo events in this plot; the scattered photon gets absorbed. As we can see from this plot the mean corrected charge is independent of the muon path-length.

figure 7.8

$$Q(l) = -0.0053l^2 + 0.4084l + 8.1035 \tag{7.5}$$

where l is the muon path-length in meters and $Q(l)$ is the expected value of $< Q_{corr} >$ for a non-showering muon.

7.3.4 Charge Dependence on Energy Deposited

In addition to effects caused by scattering of Cherenkov light into the cone non-showering muons within the same path-length range also show a variation which is correlated with $\frac{\Delta E}{\Delta X}$. This is shown in Fig. 7.9 (for 40-year atmospheric neutrino Monte Carlo) where we show the correlation with the mean charge for muons in two path-length regimes (7$< l <$10 m) and ($40 < l < 45m$). Since our goal is to select detect muons with $\frac{\Delta E}{\Delta X} > 2.85 MeV/cm$, we must account for the variation in charge

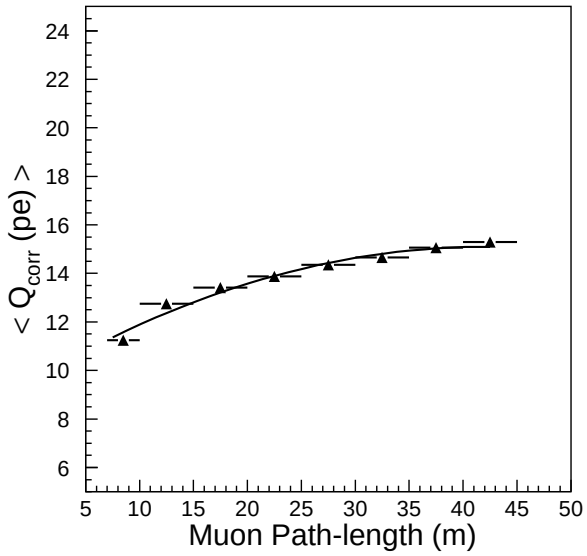

Figure 7.8: Mean corrected charge $< Q_{corr} >$ as a function of muon length and the second order fit

Path-length range	σ_q
$7\ m < l < 10\ m$	1.3
$10\ m < l < 15\ m$	0.8
$15\ m < l < 20\ m$	0.8
$20\ m < l < 25\ m$	0.88
$25\ m < l < 30\ m$	1.0
$30\ m < l < 35\ m$	2.0
$35\ m < l < 40\ m$	2.0
$40\ m < l < 45\ m$	1.08

Table 7.1: σ_q as a function of muon path-length

within the same path-length regime for different values of $\frac{\Delta E}{\Delta X} < 2.85$ MeV/cm. Therefore for each path-length region we assigned a systematic error $\sigma_{Q(l)}$ which was equal to the rms of the mean charge of all muons with $\frac{\Delta E}{\Delta X} < 2.85$ MeV/cm and within the same path-length interval. This is tabulated in Table 7.1.

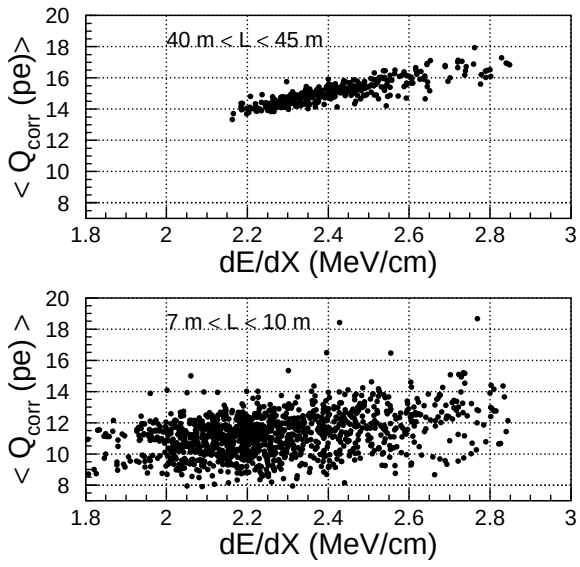

Figure 7.9: $< Q_{corr} >$ vs $\frac{\Delta E}{\Delta X}$ for non-showering muons obtained using 40 year Monte Carlo within the same range of path-lengths

7.4 Strategy to Select Showering Muon Events

We have plotted the corrected average charge (after the corrections and cuts as described) over 0.5 m along the muon path-length for a normal ionizing Monte Carlo muon event in Fig. 7.10. This is essentially a corrected dE/dX plot at various points along the muon track and we can see that it is approximately constant. On the other hand the dE/dX plot for a showering muon which has the same muon entry point and direction as the ionizing one can be seen in Fig. 7.10(right panel) where we can see huge upward fluctuations as opposed to an ionizing muon. Our aim is to construct a function which can distinguish between these two cases. We shall discuss this in the next section.

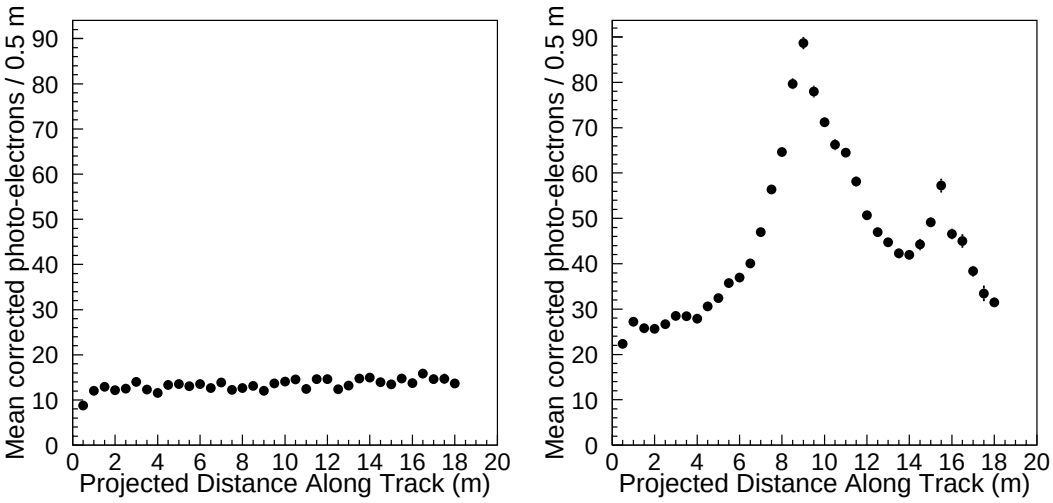

Figure 7.10: dE/dX distribution of a normal ionizing muon Monte Carlo event (left panel) and a showering muon event (right panel) with the same entry point and direction.

7.4.1 Algorithm for Identifying Showering Muon Events

Our aim is to quantitatively distinguish between the two cases shown in Fig. 7.10. We define a χ^2 as follows:

$$\chi^2 = \sum_{i=3}^{N-2} \left\{ \frac{[Q^i_{corr} - < Q_{corr} >]^2}{\sigma^2_{q_i}} + \frac{[< Q_{corr} > - Q(l)]^2}{\sigma^2_{Q(l)}} \right\} \tag{7.6}$$

where Q^i_{corr} is defined in Eqn 7.3, $Q(l)$ is defined in Equation 7.5; $\sigma_{Q^i_{corr}}$ is the statistical error in Q^i_{corr}, $< Q_{corr} >$ is defined in Eqn. 7.4. The sum in Eqn. 7.6 is taken upto the last 1 m of the muon track and is taken over only those bins for which $Q^i_{corr} - Q(l) >= -2.0$. The reason for this is that for some events of particularly short path-lengths for which the fit is not good, there are many bins for which the average corrected charge is much smaller than the expected value and since we are only interested in upward fluctuations from the mean value while searching for showering events; these large negative excursions from the mean value can mimic χ^2 values of

real showering events. To remove such cases we define another variable (Δ) which is defined as :

$$\Delta = [< Q_{corr} > -Q(l)] \tag{7.7}$$

7.4.2 Behavior of Showering Variables

Before we applied the cut to separate between showering and non-showering muons we applied the chi-square in Eqn. 7.6 and the variable Δ defined in Eqn. 7.7 to all the 1892 days of upward thrugoing muon data and 40 year atmospheric neutrino Monte Carlo described in Sect. 4.4. The behavior of χ^2 and Δ on data and Monte Carlo is shown in Fig. 7.11.

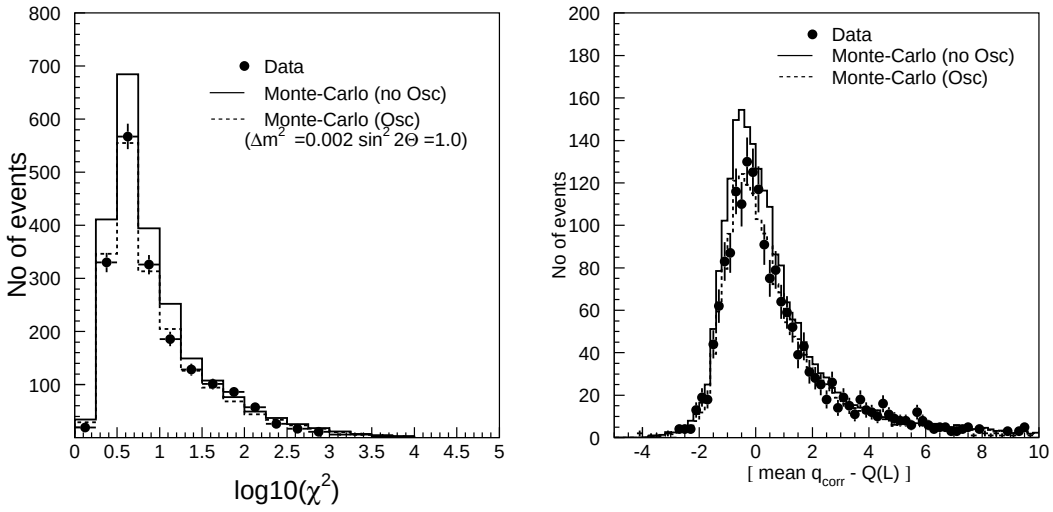

Figure 7.11: Distributions of the variables χ^2 (left panel) and Δ (right panel) for data as well as Monte Carlo.

We then applied this algorithm to our Monte Carlo events and an event was considered showering if $\chi^2 > 25 \& \Delta > 2.0$ or $\Delta > 4.0$. With this cut we found a total of 3129 showering muon events in the 40-yr atmospheric ν Monte Carlo. With this cut the efficiency of detecting showering muon events as a function of path-length is

plotted in Figure 7.12. These estimated background from non-showers in this sample is about 5%.

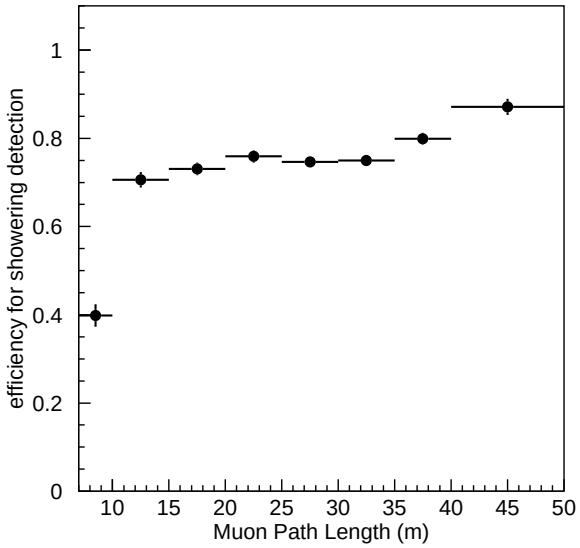

Figure 7.12: Efficiency of the χ^2 cut in identifying showering muon events (i.e. all muons for which $\frac{\Delta E}{\Delta X} > 2.85$ MeV/cm)

7.5 Upward Showering Muons

We then applied the algorithm with the cuts and the threshold as described in the previous section to all the upward thrugoing muon events in the 40 year Monte Carlo sample. The energy spectrum of the upward showering muon events from the 40 year atmospheric neutrino Monte Carlo is shown in Fig. 7.13. As we can see the mean energy of the parent neutrinos of upward showering muons about 1 TeV. In Fig. 7.13 we have also plotted the energy spectrum of all non-showering upward thrumuons. Since the number of upward showering muons is small compared to entire thrugoing muon sample, the mean energy of non-showering muon sample is same as that of

all thrugoing muons viz. 100 GeV. The muon energy spectrum of the 3 categories of events is shown in Fig. 7.14. The mean muon energy of the showering sample is about 250 GeV.

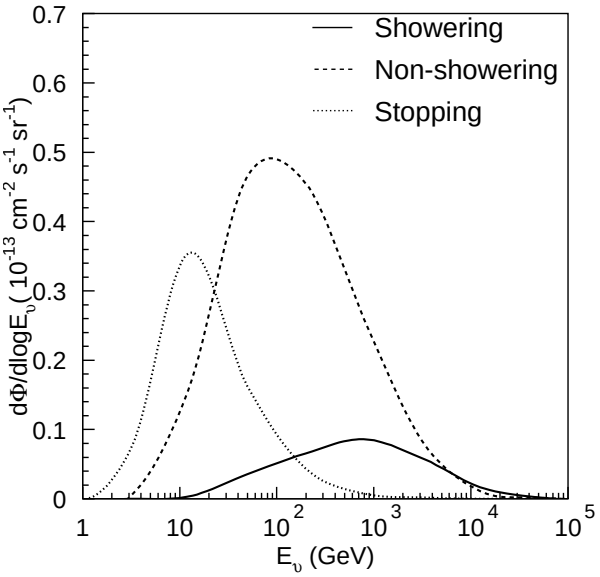

Figure 7.13: Neutrino energy spectrum of all the 3 categories of upward muons.

Thus, the showering sample represents the highest energy neutrino dataset seen in Super–Kamiokande. An event display of an upward showering muon is shown in Fig. 7.32. The angular resolution of upward showering muons is estimated to be 1.25° by looking at the difference in reconstructed and truth muon directions. This is shown in Fig. 7.15. Now that we have isolated this dataset among the Monte Carlo we would like to do the same for the data.

7.6 Distribution of Showering Muon Data

When we applied the showering algorithm to the upward thrugoing muon dataset we obtained a total of 332 events. Before we plot their zenith distribution, we need to

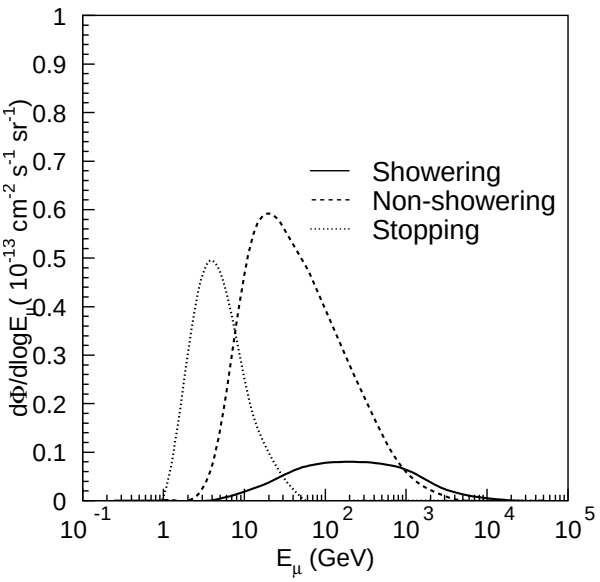

Figure 7.14: Muon energy spectrum of all the 3 categories of upward muons.

estimate the background from downward going cosmic ray muons in the bin closest to the horizon just like for upward thrugoing and stopping muons.

7.6.1 Background Subtraction from Cosmic ray Muons

We applied our showering algorithm to all horizontal thrugoing cosmic ray muons from Sect. 3.8. The zenith vs azimuthal distribution of showering muons near the horizon is shown in Fig. 7.16. As we can see the thin rock region from where most of the contamination arises is same as for thrugoing muons: $60^\circ < \Phi < 240^\circ$. We then rejected all events for which the entry point is at the top of the tank or the exit point at the bottom of the tank. However when we try to do a fit using Eqn. 4.2, there is a bump mainly in the $0 < cos(\theta) < 0.01$. This is mainly caused by showering corner-clippers near the bottom of the tank, for which the direction is badly reconstructed by more than 7°. To remove these events, all events for which the precision

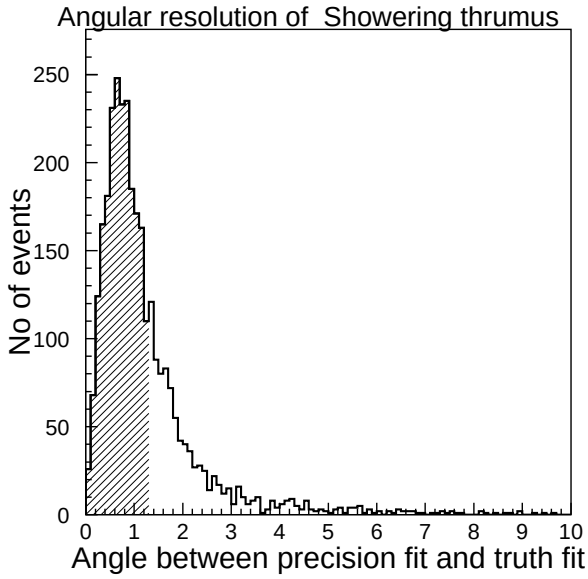

Figure 7.15: Angular direction between the precision fit and true fit directions for upward showering muons as measured with a 40 year Monte Carlo sample. The shaded histogram represents 68 % of the total area and corresponds to $\simeq 1.25^{\circ}$

fit determined exit point was within 2 m of the bottom, were passed to an OD clustering algorithm called `NNcluster` [48]. If the `NNcluster` based exit point was at the bottom of the tank, then these events were removed. The `NNcluster` efficiency to remove these events is about 50%. The near horizontal distribution of showering muons with and without the `NNcluster` cut is shown in Fig. 7.17. With this `NNcluster` cut the bump goes away slightly but not completely. For this analysis we use the background estimated after the `NNcluster` cut. The estimated background is $7.315^{+10.38}_{-4.225}$. Because of the highly asymmetric error bars (caused by the bump) we choose error which is the average of the upward and downward errors. Thus for showering muons $N_{bkgd} = 7.32 \pm 7.3$. The distribution of upward showering muon data with and without background subtraction is shown in Fig. 7.18.

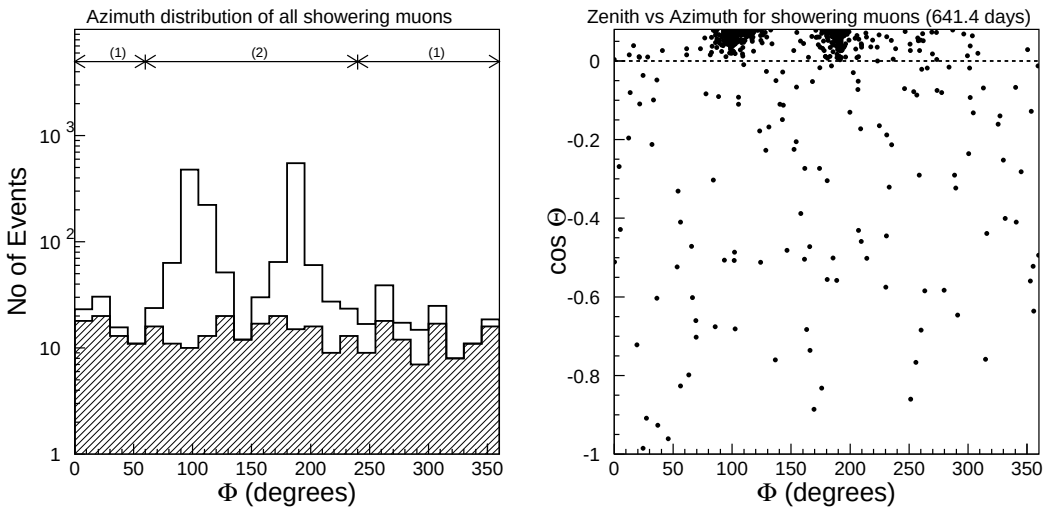

Figure 7.16: The azimuthal distribution of all showering muons in Super–Kamiokande with $-1.0 < cos(\theta) < 0.08$ The region labeled (2) which corresponds to $60^\circ < \Phi < 240^\circ$ represents the thin rock region of the mountain.

7.7 Oscillation Analysis

At neutrino energies of about 1 TeV and higher the neutrino oscillation probability (assuming $\Delta m^2 \simeq 0.002$ eV^2, and $sin^2 2\theta = 1.0$) is negligible. Thus the observed distribution of showering muons should agree with the predictions from no oscillation. Before we do a full-scale oscillation analysis, we compare the the number distribution of observed showering data and Monte Carlo after normalizing to each other. As we see from Fig. 7.19, they agree reasonably well. However we would like to demonstrate this with a formal oscillation analysis.

7.7.1 Effects of Neutrino Absorption

At very high energies, the earth becomes optically thick to neutrinos and neutrinos can have a finite probability of getting absorbed [154]. The neutrino absorption

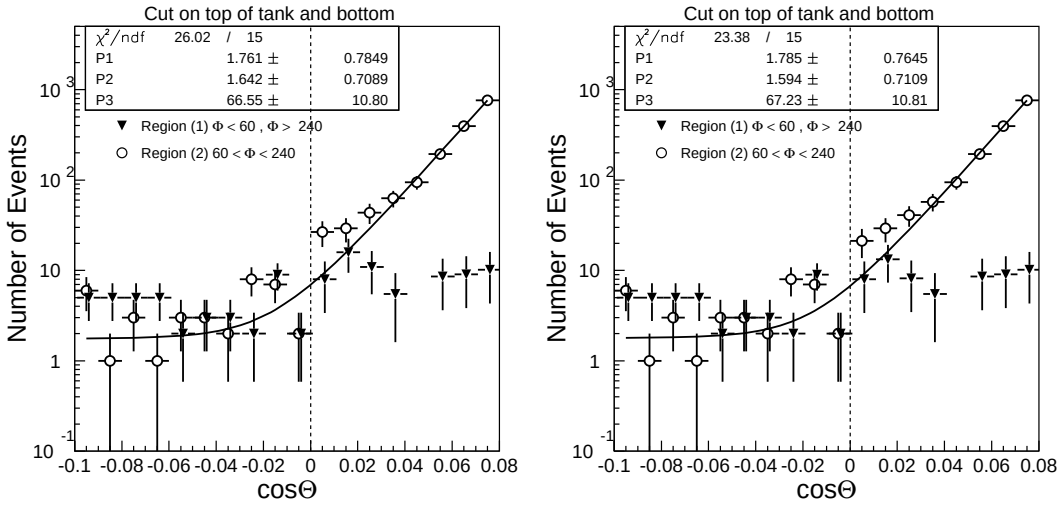

Figure 7.17: Near-horizontal distribution of showering muons for $-0.1 < cos(\theta) < 0.08$ in the thin and thick rock region. The left panel shows this distribution without the `NNcluster` cut and the right panel shows this distribution with the `NNcluster` cut. Other cuts are same as in Fig. 4.7

.

probability is given by,

$$P_{abs} = exp\,[-N_a \sigma_\nu(E) z(\theta)] \tag{7.8}$$

where $z(\theta)$ is the effective column depth through the earth at a given line of sight angle θ, σ_ν is the neutrino cross-section at a given energy E. The mean free path of a neutrino becomes equal to Earth's diameter at about 40 TeV. To evaluate the effects of neutrino absorption we applied Eqn. 7.8 to the all showering Monte Carlo events using the values of σ_ν and $z(\theta)$ compiled in Ref. [154]. This is shown in Fig. 7.20. As we can see the effects of absorption are negligible for the highest energy neutrino sample in Super-K.

To perform oscillation analysis with upward showering muons, we use the same definition of χ^2 as in Eqn. 4.8 for thrugoing muons and with the same values for σ_α and σ_ϵ. These errors are conservative since above 1 TeV, the errors in absolute flux as well as the horizontal to vertical ratio could be much larger [52]. The best

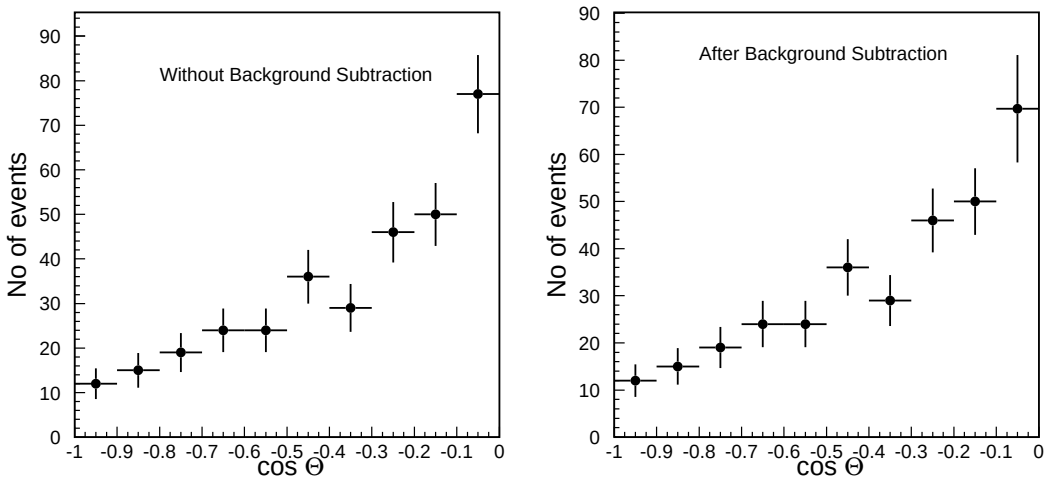

Figure 7.18: Zenith angle distribution of all events identified as upward showering muons without background subtraction (left panel) and after background subtraction (right panel) in Super–Kamiokande.

fit value of χ^2 in Eqn. 4.8 for null-oscillation occurs at $\chi^2 = 10.78$ for 10 d.o.f when $\alpha = -0.127$ and $\epsilon = 0.019$ corresponding to chi-square probability of 0.38. Thus the zenith angle distribution of upward showering muons agrees well with null-oscillation. The best fit occurs at $\chi^2 = 5.35$ corresponding to 8 d.o.f when $sin^2 2\theta = 0.825$, $\Delta m^2 = 0.00329$ eV^2, $\alpha = 0.022$ and $\epsilon = 0.06$. The allowed regions are shown in Fig. 7.21. Note that because of the large allowed regions the best fit point has no physical significance. Also from the difference in $\Delta\chi^2$ between the best fit and null oscillation point, one concludes that the the observed flux is consistent with null-oscillation at 93.4 % c.l.

7.7.2 Oscillation Analysis with 3 Kinds of Upward Muons

Now that the upward muon dataset has been split into 3 categories, we would like to use the full power of the 3 datasets with energies spanning 3 decades. The chi-square

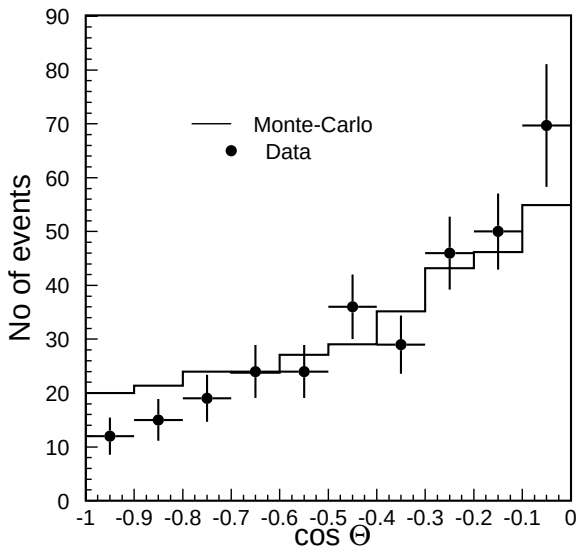

Figure 7.19: Comparison of upward showering muon data and Monte Carlo.

definition used is:

$$\chi^2 = \sum_{i=1}^{10(non-shower)} \left[\frac{\left(\frac{d\phi^{data}}{d\Omega}\right)_i - (1+\alpha)(1+2\epsilon(cos\theta_i+0.5))\left(\frac{d\phi^{MC}}{d\Omega}\right)_i (sin^2 2\theta, \Delta m^2)}{\sqrt{(\sigma^i_{stat})^2+(\sigma^i_{syst})^2}} \right]$$
$$+ \sum_{i=1}^{10(shower)} \left[\frac{\left(\frac{d\phi^{data}}{d\Omega}\right)_i - (1+\alpha)(1+\gamma)(1+(1+2\epsilon(cos\theta_i+0.5))\left(\frac{d\phi^{MC}}{d\Omega}\right)_i (sin^2 2\theta, \Delta m^2)}{\sqrt{(\sigma^i_{stat})^2+(\sigma^i_{syst})^2}} \right] \quad (7.9)$$
$$+ \sum_{i=1}^{10(stop)} \left[\frac{\left(\frac{d\phi^{data}}{d\Omega}\right)_i - (1+\alpha)(1+\beta)(1+(1+2\epsilon(cos\theta_i+0.5))\left(\frac{d\phi^{MC}}{d\Omega}\right)_i (sin^2 2\theta, \Delta m^2)}{\sqrt{(\sigma^i_{stat})^2+(\sigma^i_{syst})^2}} \right]$$
$$+ \left(\frac{\alpha}{\sigma_\alpha}\right)^2 + \left(\frac{\beta}{\sigma_\beta}\right)^2 + \left(\frac{\epsilon}{\sigma_\epsilon}\right)^2 + \left(\frac{\gamma}{\sigma_\gamma}\right)^2$$

α, β and ϵ are the same as in Eqns. 4.8 and 4.9. The term γ in Eqn. 7.9 is a free normalization constant for the ratio of absolute flux of showering to non-showering muons. The uncertainty σ_γ is estimated by weighting each showering and non-showering muon event in the Monte Carlo by $\left(\frac{E}{E0}\right)^{\pm 0.05}$. The ratio changes by -7% to +7.6%. σ_γ is estimated to be 7.6%. The best-fit is obtained when $\chi^2 = 22.05$ for 30 dof at $sin^2 2\theta = 0.986$, $\Delta m^2 = 0.00229$ eV^2, $\alpha = -0.056$, $\beta = -0.088$, $\gamma = -0.020$,

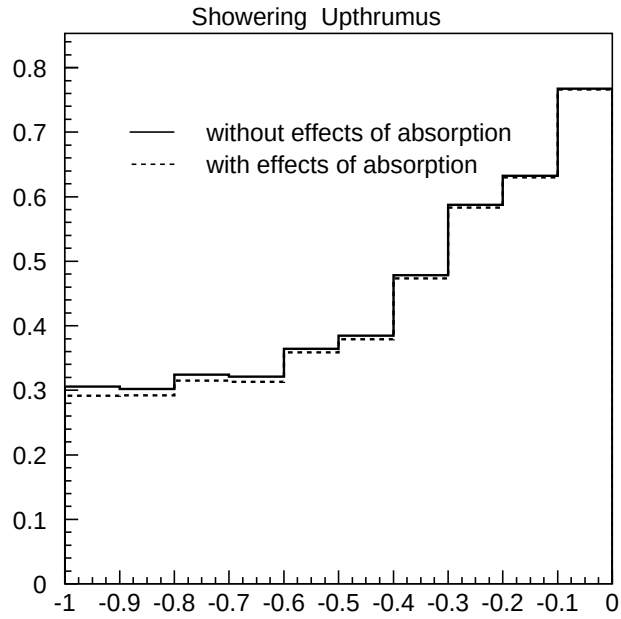

Figure 7.20: Distribution of showering upward muon Monte Carlo with and without absorption.

$\epsilon = 0.009$. The corresponding χ^2 for null-oscillation occurs at $\chi^2 = 47.3$ for 30 dof when $\alpha = -0.203$, $\beta = -0.373$, $\gamma = 0.049$, $\epsilon = 0.069$. The allowed region in $(\Delta m^2, sin^2 2\theta)$ parameter space with all the 3 datasets is shown in Fig. 7.22. The flux of upward showering, non-showering and stopping muons using all 3 datasets is shown in Fig. 7.24. The comparison of the allowed region along with the allowed region obtained by combining all the neutrino datasets (including contained events) in Super-K is shown in Fig. 7.23.

7.8 Astrophysical Searches

Since we have isolated a the highest energy dataset we would like to use this sample for astrophysical searches since the atmospheric neutrino background (which follows a $E^{-3.7}$ spectrum) is reduced. Also with the highest energy sample the angular

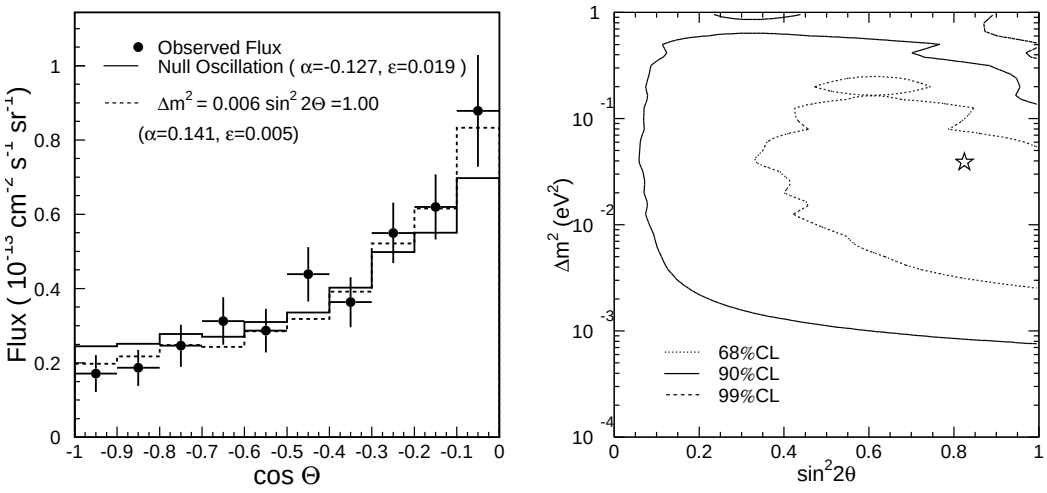

Figure 7.21: Oscillation results using upward showering muons.

distortion between muon and parent direction is very small and is estimated to be $\delta\phi \approx \frac{0.7^\circ}{(E_\nu/TeV)^{0.7}}$ [153]. This can also be seen in Fig. 7.25 where we have plotted the angle between true neutrino direction and the reconstructed muon direction for all upward showering muons. The mean angle is $\approx 2.1^\circ$. We will try to do all astrophysical searches done in previous chapter with this subsample.

7.8.1 WIMP Searches

Only WIMPs with $M_w > 200$ GeV will make neutrinos energetic enough to produce upward showering muons. Thus from Fig. 5.16 we can see that most of the WIMP signal in the upward showering muon dataset will come within 10 degrees. Thus we looked for an excess in cones with half-angles 3°, 5°, and 10° around the center of Earth and Sun and Galactic Center. This is shown in Table 7.2. As we can see there is no excess in these cones and the observed data is consistent with background. We then calculated the 90% c.l. flux limit of WIMP-induced upward muons as a function of WIMP mass using the same recipe as in Sec. 5.15.2. A comparison of

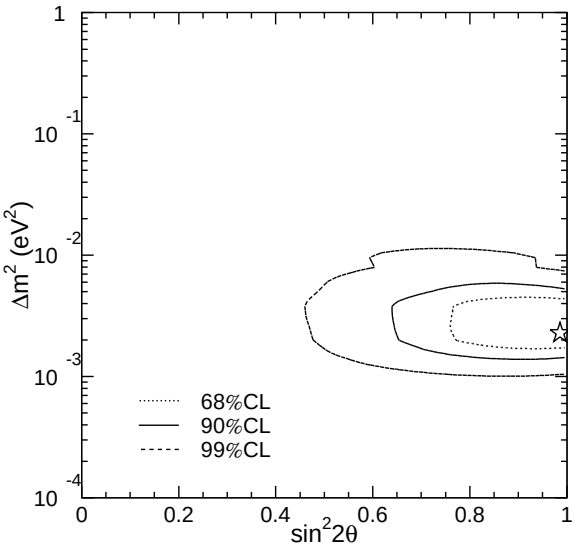

Figure 7.22: Allowed regions using upward non-showering, upward stopping and upward showering muons.

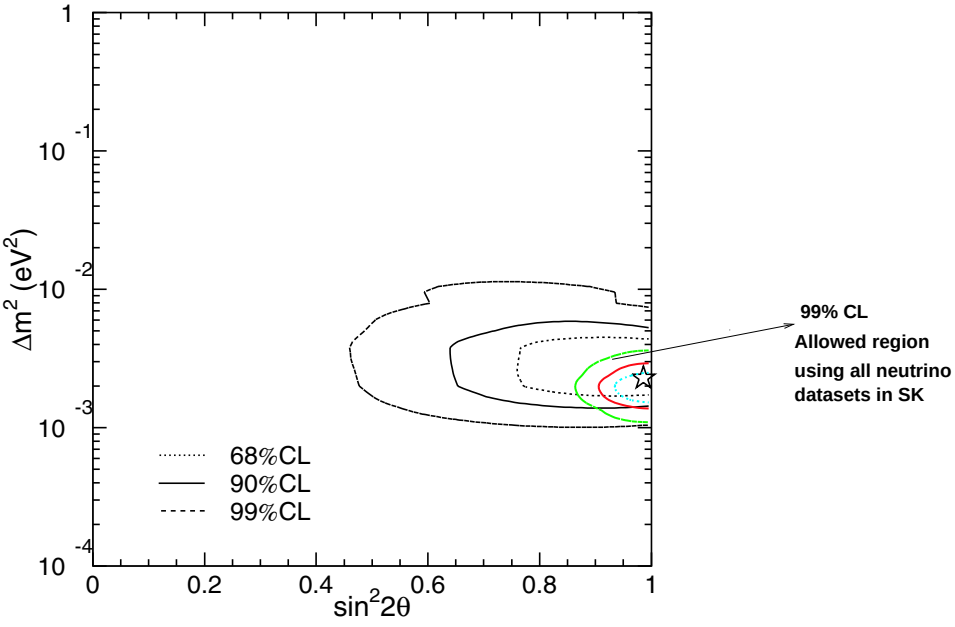

Figure 7.23: Comparison of the allowed regions using all 3 categories of upward muons along with the 68%, 90%, and 99% CL allowed regions (near the arrow) obtained by doing oscillation analaysis using all the neutrino datasets in Super-K.

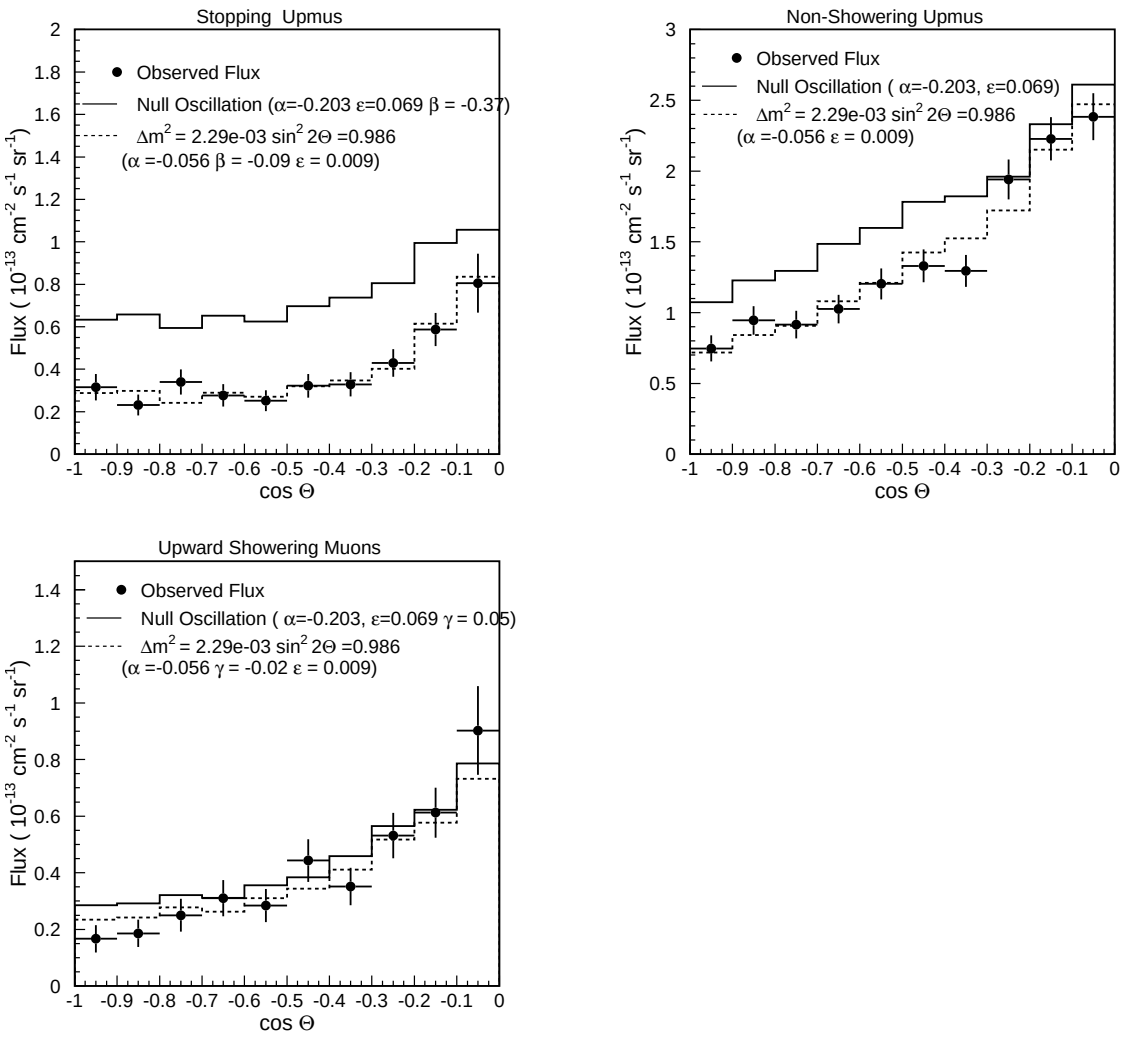

Figure 7.24: Flux of all 3 categories of upward muons together with the best-fit with oscillations using all the 3 categories.

the flux limits with only showering upmus as compared to all upthrumus is shown in Figs. 7.26, 7.27, and 7.28 for the Earth, Sun and Galactic Center respectively.

7.8.2 Diffuse Flux Searches

We then looked for an excess around Galactic latitude = 0° to see if this subset comes from cosmic ray interactions in the interstellar medium. As we can see from such

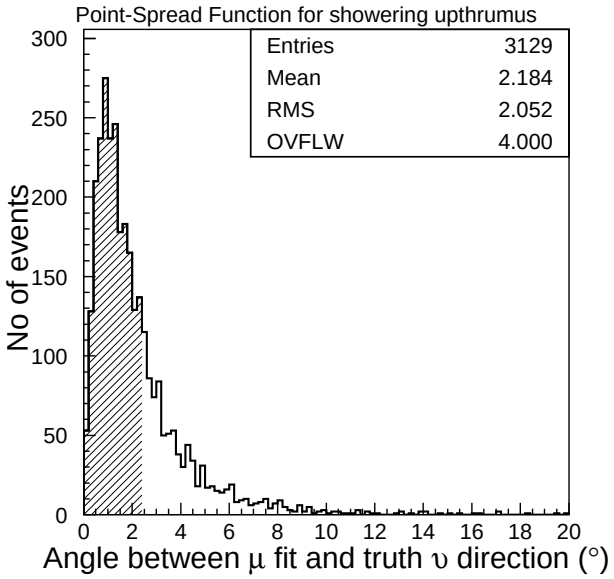

Figure 7.25: Point-Spread function between neutrinos and muons for the upward showering sample. Shaded area indicates 68% of the total area and is equal to 2.1°.

	Earth		Sun		Galactic Center	
Cone	Data	Background	Data	Background	Data	Background
3°	0	0.1	0	0.3	0	0.5
5°	0	0.3	0	0.4	0	1.2
10°	2	2.4	2	2.1	2	3.3

Table 7.2: Observed and expected upward showering muons in cones with half-angles $3°, 5°$ and $10°$ around Sun, Earth and Galactic Center.

Fig. 7.29, no statistically significant excess was seen around $b = 0°$.

7.8.3 Other Astrophysical Searches

No SGRs and GRBs were seen within $\pm$ 1 day window and $\Delta\theta = 5°$ around any of the showering upmus. A skymap of all showering upmus is shown in Fig. 7.30. Searches using angular clustering as well as from selected point sources has been done with upward showering muons [155]. No evidence for point sources was seen in this

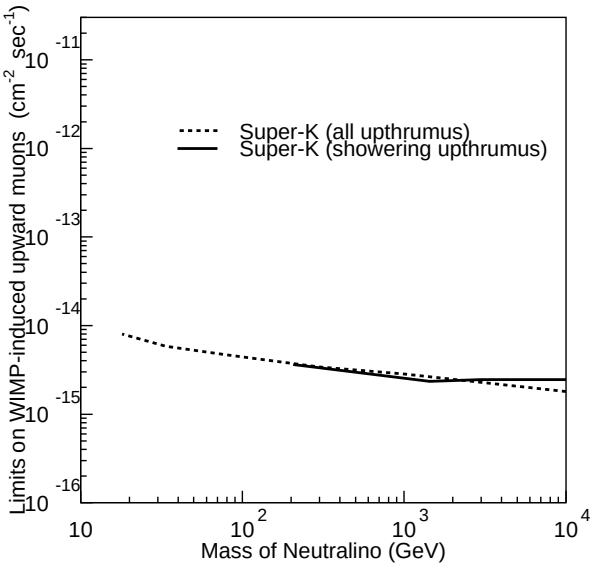

Figure 7.26: WIMP-induced upward muon flux limits from Earth using only upward showering muons and all upthrumuons.

dataset.

Thus we conclude that there is no evidence for astrophysical sources in the showering upward muon dataset.

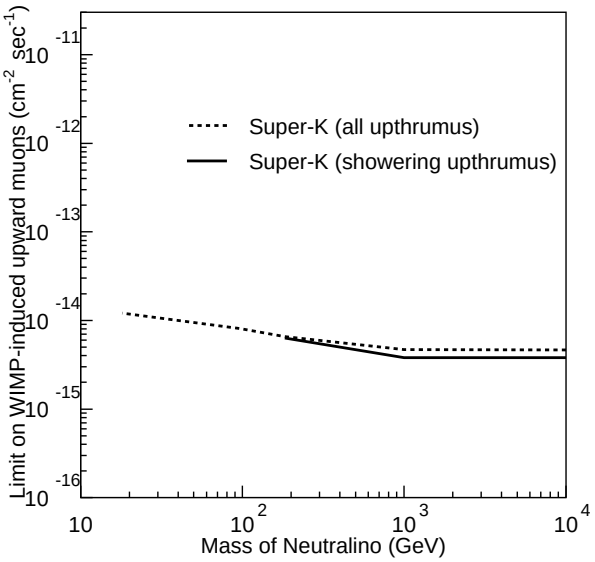

Figure 7.27: WIMP-induced upward muon flux limits from the Sun using only upward showering muons and all upthrumuons.

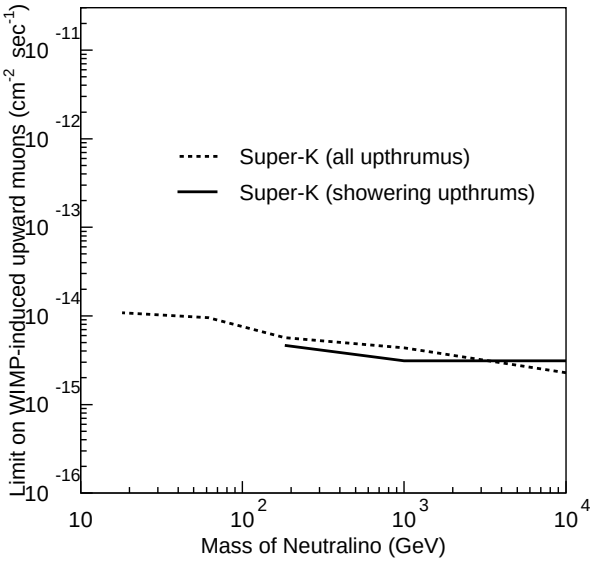

Figure 7.28: WIMP-induced upward muon flux limits from the Galactic Center using only upward showering muons and all upthrumuons.

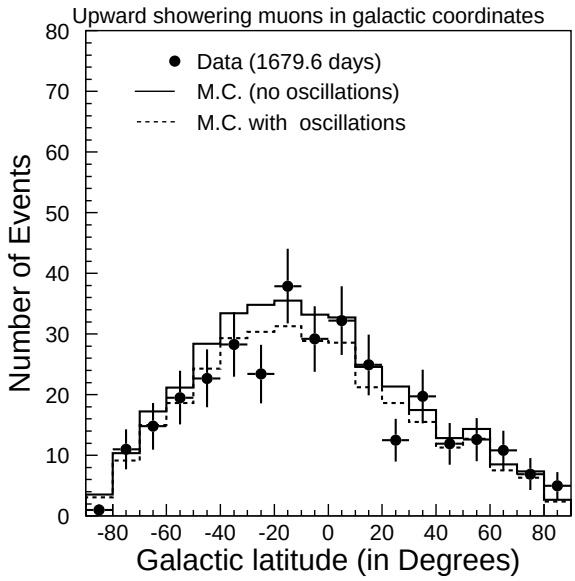

Figure 7.29: Galactic latitude distribution of upward showering muons.

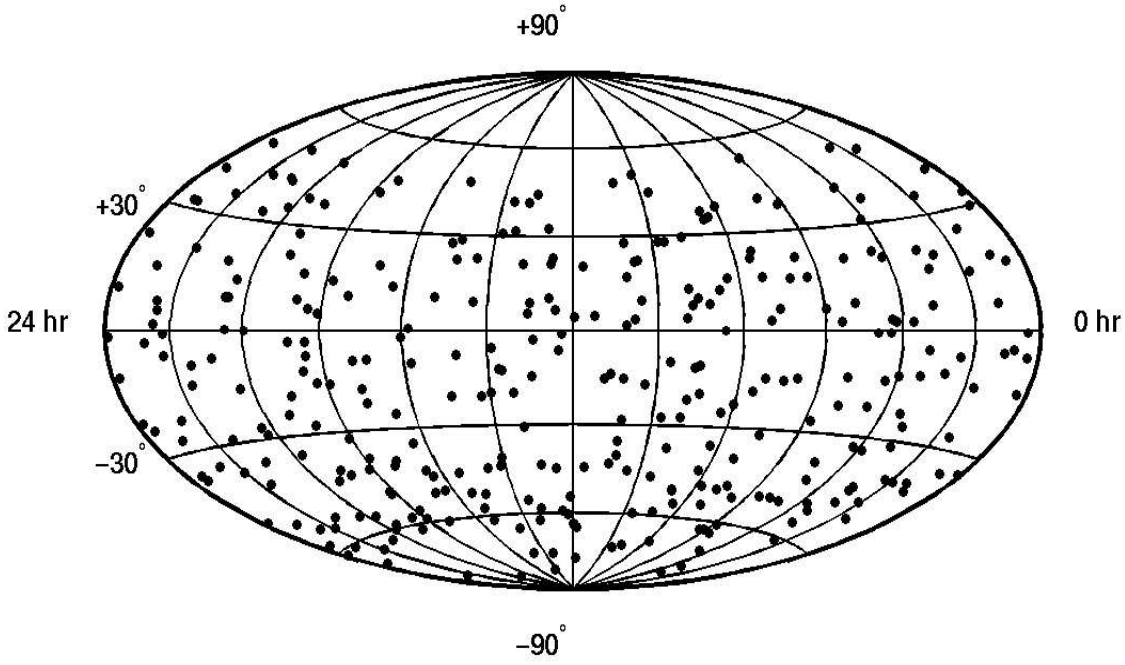

Figure 7.30: Equatorial coordinates of all upward showering muons in Super–Kamiokande. Right ascension is in hours and declination is in degrees.

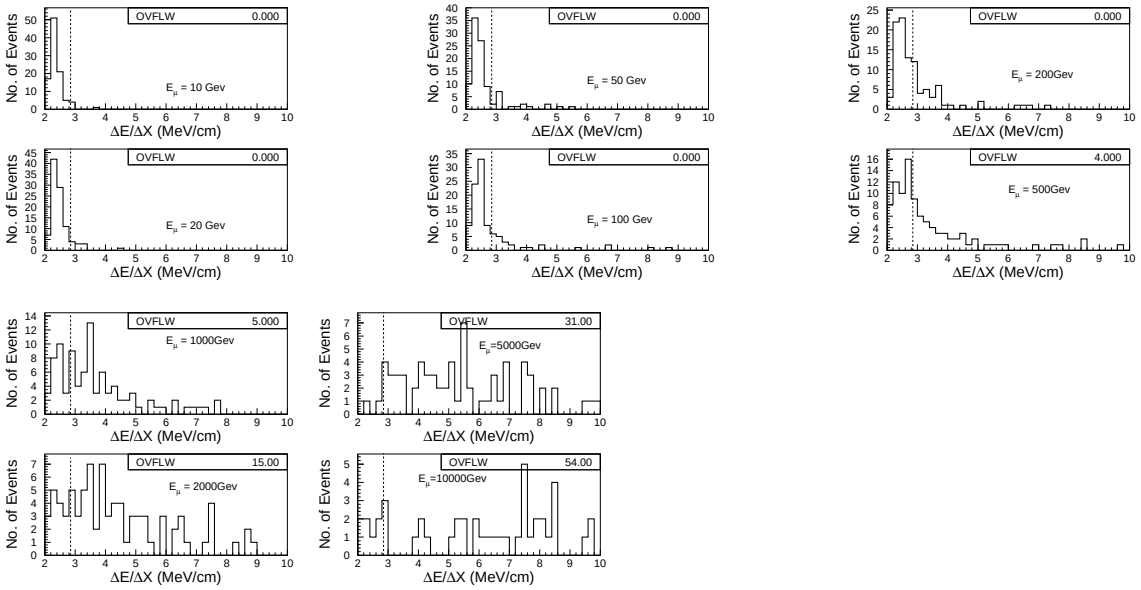

Figure 7.31: $\frac{\Delta E}{\Delta X}$ distribution for muon Monte Carlo events at various muon energies from 20 GeV to 10 TeV. The dashed line in each plot represents the threshold used to separate showering and non-showering muon events which corresponds to $\frac{\Delta E}{\Delta X} = 2.85$ MeV/cm.

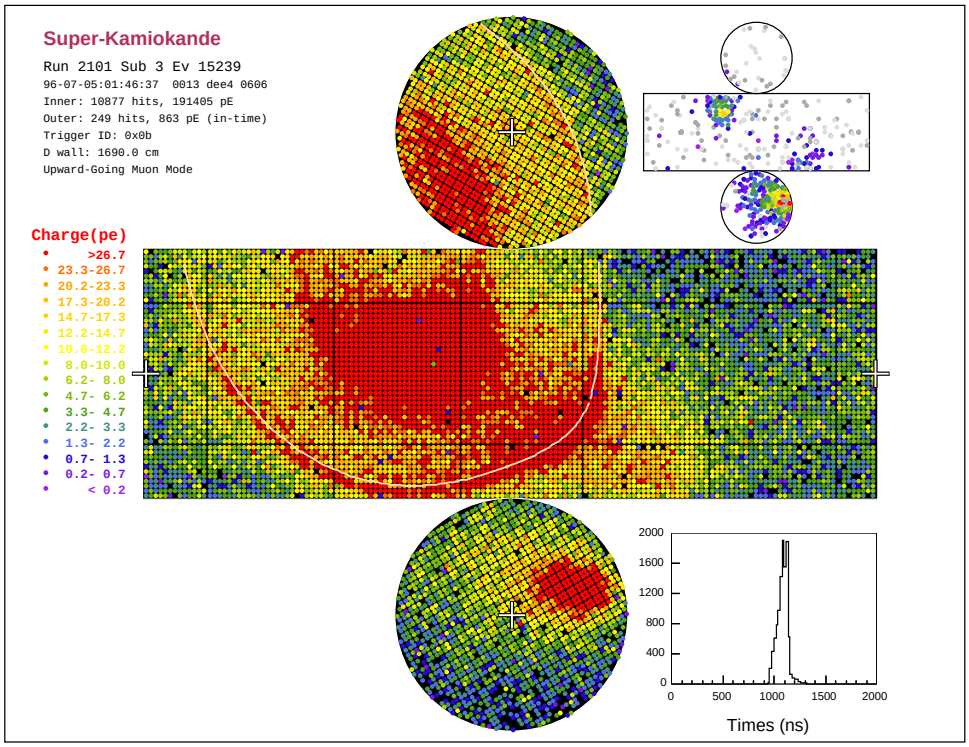

Figure 7.32: Event display of an upward showering muon.

Chapter 8

Conclusion

The phase-1 of Super–Kamiokande experiment operated from April 1996 to July 2001. It collected 1892 upward thrumuons and 467 upward stopping muons during this period with total livetime of 1680 days. The zenith angle distribution of upward thrugoing and stopping muons is consistent with $\nu_\mu \rightarrow \nu_\tau$ oscillations. A variety of astrophysical searches have also been done with the upward going muons such as searches for WIMP annihilations in the center of Earth, Sun and Galactic Center, diffuse flux from the galactic plane, as well as from transient sources such as GRBs and SGRs. No signals were seen. However the results from WIMP searches have enabled us to obtain stringent limits on annihilation rate as well as WIMP elastic scattering cross-sections. Our limits on WIMP-nucleon scalar couplings partially rule out some of the DAMA allowed region and the limits on WIMP-proton spin coupling are more sensitive than any direct detection experiment.

Also we have been able to isolate a sample of upward muons which loses energy through radiative processes. This sample is the highest neutrino energy dataset in Super–Kamiokande with mean neutrino energy of $\simeq 1$ TeV. At such high energies the neutrino oscillation probability is negligible and hence the zenith angle distribution

of this dataset should be consistent with null oscillation and this is observed. Finally an oscillation analysis is done by combining all the three categories of upward going muons. The combined flux of all the three categories of upward muons is consistent with oscillations. All the astrophysical searches were repeated with this sample, since the atmospheric neutrino background is reduced at these high energies. No signatures of astrophysical sources were seen in this dataset.

Currently Super-K-II is operating since January 2003 with reduced inner detector PMTs. It is continuing to record upward going muon data. All searches in this thesis will be continued with Super-K-II dataset. Unfortunately because we are background limited, the limits on WIMPs and other point sources can only grow as the square root of the exposure. If we are lucky we could detect a neutrino signals from transient sources such as gamma ray bursts. However the results of future generation of underwater/underice detectors with their large effective areas are anticipated with enthusiasm.

Appendix A

Description of Muon fitters

A.1 Stopmu1st

`Stopmu1st` is the first fitter used in the reduction chain. The main goal of this fitter is to classify the topology of the muon event using only the Outer-Detector information (OD) and pass the event to the next fitter. The charge cut as well as the selection of decay electron candidates takes place in this fitter.

`Stopmu1st` initially rejects any event which has the pedestal flag on or the inner detector or the Outer Detector off. `Stopmu1st` then checks if the previous saved event has been an upward stopping muon in order to save decay electron candidates. `Stopmu1st` then proceeds to classify the topology of the muon event. When a muon passes through the outer-detector all PMTs located close to each other have approximately the same timing and charge information. Using this physics motivation, `Stopmu1st` calls a clustering algorithm ``smfclustac'' (written by K. Kaneyuki) which counts such clusters of PMT's in OD which are closely spaced, hit around approximately the same time. The initial guesses for the PMTs around which the cluster is chosen is decided in order of decreasing PMT charge, i.e. `Smfclustac`

looks for the first cluster around the PMT with maximum charge and so on. A cluster around these maximum hit PMT's is selected if this PMT and at least 7 of its nearest neighbors satisfy both the conditions below :

- Charge of all PMTs in this cluster is greater than 8 pe
- The timings of all PMTs in this cluster fall within 500 to 1300 ns.

Once all such clusters have been counted, a check is done to ensure that the distance between the PMTs having maximum charge in each cluster is greater than 8 meters. If not, all such closely spaced clusters are counted as 1. If the total number of clusters found this way is greater than 2, the event is classified as a multiple-muon.

`Stopmu1st` then calls another algorithm "smftdistc" which looks at the number of OD hits within a time-window of width T_{wid} which is determined as follows : `Smftdistc` counts the number of OD hits in a sliding window of width 100 nanoseconds starting from 800 ns upto 1300 ns in steps of 1 ns. The first time this sliding window encounters number of hits greater than 15 is noted T_{start}. The time at which the number of hits falls below 15 is denoted as T_{end}. (If the number of hits never falls below 15 for the rest of the loop T_{end} is taken to be 1300 ns). Then it calculates T_{wid} where T_{wid} is given by :

$$T_{wid} = T_{end} - T_{start} \tag{A.1}$$

Thus T_{wid} roughly gives the total width of the time window when the number of OD hits is at least 15.

At this stage `Stopmu1st` is finished with both its clustering algorithms and classifies the muon event based on these results. If either the number of clusters found by smfclustac is equal to 2 or $T_{wid} > 260$ then `Stopmu1st` classifies the event as

No of tubes hit	Threshold Charge of selected ID PMT for first Cleaning Cut
> 10000 tubes	3.0 pe
$8000 - 10000$ tubes	2.5 pe
< 8000 tubes	2.0 pe

Table A.1: Number of tubes hit and the corresponding lower limit on the PMT charge of all selected tubes in `Muboy` for the first cleaning cut.

thrugoing. If neither of the above two criterion are satisfied the event gets classified as a stopping muon.

A.2 Muboy

This fitter is the heart of the upmu reduction and most background events are rejected after this fitter. Of all fitters used, this is the only one which gives a direction as well as a classification of the topology of the muon event. `Muboy` has been written by R. Svoboda, originally for fitting the muons which produce spallation products which are a source of background for low energy solar neutrino analysis. The same program has been used in the upmu reduction. However some changes had to be made to the original program to suit the needs of the upmu reduction. We shall discuss the main features of `Muboy` which are important for upward muon analysis. More details on `Muboy` can be found in Ref. [44]

`Muboy` mainly uses ID information. `Muboy` starts by making hierarchical sets of cleaning cuts for PMT selection as follows : Only those PMTs whose charge is greater than a certain threshold are selected. This threshold depends upon the number of hit PMTs (N_{hit}) in the event and is determined by the table A.1

At this stage `Muboy` makes its first guess for the exit point as the PMT which has the maximum charge and satisfies the first cleaning cut. `Muboy` counts the number

No of Tubes after first cut	Nearest neighbor cut
> 7500	5
$5000 - 7500$	4
$2500 - 5000$	3
$500 - 2500$	2
< 500 tubes	1

Table A.2: Lower limit on the number of nearest neighbors corresponding to the number of tubes selected after the first cleaning cut.

of nearest neighbors of each PMT (which satisfies the first cleaning cut) which have been hit within 10 ns window(N_{nn}). Then, `Muboy` makes its second cleaning cut and selects only those PMTs which have N_{nn} greater than a certain threshold which depends upon the number of tubes after the first cleaning cut as shown in Table A.2

`Muboy` now starts with the fitting. The initial guess for the entry point is made by selecting the earliest PMT which has at least 3 nearest neighbors hit within a 10 ns window. If no such PMT is found then the required condition for the number of nearest neighbors is reduced one at a time. The first guess for the direction is the vector from this entry point to the first guess exit point. If the exit point and the entry point are located close to each other then the charge-weighted center of mass of all remaining tubes is used as the first guess exit point.

`Muboy` then makes further causality cuts to get rid of hits produced by multiple muons and by scattered light. If the position/time of the entry point is known then no tube can get hit *earlier* than the muon travel time in water. However, if there are multiple muons then there can be many early hits. At the other extreme any PMT produced by direct light cannot be hit later than the travel time of light in water. `Muboy` counts the total number of PMTs (N_{early}) which have hit times less than than T_{early} where :

$$T_{early} = T_{ent} + \frac{D}{18} \tag{A.2}$$

where T_{ent} is the hit time of entry point PMT
and D is the distance from the entry point to the hit PMT. If $N_{early} > 45$ then the event is classified as a multiple muon-category-1 and all events of this category are treated separately to find their entry points and directions. We shall skip these details since we don't need the direction and entry point of the multiple muon events. This is discussed in greater detail in [44].

For all other events `Muboy` makes its third cleaning cut for rest of the analysis. Only those PMTs are chosen whose hit times are between T_{early} where T_{early} is defined in equation A.2 and T_{later} where:

$$T_{later} = T_{ent} + \frac{D}{34} \tag{A.3}$$

The rigorous direction fitting now begins. For a given muon track entry point and direction a PMT is considered to be in the Cherenkov cone if it satisfies at least one of the following two conditions :

- $\hat{d}.\vec{r} > 0.74$

  where $\hat{d}$ is a unit vector from entry point to the PMT and

  $\vec{r}$ is direction cosine of the muon track.

- Distance between the entry point and the PMT is less than 2m

The direction is jiggled around the first guess direction (without changing the location/time of the entry PMT) until the goodness of fit parameter is maximized.

This goodness of fit parameter is defined as follows:

$$G.O.F. = F(f_{frac}) = \sum_{i=1}^{N} g(\delta t_i), \tag{A.4}$$

where δt_i is the timing residual between the expected and measured PMT times for

a given muon track and direction and f_{frac} which is the ratio of number of PMTs in the Cherenkov cone to the total selected PMTs. The function $F(f_{frac})$ is defined as follows :

$$\begin{aligned} &\text{if } f_{frac} < 0.75 \quad \text{then} \qquad F(f_{frac}) = f_{frac}\frac{0.9}{C_{cut}} \\ &\text{if } f_{frac} > 0.75 \quad \text{then} \quad F(f_{frac}) = \frac{0.1 f_{frac} + 0.9 - C_{cut}}{1 - C_{cut}}, \end{aligned} \tag{A.5}$$

where $C_{cut} = 0.74$ The function $g(\delta t_i)$ is defined as follows:

$$\begin{aligned} \text{if } \delta t_i < 0 \text{ or } q_i > 30pe \quad & g(\delta t_i) = exp\left[-\frac{(\delta t_i - t_{mean}(q_i))^2}{2\sigma(q_i)^2}\right] \\ \text{if } \delta t_i > 0 \qquad\qquad\quad & g(\delta t_i) = exp\left[-\frac{\delta t_i}{\lambda(q_i)}\right], \end{aligned} \tag{A.6}$$

The direction is jiggled around the 1st guess direction while keeping the entry point PMT fixed until GOF is maximized. Once a best fit-direction is found then the second set of jiggling operations begins for all events other than multi-muon-1 and this time both the direction and the entry point PMT are varied. These are chosen from hits which occur within a 26.7 ns timing window around the track. The goodness of fit is again calculated with C_{cut} in Eqn.A.5 replaced by 0.65. The number of PMTs with $\delta t_i - t_{mean}(q_i) > 250$ ns are counted and if this number is greater than 35 the muon is labeled as multi-muon-2. Any other event is now classified as thrugoing muon.

At each trial direction `Muboy` also calculates another goodness parameter which is used by the upmu reduction in assessing the quality of the fit. This goodness (f_{cone}) is defined as follows:

$$f_{cone} = \frac{\sum q_i}{\sum Q} \tag{A.7}$$

where the numerator extends over all PMTs in Cherenkov cone and the denominator is over sum of all charges after the 3 sets of cleaning cuts. At this stage the muon

entry point and direction is finalized. During the rest of the algorithm `Muboy` now classifies the topology of the tagged event.

All thrugoing muons which have the total number of hit PMT's less than 2000 are examined to check if they are corner-clippers. These are muon events which scrape the edges of the ID and hence have very short path-lengths. If a muon enters near the top corner and if

$$\left(\frac{X_{ent}.cos(\theta_x) + Y_{ent}.cos(\theta_y)}{\sqrt{X_{ent}^2 + Y_{ent}^2}} > 0.05 \right)$$

the event is classified as a corner clipper. Alternately if the muon enters near the bottom corner and the distance between the entry point and the PMT with maximum charge is less than 4m, then this event is classified as a corner-clipper.

`Muboy` then looks for stopping muons among the remaining events. Stopping muons are recognized by looking at the number of photo-electrons produced within 2 meters(Q_{id}) of the projected exit point in the ID and also the number of photo-electrons within 4 meters of the projected exit point in the OD (Q_{od}). An event is classified as stopping if it satisfies at least one of the following conditions:

- $Q_{id} < 200$ pe
- $Q_{id} < 400$pe & $Q_{od} < 30$ pe
- $Q_{od} > 30$pe & $Q_{id} < 150$ pe
- No OD data available & $Q_{id} < 150$ pe

`Muboy` now proceeds to calculate the length of stopping muons. This is determined by constructing a dE/dX histogram of the observed energy loss by the muon. If at any stage the number of photo-electrons in a one-meter interval is less than 40% of

the average value over the first 1.5 meter of track and if this point is greater than the peak position of the dE/dX histogram then this point is considered to be the stopping point. This is shown in Figure A.1.

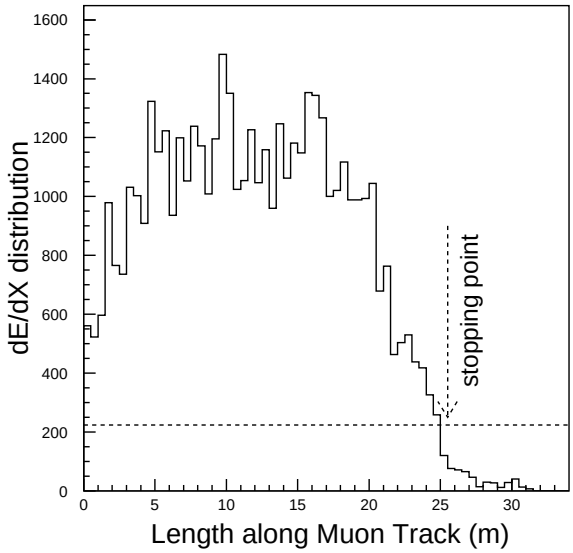

Figure A.1: Length determination in muboy for a stopping muon. The histogram shows the $\frac{dE}{dX}$ distribution for a stopping muon. the dashed line indicates the $\left(\frac{dE}{dX}\right)_{cutoff}$ and the first bin with a value lower than this is chosen to be the length of the stopping muon

Thus `Muboy` is finished. What `Muboy` calculates for each muon event is its entry point and direction, its topology (whether it is a thrugoing,stopping, multiple muon-1,multiple-muon-2 or corner-clipper) and two goodness of fits (GOF and f_{cone}). which indicates the quality of the fit. Distribution of both GOF and f_{cone} for events for which `Muboy` gave good fits from one run can be found in Figure A.2

A.3 Stopmu2nd

`Stopmu2nd` is designed to efficiently fit stopping muons and is run on only those

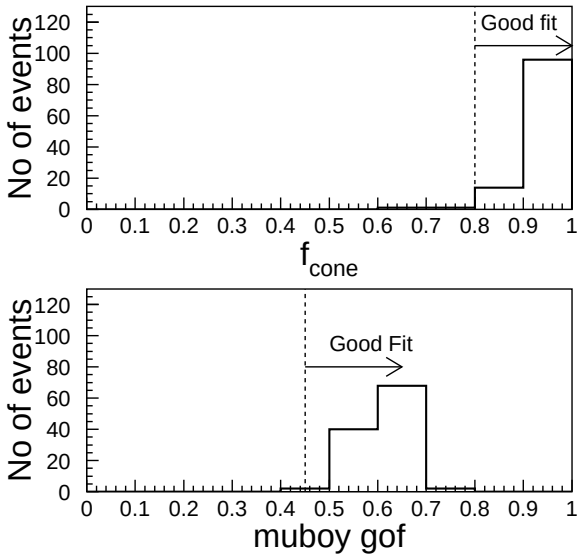

Figure A.2: Distribution of the two goodness variables used in `Muboy` for horizontal muon events which were classified as both thrugoing and stopping for which muboy gave good fits. For all events in this plot the fit was considered "good fit" when the hand-fit direction agreed with the muboy direction within $\simeq 2^{\circ}$. The vertical line represents the threshold values for the two goodnesses used in the reduction for the fit to be considered good.

events which are classified as stoppers either by `Muboy` or `Stopmu1st`.

It starts by locating the 5 earliest hit PMTs with charge greater than 4 pe which has at least 2 neighboring PMT's hit within a 5 ns window and with a minimum charge of 4 pe. The PMT which has the maximum charge among these 5 and whose time is within 5 ns of the first PMT is selected as the initial entry point. If any two PMTs have equal charge then the PMT which has more neighbors hit within 5 ns is chosen as the initial entry point. The initial exit point is taken to be the charge-weighted center of mass of all PMTs with charge greater than 0.5 pe.

With these as initial guesses for the starting and exit points, `Stopmu1st` calculates

the two goodness parameters called R_{cone} which is defined as follows:

$$R_{cone} = 1 - \frac{N_{hit42}}{N_{pmt42}} + \frac{N_{hit70}}{N_{pmt70}} \tag{A.8}$$

where N_{hit42} is the number of PMTs with charge greater than 5 pe in a Cherenkov cone with half angle 42°,

where N_{pmt42} is the total number of PMTs in a Cherenkov cone with half angle 42°,

N_{hit70} is the number of PMTs with charge greater than 7 pe in a Cherenkov cone between 45 and 70°,

N_{pmt70} is the total number of PMTs in a Cherenkov cone between 45 and 70°

The term $\frac{N_{hit42}}{N_{pmt42}}$ indicates how filled the Cherenkov cone is and the term $\frac{N_{hit70}}{N_{pmt70}}$ indicates the sharpness of the edge of the Cherenkov ring. A rough sketch of R_{cone} is shown in Fig. A.3. `Stopmu2nd` now begins a more precise reconstruction by a grid

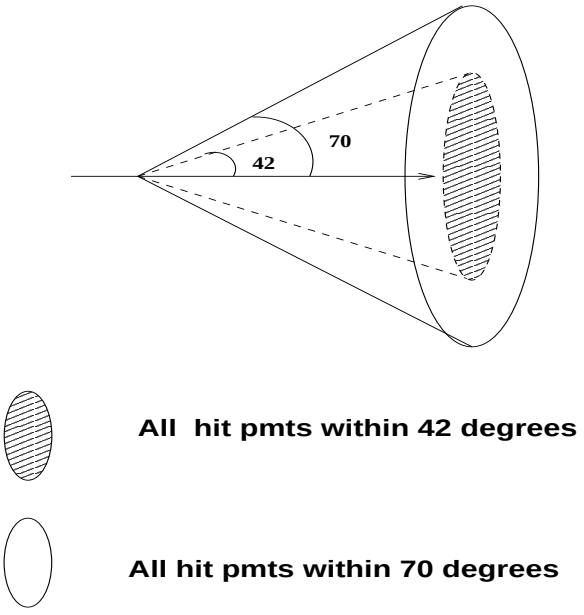

Figure A.3: Schematic view of the goodness variable R_{cone}

search by keeping the entrance point fixed and varying the muon track direction until the following goodness of fit is maximized.

$$stopmu2ndgof = \frac{1}{\sum_{i=1}^{N} \frac{1}{\sigma^2}} \sum_{i=1}^{N} \frac{1}{\sigma^2} exp\left[-0.5\left(\frac{t_i - T_{ent}}{1.5\sigma_i}\right)^2\right] \tag{A.9}$$

where T_{ent} is the hit time of entry ID PMT, σ_i is the timing resolution which is chosen to be 3 ns for all PMTs and t_i is given by :

$$t_i = T_i - \frac{d_{mu}}{c} - \frac{d_{ph}}{c/n} \tag{A.10}$$

where c is the speed of light in vacuum, n is the refractive index of water, d_{mu} is the distance between the muon entry point and the point along the muon track where photon is emitted to a given PMT, and d_{ph} the distance traveled by photon from the emission point along the muon track to a given PMT. The sum is taken over all PMTs for which $\frac{l}{3} < d_{ph} < l$, where l is the length of the trial muon track inside the ID. A schematic view of the variables used for calculating $stopmu2ndgof$ is shown in Fig. A.4.

After the muon direction has been finalized using the above method the function R_{cone} is recalculated using Eqn. A.8 with the final fit. Thus at the end, `Stopmu2nd` returns the muon entry point, direction, and two goodness values R_{cone} and $stopmu2ndgof$. The distribution of $stopmu2ndgof$ and R_{cone} for events in which the fit was good is shown in Figure A.5

A.4 Thrumu1st

`Thrumu1st` is specialized to quickly fit through-going muons and is more likely to

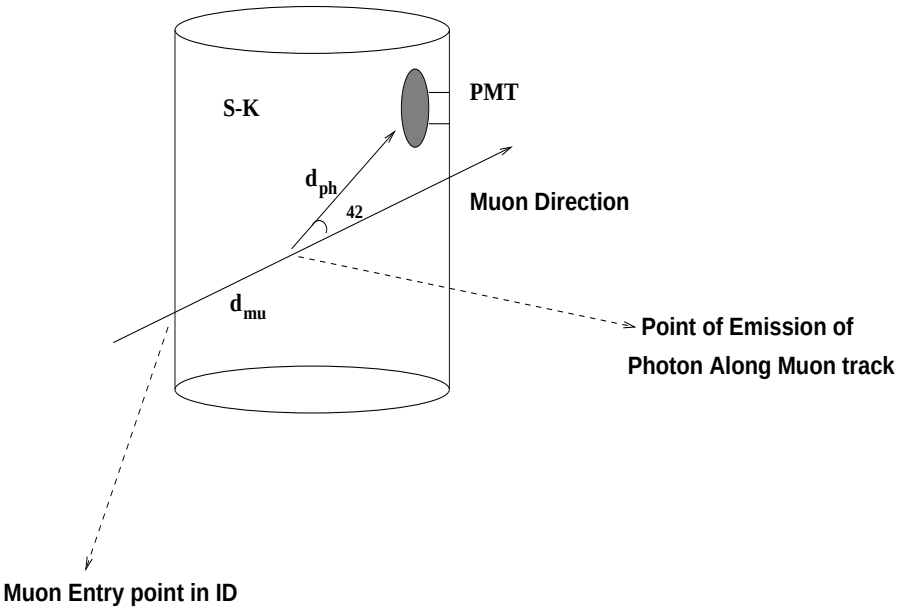

Figure A.4: Schematic view of the variables used for calculating *stopmu2ndgof*

return misfits. The main features of this algorithm are similar to `Stopmu2nd`. The first guess for the entry point is exactly the same as in `Stopmu2nd`. The first guess for the exit point is given by the charge weighted center of mass of all PMTs with charge greater than 231 pe.

Once the initial guess has been made for the entry and exit points thrumu1st counts the number of PMTs ($N_{entge300}$) whose total charge > 231 pe and are located at more than 3 meters from the entry point. It also counts the list of PMTs among the above $N_{entge300}$ PMTs which are located at less than 3 m from the exit point ($N_{exitle300}$). If either $N_{entge300} = 0$ or $N_{exitle300} = 0$ then the exit point is evaluated using the same precise grid search method used in `Stopmu2nd` by maximizing equation A.9, except that the sum is carried over all PMTs for which $D_{ph} > l$ for the case $N_{entge300} = 0$ and $D_{ph} > l/2$ for the case $N_{exitle300} = 0$.

With this as final fit, `Thrumu1st` calculates the minimum distance between the entry point and PMTs with total charge greater than 231 pe. If this distance is less

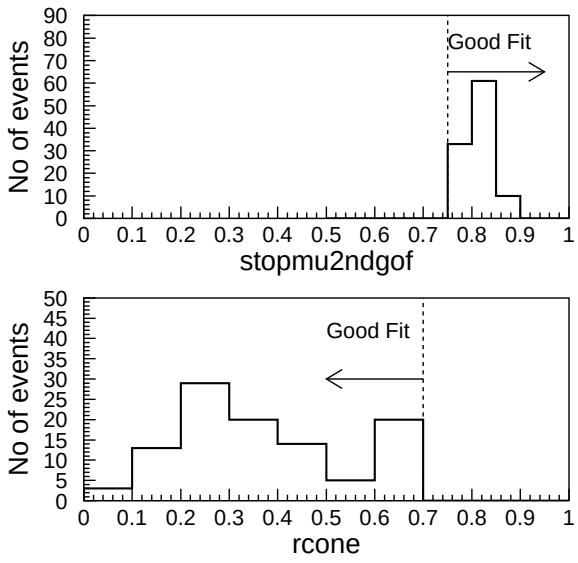

Figure A.5: Distribution of stopmu2ndgof (top panel) and R_{cone} (lower panel) in `Stopmu2nd` for horizontal stopping muon events in which the fit was considered good (using the same criterion as in Fig A.2). The vertical lines represents the threshold values for the `Stopmu2nd` fit to be considered good.

than 300 m and goodness is greater than 0.88 then the value of muyn is taken to be 1. `Thrumu1st` then calculates the goodness value R_{cone} using equation A.8. Distribution of R_{cone} for good `Thrumu1st` fits can be found in Fig. A.6

A.5 Fstmu

`Fstmu` is also specialized to quickly fit thrugoing muons like thrumu2nd. `Fstmu` initially makes cleaning cuts to get rid of dark noise hit PMTs and selects only those PMTs (N_{fstmu}) which have at least 1 nearest neighbor hit within 4 ns. `Fstmu` then selects the earliest 20 PMTs hit among these clean tubes. Among these 20 tubes `Fstmu` then looks for clusters of PMTs (minimum number of 4 tubes required for a cluster) which are all hit within 50 ns and such that the charge of each PMT in the

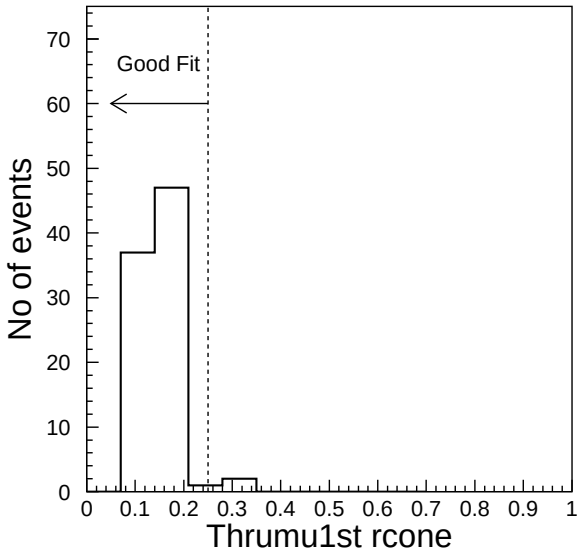

Figure A.6: Distribution of R_{cone} used in `Thrumu1st` for events for which it gave good fits (using the same criterion as in Fig A.2). The vertical line represents the threshold value for R_{cone} for the fit to be considered a good one.

cluster $< 1.15\ q_0 + 1.0$ where q_0 is the charge of the PMT around which the cluster is made. Once such clusters of PMTs have been found then the cluster with the largest PMTs is chosen and the cluster position and time is given by average of the positions and times of all PMTs in this cluster. Then, `Fstmu` selects all PMTs which were hit earlier than this average time. The muon entry point and time is given by the average position and time of these early hits. This finishes selection of the entry point.

A similar procedure is followed to select the exit point. `Fstmu` selects 50 PMTs with maximum charge among the list of clean PMTs used in the analysis. It then looks for clusters of PMTs around these 50 PMTs. Then for each cluster all PMTs with more charge than the average charge of this cluster are selected. Then from this list fstmu locates the PMT which is farthest from the entry point and calculates its

distance (D_{max}). `Fstmu` filters out all PMTs whose distance from the entry point is less than $\sqrt{D_{max}^2 - 2 * 141.4 * D_{max}}$ The trial exit points corresponding to each cluster is obtained by the charge weighted average position and time of these remaining PMTs. The speed of muon from the entry point to each of these trial exit point is calculated. `Fstmu` then finds the minimum deviation of each of these muon speeds from the speed of light. If the smallest deviation $> 0.2 \times c$ then the trial exit point for which muon speed is closest to speed of light is chosen as the final exit point. Else the trial exit point with the maximum distance from the initial entry point is chosen as the final exit point. The track fitting is now finished. `Fstmu` calculates a goodness which is calculated as follows

$$G = \left[\sum_{i=1}^{N_{fstmu}} q_i t_i \right] / \left[\sum_{i=1}^{N_{fstmu}} q_i - 1 \right] \tag{A.11}$$

where t_i is the timing residual and is given in Eqn A.10. Distribution of `Fstmu` goodness for events in which the fit was considered good is shown in Figure A.7.

A.6 Thrumu2nd

`Thrumu2nd` is specialized to fit multiple muons and Bremsstrahlung muon events. To make the entry point selection thrumu2nd selects only PMTs with total charge between 5 and 150 pe and the initial entry point is given by the average position of all PMTs from this list which have at least 3 PMTs from the above list within 1.5 m.

Similarly to make the exit point selection `Thrumu2nd` selects only PMTs with total charge greater than 150 pe and the initial exit point is the average position of all PMTs from this list which have at least 3 PMTs from the above list within 2 m.

To find the entry time the PMT closest to the position of the entry point is

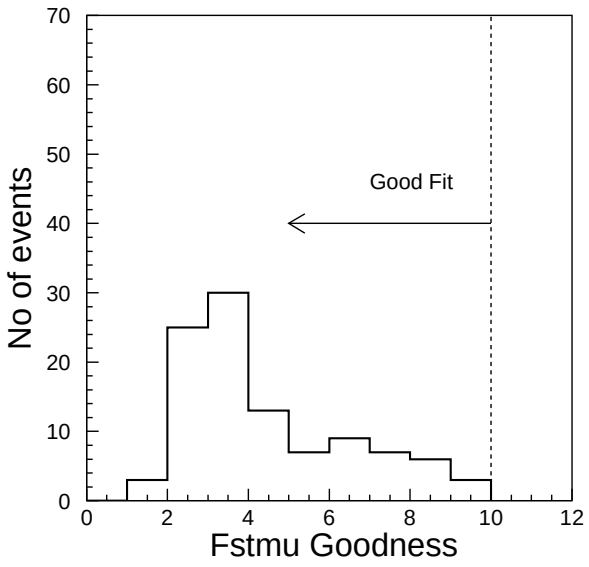

Figure A.7: Distribution of `Fstmu` goodness for horizontal thrugoing events for which it gave good fits (using same criterion as in Fig A.2). The vertical line represents the threshold goodness value where the fit was considered good

found and the entry time is given by the average time of this PMT and all its nearest neighbors which are hit between 100 and 1200 ns. `Thrumu2nd` calculates three goodness values $tofsgm$, $rtofsgm$, and $rcone$. The goodness parameter $rcone$ is defined in the same way as in equation A.8 To calculate the two other two goodness parameters it first sets up a histogram of the timing residuals of all PMTs which are between -150 ns and 50 ns with bin size of 1 ns and finds the time where peak occurs(t_{peak}) and the the value of this peak N_{peak}. `Thrumu2nd` calculates sigm1 which is :

$$sigm1 = \frac{t_{peak} - t_{earliest}}{2.146} \tag{A.12}$$

where $t_{earliest}$ is the value of the earliest time bin as compared to t_{peak} which has less than $0.1N_{peak}$.

Similarly another quantity sigma2 is calculated which is

$$sigm2 = \frac{t_{peak} - t_{latest}}{2.146} \tag{A.13}$$

where t_{latest} is the value of the latest time bin as compared to t_{peak}which has less than $0.1N_{peak}$ is earliest as compared to t_{peak}. tofsgm is given by the average of sigm1 and sigm2 which are calculated in equations A.12 and A.13.

Another goodness value returned by thrumu2nd is given by

$$rtofsgm = 1 - \frac{\sum_{t=t_{peak}-10}^{t=t_{peak}+10} N(t)}{N_{tot}} \tag{A.14}$$

where N(t) represents values of the residual time histograms and N_{tot} is the sum of all values used in the histogram.

The distribution of $rcone$ and $tofsgm$ in `Thrumu1st` can be found in Figure A.8

A.7 NNfit

`Nnfit` is a fitter which is specialized for fitting Bremsstrahlung muons and was written by S. Matsuno. This fitter is optimized for events with total charge exceeding 50000 pe.

This algorithm starts by dividing the detector into patches which consist of 5 tubes/supermodule or 3 × 3 square. The wall of the detector is divided into 850 equi-area circular patches and the top and bottom of the detector is divided into 256 equi-area square patches. The nearest patch corresponding to each tube is found and the number of tubes in each patch is found. Next all patches are searched for PMTs which have charge greater than a certain threshold (which is described in Table A.3)

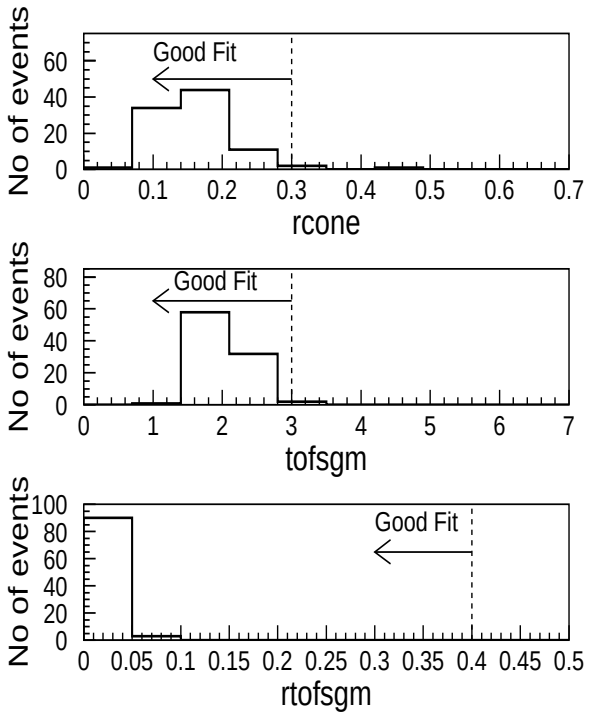

Figure A.8: Distribution of R_{cone} tofsgm and rtofsgm used in `Thrumu2nd` for horizontal through-going muons for which it gave good fits (determined using same criterion as in Fig. A.2). The vertical lines represents the threshold goodness values at which the `Thrumu2nd` fit is considered good when the direction was horizontal.

depending upon the total charge in the event. The number of patches which have at least one such hit are counted ($N_{fitpatches}$) and the number of tube hits in each patch (N_{hit}) are counted.

Then further cleaning cuts are done on tubes used in each patch. All tubes in a given patch with charge greater than 350 pe or with time less than T_{cut} (which is described in Table A.4) are subtracted from N_{hits}.

Also tubes which are hit outside a 10ns window from the median tube in the patch (when arranged in increasing order of hit time) are subtracted from N_{hits}. After this additional cleaning cuts if $N_{hits} < 5$ then this patch is not used for rest of the fitting.

Total Charge	Threshold Charge of selected ID PMT
< 25000 pe	$\frac{2Q}{N_{hits}}$
$25000 - 50000$ pe	$\frac{1.7Q}{N_{hits}}$
< 100000 pe	$\frac{1.4Q}{N_{hits}/1.4}$
$100000 - 250000$ pe	$\frac{1.2Q}{N_{hits}}$
> 100000 pe	$\frac{Q}{N_{hits}}$

Table A.3: Threshold charge cut of each used PMT in `NNfit`. In the second column Q is the total charge in the event and N_{hits} is the total number of tubes hit in the event

Total charge	T_{cut}
< 500000	$T\ (N_{hits}/300)$
$500000 - 1000000$	$T\ (N_{hits}/200)$
> 100000	$T\ (N_{hits}/100)$

Table A.4: Threshold time cut T_{cut} for each tube in a patch. The second column indicates the time of the PMT used (when arranged in increasing order of hit time) as the threshold T_{cut} value.

`NNfit` fits a plane-wave normal to all patches. `NNfit` then starts the fitting procedure on each of the clean patches For each patch which will be used, `Nnfit` constructs a matrix defined as:

$$A = \begin{bmatrix} \frac{\sum_{i=1}^{N} dx^2}{N} & \frac{\sum_{i=1}^{N} dxdy}{N} & \frac{\sum_{i=1}^{N} dx}{N} \\ \frac{\sum_{i=1}^{N} dxdy}{N} & \frac{\sum_{i=1}^{N} dy^2}{N} & \frac{\sum_{i=1}^{N} dy}{N} \\ \frac{\sum_{i=1}^{N} dx}{N} & \frac{\sum_{i=1}^{N} dy}{N} & 1 \end{bmatrix} \tag{A.15}$$

where dx= difference in x-coordinate of each tube in patch from x co-ordinate of patch-center in decimeter; dy = difference in y-coordinate of each tube in patch from y co-ordinate of patch-center in decimeter; N = No of tubes in each patch.

Only those patches for which the determinant of the above matrix is greater than 0.2 are used for rest of the analysis and the total number of these patches is noted

$N_{fitpatches}$. Then `Nnfit` calculates:

$$\begin{bmatrix} \frac{vx}{c_w} \\ \frac{vy}{c_w} \\ t_0 - 1000 \end{bmatrix} = A^{-1} \begin{bmatrix} \frac{\sum_{i=1}^{N} dtdx}{N} \\ \frac{\sum_{i=1}^{N} dtdy}{N} \\ \frac{\sum_{i=1}^{N} dt}{N} \end{bmatrix} \tag{A.16}$$

where dt = Time of each PMT in the patch minus 1000 ns and c_w is the speed of light in water, the matrix A is calculated in Eqn A.15.

The actual fitting procedure now starts. The initial track is chosen to pass through the center of all the patches which pass all cleaning cuts and track direction is chosen by varying the zenith and azimuth angles uniformly between 0 to 90° and 0 to 180° respectively. A χ^2 is calculated for each of the above tracks where

$$\chi^2 = \sum_{i=1}^{N_{fitpatches}} \frac{N_{hits} x}{9} \left(t_0 - t_{res} - t_{ent}\right)^2 \tag{A.17}$$

The sum extends over all patches defined and t_{res} is the timing residual and is given in equation A.10; $x = 1$ for all patches in Cherenkov cone and 100 otherwise; t_0 is obtained from equation A.16 and t_{ent} is given by

$$t_{ent} = \frac{1}{N_{fitpatches}} \sum_{i=1}^{N_{fitpatches}} \left(t_0 - t_{res}\right) \tag{A.18}$$

With these initial directions the minimum χ^2 is found and this entry point and direction with this minimum χ^2 is taken as the initial guess for the second round of chi-square minimization iterations. This is done with a gradient search method by varying the entry point (and finding the best fit direction for each entry point using the same method as in the first round of iterations) until we approach the minima of

the chi-square functional where the derivative becomes 0. This is taken as the best fit entry point and direction. The `Nnfit` goodness is given by:

$$nnfitgof = \frac{90(N_{fitpatches} - 6)}{\chi^2} \tag{A.19}$$

where χ^2 is defined in equation A.17. This finishes `Nnfit` and it returns a goodness value and track-direction. The distribution of `Nnfit` goodness for events where the fit was good is shown in Fig. A.9

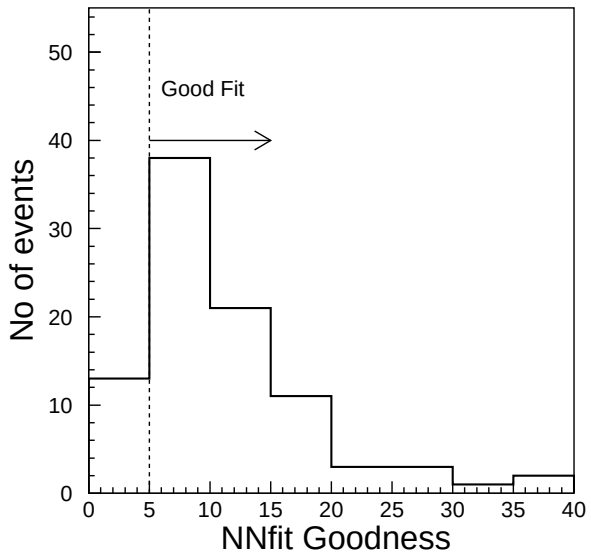

Figure A.9: Distribution of `NNfit` goodness for horizontal through-going muons in which fit is good (determined using same criterion as in Fig. A.2). The vertical lines represents the threshold value for the `Nnfit` goodness at which the fit is considered good.

Bibliography

[1] E.Bugaev *et al.*, Physical Review, **D58**, 54001 (2001)

[2] B.V. Achar *et al.*, Physics Letters, **18**, 196 (1965)

[3] F.Reines *et al.*, Physical Review Letters, **15**, 429 (1965)

[4] T.K. Gaisser, hep-ph/0209195 (2002)

[5] Y.Fukuda *et al*, Super-Kamiokande Collaboration, Physical Review Letters, **81**, 1562 (1998)

[6] M Messier, *Evidence for Neutrino Mass From Observations of Atmospheric Neutrinos with Super–Kamiokande*, Ph.D. Thesis, Boston University, (1999)

[7] Q.R. Ahmad *et al*, SNO Collaboration, Physical Review Letters, **89**, 011301 (2002)
Q.R. Ahmad *et al*, SNO Collaboration, Physical Review Letters, **87**,071301 (2001)

[8] S. Fukuda *et al*, Super-Kamiokande Collaboration, Physics Letters, **B539**, 179 (2002)

[9] K. Eguchi *et al*, Kamland Collaboration, Physical Review Letters, **90**, 021802 (2003)

[10] M.A. Ahn *et al*, K2K Collaboration, Physical Review Letters, **90**, 041801 (2003)

[11] M.C. Gonzalez-Garcia and Y. Nir, Reviews of Modern Physics, **75**, 345 (2002)

[12] M. Fukugita and T. Yanagida, Physics Letters, **B174**, 45 (1986)

[13] R.A. Alpher, J.W. Follin, and R.C. Hermann, Physical Review, **92**, 1347 (1953)

[14] J. Primack, astro-ph/0007187 (2000)

[15] H. Lipkin, hep-ph/9901399 (1999)

[16] A.B. Mcdonald *et al.*, astro-ph/0311343 (2003)

[17] D.N. Spergel *et. al.*, WMAP Collaboration, Astrophysical Journal Supplement, **148**, 175 (2003)

[18] J.H. Taylor, Reviews of Modern Physics, **66**, 711 (1994)

[19] I. Stairs, Living Reviews in Relativity, **6**, 5 (2003)

[20] J.N. Bahcall and Raymond Davis , Publications of Astronomical Society of Pacific, **112**, 429 (2000)

[21] R. Bionta *et al.*, Physical Review Letters, **58**, 1494 (1987)

[22] K.Hirata *et al.*, Physical Review Letters, **58**, 1490 (1987)

[23] V. Trimble, Reviews of Modern Physics, **60**, 859 (1988)

[24] M. Malek *et al.*, Super-Kamiokande Collaboration, Physical Review Letters, **90**, 061101 (2003)

[25] M. Fukugita and M Kawasaki, Monthly Notices of Royal Astronomical Society, **340**, L7 (2003)

[26] C. Spiering, Journal of Physics, **G29**, 843 (2003)

[27] F. Halzen and D. Hooper, Reports of Progress in Physics, **65**, 1025 (2002)

[28] M.S. Turner, International Journal of Modern Physics, **A17**, 180 (2002)

[29] J. Edsjo and P. Gondolo, Physics Letters, **B357**, 595 (1995)

[30] J.Rich, Astroparticle Physics, **4**, 387 (1996)

[31] A. Gould, Astrophysical Journal, **388**, 338 (1992)

[32] S.Fukuda *et al.*, Super-Kamiokande Collaboration, Physical Review Letters, **85**, 3999 (2000)

[33] Super-Kamiokande Collaboration, Nuclear Instruments and Methods, **501A**, 418 (2003).

[34] L. D. Landau and E. M. Lifshitz, *Classical Theory of Fields*, London Addison-Wesley (1962).

[35] H. Kume *et al.*, Nuclear Instruments and Methods, **A329**, 299 (1993).

[36] R. Claus *et al.*, Nuclear Instruments Methods in Physics Research, **A261**, 540 (1987);

[37] T. Tanimori *et al.*, IEEE Transactions on Nuclear Science **36**, 497 (1989).

[38] M Earl, *A Search For Nucleon Decay Into Modes Favored By SuperSymmetry Using Super–Kamiokande* Ph.D. Thesis, Boston U., (2000)

[39] J.S. George, *Experimental Study of the Atmospheric ν_μ/ν_e Ratio in the Multi-GeV Energy Range*, Ph.D. Thesis, U. Washington, (1998)

[40] M.Shiozawa, *A Search for Proton Decay $p \to e^+ + \pi^0$ in a Large Water Cherenkov Detector*, PhD Thesis, University of Tokyo, Nov. 1999

[41] http://tdserver1.fnal.gov/foster/BooNE_Photomultiplier_Implosion.pdf

[42] http://www-sk.icrr.u-tokyo.ac.jp/cause-committee/index-e.html
(Partial English translations of reports are available at http://nngroup.physics.sunysb.edu/)

[43] MACRO Collaboration, M. Ambrosio *et al.*, Astroparticle Physics, **9**, 105 (1998)

[44] Zoa Conner, *A Study of Solar Neutrinos using the Super–Kamiokande Detector* Ph.D. Thesis, University of Maryland, (1997)

[45] W. Lohmann, R. Kopp and R. Voss, CERN yellow report 85-03, (1985)

[46] *Study of $\nu_\mu -> \nu_\tau$ and $\nu_\mu -> \nu_{sterile}$ Neutrino Oscillations with Atmospheric Neutrino Data in Super–Kamiokande* K. Ishihara, Ph.D. Thesis, University of Tokyo, (1999)

[47] K. Nitta, *Neutrino Oscillation Analysis of Upward Through-going and Stopping Muons in Super–Kamiokande* Ph.D. Thesis, Osaka University (2003)

[48] K. McConnell *A search for ultra high energy neutrinos from extra-galactic sources* S.B. Thesis, Massachusetts Institute of Technology (2002)

[49] D. Casper, Nuclear Physics Proceedings Supplement **112**, 161 (2002)

[50] M.Honda *et. al.*, Physical Review **D52**, 4985 (1995)

[51] V. Agrawal *et. al.*, Physical Review **D53**, 1313 (1996)

[52] G. Battistoni *et. al.*, Astroparticle Physics, **19**, 269 (2003)

[53] T.K. Gaisser and M. Honda, Annual Review of Nuclear and Particle Science, **52**, 153 (2002)

[54] M. Glück, E. Reya, and A. Vogt, Z. Physics **C67**, 433 (1995)

[55] P. Lipari and T. Stanev, Physical Review **D44**, 3543 (1991)

[56] T.K. Gaisser, *Cosmic Rays and Particle Physics*, Cambridge University Press (1990)

[57] Y.Fukuda *et al*, Super-Kamiokande Collaboration, Physical Review Letters, **82**, 2644 (1998)

[58] Y.Fukuda *et al*, Super-Kamiokande Collaboration, Physics Letters, **B467**, 185 (1999)

[59] K. G. Begeman *et. al*, Monthly Notices of Royal Astronomical Society, **249**, 523 (1991)

[60] T. Sakamoto, M. Chiba and T.C. Beers, Astronomy and Astophysics, **397**, 899 (2003)

[61] J. Navarro, C.S. Frenk, and S.D.M. White, Astrophysical Journal, **462**, 563 (1996)

[62] C. Alcock *et al* MACHO Collaboration, Astrophysical Journal, **550**, L169 (2001)

[63] S. Burles, K.M. Nollett, and M.S. Turner, Astrophysical Journal, **552**, L1 (2001)

[64] S.D.M White, C. S. Frenk, and M. Davis, Astrophysical Journal, **274**, L1 (1983)

[65] J. Primack and M.K. Gross, astro-ph/0007165 (2000)

[66] S Tremaine and J.E. Gunn, Physical Review Letters, **42**, 407 (1979)

[67] E.W. Kolb and M.S Turner, *The Early Universe*, Addison-Wesley , Redwood City (1990)

[68] P. Gondolo and G. Gelmini, Nuclear Physics, **B360**, 145 (1991)

[69] S. Perlmutter *et. al.*, Astrophysical Journal, **517**, 565 (1999)

[70] B.W. Lee and S. Weinberg, Physical Review Letters, **39**, 165 (1977)

[71] M. Kamionkowski, hep-ph/9609531 (1996)

[72] D. Caldwell *et al*, Physical Review Letters, **65**, 510 (1988)

[73] K. Griest and J. Silk, Nature, **343**, 26 (1990); L.M. Krauss, Physical Review Letters, **65**, 510 (1988)

[74] M. Mori *et al*, Kamiokande Collaboration, Physics Letters, **B289**, 463 (1992)

[75] H.E. Haber and G.L. Kane, Physics Reports, **117**, 75 (1985)

[76] S.L. Glashow, Nuclear Physics, **22**, 579 (1961); A. Salam and J.C. Ward, Physics Letters, **13**, 168 (1964); S. Weinberg, Physical Review Letters, **19**, 1264 (1967).

[77] E. Witten Physics Letters, **B105**, 267 (1981)

[78] F. Wilczek, Nuclear Physics Proceedings Supplement, **117**, 410 (2003)

[79] H. Goldberg, Physical Review Letters, **50**, 1419 (1983)

[80] J. Ellis *et. el.*, Nuclear Physics, **B238**, 453 (1984)

[81] G. Jungman, M. Kamionkowski, and K. Griest, Physics Reports, **267**, 195 (1996)

[82] J. Edsjö, *Aspects of Neutrino Detection of Neutralino Dark Matter.* PhD Thesis, Uppsala University, Sweden (1997)

[83] L. Girardello and M.T. Grisaru, Nuclear Physics, **B194**, 65 (1982)

[84] T. Falk, K.A. Olive and M. Srednicki, Physics Letters, **B339**, 248 (1994)

[85] T. Hebbeker, Physics Letters, **B470**, 259 (1999)

[86] D. Hooper and T Plehn, Physics Letters, **B562**, 18 (2003)

[87] J. Edsjö and P. Gondolo, Physical Review, **D56**, 1879 (1997)

[88] M. Goodman and E. Witten, Physical Review, **D31**, 3059 (1985)

[89] A. Gould, private communication

[90] A. Gould, Astrophysical Journal, **321**, 571 (1987)

[91] A. Gould, Astrophysical Journal, **388**, 338 (1991)

[92] M. Kamionkowski, Physical Review, **D44**, 3021 (1991)

[93] D. Anderson *Theory of the Earth*, Blackwell Scientific Publications (1989)

[94] G. Jungman and M. Kamionkowski, Physical Review, **D51**, 328 (1995)

[95] L. Bergstrom, J. Edsjo,and P. Gondolo, Physical Review, **D55**, 1765 (1997)

[96] L. Bergstrom, J. Edsjo, and P. Gondolo, Physical Review, **D58**, 103519 (1998)

[97] A Bottino *et. al.*, Astroparticle Physics, **3**, 63 (1995)

[98] S. Ritz and D.Seckel, Nuclear Physics, **B304**, 877 (1988)

[99] V. Berezinsky *et. al.*, Astroparticle Physics, **5**, 333 (1996)

[100] J. Edsjö, *Neutrino-Induced Muon fluxes From Neutralino Annihilations in the Earth and the Sun* Diploma Thesis, Uppsala University, Sweden (1993)

[101] P.Gondolo and J. Silk, Physical Review Letters, **83**, 1719 (1999)

[102] A.M. Ghez *et. al.*, Nature, **407**, 349 (2000)

[103] J. Binney and S. Tremaine, *Galactic Dynamics* , Princeton University Press, (1987)

[104] Kamiokande Collaboration, M. Mori *et al.*, Physical Review, **D48**, 5505 (1993)

[105] MACRO Collaboration, M. Ambrosio *et al.*, Physical Review, **D60**, 082002 (1999).

[106] D. Seckel, T. Stanev, and T.K. Gaisser, Astrophysical Journal, **382**, 652 (1991)

[107] Baksan Collaboration, M.M. Boliev*et al.*, Nuclear Physics (Proceedings Suppl), **B48**, 83 (1996)

[108] IMB Collaboration, J.M. LoSecco *et al.*, Physics Letters, **B188**, 388 (1987)

[109] MACRO Collaboration, M. Ambrosio *et. al.*, Astrophysical Journal, **546**, 1038 (2001)

[110] Kamiokande Collaboration, Y. Oyama *et al.*, Physical Review, **D39**, 1481 (1989)

[111] Baksan Collaboration, M.M. Boliev *et al.*, Proceedings of 24th International Cosmic Ray conference (Rome) **1**, 722 (1995)

[112] IMB Collaboration, R. Svoboda *et al.*, Astrophysical Journal, **315**, 420 (1987)

[113] AMANDA Collaboration, J. Ahrens *et al.*, Physical Review, **D66**, 032006 (2002)

[114] http://lisa.physto.se/cgi-bin/edsjo/amanda/flx2ann.cgi

[115] A.Morales, Nuclear Physics Proceedings Supplement, **110**, 39 (2002)

[116] J. Primack, D. Seckel, and B. Sadoulet, Annual Review of Nuclear and Particle Science, **38**, 751 (1988)

[117] S. Golwala *Exclusion Limits on the WIMP-Nucleon Elastic-Scattering Cross-Section from the Cryogenic Dark Matter Search*, Ph.D thesis, University Of Califonia, Berkeley (2000)

[118] DAMA Collaboration, R. Bernabei *et al.*, Physics Letters, **B480**, 23 (2000)

[119] DAMA Collaboration, R. Bernabei *et al.*, Reviews Nuovo Cinemto, **26**, 1 (2003)

[120] CDMS collaboration, R. Abusaidi *et al.*, Physical Review Letters, **84**, 5699, (2000).

[121] CDMS collaboration, R. Abusaidi *et al.*, Physical Review, **D66**, 122003 (2002)

[122] CDMS Collaboration, R. Abusaidi *et al.*, hep-ex/0306001 (2003)

[123] EDELWEISS collaboration, A Benoit *et al.*, Physics Letters, **B545**, 43 (2002)

[124] ZEPLIN Collaboration, D.Cline *et al.*, Proceedings of 4th International Workshop on the Identification of Dark Matter, edited by N.J.C. Spooner and V. Kudryavtsev (2003)

[125] M. Kamionkowski *et. al*, Physical Review Letters, **74**, 5174 (1995)

[126] UK Dark Matter Collaboration, T.J. Sumner *et al.*, Nuclear Physics (Proceedings Supplement), **B70**, 74 (1999)

[127] S. Yoshida et. al. Spin 2000 Proceedings, American Institute of Physics Conference Proceedings, **570**, 343 (2001)

[128] P. Ullio, M. Kamionkowski, and P Vogel, Journal of High Energy Physics, **0107**, 044 (2001)

[129] D. Groom, N.V. Mokhov, I.S. Striganov, Atomic Data and Nuclear Data Tables, **78**, 183 (2001)

[130] C. Saji, *Study of upward-going muons in in Super–Kamiokande* Ph.D. Thesis, Niigata University (2002)

[131] R. Atkins *et. al.*, Astrophysical Journal, **533L**, 119

[132] P.Meszaros, Science, **291**, 5501 (2001)

[133] T. Piran, Physics Reports, **333**, 529 (2000)

[134] C.A. Meegan *et al.*, Nature, **355**, 143 (1992)

[135] http://gammaray.msfc.nasa.gov/batse/grb/lightcurve/

[136] http://www.batse.msfc.nasa.gov/batse/grb/catalog/current/

[137] W.S. Paciesas *et al.*, Astrophysical Journal Supplement, **122**,465 (1999)

[138] J. Kommers *et. al.*, Astrophysical Journal Supplement, **134**,385 (2001)

[139] A. Dar and A. De Rujula, astro-ph/0308248 (2003)

[140] M. Lyutikov and R. Blandford, astro-ph/0210671 (2002)

[141] P. Meszaros, Annual Review of Astrononomy and Astrophysics, **40**, 137 (2002)

[142] D. Guetta *et. al.*, astro-ph/0302524 (2003)

[143] Super–Kamiokande Collaboration, S.Fukuda *et. al.*, Astrophysical Journal, **578**, 317 (2002)

[144] P. Woods, astro-ph/0304372 (2003)

[145] F.P. Gavrill, V.M. Kaspi and P.M. Woods, Nature, **419**, 142 (2002)

[146] R. Duncan and C. Thompson, Astrophysical Journal, **392**, L9 (1992)

[147] B. Zhang, astro-ph/0212016 (2002)

[148] B. Zhang *et. al.*, Astrophysical Journal, **595**, 346 (2003)

[149] G. Ingelman and M. Thunman, hep-ph/9604286 (1996)

[150] A. Stachyra, *A Search for Astrophysical Point Sources of Neutrinos with Super-Kamiokande*, Ph.D thesis, University Of Washington, Seattle (2002)

[151] J. Learned and K. Mannheim, Annual Review of Nuclear and Particle Science, **50**, 679 (2000)

[152] Dutta S.I. *et. al*, Physical Review **D63**, 094020 (2001)

[153] A.M. Stasto, astro-ph/0310636 (2003)

[154] R. Gandhi *et. al.*, Astroparticle Physics, **5**, 81 (1996)

[155] K. Washburn *for the Super-K Collaboration*, Proceedings of International Cosmic Ray conference 2003, Tsukuba, Japan (2003). A. Habig, talk at the Chiba neutrino workshop, August 2003